Search for Physics Beyond the Standard Model in Multi-jet Events Recorded with the ATLAS Detector in p-p Collisions at $\sqrt{s} = 8$ TeV Using the Large Hadron Collider

Kuhan Wang
Department of Physics
McGill University

May 2015

A thesis submitted to McGill University in partial fulfilment of the requirements of the degree of Ph.D.

Abstract

A search for physics beyond the Standard Model with multi-jet signatures is presented using 20.3 inverse fb of proton-proton collision data recorded using the ATLAS detector at the Large Hadron Collider at a center-of-mass energy of 8 TeV. An original fit and extrapolation technique is used to estimate the QCD multi-jet background. No statistically significant deviations from Standard Model predictions are observed. The results are interpreted in terms of model-independent limits on the fiducial production cross section of multi-jet events and model-dependent limits in the context of TeV-scale gravity. The fiducial limits at 95% confidence level on multi-jet production are as low as 0.16 fb and the exclusion power in threshold mass for black hole and string ball production varies from 4.6 to 6.2 TeV for particular models. These results are amongst the most stringent limits on TeV-scale gravity to date.

Résumé

Une recherche d'événements au-delà des prédictions du Modèle Standard est effectuée. Une quantité de 20.3 fb inverses de données, provenant du détecteur ATLAS dans le Grand Collisionneur de Hadrons (Large Hadron Collider; LHC), sur des collisions entre proton-proton d'une énergie de 8 TeV sont analysés dans leur état final consistant d'une topologie à jets multiples. Aucune déviation statistiquement significative des prédictions du Modèle Standard est observée. Les résultats sont interprétés en termes de limites (modèles indépendantes) sur la section efficace fiducial de production d'événements à jets multiple et en termes de limites (modèles dépendantes) dans le contexte de la supergravité l'échelle du TeV. Les limites fiduciaires sur la production de multi-jets sont, avec 95% de confiance, aussi faible que 0.16 fb et l'exclusion de la puissance en M_{Th} varie entre 4.6 à 6.2 TeV pour des modèles particuliers. Ces résultats produisent les plus sévères limites sur les modèles de gravité à l'échelle du TeV jusqu'à présent.

Acknowledgements

The outcome of this dissertation and research could not have been possible without the help of many people. In addition to the many great scientists I was able to work with, I would foremost like to thank my supervisor, Andreas Warburton. Andreas gave me the latitude to define my own research project and provide excellent guidance and counsel during the critical points of my academic career.

At the University of Alberta I worked with Francesc Vives-Vaque, Patrick Czodrowski, Halasya Siva Subramania and Professor Douglas Gingrich who worked extensively on the phenomenology of microscopic gravity states and advised and guided the analysis. Professor Gingrich was also the editor of our internal supporting documentation and paper draft. By taking on these tasks I was given the freedom to focus exclusively on the technical analysis. At CERN I was able to work with Michiru Kaneda who at the time spearheaded the 7 TeV microscopic black hole analysis as his PhD dissertation. I benefited from his insight the majority of the data samples used in this analysis were produced by him. I also benefited from the support of the Exotics Jet+X sub-convenors, in particular, Caterina Doglioni (University of Geneva) who pushed me throughout the analysis. I would also like to thank Ning Zhou (UC Irvine) who succeeded her position and Diego Casadei (University of London) with both of whom I had very useful discussions about the limit interpretations and statistical methods of the analysis. I would like to thank Bertrand Chapleau for getting me started on my authorship task and making it run much faster, and Sue Cheatham for her editing skills. I had very useful help from Michael Stoebe for assistance in the difficult production of multi-jet Monte Carlo samples.

I would like to thank all the friends that I met at McGill, those who have moved on and those who are still present, Francis Duplessis (el franko), Philippe Gigure, Grant Salton, Ginny Phixaykoune, Joel Beaudry, Bertrand Chapleau, Eliot Hijano, Alexander Bellin, Mohammed Harb, Robert Keyes, Michael Stoebe, Benoit Lefebvre, Annabelle Chuinard, Sébastien Prince, Wei Wu and Sam Selmani.

Statement of Originality and Contributions of Co-authors

This analysis was initiated and produced by the TeV-scale gravity multi-jet group of the Exotics working group in the ATLAS collaboration. The members of the group as given by the author list of the internal documentation in alphabetical order are: Aatif Butt, Marco Cardaci, Patrick Czodrowski, James Dassoulas, Yuriy Davygora, Ehud Duchovni, Douglas M. Gingrich, Michiru Kaneda, Itamar Roth, Asif Saddique, Halasya Siva Subramania, Daniel Turgeman, Francesc Vives Vaque, Kuhan Wang, Andreas Warburton.

The author of this dissertation was the principal analyzer and played a leadership role in the group. The new, original background estimation method was developed by the author, Francesc Vives-Vaque, Douglas Gingrich and Patrick Czodrowski. Douglas Gingrich was also the primary editor of the supporting document and paper draft. The trigger efficiency study was performed by Yuriy Davygora. The search algorithm used to test for BSM physics in the unblinded data was developed by Douglas Gingrich. The precursors [1] that went into the analysis were borrowed from the analogous shape invariance method which the author also worked on extensively but was initiated in ATLAS by Halasya Siva Subramania, Aatif Butt and Asif Saddique and Douglas Gingrich. Most of the data and MC samples used in this analysis were produced by Michiru Kaneda.

The author was the primary analyzer of the fit method used in this dissertation. The background estimation, associated uncertainties and studies related to the method unless otherwise stated were completed by the author. The limit calculations and associated uncertainties on the signal samples were also determined by the author. The author was also responsible for the coordination, private production and validation of the multi-jet Monte Carlo samples. In addition, the author guided the analysis through the ATLAS review process, presenting the analysis in the sub-group, group and open circulation approval meetings.

1. These involve the jet definitions, algorithms, cone radii choice.

Public Results

As of the time of submission, the work performed in this dissertation has been approved for public dissemination by the ATLAS collaboration. A preprint has been submitted to the Journal of High Energy Physics. The preprint can be viewed on arXiv as "Search for low-scale gravity signatures in multi-jet final states with the ATLAS detector at $\sqrt{s}$=8 TeV", arXiv:1503.08988v1 and the standalone figures can be viewed at `https://atlas.web.cern.ch/Atlas/GROUPS/PHYSICS/PAPERS/EXOT-2014-02`. In addition, the analysis output data set has been uploaded to HEPData and are available for recasting or further manipulation at `http://hepdata.cedar.ac.uk/view/ins1357199`.

Contents

List of Figures

List of Tables

1
Introduction

This dissertation presents a blinded analysis conducted using proton-proton collision data obtained from the ATLAS detector in 2012 at a center of mass energy of $\sqrt{s} = 8$ TeV. The purpose of the study was to search for physics beyond the Standard Model in the multi-jet final state topology.

The analysis utilized an original method of estimating the background in a data-driven way. In examining 20.3 fb^{-1} of collected data no evidence of new physics is found and model-independent limits on the cross section for multi-jet production are presented. In addition, the results are interpreted in a model-dependent manner in the context of TeV gravity and exclusion contours are presented that constrain the parameter space of several generic models of non-perturbative strong gravity states.

This dissertation begins with a brief overview of the current state of theoretical particle physics and presents a discussion of challenges to the prevailing theory as well as a brief literature review of the state of the art of constraints on strong gravity from experimental results. Subsequent chapters discuss the physical and performance characteristics of the Large Hadron Collider and ATLAS detector. In addition, the usage of Monte Carlo simulation software and its context with respect to the phenomenology of Quantum Chromodynamics (QCD) is briefly reviewed.

The main body of the dissertation consists of the presentation of the data analysis. The discussion begins by categorizing the behaviour of several benchmark strong gravity models of interest and presenting an appropriate methodology with which to approach the analysis. This is followed by a study of the relevant Standard Model physics background processes.

An original method of modeling the Standard Model background using an ansatz empirical function is described and applied. The analysis follows by evaluating various studies to test the validity and robustness of the method and explores the impact of various systematic effects on the background estimation.

A search algorithm that takes into account the impact of the trial factors is discussed and utilized to exclude new physics in the unblinded observed data.

The dissertation is concluded by presenting the physical results in terms of model-independent limits on the fiducial production cross section for multi-jet events and exclusion limits on the existence of new strong gravity physics. The latter is interpreted in terms of microscopic black holes and string ball states.

This dissertation, viewed as an electronic file, displays textual links to Figures and Tables outlined in red, hyperlinks in cyan and bibliographical citations in green. A complete breakdown section by section of the dissertation is given below.

1.1 Overview

Introduction: A summary of the dissertation is given.

Theory: The Standard Model of particle physics is reviewed. The challenges of beyond the Standard Model are discussed. The resolution of the Hierarchy problem via extra dimension models of particle physics is briefly reviewed. The phenomenology of observable strong gravity states is dis-

cussed and the current state of searches for microscopic gravitational signatures is reviewed.

Particle Accelerators and Colliders: A brief introduction to particle accelerators and accelerator physics is presented. The Large Hadron Collider is discussed in terms of its performance requirements and physical characteristics.

The ATLAS Detector: The design and performance of the ATLAS detector and its various components are discussed. The physics of particle detection is briefly discussed as relevant to this analysis.

Monte Carlo and Event Reconstruction: The usage of Monte Carlo software to model collision events is presented in the context of QCD phenomenology and collisions. The software reconstruction of data and simulation events is briefly reviewed.

Analysis: The main work of this dissertation is contained in this section. The data analysis is presented, illustrating the rationale, method and determination of the background Standard Model effects and the evaluation of systematic uncertainties. The search algorithm that is used to test for statistical excess beyond expectations in the unblinded data is discussed.

Results: The physical results in terms of model-independent and dependent exclusion limits are presented in this section. The statistical techniques used to extract such limits are discussed. The results are commented on with respect to theoretical models.

Conclusions: The dissertation is summarized.

2

Theory

2.1 The Standard Model

The Standard Model (SM) of particle physics is the most widely accepted fundamental microscopic theory of nature [1]. The SM is a theory that describes the interaction of three fundamental forces of nature in terms of two types of particles, fermions and bosons. Fermions are the constituents of matter while bosons are the mediators of the forces.

The fundamental forces of electromagnetism and strong and weak nuclear forces are described in terms of particles. The SM particles are considered point-like in space and without substructure; as such they can be said to be fundamental.

The fermions can be divided in two categories based on their interactions. The top two rows of Figure 2.1 describe the quarks which interact through the electromagnetic, and the strong and weak nuclear forces. The bottom two rows are occupied by the leptons which are sensitive to the electromagnetic and the weak nuclear force. In addition, along the columns, the fermions are further divided into identical generations that are only separated by mass.

The mediator particles are known as bosons and propagate the fundamental interactions from fermion to fermion and for some forces amongst themselves.

These are represented in the fourth column by the gluon for the strong nuclear force, the photon for electromagnetic force and the massive $W^{\pm}$ and Z bosons for the weak nuclear force.

The massive property of certain particles is generated via the Higgs mechanism [2], [3]. This mechanism leads to the prediction of an additional heavy particle, the Higgs boson.

The particles are sensitive to a particular interaction via their charge. The quarks are sensitive to strong, weak and electromagnetic interactions and as such are said to carry color, electric and weak charges. The leptons only carry electric and weak charges. Finally for each particle, in a suppressed index, there is an identical anti-particle of the same mass and spin but opposite charge. The SM does not include a description of the fundamental nature of gravity. Mathematically, the SM is a quantum field theory based on the symmetry group,

$$SU(3) \times SU(2) \times U(1), \tag{2.1}$$

that describes the interaction of bosonic spin 1 quantum fields with spin 1/2 fermionic fields. The Lagrangian density [4], [5] representing the SM as bosonic and fermionic fields that transform according to the symmetries (2.1), can be generally written as,

$$L = L_{\text{Dyn}} + L_{\text{M}}, \tag{2.2}$$

where L is divided between a term L_{Dyn} that describes the dynamics of the fields and a term L_{M} that involves the Higgs field and generates the particle masses. The dynamical term itself can be further divided into those involving the com-

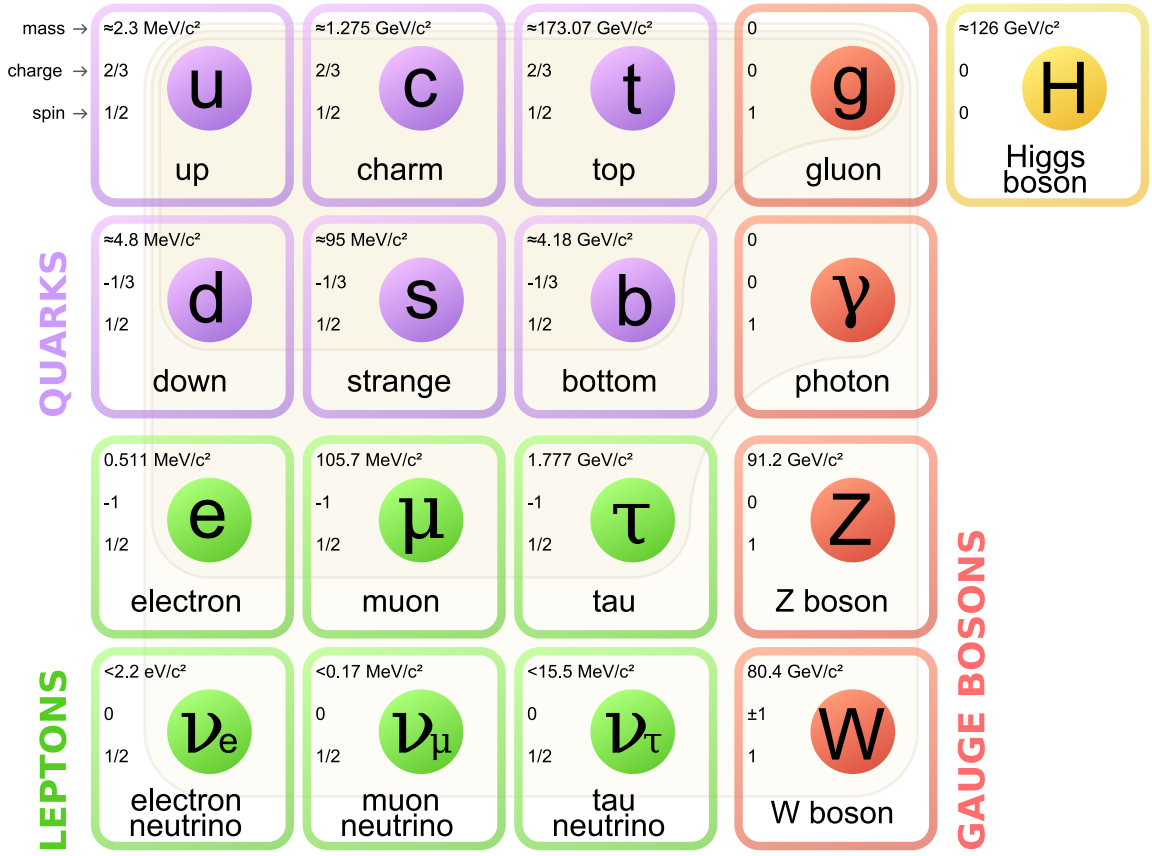

Figure 2.1: The Standard Model of Particle Physics. The fundamental particles are shown for the quarks (purple), leptons (green), gauge bosons (red) and Higgs boson (yellow) with their physical mass, charge and spin [1].

bined electromagnetic and weak (electroweak) interactions and strong interactions, $L_{\text{Dyn}} = L_{\text{EW}} + L_{\text{QCD}}$.

The SM is typically written in a mathematically succinct way that hides complex mathematical structures in condensed or suppressed notation. The hermitian conjugate of a field, ψ is written as $\bar{\psi}$. The slash notation $\not{p}$ is used to describe a contraction indicating tensor multiplication $\gamma^\nu p_\nu$ for two matrices γ^ν and

1. Image credit: `http://commons.wikimedia.org/wiki/File:Standard_Model_of_Elementary_Particles.svg`.

p_ν where the matrices, γ^ν, are the Dirac/Gamma matrices. The covariant derivatives D_μ preserve the form of the dynamical terms in the Lagrangian under the gauge transformations of $SU(3) \times SU(2) \times U(1)$.

2.1.1 Interaction Terms

The electroweak interactions, containing the Quantum Electrodynamic (QED) interactions and the weak interactions, which obey the symmetry $SU(2) \times U(1)$, are described by,

$$L_{\text{EW}} = -\frac{1}{4}B_{\mu\nu}B^{\mu\nu} - \frac{1}{8}tr(\mathbf{W}_{\mu\nu}\mathbf{W}^{\mu\nu}) + i(\bar{Q}\not{D}Q + \bar{u}\not{D}u + \bar{d}\not{D}d + \bar{L}\not{D}L + \bar{e}\not{D}e), \quad (2.3)$$

where the first two terms describe the self-interaction of the electroweak force carriers (known as the gauge bosons). The $W_{\mu\nu}$ and $B_{\mu\nu}$ field strength tensors transform according to $SU(2) \times U(1)$ and can be related to the $W^\pm$, Z, and photon, γ, particles through interaction with the scalar Higgs field.

The terms following correspond to the dynamical electroweak interaction of the quarks, $\bar{Q}\not{D}Q + \bar{u}\not{D}u + \bar{d}\not{D}d$, and leptons, $\bar{L}\not{D}L + \bar{e}\not{D}e$. The weak interaction violates parity symmetry. In addition, there has been evidence of CP symmetry violation in the electroweak sector [2]. In the SM, the left handed fermions Q and L transform as doublets under $SU(2)$ while the the right handed components, u, d, e transform as singlets. Therefore,

$$Q = \begin{pmatrix} U_L \\ D_L \end{pmatrix}, \quad (2.4)$$

2. This was first observed in the decays of the kaon system to two neutral pions [6].

and

$$L = \begin{pmatrix} e_L \\ \nu_L \end{pmatrix}, \tag{2.5}$$

where U_L, D_L, e_L and ν_L represent the "up" and "down" types of the fermions.

The doublet Q can be thought of as representing the left handed up and down quark families (U_L and D_L). The interaction terms are repeated for each generation of fermions in a suppressed index.

The other interaction of the SM is known as the strong nuclear interaction, describing Quantum Chromodynamics (QCD); it is represented by,

$$L_{\text{QCD}} = \frac{1}{4} tr(\mathbf{G}_{\mu\nu}\mathbf{G}^{\mu\nu}) + i(\bar{Q}\not{D}Q + \bar{u}\not{D}u + \bar{d}\not{D}d). \tag{2.6}$$

Analogous to the electroweak Lagrangian [3], the first term represents the self interaction of the gluon fields, while the remaining terms make a reappearance from L_{EW} due to the fact that the quarks couple via both the strong and electroweak forces. Despite the similarities, Quantum Chromodynamics differs significantly from its electroweak counterpart and the full details are discussed below in Section 2.2.

2.1.2 Mass Terms

Without the Higgs field, the SM describes only the interaction of massless fields that can only be interpreted as massless particles. In order to generate

3. There are not two fermion, boson coupling terms, for instance, there is only one $\bar{Q}\not{D}Q$ shared between L_{EW} and L_{QCD} (the sum of $L_{\text{QCD}} + L_{\text{EW}}$ does not give $2\bar{Q}\not{D}Q$). The term is replicated in Equations 2.3 and 2.6 for illustrative purposes, alternatively, the reader may suppose the covariant derivative only contains the respective EW or QCD boson coupling terms in L_{EW} and L_{QCD} respectively.

particle mass, the fermion and boson fields interact with a complex doublet scalar field via the Higgs mechanism [5]. The part of the SM Lagrangian that describes this process is,

$$L_{\mathrm{M}} = D_{\mu}\phi D^{\mu}\phi - V(\phi) + L_{\mathrm{Yukawa}}. \tag{2.7}$$

The first two parts of the equation describe the kinetic motion of the Higgs field and the form of its potential while the last term represents the Yukawa coupling of the SM fermion fields to the Higgs field. These Yukawa terms have the form,

$$\sim g\bar{\psi}\psi\phi, \tag{2.8}$$

where g represents a generic coupling strength, ψ the fermion fields and ϕ the scalar field. It is through these Yukawa couplings that the fermions acquire mass. In terms of the SM this is analogously written,

$$L_{\mathrm{Yukawa}} = f\bar{L}e\phi + h\bar{Q}d\phi + g\bar{Q}u\phi^{*} + \text{Hermitian Conjugates}, \tag{2.9}$$

representing the coupling of the leptons, down type and up type quarks to the Higgs field [4]. Here, f, h and g represent specific couplings of the particle.

The Higgs potential has the form,

$$V(\phi^{\dagger}\phi) = \lambda(\phi^{\dagger}\phi - \frac{\mu^{2}}{2\lambda})^{2}. \tag{2.10}$$

The minimum of the potential can be found at $\phi = \mu/\sqrt{\lambda}$; this is also called the Higgs vacuum expectation value, v. Through interaction with the Higgs field the

4. The indices over fermion generation have been suppressed and f, h and g should be thought of as matrices.

particle masses are generated.

The boson masses are extracted from the first term of equation (2.7) by unpacking it in terms of the Higgs field and are given by,

$$W^{\pm} \equiv g_2 \frac{\mu}{2\sqrt{\lambda}}, \tag{2.11}$$

$$Z \equiv \sqrt{g_1^2 + g_2^2} \frac{\mu}{2\sqrt{\lambda}}, \tag{2.12}$$

where g_1, g_2 are the coupling strengths with respect to $B_{\mu\nu}$ and $\mathbf{W}_{\mu\nu}$. The final mass state is orthogonal to the Z and has zero mass. This is the photon.

In addition, the Higgs self coupling gives the Higgs mass itself,

$$H \equiv \sqrt{2}\mu. \tag{2.13}$$

The fermion masses are similarly obtained by expanding out L_{Yukawa} and they are of the form,

$$M_n \equiv f_n \frac{\mu}{\sqrt{\lambda}}, \tag{2.14}$$

where M_n labels a fermion of type n with coupling constant f_n.

The masses of the heavy bosons and fermions are proportional to the vacuum expectation value through particular coupling constants and in the case of the fermions additionally accounting for their generation and type, and therefore are not known a priori from the theory. They must instead be measured from experiment.

2.2 Quantum Chromodynamics

One of the most important distinctions between Quantum Chromodynamics (QCD) and its electroweak counterpart is the behavior of the strength of their respective couplings to boson and fermion fields [7].

The way in which the coupling constant scales with the energy μ of the particular physical process is known as the "running" and is encoded in the β function of the theory. The quantitative calculation of β functions involve the evaluation of self energy terms of the quark/lepton in QCD/QED [7]. The qualitative effect is as follows; in QED an electron in space is affected by vacuum polarization. The charge of the electron is effectively screened by the "sea" of electron and anti-electron pairs that arise out of the vacuum. These fermion pairs align such that the positive charge is close to the original electron and the negative charge is away from it. The overall effect is to reduce the observed charge strength. Conversely as one moves closer to the electron more of the bare charge is sampled and the charge strength increases.

In QCD the analogous effect occurs with color charge. Vacuum quark, anti-quark pairs create a polarized color charge field in the vicinity of a bare quark thus reducing the observed color charge at large distances. In QCD, however, the gluons themselves also carry color charge and form vacuum pairs. The effect of these gluon-gluon pairs is to counter-intuitively "anti-screen" the bare quark color charge. The overall net effect of screening and anti-screening is determined by the number of types of quarks and gluons.

The running of QCD is,

$$\alpha_{\rm s} = \frac{\alpha(\mu_R^2)}{1 - \beta_0 \alpha(\mu_R^2) \ln(Q^2/\mu_R^2)}, \tag{2.15}$$

where Q is the scale of process and μ_R is the renormalization scale, the reference scale of the calculation [5] and α_s represents the strength of the coupling of QCD interactions as a function of the scale of the interaction process Q. For instance in a collider experiment Q can be the total momentum exchanged between two incoming quarks.

The term, $\beta_0 = (2N_{\rm q} - 33)/12\pi$ determines the behaviour of the running . For a theory with less than 16 types of quarks, $N_{\rm q} < 16$, $\beta < 0$ and the running increases for lower μ. Therefore, at high energy scales the theory is weakly coupled and perturbative methods are useful but at low energy scales QCD is strongly coupled and perturbation theory breaks down. The theory is said to have asymptotic freedom. This is contrary to QED where the coupling strength decreases with distance away from the charged fermion and increases closer to it. Figure 2.2 shows the running of $\alpha_{\rm s}$ as measured by a number of particle physics experiments.

In addition, QCD has the property of color confinement. In QED when two opposite charges are separated the force between them decreases rapidly with distance. In QCD, the gluons carry a color charge and the force between two oppositely colored charges increases as the distance between them grows. As in QED, where charge-neutral bound states are energetically favoured over charged bound states, color-neutral bound states are formed in QCD. However, because of con-

5. The renormalization scale, μ_R, is not a physical scale. A measurement of α will depend on Q, the scale of the measured process. The renormalization scale represents the scale beyond which corrections to the calculated value of $\alpha_{\rm s}$ are discarded.

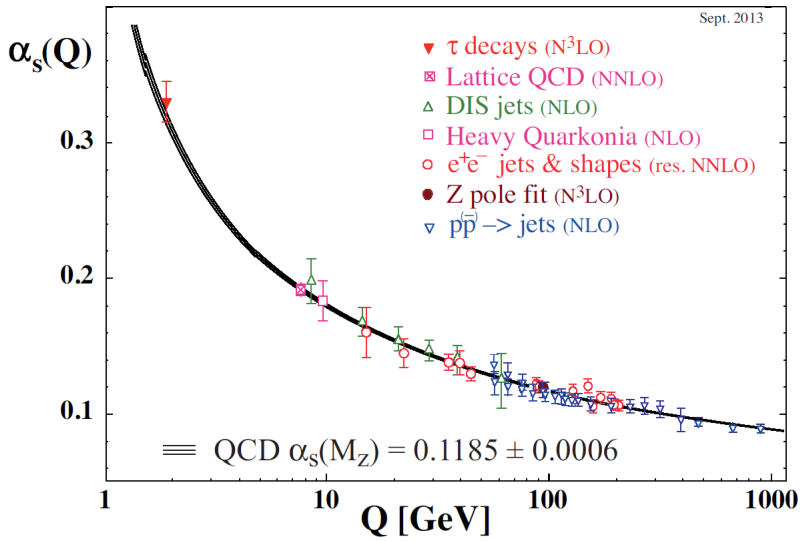

Figure 2.2: The strong coupling constant α_s as a function of Q, for a number of experimental and calculated results compared with theoretical predictions (solid black line) [1]. The asymptotic freedom of QCD is apparent as α_s is dependent on the energy scale Q of the observed process.

finement, bare quarks and gluons are not observed in nature. When two quarks are pulled apart the force between them increases linearly with distance and at some point it will become energetically more favorable to create a quark, anti-quark pair out of the vacuum than to continue to allow the original two quarks to separate and instead two bound states of quarks are formed from the original single state.

2.2.1 Hadrons

The confined nature of QCD implies that only bound states of quarks can be experimentally observed. For largely historical reasons the constituents of hadrons are known as partons. There are six flavors of quarks in nature that are divided

into three generations. Of these six, five are able to form bound states [6]. These bound states of quarks are referred to as hadrons and the process of evolving from the final state quark level particles to the actual observed bound states is known as "hadronization".

Only color neutral bound states are observed in nature and as such the quantitative composition of hadrons is restricted. States consisting of a quark and anti-quark pair are known as mesons. In addition, it is possible to form color neutral states out of three quarks or three anti-quarks. These are known as baryons and include the familiar protons and neutrons.

The measured mass of a hadron is shared between its constituent partons (quarks) and the vacuum energy of quark-anti-quark fluctuations. A hadron is a bound state of quarks in motion; at any given time the momentum of individual quarks is not well defined. This non-perturbative nature of the quark interactions within a hadron is expressed in terms of parton distribution functions (PDF). A PDF describes the momentum distribution of a given type of parton in a given hadron probed at a given energy scale and is not calculable from first principles. PDF's must be created via analyzing experiments that probe the hadron structure at various energy scales. A PDF will typically show the fraction of the total hadron momentum that is carried by the parton. The sum of all PDF's for a hadron integrated over the momentum space must be unity. The PDF of the proton is shown in Figure 2.3.

6. The outlier is the massive top, t quark, which has an extremely short life time (half-life $< 10^{-23}$ seconds) and decays before it can form into a hadron.

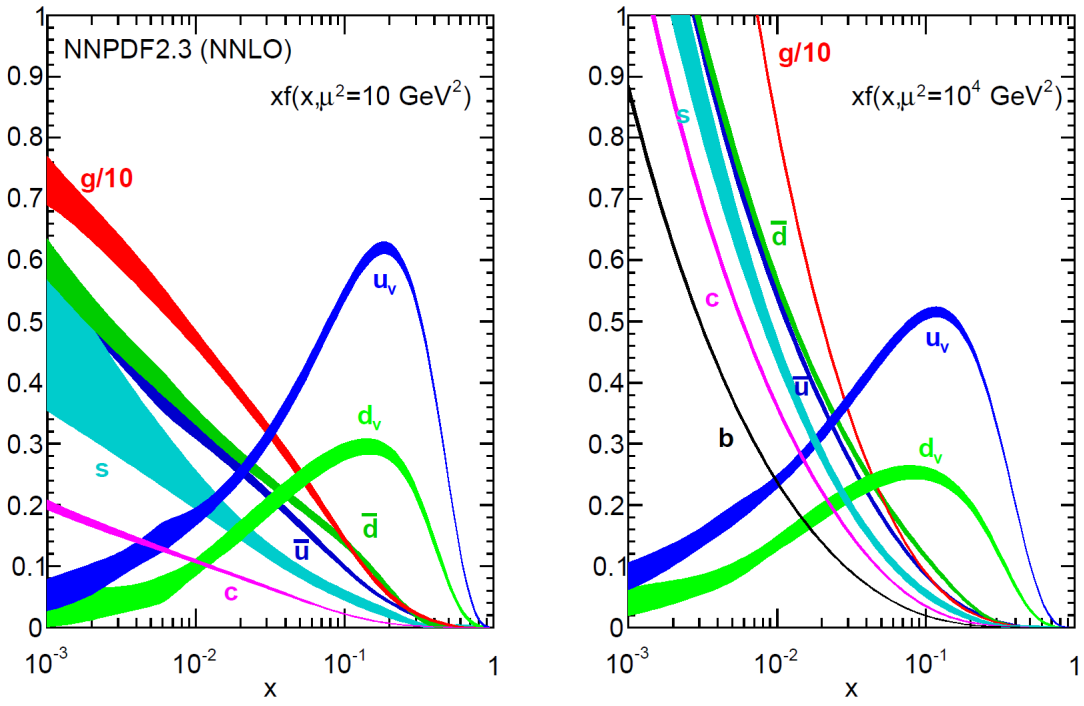

Figure 2.3: The parton distribution functions of the proton at two probe scales, $\mu = 10^2$ GeV^2 (left) and $\mu = 10^4$ GeV^2 (right) calculated using experimental data [1]. Notice the constituent partons consist of not only the original quarks u_v and d_v but the combination of vacuum fluctuations of other quarks, $\bar{u}, \bar{d}, s, c, b$ and gluons g depending on the probe scale. The internal structure can change dramatically depending on the scale of the probe, as is illustrated in the two plots. The anti-quarks $\bar{c}, \bar{s}, \bar{b}$ approximate their matter counterparts. The thickness of the bands represents the uncertainty.

2.2.2 Jet Phenomenology

Bare quarks have heretofore never been observed in nature. Instead particle detector experiments observe the experimental signature of hadrons. For instance, in a collider experiment the final state quarks would undergo hadronization and the final observed particles result in collections of these bound states in the form of "jets". It is important to recognize that jets are not fundamental particles; they are a utilitarian description of hadrons.

These jets consist of collimated bundles of hadrons and their decay particles.

A jet can also contain an electromagnetic component due to further secondary decay. As jets are not fundamental particles, the definition of what is a jet is particular to the algorithm used to create it. Broadly speaking, in a particle detector experiment, a jet algorithm can create jet objects by categorizing and separating calorimeter energy deposits or some other input constituents into groups that are roughly conical in geometry. Different jet algorithms can produce jets with different four vectors and even different numbers of jets.

Modern jet algorithms typically have two important features. The number of final jets identified by the algorithm and their four vectors should not change if any particular jet is replaced by two colinear jets or if any jet is replaced with the same jet and an additional infinitesimal soft radiation component. These two features are known as colinear and infrared safety [7]. The specific Anti-k_t algorithm [8] used in this analysis for jet finding is discussed in Section 5.2.1.2.

2.3 Beyond the Standard Model

As of the time of writing, the SM is a theory that has stood up to the rigorous examination of experimental particle physics. The results of particle-detector-based experiments have uniformly confirmed the SM theoretical predictions. Nevertheless, there have been experimental hints over the years as to the incompleteness of the SM.

Several of the most well known of these deficiencies are the existence of

7. Consider the differential cross section for the production of two quarks through an s-channel process by electron-positron annihilation; the cross section to additionally emit a gluon from either outgoing quark diverges if the gluon is exactly aligned (colinear) with its parent quark, or if it is infinitely soft (infrared). Therefore, any quantity or observable defined with respect to such a cross section must go to zero in these kinematic regions. They must be colinear and infrared safe.

neutrino oscillations [9], the existence of dark matter [10] and a lack of any description of the gravitational force. A well known issue of the SM is the "Hierarchy" problem.

2.3.1 The Hierarchy Problem

The strengths of the fundamental forces exist in a hierarchy of scales proceeding from strongest to weakest according to strong, electromagnetic, weak and gravitational. The energy scale of the electroweak interaction is of the order of magnitude of the heavy boson masses, $\sim 10^2$ GeV/c^2. The gravitational scale can be heuristically estimated from the Newtownian gravitational constant, $G = 6.67 \times 10^{-11}$ Nm^2/kg^2. Inverting this and with some dimensional analysis, $M_{\mathrm{Pl}} = \sqrt{\hbar c/G}$, where M_{Pl} is the Planck mass [8], defined in terms of $\hbar$, the reduced Planck constant and the speed of light c. The value is $M_{\mathrm{Pl}} = 2.4 \times 10^{18}$ GeV/c^2. Thus the electroweak scale and the fundamental gravitational scale differ by approximately $\sim 10^2/10^{18} = 10^{-16}$.

Such a large discrepancy in scale is unusual and considered unnatural from a theoretical perspective. This problem is manifest in multiple ways but the most well known is likely the calculation of the square of the Higgs Boson mass. A calculation of the Higgs boson mass shows that it must receive correction factors due to internal loops from all massive particles. These radiative corrections can be expected to grow as the energy scale approaches the Planck scale. As of the time of writing, the tentative Higgs boson mass is measured to be ~ 125 GeV/c^2. In principle, radiative corrections to the Higgs boson can lead to contributions to

8. To explicitly obtain units of energy, dimensional analysis can be used to add and subtract the appropriate number of $\hbar$'s and c's.

the square of the mass up to the Planck energy scale $\sim 10^{18}$ GeV. Therefore, the observed Higgs boson mass appears unnaturally small in comparison.

The Hierarchy problem is colloquially posed as: "why is the difference between electroweak and gravitational scales so large?"

2.3.2 TeV-scale Gravity

A number of solutions to this problem have been proposed over the years. In the large extra dimension model, [11], [12], of TeV-scale gravity the hierarchy of scales is explained by embedding the SM in a higher spatial dimension theory. In such a theory the SM forces can only propagate on a surface while gravity can freely propagate through the entire bulk. Thus, the effective gravity measured on the surface is reduced due to "leakage" into the additional dimensions that are not accessible to SM forces. Intuitively, the relevant parameters of such a theory must be the number of extra spatial dimensions n and their size R.

A simple heuristic argument of this type of theory is given. The force of macroscopic gravity is described by,

$$F = G\frac{m_1 m_2}{r^2}. \tag{2.16}$$

In a theory with n extra spatial dimensions the simple modification is,

$$F = A\frac{m_1 m_2}{r^{2+n}}, \tag{2.17}$$

where A is the now true gravitational constant. At some intermediate distance scale, between the macroscopic and microscopic scale, they would be expected to

match and thus,

$$G = A\frac{1}{R^n}, \tag{2.18}$$

the observed gravitational scale is weak because it is suppressed by a factor related to the number and size of the extra dimensions. In this formulation the Hierarchy problem is no longer a problem as the fundamental gravity scale is lowered in energy and what is observed is a "screened" gravitational strength. In these large extra dimension models the hierarchy between the weak and gravitational scales is replaced by a hierarchy between the weak scale and the size parameter of the dimensions, R.

Alternatives to the large extra dimension models, "warped" metric models, [13], [14], resolve the hierarchy of states by identifying the observed gravitational effects as exponentially suppressed by a "warp" factor that is a function of the length scale of a single extra dimension. In these models, the metric of space time is taken to be of the form,

$$ds^2 = e^{-2kr_c\phi}\eta_{\mu\nu}dx^\mu dx^\nu + r_c^2 d\phi^2, \tag{2.19}$$

where the first term represents the regular 3+1 dimensions and ϕ is the coordinate of a single extra dimension and r_c is the length of the extra dimension, which is set in terms of a scaling parameter, k. The normal 3+1 dimensions (3-brane) are exponentially coupled to the extra dimension. In such a theory it can shown that a mass measured on the 3-brane is suppressed by a factor $e^{-kr_c\pi}$ with respect to its intrinsic mass. Thus the observed gravitational strength is exponentially suppressed by the "warp" factor. The exponential factor ensures that the hierarchy

problem is not recast in terms of kr_c as $kr_c \approx 50$ is sufficient to reproduce the known electroweak-gravitational hierarchy.

These models allow for the production of non-perturbative gravity states beginning at some threshold energy scale. These include the formation of microscopic (thermal) black holes, quantum and string balls.

In the absence of the observation of such states it is possible to set limits on the threshold for the production of such states by excluding regions of parameter space for the existence of such objects as microscopic black holes, quantum black holes and string balls.

There is therefore a powerful incentive to conduct such an analysis, especially at collider experiments which can be optimally suited to produce and observe the decay signatures of such objects.

2.3.2.1 Phenomenology

Gravity states such as thermal black holes and string balls are treated general relativistically in collider experiments [15], [16]. As such they are analogous to stellar black holes in higher dimensions in the treatment of their phenomenology. Let M_{D} be the equivalent Planck mass to M_{Pl} in the higher dimension theory ($M_{\mathrm{D}} < M_{\mathrm{Pl}}$); for states which have masses, M, on the order of M_{D} a quantum theory of gravity is necessary for quantitative understanding. This analysis is not sensitive to such so called quantum black holes. For the case where $M >> M_{\mathrm{D}}$, the formation and evaporation of gravity states such as black holes is well understood within the context of general relativity and these states are often labeled microscopic or thermal black holes. The following discussion is made within the latter context.

When the impact parameter of two initial state particles approaches within the Schwarzschild radius, r_h, determined by their combined mass a black hole is formed. Therefore, the intrinsic cross section for black hole production goes as,

$$\sigma_{bh} \sim \pi r_h^2. \tag{2.20}$$

The black hole production cross section is related to the mass of the black hole, M, the number of spatial dimensions, n through r_h. In addition, the black hole can have angular momentum, J. The form of r_h can be written,

$$r_h^{n-5}(r_2^h + \frac{(n-2)^2 J^2}{4M^2}) = \frac{16\pi G_n M \Gamma(n-1/2)}{(n-2)2\pi^{(n-1)/2}}, \tag{2.21}$$

where G_n is the fundamental n dimension gravitational scale and Γ is the Gamma function. These states decay via Hawking radiation into a thermal (Boltzmann) spectrum of particles.

In a hadron collider experiment the intrinsic production cross section, equation (2.21), scales with center of mass energy, $\sqrt{s}$, through M but the proton-proton collision production cross section [17], [18] must be convolved with the parton distribution functions of the colliding hadrons which describe the momentum fraction, x, of the individual partons. Therefore, the production cross section goes as,

$$\sigma_{pp\to bh}(\tau_m, s) = \sum_{ij} \int_{\tau_m}^{1} d\tau \int_{\tau}^{1} \frac{dx}{x} f_i(x) f_j(\tau/x) \sigma_{bh}(\tau s), \tag{2.22}$$

where $\tau = x_i x_j$ is the fraction of the square of the center of mass energy that the colliding partons i and j possess and τ_m is the minimum cut-off value of τ for which the black hole can be produced.

These microscopic black holes evaporate into a thermally distributed spectrum of particles. The black hole can emit radiation into both the 3+1 dimensions of the SM, referred to as the brane, and into any possible extra dimensions, the bulk. For radiation into the brane, the SM particles are assumed to be the only available channels. The radiation into the bulk is in the form of gravitons and may possibly be inferred through missing energy studies.

For emission into the brane, the particular type of particles the black hole emits is governed by the grey body factors as in general relativity [15], [19]. The emission rate of particles from the black hole per unit of time, t, and energy, E, is given by,

$$\frac{d^2N}{dEdt} = \frac{1}{2\pi}\frac{\gamma_{i,E,l,m,\lambda}}{\exp(E - m\Omega/T_{\rm H}) \mp 1}, \tag{2.23}$$

where Ω is the angular frequency of the black hole and spin statistics is accounted for fermions and bosons by ∓ 1. Therefore, the grey body factor, $\gamma_{i,E,l,m,\lambda}$ modifies the pure black body decay spectrum and distinguishes particles by their attributes such as energy E, angular quantum numbers, l, m and polarization, λ.

The relative emission of different particle types is governed by their spin through the grey body factors. For SM particles with six flavours of quarks, three color charges, three types of leptons and two electric charges, in 3+1 dimensions the relative emission is estimated to be 72%:11%:8%:6%:2%:1% [15] for a non-rotating black hole. The ratio represents quarks and gluons:leptons:heavy gauge bosons:neutrinos:Higgs boson:photons.

Thus, the dominant mode of decay with respect to the SM is into the hadronic sector with smaller electroweak contributions.

The number of particles that are evaporated will go as the entropy, S, of the black hole. The average number of particles, $\langle N \rangle$, can be written as,

$$\langle N \rangle = \frac{2\sqrt{\pi}}{n+1} \left(\frac{M}{M_{\mathrm{D}}} \right)^{\frac{n+2}{n+1}} \left(\frac{8\Gamma(\frac{n+2}{3})}{n+2} \right)^{\frac{1}{n+1}} . \tag{2.24}$$

The evaporation is characterized by relatively large particle multiplicities [17]. As an example, for a model with two extra dimensions $n = 2$, and ratio of black hole to fundamental Planck mass $M/M_{\mathrm{D}} = 5$, $\langle N \rangle \sim 15$.

As the black hole evaporates its radius will contract. At some point a transition will occur and the general relativistic description must break down as quantum effects become non-negligible. In string theory this transition occurs when the Schwarzschild radius of the black hole approaches the string length, l_{s}. The black hole can be theorized to make a transition into a state dominated by a single highly excited long string, so called "string ball" [20]. Such states will continue to lose mass via evaporation, now characterized by the Hagedorn temperature [21]. The emission process can be similarly characterized as in the case of black holes with possible decay into the bulk and brane. As in the case of black holes the largest contributions come from the hadronic sector due to the density of states and thus the observation of a large number of high transverse momentum jets is an important signature.

2.3.3 Current Experimental Constraints

As of the time of writing a number of public results from the ATLAS and CMS collaborations have been released that search for strong gravity states in a

variety of different physics channels [9]. No evidence of new physics has been positively confirmed; the unblinded results have conformed to SM predictions. The resulting, calculated, limits are the most stringent in the world.

Table 2.1 details the current experimental limits in the respective channels for microscopic black hole models and string balls.

Physics	Channel	Limit [TeV]	$\sqrt{s}$ [TeV]	Lumi
ADD Extra Dimensions [10]	jet + E_T^{Miss}	$M_D > 2.5$ at $n = 6$ [22]	7	4.7 fb^{-1}
Black Hole	$\mu\mu$	$M_{Th} > 4.4$ at $M_D = 4$ [23]	8	20.3 fb^{-1}
Black Hole	l + jets	$M_{Th} > 5.7$ at $M_D = 4$ [24]	8	20.3 fb^{-1}
Black Hole	multi-jets	$M_{Th} > 5.7$ at $M_D = 4$ [25]	8	12.1 fb^{-1}
Black Hole	multi-jets	$M_{Th} > 3.5$ at $M_D = 3$ [26]	7	35 pb^{-1}
String Ball	$\mu\mu$	$M_{Th} > 4.9$ at $M_S = 1.7$ [23]	8	20.3 fb^{-1}
String Ball	l + jets	$M_{Th} > 5.4$ at $M_S = 1.7$ [24]	8	20.3 fb^{-1}
String Ball	multi-jets	$M_{Th} > 5.4$ at $M_S = 1.7$ [25]	8	12.1 fb^{-1}

Table 2.1: Current experimental limits in fundamental mass units M_D / M_S, threshold mass M_{Th} for various BSM searches conducted at the LHC by the ATLAS and CMS collaborations. The cited limits represent the best case model-dependent results, for specific models the results may be worse.

Searches for microscopic black holes in the same sign dimuon [23], single lepton+jets [24] and multi-jet [25] channels have excluded threshold masses up to 4.8 and 5.7 TeV at $M_D = 4$ TeV respectively for models with six extra dimensions [11]. These searches typically develop exclusion contours in the space of M_{Th} vs M_D, where the level of exclusion in threshold mass for black hole production is read as a

9. Searches for strong gravity effects are signature based. The evaporation of a black hole is governed by the grey body factors as discussed in the previous section. The term "channel" in this dissertation refers to the particular component(s) of the overall evaporation that the search is focused on.

10. The abbreviation is for Nima Arkani-Hamed, Savas Dimopoulos, and Gia Dvali, the authors of the original paper in 1998 discussing the framework of extra spatial dimensions [11].

11. Models with more dimensions result in higher fiducial acceptance, therefore generally speaking the most optimistic limits are quoted in contrast to quoting limits of models with smaller number of dimensions.

function of the fundamental Planck mass M_D of the model. A weaker 7 TeV multi-jet limit by ATLAS, produced as a conference proceeding [26], does not extend the exclusion contour to $M_{\mathrm{D}} = 4$ TeV; the result provides $M_{\mathrm{Th}} > 3.5$ TeV up to $M_{\mathrm{D}} = 3$ TeV. In the ATLAS search looking for a final state with a single jet recoiling against missing transverse energy, $\mathrm{E_T^{Miss}}$ [22], the most powerful discrimination excludes M_D up to 2.5 TeV for all models with $n = 6$ extra dimensions within the ADD framework.

For string balls the exclusion limits in the dimuon [23] and lepton+jets [24] channels are directly comparable using their respective exclusion contours with the former generally providing a better limit. The CMS multi-jet analysis [25] did not publish an exclusion contour in the space of M_{Th} versus M_{S}; only the exclusion limit at $M_S = 1.7$ TeV is available and can be inferred as $M_{\mathrm{Th}} \sim 5.4$ TeV. For Table 2.1, the ATLAS channel results have been quoted at the identical M_{S} to allow direct comparison, however it cannot be concluded if the CMS result matches the ATLAS lepton+jets result at all values of M_{S}.

No multi-jet final state analysis has ever been published by the ATLAS collaboration. In the same channel the CMS collaboration has published results at 7 TeV and 8 TeV showing competitive limits [27], [28], [25] using a maximum of 12.1 fb^{-1} of p-p collision data at 8 TeV. The principle background estimation technique of the CMS searches uses the shape invariance hypothesis. An application of an analogous method in the ATLAS collaboration is fully documented in the following dissertation [29]. The present author collaborated extensively on this method before the analysis was shifted to the present method in this dissertation, so as to not impinge on the work of [29]. The method of shape invariance and the rationale for utilizing a different approach with respect to CMS is discussed in Appendix B

only in so far as it is relevant to the current analysis.

This dissertation represents the latest ATLAS collaboration BSM search for strong gravity states in the multi-jet channel as of the time of submission.

3

Particle Accelerators and Colliders

3.1 Overview

Particle accelerators have a long history. Early cyclotron accelerators used a constant magnetic field to fix particles in a spiral pattern, gyrating outwards from the center and accelerated them with a rapidly changing electric field.

A basic schematic of a cyclotron is shown in Figure 3.1. The particle is injected at the center of the cyclotron, two electrodes hold a rapidly varying electric field between them. As the particle crosses the field it is accelerated. A constant magnetic field in the perpendicular direction gyrates the particle allowing it to repeatedly sample the field until it reaches the outer circumference and is passed off to the detector experiment.

3.1.1 Synchrotrons

A further refinement of the cyclotron is the concept of the synchrotron. A synchrotron is defined by the synchronization of the accelerating electric field with the guiding magnetic field such that the accelerated particles are maintained in a constant orbit even as their energies increase. Whereas the maximum achievable energy with a cyclotron is limited by the strength of the holding magnetic field

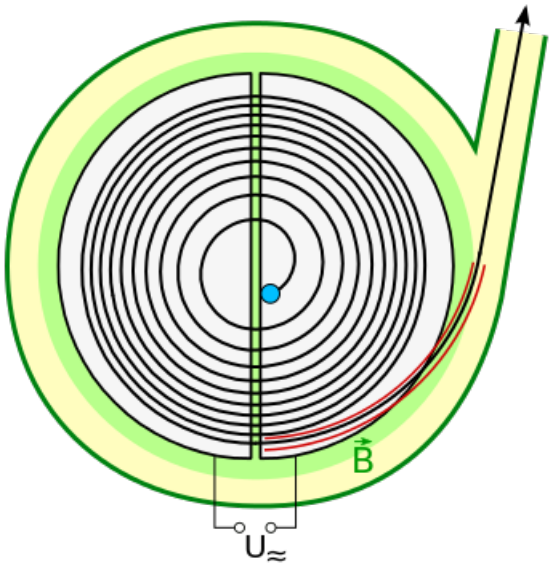

Figure 3.1: A basic diagram of a cyclotron. A charged particle is placed at the center of the spiral and is accelerated each time it cross the potential gap between the two half disks. Under a constant magnetic field it follows a spiral path outwards [1].

and the physical space required to hold a particle in an outward spiral trajectory, a synchrotron can maintain particles in a constant orbit. Therefore, instead of a solid disk-like structure a synchrotron may be built as a ring.

A synchrotron accelerator uses a radio frequency cavity to accelerate particle bunches. Dipole bending magnets are used to bend the moving particles into a closed loop. Unlike a cyclotron, the magnetic field that guides the particles is increased with each successive revolution as the particle gains velocity. The upper limit on the achievable energy for the accelerated particles is then limited by the strength of the guiding magnetic system, physical radius of the ring and synchrotron radiation loss.

1. Image credit: `http://upload.wikimedia.org/wikipedia/commons/8/8e/Zyklotron_Prinzipskizze02.svg`.

3.2 The Large Hadron Collider

The Large Hadron Collider (LHC) is a synchrotron particle accelerator located in the suburbs of Geneva, Switzerland [30]. Its construction and maintenance was and is undertaken by an international collaboration through the European Organization for Nuclear Research (CERN). CERN consists of 21 member states that are geographically within or close to Europe, a handful of observer states and a large number of non-member states around the globe with co-operation agreements (of which Canada is one).

The LHC project can be thought of as a successor to the Large Electron Positron collider project at CERN. The LHC project was initiated in March 1984 at a physics workshop in Lausanne but due to funding and political constraints full approval was not received until 1994. Construction began in 1998 and was completed in 2008. The first beam collisions occurred on November 23, 2009 and the week after the LHC officially became the most powerful particle accelerator in the world by colliding proton beams with 1.18 TeV per beam. Since then, the LHC has recorded data at increasing beam energy and luminosity. In February 2013, the LHC entered a long shutdown period in preparation for machine upgrades in order to sustain collisions at a center of mass energy of $\sqrt{s} = 13$ TeV that will begin in 2015.

The LHC is contained within a 27 kilometer tunnel and hosts five major particle detector experiments. These are **A** **T**oroidal **L**HC Apparatu**S** (ATLAS), **C**ompact **M**uon **S**olenoid (CMS), **LHC** **b**eauty (LHCb), **A** **L**arge **I**on **C**ollider **E**xperiment (ALICE) and **TOT**al **E**lastic and diffractive cross section **M**easurement (TOTEM).

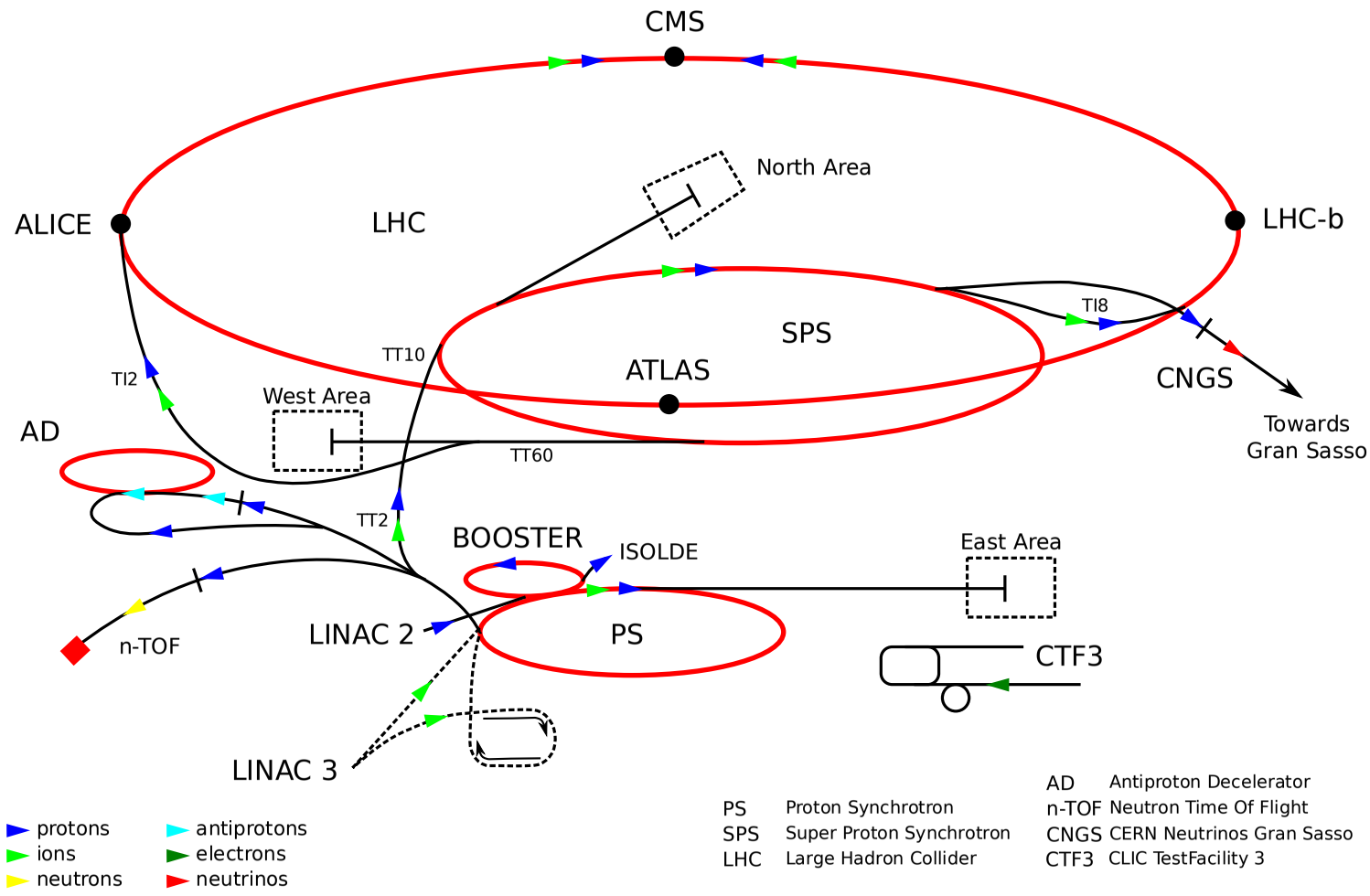

Figure 3.2: A schematic overview of the LHC facilities and the major detector experiments.

3.2.1 Machine Characteristics

The LHC is capable of proton-proton or heavy ion, Pb-Pb collisions. The LHC is proton-fed by an injection system as shown in Figure 3.3. Hydrogen gas is used as a source of protons. A linear particle accelerator (LINAC) first accelerates the protons to 50 MeV. They then enter the first of several synchrotron boosters in which the proton energy is increased to 1.4 GeV, 25 GeV and 450 GeV. The final booster, the Super Protron Synchrotron, dumps the proton bunches directly into the main LHC synchrotron ring. The production of heavy ion lead particles follows an analogous method.

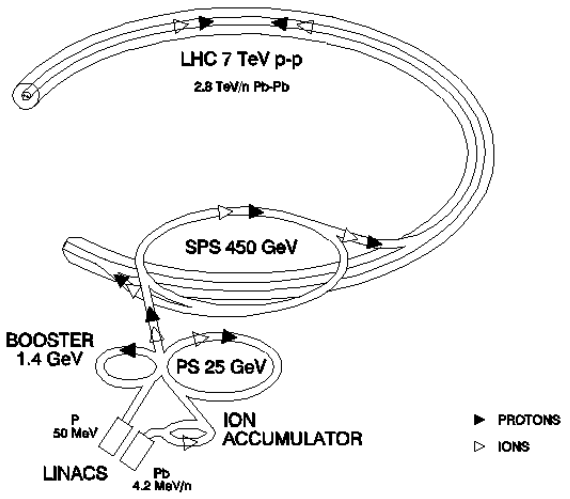

Figure 3.3: The injection apparatus of the LHC [30].

Within the main cavity, the protons are guided by a superconducting magnet system around the ring. The magnetic system consists of magnetic dipoles that are capable of reaching field strengths in excess of 8 Tesla. A schema [2] of this is

2. Image credit: `http://upload.wikimedia.org/wikipedia/commons/b/ba/Cern-accelerator-complex.svg`.

shown in Figure 3.4. In order to achieve such field strength requirements the LHC uses NbTi superconducting cables cooled to below 2 K using superfluid Helium.

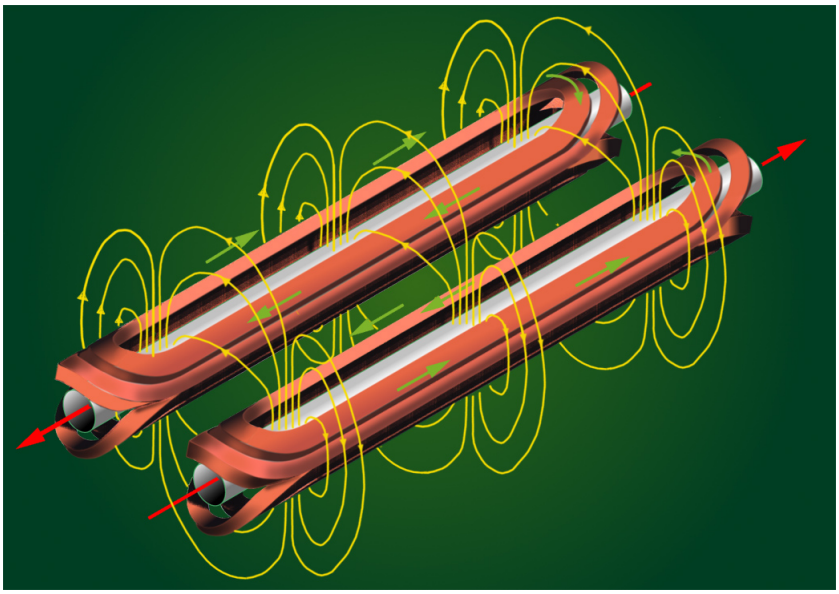

Figure 3.4: A schematic overview of the magnetic dipole system that guides the proton beams within the main LHC cavity [30].

Within the main cavity, the particle acceleration and storage is provided for by a 400 MHz radio frequency injector system. The system consists of a series of eight cavities where an oscillating radio frequency electric field provides an accelerating gradient of 5 MV/m per cavity. Thus for a proton that completes in excess of 10,000 revolutions per second the gain in beam energy is $\sim$0.18 TeV/s. Therefore, within 20 minutes it is possible to reach the peak beam energy.

Finally, a dedicated beam dump system exists to extract the beams from the main ring and pass them to an absorber material. At its peak performance the LHC machinery will be capable of delivering proton beams in 25 ns bunches with $\sqrt{s} = 14$ TeV and instantaneous luminosity of $10^{34}\,\mathrm{cm}^{-2}\mathrm{s}^{-1}$. In addition, as a heavy ion collider the LHC extracts Pb ions from vaporized lead and is able to

collide them at $\sqrt{s}$=2.76 TeV and with a luminosity of $10^{27}\,\mathrm{cm}^{-2}\mathrm{s}^{-1}$.

3.3 Detector Experiments

The LHC is host to several detector experiments. Of these the two major general purpose experiments are:

ATLAS, **A T**oroidal **L**HC Apparatu**S**, which is designed to search for new physics beyond the SM and to conduct precision tests of it. It is designed to operate at a beam luminosity of $10^{34}\,\mathrm{cm}^{-2}\mathrm{s}^{-1}$. The detector is based around a non-compensating sampling calorimeter core. Efficient and precise tracking is provided for by an inner detector system (ID) based around semiconductor and pixel detector tracking technology. Muon detection and measurement is handled by a spectrometer system that encases the calorimeter and is based around the measurement of muon tracks using superconducting toroid magnets.

ATLAS is the detector experiment used in this dissertation and will be extensively discussed in Section 4.

CMS, **C**ompact **M**uon **S**olenoid, is a companion detector to ATLAS. The physics program of CMS is broadly similar to ATLAS and the two serve as experimental confirmation of one another's results in the event of new physics discoveries and detector calibration. The CMS detector is primarily distinguished from its ATLAS counterpart by the presence of a large 4 Telsa solenoid magnet that forms the core of the detector and is used to measure the charge to mass ratio of particles. In addition, the CMS particle ID, and calorimetry have slightly different performance with respect to

their ATLAS counterparts due to differing choice of materials. In the case of the ID the total usage of silicon for tracking technology leads to a improvement in tracking performance. The choice of brass for the hadronic calorimetry worsens its performance with respect to ATLAS.

In addition to these general purpose detector experiments several smaller refined experiments aimed at examining specific physical processes are present at the LHC.

LHCb, **LHC b**eauty is a fixed target experiment dedicated to searching for and measuring CP violation in the decay of neutral and charged B mesons

ALICE, **A L**arge **I**on **C**ollider **E**xperiment, is a heavy ion collider detector experiment. As the LHC is capable of Pb-Pb collisions (as well as p-Pb), the physics program of ALICE is designed to explore the phase diagram of QCD, the effects of quarks and gluons in high pressure and temperature environments.

TOTEM, **TOT**al **E**lastic and diffractive cross section **M**easurement, is a experiment designed to examine elastic and diffractive physics and to measure the total p-p collision cross section. Its goal is to examine physics at the low energy QCD regime, including processes that are not well understood, such as diffractive scattering.

4

The ATLAS Detector

4.1 Overview

ATLAS is a detector experiment for the LHC based at CERN. It is an international collaboration of some 3000 scientists in 175 institutions in 38 countries around the world. ATLAS is a high performance detector designed to search for new physics and test the current SM of physics. Its design is based around several central criteria [31], [32],

Calorimetry, electromagnetic calorimetry with the ability to separately identify electrons and photons and hadronic calorimetry with accurate and precise jet energy measurements.

Muon Spectrometer, high precision momentum measurement of muons using a spectrometer design.

Tracking, high efficiency tracking in intense beam luminosity environments, especially with regards to object identification in terms of leptons and heavy quarks.

Hermeticity, complete coverage in the azimuthal angle and excellent coverage in the forward regions of the detector.

Trigger and Data Acquisition, a trigger system that is able to provide high acceptance for most of the targeted physics of interest.

4.2 Geometry and Notation

In collider physics it is useful to define a coordinate system suitable to the geometry of the accelerator. A coordinate system is illustrated in Figure 4.1 and defined with the nominal interaction point at its origin. The positive x and y directions are defined with respect to the center of the ring and the surface. The positive and negative z directions are defined with respects to the ends of the ATLAS detector which are labeled "A" and "C".

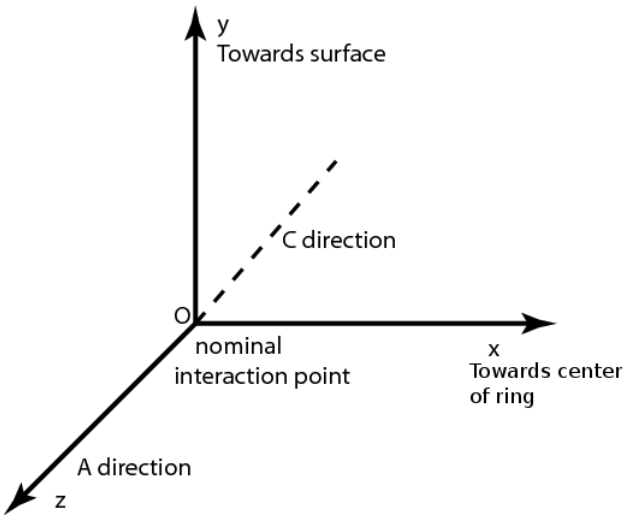

Figure 4.1: The ATLAS detector coordinate system.

In collider physics it is useful to define a particle's rapidity, y,

$$y = \frac{1}{2} \ln \left(\frac{E + p_z}{E - p_z} \right), \tag{4.1}$$

where E and p_z are the particle's energy and its momentum with respect to the beam axis. The rapidity has the useful property of differing only by a constant between any two reference frames under Lorentz boost in the z direction. Thus the difference in rapidity between any two particles is Lorentz invariant in the beam direction. In the relativistic limit, when the rest mass is negligible, the easier to calculate variable, the pseudorapidity, η is defined as,

$$\eta = \frac{1}{2}\ln\left(\frac{p+p_z}{p-p_z}\right) = \frac{1}{2}\ln\left(\frac{1+\cos\theta}{1-\cos\theta}\right) = -\ln(\tan\frac{\theta}{2}) \tag{4.2}$$

where θ is the polar angle measured with respect to the positive beam axis direction. The variable η takes on the property from y that particle production is roughly constant as a function of it [33]. The azimuthal angle ϕ is orthogonal to the η direction.

A number of useful parameters can be defined with respect to these two variables.

$R = \sqrt{\eta^2+\phi^2}$, the absolute distance in the parameter space of η and ϕ with respect to the origin or between particles (i.e. ΔR).

$p_T = p/\cosh\eta$, the transverse momentum of a particle. The overall transverse momentum of a collision event is conserved unless particles escape the detector.

$E_T = E/\cosh\eta$, the transverse energy of a particle. This is distinguished from p_T by taking into account the particle rest mass.

4.3 Detector Structure

The ATLAS detector is shown in Figure 4.2. The overall detector is 44 m wide by 25 m high. The approximate weight is 7000 tonnes. The detector consists of,

Inner Detector, (ID) responsible for tracking comprised of the semiconductor and transition radiation trackers and the pixel detector and central solenoid magnet.

Calorimeters, the LAr electromagnetic calormeter and the Tile and LAr hadronic calorimeters.

Muon Spectrometer, the muon spectrometer system comprised of the toroid magnets and muon drift chambers.

Trigger and Computing, the hardware and high level trigger system along with the data acquisition and storage facilities.

The overall performance requirements of the ATLAS detector is shown in Table 4.1.

Detector Component	Required Resolution	η coverage*	η coverage*
Tracking	$\sigma_{p_T}/p_T = 0.05\%\ p_T \oplus 1\%$	$\pm$2.5	-
EM Calorimetry	$\sigma_E/E = 10\%\ /\sqrt{E} \oplus 0.7\%$	$\pm$3.2	$\pm$2.5
Hadronic Calorimeter barrel, end-cap	$\sigma_E/E = 50\%\ /\sqrt{E} \oplus 3\%$	$\pm$3.2	$\pm$3.2
Hadronic Calorimeter forward	$\sigma_E/E = 100\%\ /\sqrt{E} \oplus 10\%$	$3.1 < \lvert\eta\rvert < 4.9$	$3.1 < \lvert\eta\rvert < 4.9$
Muon Spectrometer	$\sigma_{p_T}/p_T = 10\%$ at $p_T = 1$ TeV	$\pm$2.4	$\pm$2.7

Table 4.1: The principle performance specifications of ATLAS, the right two columns represent the η requirements for measurement (left) and Level 1 trigger (right) coverage.

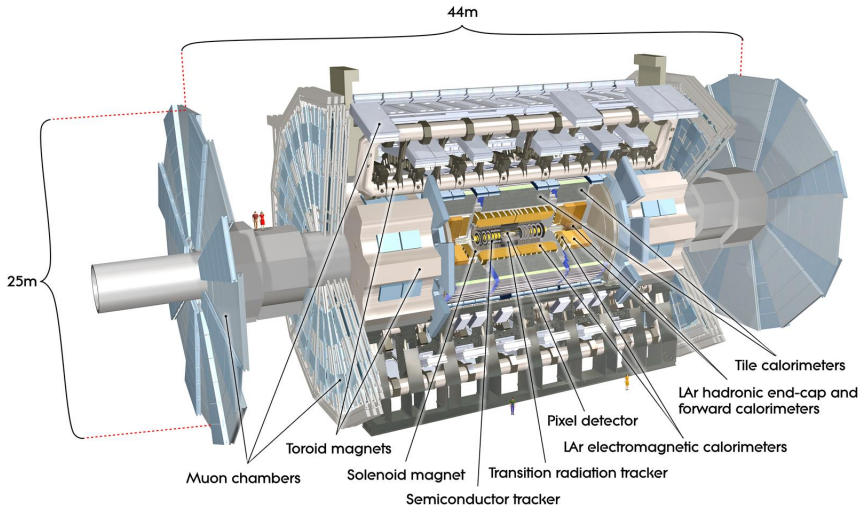

Figure 4.2: A cut out view of the ATLAS detector [31]. The principle components of the detector are labelled, in radial order, the pixel detector, semiconductor tracker, transition radiation tracker, solenoid magnet, liquid argon calorimeteres, tile calorimeters, toroid magnets and muon chambers.

4.3.1 Inner Detector

The ID is responsible for precision tracking of charged particles from the collision vertex. It is held within a central solenoid that provides a 2 Tesla field. The trajectory of charged particles bends within the magnetic field and can be reconstructed as it transverses the multiple tracking layers (in what is known as *hits*). The momentum of tracked particles can then be measured if the magnetic field strength and structure is well understood.

A cut out view of the ID is shown in Figure 4.3. The overall dimensions of the ID are 2.1 m by 6.2 m. At its core, where the density of particle tracks, is largest semiconductor pixel detectors fulfill the precision requirements. Surrounding this in the barrel region are silicon strip detectors (SCT) that provide added tracking. Finally this layer is followed by the transition radiation tracker that provides con-

tinuous tracking of the particles as they enter the electromagnetic calorimeter.

The overall design of the ID provides coverage up to $|\eta| < 2.5$ and is robust with respect to identifying heavy quark flavours and τ particle decays. Due to the intense radiation within the vicinity of the collision point, it is expected that after a few years nearby components of the ID will have to be replaced.

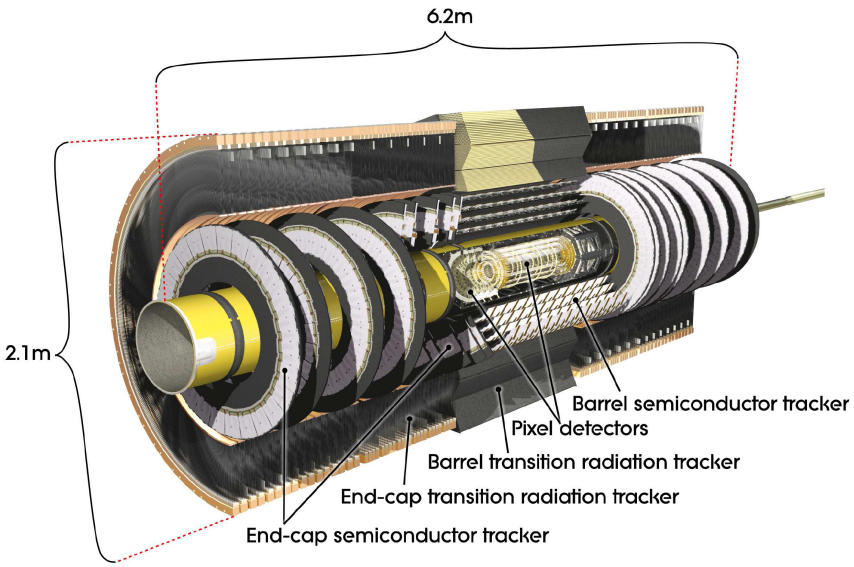

Figure 4.3: A cut out view of the ATLAS inner detector system [31].

4.3.1.1 Pixel Detector

The pixel detector is the innermost of the three tracking systems. It is comprised of 3 concentric cylindrical layers in the barrel and 3 end-cap disks on sides A and C of the detector. The inner most layer is as close as 5 cm with respect to the beam, successive layers are at 9 and ∼12 cm. Meanwhile in the end-cap region the disks vary in radii from 11 to 20 cm.The resolution performance of individual pixel modles is up to 10 μm in the radial $\times$ azimuthal direction, $R\phi$ and 115 μm in z.

The pixel detector provides 3 precision measurements of any transversing particle's tracks. The precision and performance of the pixel detector is critical to the identification of short lived heavy hadrons and τ particles.

The overall system, including the readout chips are designed for radiation hardness and can be seen in Figure 4.4.

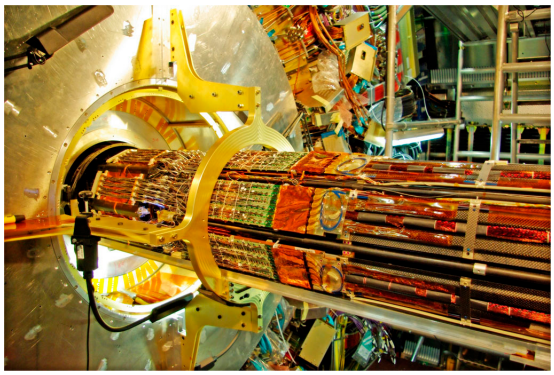

Figure 4.4: The ATLAS pixel detector as it is being installed [31].

4.3.1.2 Semiconductor Tracker

In the intermediate radial range is the SCT system that uses similar silicon semiconductor-based tracking technology to provide 8 precision space points for outward going particles. The system consists of 8 barrel layers and 9 end-cap wheels on each side of the detector. The complete system consists of 61 m^2 of silicon detectors paired with 6.2 million readout channels.

4.3.1.3 Transition Radiation Tracker

The final sub-detector of the ID uses straw tube detectors in order to provide almost continuous tracking of charged particles at a lower resolution. The TRT

consists of straw tube proportional chambers embedded in a matrix filled radiating material. The straw tubes are filled with a gas mixture that consists primarily of Xenon in order to catch transition radiation created by particles that transverse the straw and radiator material. This is especially useful for electron identification.

The entire module consists of 50 000 straw tubes in the barrel region aligned parallel to the beam pipe and another 320 000 radially aligned straws in the end caps. These are combined with a total of 420 000 digital readout channels. Overall, the resolution performance per straw is 170 μm.

4.3.2 Calorimetry

Surrounding (and limiting the dimensions) of the ID is the ATLAS calorimetry system. Broadly, it can be divided into electromagnetic and hadronic components for the purposes of particle energy measurement and barrel and end-cap modules for the purposes of geometry. The system, including forward region detectors is able to provide coverage up to $|\eta| < 4.9$. The overall struture of the calorimetry is shown in Figure 4.5. The system consists of Liquid Argon (LAr), Pb electromagnetic calorimeters in the barrel and end-cap regions encased by a Tile calorimeter based on scintillating fiber and steel absorber plates. In the end-cap region the setup is analogous however for performance reasons the hadronic calorimetry is also designed around LAr technology. In the very forward region is the LAr based forward calorimetery. Finally not shown in Figure 4.5 is the presampler that precedes the electromagnetic calorimetry. The presampler is designed to correct for energy losses of electrons and photons within the tracker and detector regions radially prior to the calorimeters.

The majority of the calorimeter components are housed within cryostats that

cover the barrel and end-cap regions and hold the components at approximately 90 K.

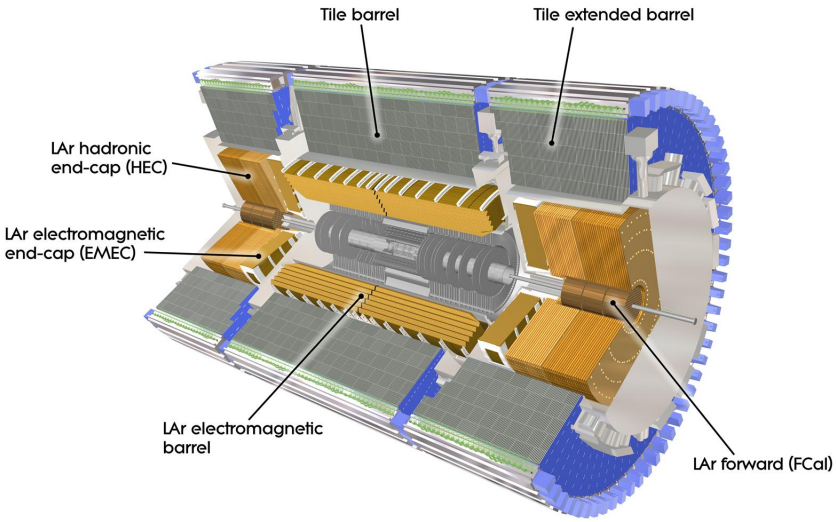

Figure 4.5: The complete ATLAS calorimetry system [31].

4.3.2.1 Particle Interactions with Matter

The accurate and precise measurement of particle energy is of prime importance to the ATLAS program. Particle physics calorimeters are ideally suited for this purpose. Calorimeters are unique in that the intrinsic relative energy resolution of a calorimeter improves with incident particle energy, this is contrary to for instance, magnetic spectrometers. A second useful property of calorimeters is linearity. This means that the response of a calorimeter is linear with respect to incident particle energy.

All components of the ATLAS calorimetry are comprised of alternating layers of shower and detector materials. The purpose of the shower layers is to force

the transversing particles to release their energy while the detector material record the lost energy. Except for muons and weakly interacting particles, the calorimeter system must completely absorb the energy of any incident particle. This forms the basic principle of a sampling calorimeter. It can be for contrasted, for instance, with a homogeneous calorimeter in which the sampling and absorbing materials are the same.

For electromagnetic calorimeters, the interaction of electrons with matter is illustrated [1] in Figure 4.6. At energies above 1 GeV the primary modes of energy loss for electrons and photons (not shown in Figure 4.6) are bremsstrahlung radiation and pair production respectively. The concept of radiation length is defined with respect to an incident particle with energy E, traveling a distance x within a material such that,

$$\frac{1}{X_0} = \frac{1}{E}\frac{\Delta E_r}{\Delta x}, \tag{4.3}$$

where ΔE_r is the energy loss. An electron or photon in matter will initiate a cascading shower of electromagnetic particles via the combination of bremsstrahlung radiation and pair production until the incident particle energy falls below a critical threshold, E_c, at which point the shower terminates. The electromagnetic shower is characterized by its length and radial spread [34]. They can be quantified in terms of the maximum depth,

$$t_{\text{max}} = \ln \frac{E}{E_c} \pm 0.5, \tag{4.4}$$

for electrons (+) and photons (-) respectively, as well as in terms of its spread, the

Moliere radius,

$$R_m = \frac{21\text{MeV}}{E_c} X_0. \tag{4.5}$$

Notice that the radial spread of the shower is only dependent on the particle energy through the radiation length.

The energy of the incident particle is proportional to the electronic signal response that arises due to the energy deposited by the particle into the calorimeter. A useful concept is that of the track length, T,

$$T = X_0 \frac{E}{E_c}. \tag{4.6}$$

The resolution of the incident particle energy is thus proportional to the number of track lengths transversed, $N = T/X_0$ and thus,

$$\frac{\sigma_E}{E} \sim \frac{\sigma_N}{\langle N \rangle} = \frac{1}{\sqrt{N}} \sim \frac{1}{\sqrt{E}}. \tag{4.7}$$

Where in the above equation, a Poisson distribution is assumed for the discrete quantity N.

In addition to the intrinsic energy resolution, an electromagnetic calorimeter is parametrized by two terms that take into account electronic noise and device instrumentation. The overall energy resolution for an electromagnetic calorimeter is thus,

$$\frac{\sigma_E}{E} = \frac{a}{\sqrt{E}} \oplus \frac{b}{E} \oplus c. \tag{4.8}$$

It is possible to characterize hadronic showers in similar fashion to that de-

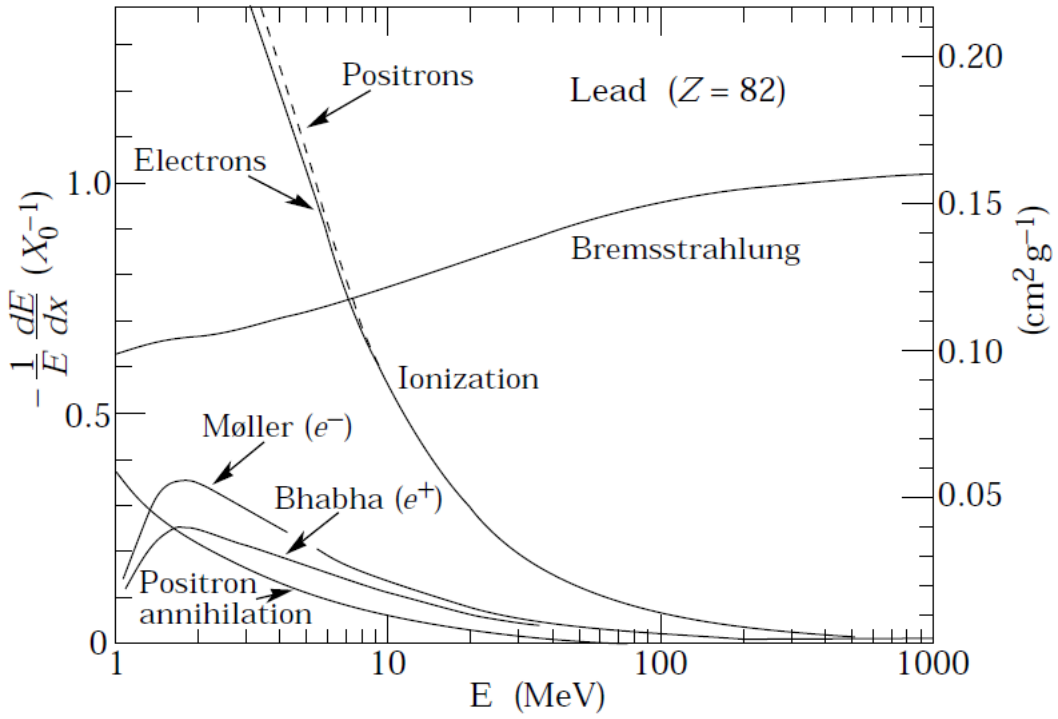

Figure 4.6: Particle interactions with matter (Pb) for electrons/positrons as a function of their incident energy. The y axis shows the energy loss as a function of distance [1].

scribed above but they tend to be more complex. A typical hadronic shower, initiated by say a pion, contains strongly interacting particles, neutrons, pions, protons in addition to an electromagnetic component. The shower tends to be larger radially and longitudinally. Hadronic showers can be characterized by the nuclear interaction length, λ_I, where λ_I is the length that a particle travels in a material for which the probability of non interaction drops to $1/e$. Typically $\lambda_I > X_0$ and thus it requires more material to contain a hadronic shower.

The presence of neutral and long lived particles in hadronic showers can cause secondary shower particles to escape the calorimeter altogether. In addition, inelastic collision of secondary particles in the shower material may entirely

dissipate their energy without ever reaching a detector layer. A portion of the hadronic shower is therefore invisible and thus the measurement, of the incident energy will not be accurate.

A typical calorimeter response characterization, the ratio of response to electrons and pions is $e/\pi > 1$, thus underestimating the hadronic energy and the intrinsic resolution can deviate from $1/\sqrt{E}$. An illustration of the response ratio for the ATLAS hadronic calorimeter is shown in Figure 4.7. In Figure 4.7 a functional form [1] is fitted to the data and used to extract the response ratio, e/h, of the hadronic calorimeter to the electromagnetic and totally hadronic components of a hadronic shower as a means of compensation for the effect.

4.3.2.2 Electromagnetic Calorimeter

The ATLAS electromagnetic calorimetery (ECAL) consists of 1 barrel and 2 end-cap components. They are based on LAr/Pb sampling layers and provide coverage up to $|\eta| < 3.2$.

The calorimeter is shaped in an accordion geometry that is able to provide full azimuthal coverage. The total thickness is in excess of $> 22\ X_0$ in the barrel and $> 24\ X_0$ in the end-caps.

The barrel is mechanically two half-barrels that cover the A and C sides of the detector. Each half barrel consists of 1024 absorber layers along with their readout electronics and is further divided into 16 modules divided equally in ϕ. These modules, including the presampler consist of 3424 readout cells each. The design of the barrel section is shown in Figure 4.8. A module consists of three

1. The functional form used is $e/\pi = \frac{e/h}{1+(e/h-1)*F(\pi^0)}$, where $F(\pi^0)$ is the fraction of neutral pions in the shower. This fraction is separately calculated [32].

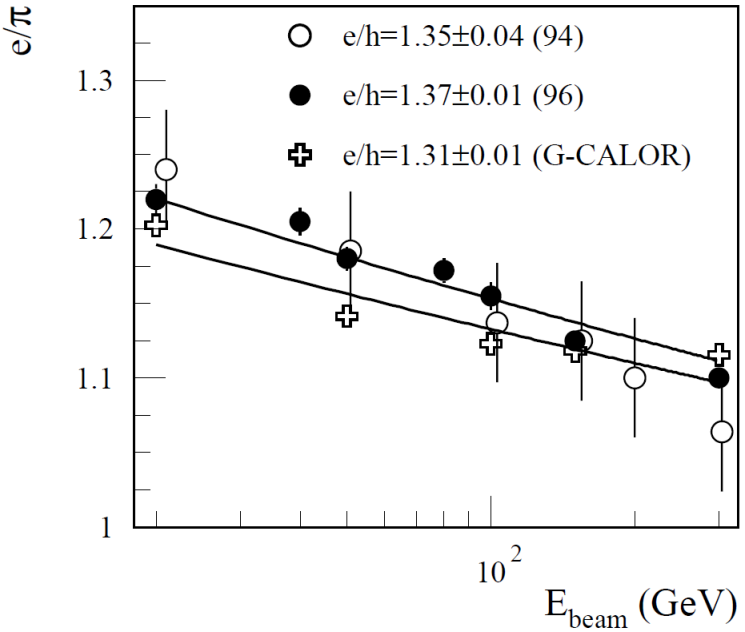

Figure 4.7: The response ratio e/π of the ATLAS hadronic calorimeter as a function of energy [32]. The circles are data results using different test beams in 1994 and 1996. The crosses are obtained from Monte Carlo simulation. The response e/h between electromagnetic and hadronic interactions with respect to the detector is obtained by fitting the response of e/π, where the denominator is the calorimeter response to pions.

layers with increasing granularity in $\eta - \phi$ radially outwards.

As previously mentioned, in front of the barrel is a presampler covering the range $0 < |\eta| < 1.8$ that uses a thin LAr layer to provide a measurement of the energy loss of particles prior to reaching the calorimeter.

In the end-cap regions, two wheels are fitted onto the ends of the barrel system. The end-cap wheels cover the range $1.375 < |\eta| < 3.2$. The end-cap calorimeters have their own presampler that provide coverage in the range $1.5 < |\eta| < 1.8$.

Mechanically, the end-caps consists of two coaxial wheels on each end; the

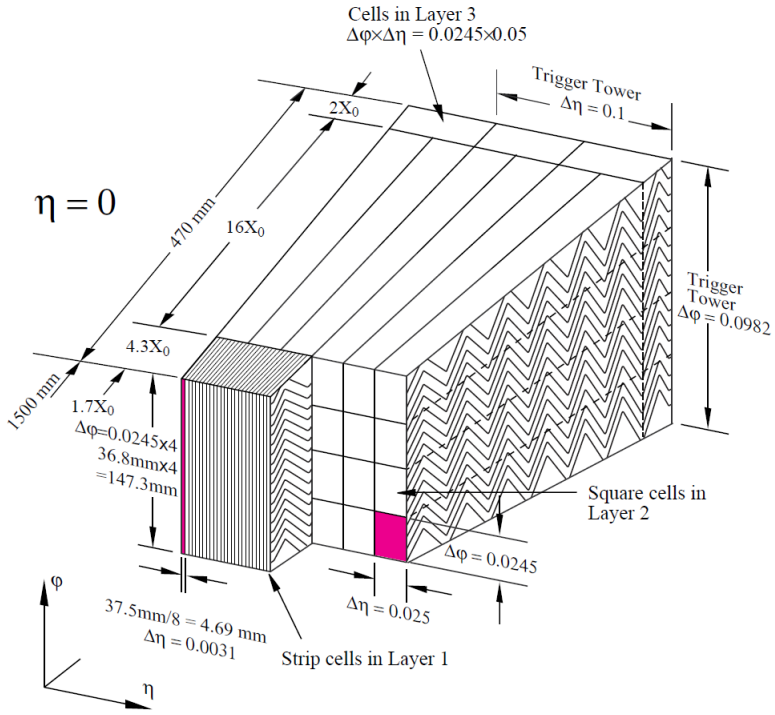

Figure 4.8: The accordion geometry of the electromagnetic calorimeter in the barrel region [31]. The radial direction points away from the collision point with respect to Layer 1.

internal and external radii of the combined wheels are 330 mm and 2089 mm. A 3 mm gap exists between the inner and outer wheels; this boundary is approximately projective of the ID η acceptance. Each wheel is segmented equally in the azimuthal direction into 8 parts. The outer and inner wheels consist of 768 and 256 absorber layers.

In the precision region of the end-cap calorimeters ($1.5 < |\eta| < 2.5$), analogous to the barrel, a 3 layer design is present. The granularity of the layers is smallest at the front and progressively coarser as a particle tranverses outwards. A profile view of the end-cap module along with its accordion structure is shown in Figure 4.9.

Similar to the barrel, each end-cap has its own presampler, consisting of 32

identical azimuthal modules with granularity $\Delta\eta \times \Delta\phi = 0.025 \times 0.1$.

Figure 4.9: A side view of the electromagnetic end-cap calorimeter module [31]. The accordion of the absorbers can be seen.

4.3.2.3 Hadronic Calorimeter

The hadronic calorimetry consists of the barrel tile calorimeter, the hadronic end-cap calorimeter (HEC) and the LAr forward calorimeters (FCal).

The barrel module is a sampling calorimeter that uses steel as absorber material and plastic (polystyrene) as the scintillating active medium. It is placed behind the barrel of the ECAL and covers the region $|\eta| < 1.7$. It mechanically consists of three components, a middle barrel and two extended side barrels. The overall depth is $7.4\lambda_I$. Each barrel consists of 64 wedges evenly divided in ϕ.

An individual module and the multi-module orientation are shown in Fig-

ure 4.10. A single module is comprised of alternating layers of steel and scintillator material connected by wavelength shifting fibre optic cables [2] to photomultiplier tubes and readout electronics. Multiple modules are stacked together to form near complete coverage in ϕ.

In the end-cap region the HEC modules are copper/LAr sampling calorimeters that cover the range $1.5 < |\eta| < 3.2$. The HEC consists of two wheels each on the A and C sides of the detector. The wheels are constructed of 32 identical wedges and have a outer radius of 2030 mm.

The inner wheels are composed of 24 copper plates, each 25 mm thick, the outer wheels are not as finely sampled with 16 plates, each 50 mm thick. Between adjacent plates are 8.5 mm gaps. Each of these gaps is further divided into 4 separate LAr drift regions. In the region the $|\eta| < 2.5$ the readout channels provide a granularity of $\Delta\eta \times \Delta\phi = 0.1 \times 0.1$. For more forward regions the granularity is $\Delta\eta \times \Delta\phi = 0.2 \times 0.2$.

4.3.2.4 Forward Calorimeters

In the forward region, $3.1 < |\eta| < 4.9$ is the FCAL system. The FCAL is comprised of both electromagnetic and hadronic calorimeters. The FCAL is located some 4.7 m from the interaction point and thus experiences greater particle flux. The FCAL is separated into three successive layers. These layers measure electromagnetic (first layer) and hadronic interactions (second and third layers). All layers use LAr as the active medium; the electromagnetic layer uses copper while the hadronic layers use tungsten as the absorber material.

Each FCAL layer consists of three 45 cm deep modules. The electromagnetic

2. The scintillation occurs in the ultraviolet regime and must be converted into visible light.

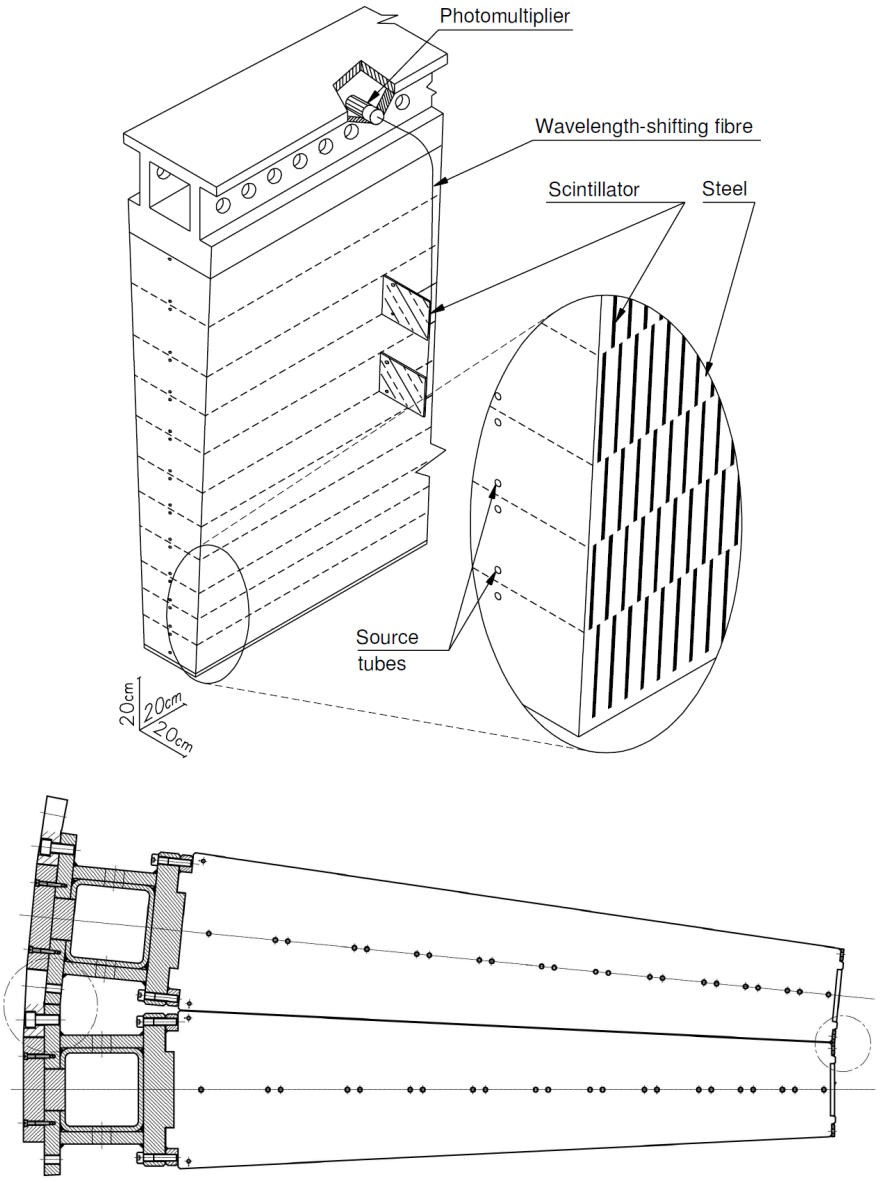

Figure 4.10: A single tile calorimeter module (top) [31]. The interface between two modules (bottom).

layer is composed of sequentially stacked copper plates. The plates are matrices with copper tube rods surrounded by a thin layer of LAr and a radiation hard plastic fiber and connected to readout electronics. The hadronic modules consist

of two copper end plates spanned by a matrix structure similar to the first layer but with tungsten as the medium. A summary of the stopping power of the ATLAS calorimetry is shown in Figure 4.11.

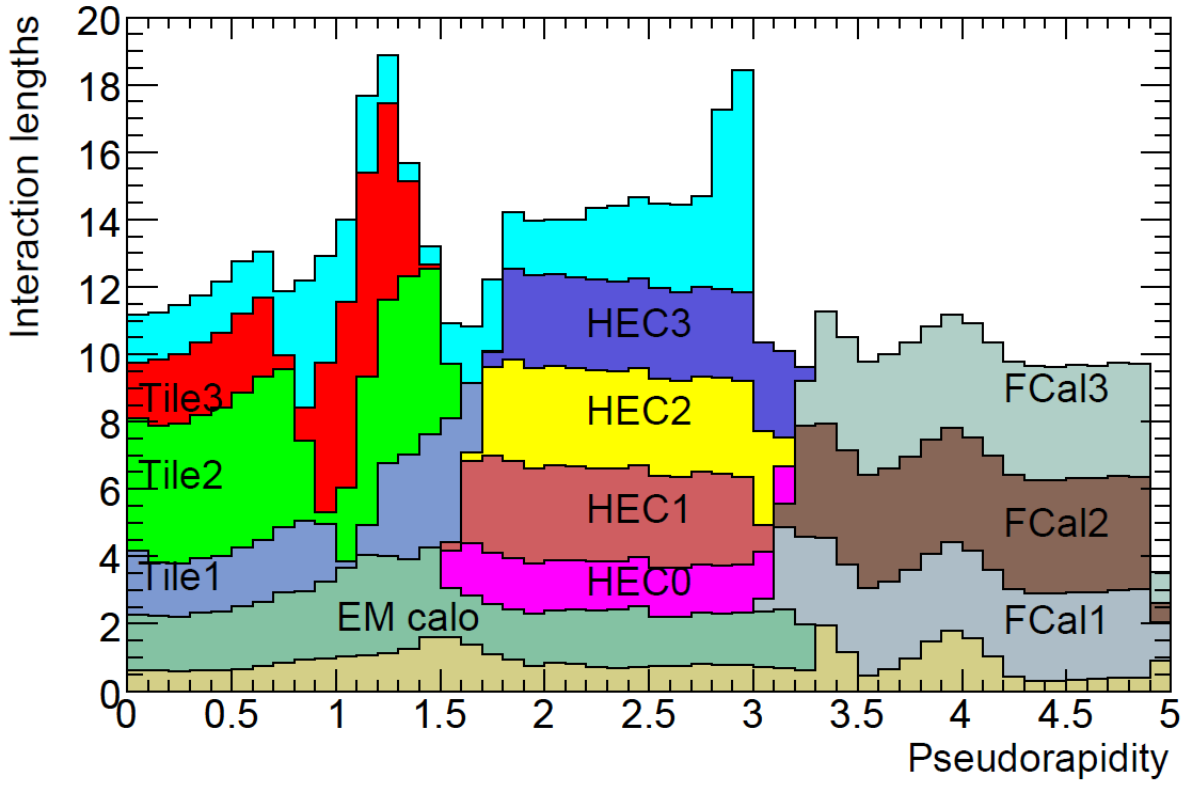

Figure 4.11: The material interaction lengths of the ATLAS detector as a function of coverage in η for its different components [31]. The unlabelled regions in tan before the ECAL and in cyan after the third layer of the hadronic end-cap (HEC3) and tile calorimeters (Tile3) represent the equivalent amount of active material in front of the ECAL and in the first layer of the muon spectrometer respectively.

4.3.3 Muon Spectrometer

In the next layer beyond the calorimetry is the muon spectrometer. The muon spectrometer is designed to measure the momentum of charged particles

that exit the barrel and end-cap calorimeters with $|\eta| < 2.7$. The performance requirement of the muon spectrometer as given in Table 4.1 is to be within 10% accuracy of the particle p_T for 1 TeV tracks. The muon spectrometer is able to independently measure the momenta of muons from a minimum of ∼3 GeV up to ∼3 TeV. In addition, the muon spectrometer is designed to be able to separately trigger on particles crossing. Thus the muon spectrometer performs the task of precision tracking and particle triggering. This feature of the system is used for bunch crossing identification, for additional physics triggers and as a means of providing an additional tracking coordinate for particle. A schematic of the muon spectrometer is shown in Figure 4.12.

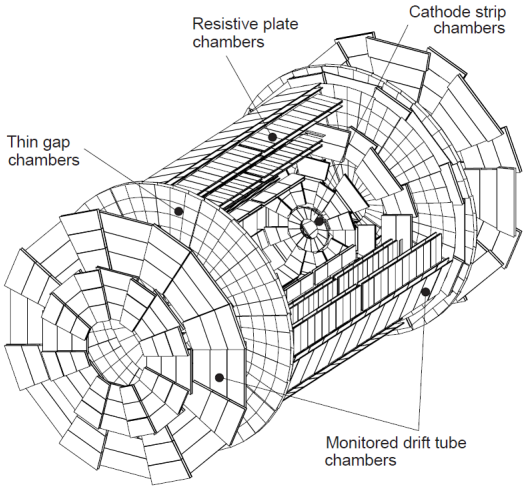

Figure 4.12: The design of the muon spectrometer showing the thin gap, resistive plate, cathode strip and drift tube chambers [31].

4.4 Trigger and Data Acquisition

The ATLAS Trigger and Data Acquisition (TDAQ) system is designed to reduce the tremendous flow of data incoming from the detector to a manageable size that is consistent with physics interests and process them for long term storage [3]. The ATLAS trigger system consists of three tiers designed to reduce the raw detector data from a nominal rate coming from p-p collisions of 40 MHz to a manageable size that can recorded to hard disk. The low level system is known as Level 1 (L1) and directly interfaces with the detector hardware to filter out background events. The High Level Trigger (HLT) trigger system, known as Level 2 (L2) and Event Filter (EF), further prune the data stream using more sophisticated and comprehensive information in order to select events of interest.

The design of the trigger system and data storage system is motivated by the physics program and the constraints given by the high collision and hadronic process rate. Figure 4.13 shows the rate of a number of relevant SM proceses the ATLAS detector will observe and the associated constraints placed by them with respect to the trigger system. The dominant background in a hadron collider is jet production at rates of $\sim 10^7$ Hz while rare processes of interest can be as rare as $< 10^{-2}$ Hz in the case of $H \to \gamma\gamma$ decays.

4.4.1 Level 1

The L1 trigger system is shown in Figure 4.14. The L1 system performs the initial selection on the collision data based on information drawn from the calorimeter and muon detectors. For the calorimeter system the L1 trigger can

3. This section deals with the general TDAQ structure of ATLAS; the trigger study of the actual analysis is detailed in Section 6.2

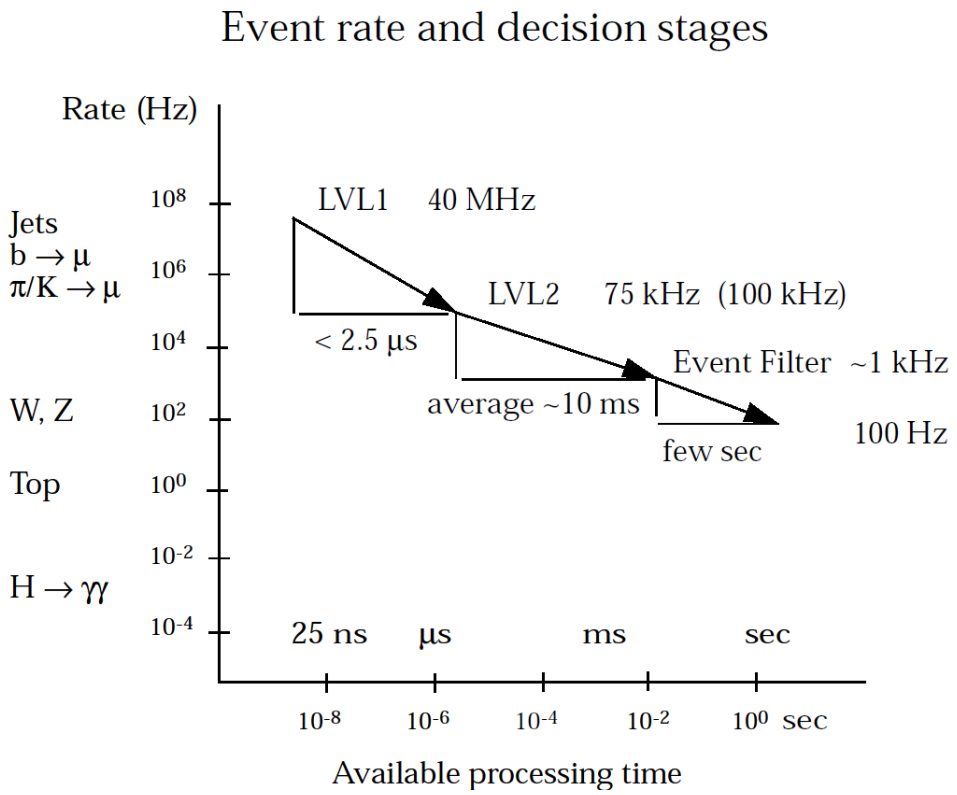

Figure 4.13: Nominal rates of various SM processes at the LHC versus processing time for trigger system [31]. The rate at which data is pushed out of the Event Filter has been superseded from this older design document value of 100 Hz to 200 Hz.

veto based on the amount of transverse energy in physics objects such as leptons or photons, jets, missing energy as well as on the total amount of transverse energy of the collision.

The final decision to accept an event is made by the central trigger processor. In making a decision, the L1 trigger only looks at the object multiplicity or the global threshold (for such cases as total p_T of the event), while the geometric information of the triggered objects is passed onto L2 as Regions of Interest (RoI). In addition, the L1 filtered information can be directly sent to storage (data acquisition) or the detector front-end electronics as part of the memory buffer.

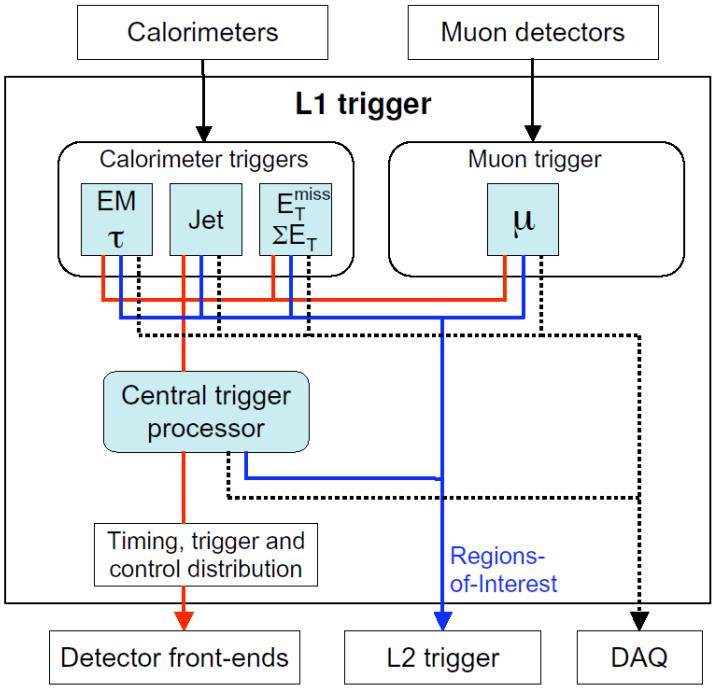

Figure 4.14: The complete L1 trigger scheme, showing input from the calorimeter and muon spectrometer and output to the detector front ends (red lines) and L2 and data acquisition system (blue lines) and directly to disk (dashed black lines) [31].

4.4.2 High Level Trigger

The HLT consists primarily of the L2 and EF trigger systems. The L1 system pushes events to the HLT at 75 kHz. The L2 system utilizes the RoI's received from L1 to make a more refined veto on the event stream. The L2 system requests additional information from various detector components and then selects the data sample based on a increasingly complex set of physics criteria, software algorithms and interesting features within the detector. The L2 will only transfer the full data set for the RoI's that fulfill the entire feature list. Thus, for events that fail the complete selection the detector data is discarded. Events that pass the any number

of L2 selection criteria have their complete detector and any reconstructed data consolidated into a single data structure and passed onto the EF.

The EF system is analogous to its L1 and L2 counterparts in the sense that a number of trigger selection criteria exist. Events that pass these selection criteria are sorted into physics "streams". The EF system will filter events based on physics criteria and additional reconstructed information according to pre-determined ATLAS event categories. These "streams" can be based on the presence of B jets, high energy muons, photons or other criteria. Overall, the EF further reduces the event rate to a design value of 200 Hz. The final events are written to disk and made available for offline analysis using specialized ATLAS software.

For loose, inclusive selection criteria it is possible to "pre-scale" events in order to suppress bandwidth usage. This is especially important at L1 and L2 where loose selection triggers, for instance for the selection of minimum bias events using the forward detectors can easily overwhelm the system. A "prescale" factor of N suppresses the event intake for a given trigger by only recording 1 in N events.

5

Monte Carlo and Event Reconstruction

The use of models and computer simulation is of great importance in experimental particle physics. Computer simulation based on the Monte Carlo (MC) method that is able to simulate the results of hadron collisions is used in ATLAS in order to test theoretical understanding of the SM, tune and calibrate the detector hardware and to simulate the event characteristics of BSM theories and models.

The MC's used to simulate event collisions at the LHC and subsequent detection by ATLAS consist of sophisticated software packages that involve theoretical calculations of the relevant physical quantities and then the subsequent propagation of these final state particles through QCD effects and the detector hardware itself. The full process of turning event generator output into formatted data for analysis is shown in Figure 5.1 with a side by side comparison between simulation and collision data.

The process of simulating data begins with MC event generators; these programs are coded with the appropriate physical cross sections and are typically self contained packages that handle the entire collision chain from the initial state parton-parton collision to the final state partons, to parton showering and hadronization and finally particle decay [1]. Detector simulations such as `GEANT4` [35] are

1. It is also possible to separately simulate the parton-parton collision and the parton showering process using two different MC software suites. This can be done to optimize the simulation of the matrix element calculations and the parton showering and hadronization.

then used to mimic the observational limits and hardware nature of the detector itself. The final output is processed in a manner identical to real data using specialized ATLAS software, ATHENA [36], in order to reconstruct the physical event from raw detector data. Data analysis can be handled also using ATHENA, or C++ based ROOT [37] analysis libraries.

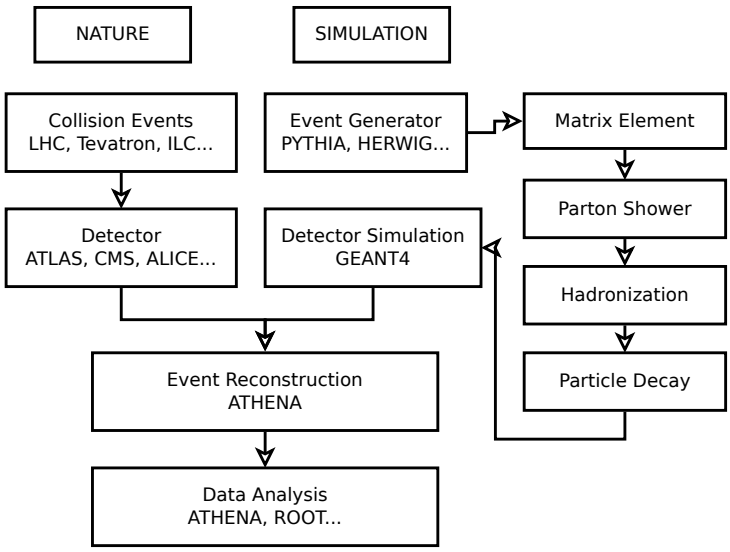

Figure 5.1: Side by side comparison of real collision events and the process of simulating collision events.

5.1 Event Generators

A large number of event generators exist, some as general purpose physics simulators and others designed to simulate very specific processes at the LHC [2]. In this analysis the primary SM background is QCD jet production. The two primary MC generators used to model the QCD background were PYTHIA8 [39] and Herwig++ [40]. These generators simulate 2→2 parton interactions, so called

2. A review of MC generators at the LHC is found in the following citation: [38].

"dijet" processes, whereby the two leading jets in transverse momentum are calculated at matrix element level and additional jets arise through parton shower algorithms. ALPGEN [41] contains libraries for the simulation of true multi-jet process up to 2→6 calculations at the matrix element level. The computational complexity and thereby the CPU resources needed, of multi-jet MC production grows dramatically with each additional jet and as such the ALPGEN multi-jet samples were produced only up to the event generator level; no detector simulation effects are applied. The present author assessed the statistical needs and produced trial samples of the multi-jet samples; ultimately the large batch samples were produced using grid computing methods by the official ATLAS MC production team [3].

These generators are used to validate the data-driven QCD multi-jet background estimation method. In addition, a number of other generators are used to model specific SM and signal processes. SHERPA [42] is used to model the majority of the non-QCD SM background that may be relevant to the analysis. Single top quark production is simulated using a combination of AcerMC [43] and Powheg [44], [45] to account for the various possible channels. In order to model the benchmark signal processes involving the semi-classical decay of microscopic black holes and string balls BlackMax [46] and CHARYBDIS2 [47] are used.

Table 5.1 provides a summary of the MC's used for this analysis and their purpose. Additional information regarding some of these samples is detailed in Appendix A.

3. The author also utilized parallel computing resources at McGill University to compute large batch samples, but once the samples were approved for official ATLAS production there was no such further rationale.

Process	Generator
QCD	PYTHIA8/Herwig++/ALPGEN
$t\bar{t}$	SHERPA
Dibosons	SHERPA
W+jets	SHERPA
Z+jets	SHERPA
γ+jets	SHERPA
single top	AcerMC/Powheg
Black Holes/String Balls	BlackMax
Black Holes/String Balls	CHARYBDIS2

Table 5.1: MC event generators and their relevant process for the purposes of this analysis.

5.1.1 Event Structure

The process of event simulation can be categorized in chronological order,

Hard Processes lie at the heart of MC generators. As most physics of any interest take place in collisions with large momentum transfer, the "hard" regime of QCD where perturbative calculation techniques can be used is essentially the beginning of the simulation process.

Parton Shower: As the particles are strongly interacting, it is possible for initial or final state partons to radiate gluons and for these gluons to form quark-based combinations and further radiation. This shower of QCD radiation is simulated using a specialized algorithm.

Hadronization: As the shower process evolves, the momenta of its components will decrease until at some point they leave the perturbative regime of QCD. At this stage a strongly interacting model takes over to produce the color singlet observable hadrons from the colored constitutent particles.

Decay: As not all hadrons are stable, models are needed to properly simulate the

decay of short lived particles into its components.

5.1.1.1 Hard Processes

Processes with large momentum transfer are the base of MC simulations. As QCD is asymptotically free, it is possible to take advantage of perturbative methods to directly calculate the processes of interest from their Feynmann diagrams. The cross section σ for a process involving two incoming partons a, b colliding to form n will go as [38],

$$\sigma_n = \sum_{a,b} \int_0^1 dx_a dx_b \int d\phi_n f_a(x_a, \mu_F) f_b(x_b, \mu_F) \times \frac{1}{2x_a x_b s} |M(\mu_F, \mu_R, \phi_n)|^2, \quad (5.1)$$

where s is the center of mass energy, $d\phi_n$ represents the available phase space of the final state particle, $f_{a,b}(x_{a,b}, \mu_F)$ are the PDFs for the longitudinal momenta of the incoming partons within their hadrons and $|M(\mu_F, \mu_R, \phi_n)|^2$ is the matrix element cross section calculation for the process. Equation (5.1) illustrates the factorization theorem, the idea that the cross section calculation can be separated into a hard, perturbative component that is directly calculable, independent of the hadron, $|M(\mu_F, \mu_R, \phi_n)|^2$ and a soft, infrared, hadron dependent component, $f_{a,b}(x_{a,b}, \mu_F)$. The scale at which transition occurs between these regimes, is known as the factorization scale, μ_F. The scale at which the calculation of a finite cross section in perturbative QCD is carried out is the renormalization scale μ_R.

The result of a MC calculation is influenced by the choice of parametrization for these scale factors. Typically, this scale is chosen such that $\mu_R = \mu_F = Q^2$. Here Q^2 is representative of some characteristic scale of the simulated processes, for

example, the resonance of an s channel process, the p_T of outgoing partons.

The process of MC generation at leading order (LO) is well understood. At next to leading order (NLO) however, the processes are yet to be well automated. A calculation of a process at NLO is composed of the LO component and the additional virtual and real emission corrections at the next order expansion in α_s, the so called additional legs and loops that contribute to the LO Feynmann diagram. These lead to infrared divergences that must be dealt with. The method of resolving the infrared divergences can be quite complex and cumbersome. As such the simulation of NLO processes is incomplete and a topic of ongoing research.

5.1.1.2 Parton Shower

The parton shower is the processes by which the final state parton are "devolved" from a hard perturbative scale into the soft QCD realm. The parton shower simulates the effects of higher order corrections to the process, and describes the internal structure of jets and other properties of the event.

Radiation in hadron collisions can find some analogy to QED radiation. As in QED bremsstrahlung, a final state quark can emit radiation in the form of gluons. In MC generators a parton shower is simulated in an iterative manner. Beginning with a final state parton, the probability for it to radiate a gluon is calculable and known. If there is radiation, the radiated parton becomes the "final state parton" and the probability for radiation is checked again. This process makes up a cascade, with each successive radiated particle smaller in scale then the previous and will continue until some cutoff value is reached. The choice of the "devolution" parameter (or scale) that determines the scale (from hard to soft QCD) can affect the properties of the shower. A natural choice, inspired in part

by the Chudakov effect in QED, is the opening angle between two color charged partons. As radiation from a collimated $e^+ e^-$ pair is highly suppressed so it is true for color charged parton pairs. Analogous to QED the color field of the individual partons of a pair can only be sampled on a scale smaller then the opening angle between them. At larger scales an observer sees only a single color neutral object. Thus, a parton shower begins at the widest possible opening angle between color parton pairs and devolves to near collimated parton pairs.

5.1.1.3 Hadronization

Hadronization describes the process of transforming the parton level particles created during the shower into the hadronic final state particles (which then can undergo decay). This is a non-perturbative process and relies on phenomenological models. One of the primary models widely used in the MC generators today is known as the string model [38].

The string model is analogous to the QED picture between two charged particles. The string model considers that any two color objects are connected by colored "strings". As the two particles at the poles move apart the strings are stretched and increase in potential energy. As this process continues the string has an increasing probability to form additional particles (i.e. quark, antiquark pair) and thus evolve into two color singlet pairs connected by their own strings and so forth for additional string pairs. In this manner a single string system can evolve until all that remain are ordinary hadrons.

5.1.1.4 Decay

The hadronization process produces a number of unstable particles such as τ or heavy baryons. The MC must enforce the decay of these particles (sometimes in a cascade) into particles that are stable compared to the collision time scale. At each point in the decay chain quantum numbers and kinematic limitations are conserved. The final observable particles are therefore stable particles from hadronization and the decay products of unstable hadronized particles.

5.2 Event Reconstruction

The final state particles produced during the hadronization and decay processes are passed through a detector simulation. The purpose of a detector simulation is to correctly model the effects of the hardware detector resolution, geometry, response and trigger system so as to reproduce the real observation of collision events. For MC's used in this analysis `GEANT4` is used to model the ATLAS detector. `GEANT4` [35] is a popular software toolkit that models the physics of the passage of particles through matter, and is used in a number of particle physics experiments.

The event reconstruction of "data" recorded with `GEANT4` is identical to that of real data. The `ATHENA` software framework [36] is used to reconstruct events (real and simulated) from raw detector data. `ATHENA` is a suite of `C++` code written to reconstruct the propagation of final state particles throughout the detector, from the initial collision point, to track trajectory in the ID, followed by energy deposition in the calorimeter and following through escaping muons into the spectrometer.

Raw detector data is sorted by their characteristics into physics objects such as electrons, muons, jets, photons, missing energy, τ particles. The four-vectors of physics objects are reconstructed at the software level.

5.2.1 Jet Finding and Reconstruction

The primary background of the analysis is QCD jet production and special attention is taken with respect to understanding their reconstruction. As jets are not true physics objects, being comprised of hadrons, their four-vectors and multiplicity depend in a large part on the particular jet finding algorithm.

5.2.1.1 Calorimeter Clusters

The basic jet constituents which are required as input for any jet finding algorithm are clusters of calorimeter energy deposits. These consist of energy clusters in the detector that are grouped together according to their topological properties. An illustration [4] of the most commonly used methods of constructing calorimeter jets is shown in Figure 5.2.

The simplest method and oldest method of clustering calorimeter energy deposits is to form towers of fixed dimensions in η-ϕ that project radially in the calorimeter. "Tower jets" have largely been superseded by cluster algorithms that offer better performance and robustness with respect to pile-up and detector noise.

In ATLAS, the primary method of building calorimeter clusters is known as topological clustering [48], constructing TopoClusters. The algorithm begins by identifying seed calorimeter cells that are above a specific signal to noise ratio. Neighboring cells with energy deposition above a noise threshold are iteratively

4. Image credit: ATLAS internal communication.

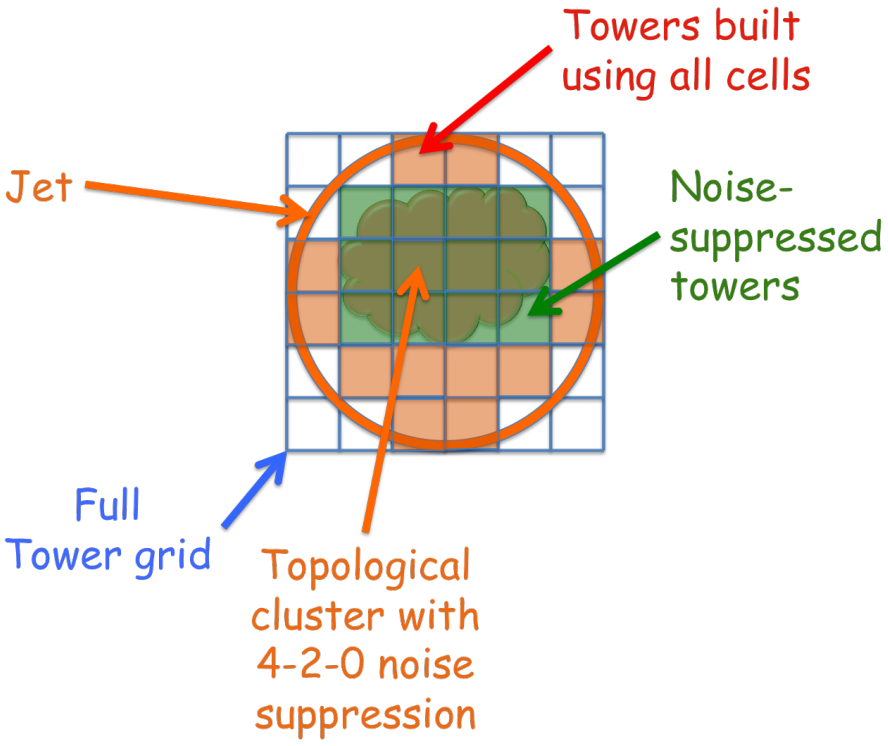

Figure 5.2: A schematic diagram of a section of the calorimeter showing its individual cells and the composition of tower, topological cluster and topological (noise suppressed) tower jets from the cells.

added followed by next nearest neighbors. Seed cells are identified by having energy deposits $E_{\text{cell}} > 4\sigma_{noise}$, neighbors by $E_{\text{cell}} > 2\sigma_{noise}$ and next nearest neighbors by $E_{\text{cell}} > 0\sigma_{noise}$. Thus, it is known as the 4-2-0 method. Therefore, the number of cells in topological clusters differ in contrast to the fixed number of clusters in towers. The clustering method offers additional noise suppression by only accepting calorimeter cells above a given energy threshold as jet inputs [5].

5. An improved tower algorithm is to only include cells selected by the topological clustering method to fill the radial towers in $\eta - \phi$. Such a method offers an alternative to topological cluters and is known as "noise suppressed towers" or topological towers (TopoTowers). The method preserves the geometric simplicity of tower jets but adds the noise suppression improvement offered by TopoCluster jets. The ATLAS authorship task of the present dissertation author involved studying the relative performance of these TopoTower jets relative to traditional TopoCluster jets.

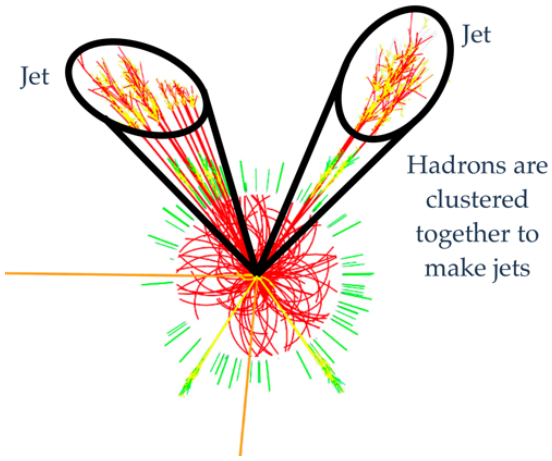

Figure 5.3: An illustration of a typical collision event in a hadron collider showing the production of jets and how they may be clustered (black cones) [6].

5.2.1.2 Jet Algorithms

As seen in Figure 5.3, a jet is a collimated cone of hadrons. A jet finding algorithm is a method implemented in software that identify and group constituents in the calorimeter into the observable jets. The particular algorithm used in this study is known as anti-k_t. The anti-k_t algorithm [8] is an infrared and collinear safe jet finding algorithm that uses an iterative method to group energy clusters into jet objects.

An iterative jet finding algorithm calculates a distance measure between all input constituents, i, j, in an event amongst themselves,

$$d_{ij} = \min(p_{Ti}^{2p}, p_{Tj}^{2p}) \frac{{\Delta R_{ij}}^2}{D^2}, \tag{5.2}$$

and with respect to the beam,

$$d_{iB} = p_{Ti}^{2p}. \tag{5.3}$$

6. Image credit: `www.atlas.ch`.

The variable ΔR_{ij} is the square of the absolute distance in η-ϕ space between two "particles" i, j and D is a scaling parameter that controls the radial spread and distance between the output final jets.

The smallest value is found between equations (5.2) and (5.3). If it is of the form d_{ij} the constituents are combined, if it is d_{iB} the constituent is considered a jet and removed from the event. The process is repeated until no constituents remain in the event.

For $p < 0$ the jet finding process proceeds from the hardest to softest jet constituents in terms of transverse momentum. The anti-k_{t} method corresponds to $p = -1$. As equation (5.2) illustrates, the value d_{ij},between a hard object and soft one will be controlled by the former and small. In contrast, between two soft objects the value of $d_{i,j}$ will be relatively large. Thus, the algorithm will cluster soft energy deposits around a hard object long before it clusters soft deposits amongst themselves. The parameter D effectively determines the scale at which an initial jet constituent will be treated as a jet from the beam and removed from the event or recombined with another constituent.

The anti-k_{t} algorithm creates hard jets and adds all the soft energy deposits in a circle of radius D. For events with two close-by hard jets the picture is determined by the relative transverse momentum between them and the conical structure of the final output jets will be modified accordingly.

5.2.1.3 Jet Energy Calibration

Jets in the ATLAS calorimeter are reconstructed at the energy scale of the non-compensating ATLAS calorimeter. As such they must be corrected at the software level to the correct hadronic scale, accounting for energy lost in the inact-

ive bulk material of the calorimeter and pile-up effects and vertex origin corrections [49].

A diagram of the current jet calibration process is shown in Figure 5.4.

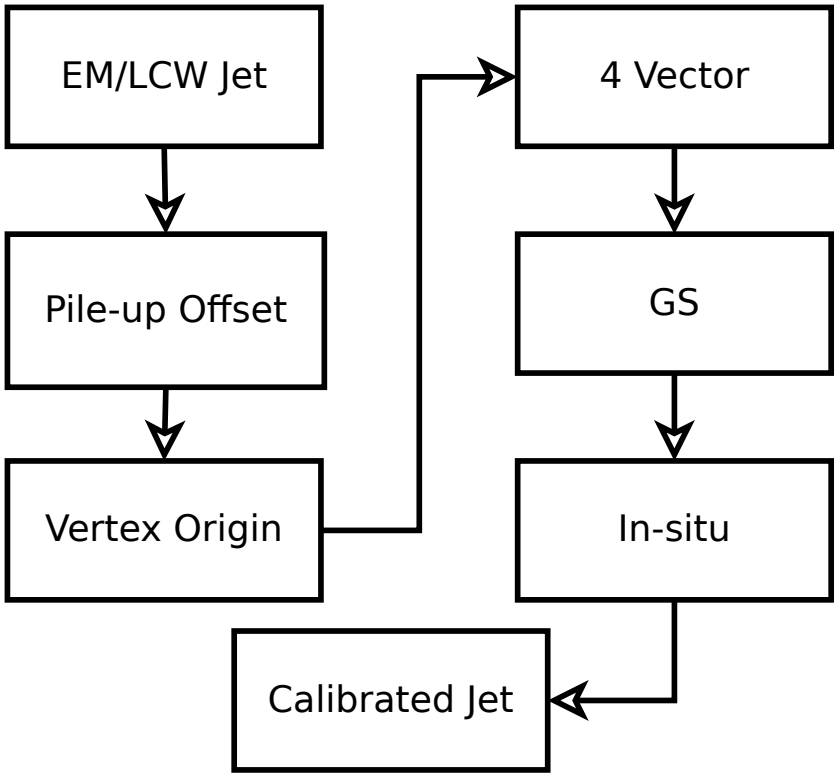

Figure 5.4: A flowchart showing the jet calibration sequence in the ATLAS framework from electromagnetic or LCW input jets to the final calibrated jet.

The inputs to the jet calibration are known as calorimeter jets. Calorimeter jets are the product of running the jet finding algorithm on calorimeter cluster inputs. These clusters can be at the original electromagnetic (EM) scale of the calorimeter or they could have already received a hadronic correction at the cluster level. This later technique is known as Local Cluster Weighting (LCW). The LCW method classifies clusters as being electromagnetic or hadronic based on additional detector information and scales the energy of the latter type by using a cor-

rection factor extracted from the MC simulation of the interaction of pions with the detector. The calibration process involves the following steps:

Pile-Up Offset: Jets are first corrected with respect to in-time and out-of-time pile-up events in the collision. This correction is derived from MC simulation and data and subtracts away the additional energy offset that pile-up creates [50].

Vertex Origin: The origin vertex of the jet is corrected to the proton-proton collision point from the geometric origin of the detector.

Four Vector: The calorimeter jet's four vector is corrected to the proper jet energy scale (JES). The JES is derived by comparing the energy difference of reconstructed and truth jets in MC simulation in bins of η and jet p_T. The correction factor is given as a function of η, an essential parameter given the different material compositions of the detector as a function of the variable. This calibration is the core of the method as it restores the jets to the correct hadronic energy scale. The inputs can be at the EM or LCW scale and are correspondingly known as EM+JES or LCW+JES. The scale of this correction is shown in Figure 5.5 for different calorimeter components. The correction factor is not a small effect and for jets with sufficiently low energy the correction factor can be significant. Figure 5.5 shows the jet response; this factor is essentially the inverse of the jet calibration. The plot illustrates the response of the different detector components due to the usage of differing physical material in their composition. In addition, the scaling with respect to incident particle energy on the detector components is shown as well.

Global Sequential Calibration, GS: The JES correction is derived by only considering the energy and pseudorapidity of jets. Additional information about the jet is essentially ignored. The GS attempts to further adjust the jet energy scale based on additional information about the jet. This can involve the jet flavour, jet charge, sub-structure or inner detector tracking information. The GS technique is therefore an extension of the four vector JES calibration to including binning in additional variables beyond η and p_T. In principle any variable that is sensitive to the difference in jet energy scale at the EM and hadronic level can be used.

In-situ: An additional in-situ calibration is applied at the end. The in-situ correction applies various balance techniques to provide further correction of the jet energy by taking advantage of the topology and structure of the event. The jet energy is compared with the energy of reference objects in the event. Balance techniques are used to correct the jet energy in this manner. These balance techniques encompass the energy balance of dijet, multijet, γ+jet and Z+jet events.

Figure 5.6 shows the fractional JES uncertainty binned in p_{T} at constant $\eta = 0.5$ and binned in η at constant $p_{\mathrm{T}} = 300$ GeV. At $\eta = 0.5$, the transverse momentum scale of the JES uncertainty is dominated by the baseline four vector correction and by close-by jet and pile-up effects for low p_{T}. At the high p_{T} end, the JES correction factor alone completely dominates the uncertainty. In units of η, at fixed $p_{\mathrm{T}} = 300$ GeV, where the jets are soft, the JES uncertainty is small at central values and grows rapidly in the forward region as p_{T} and η are correlated variables. The dominant contributions are the baseline JES correction and jet flavour effects (GS).

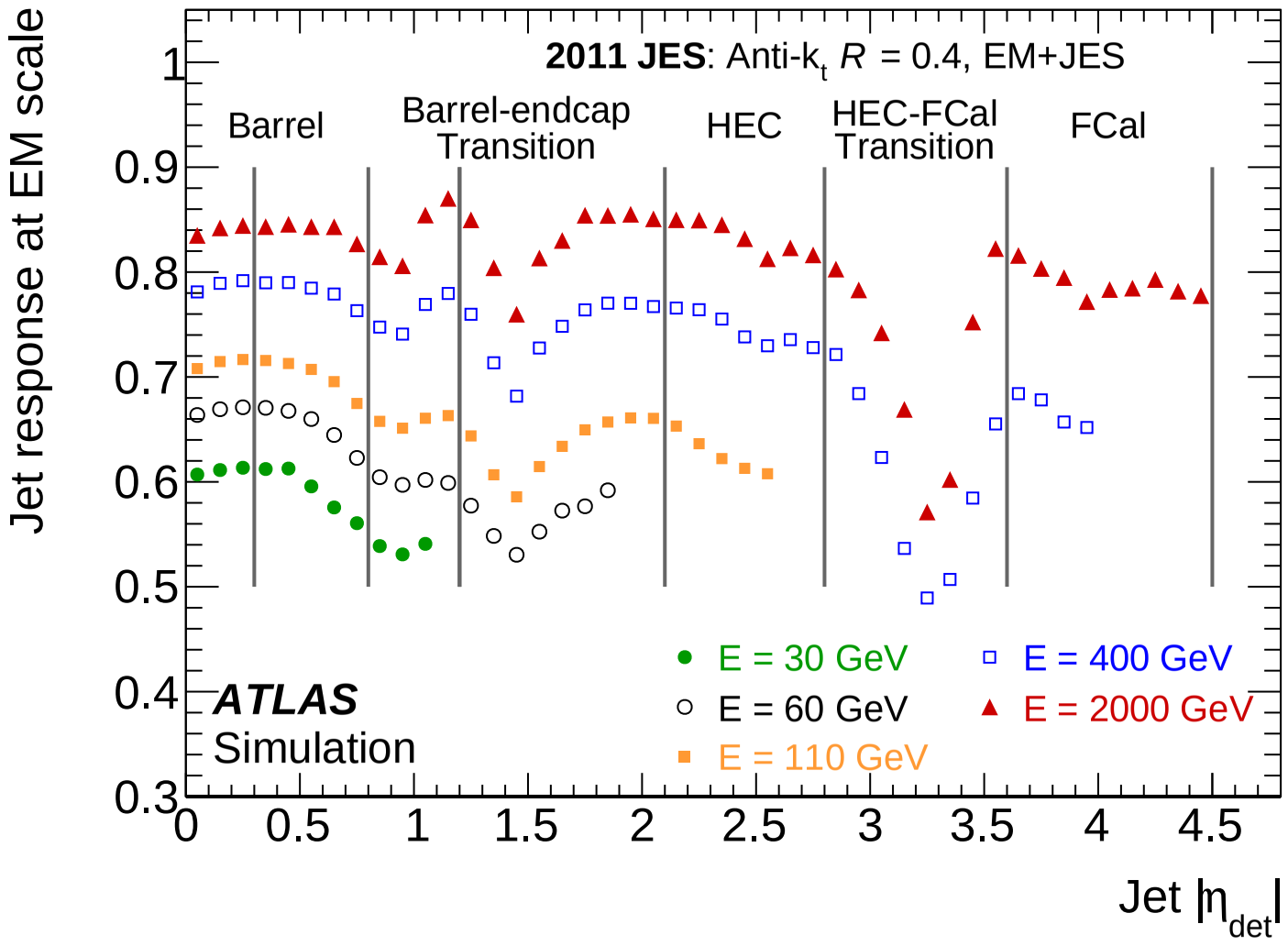

Figure 5.5: The jet energy response measured at the electromagnetic scale as a function of the η of the detector as simulated using Monte Carlo. The response is calculated as the ratio of the reconstructed jet energy versus the true jet energy [49].

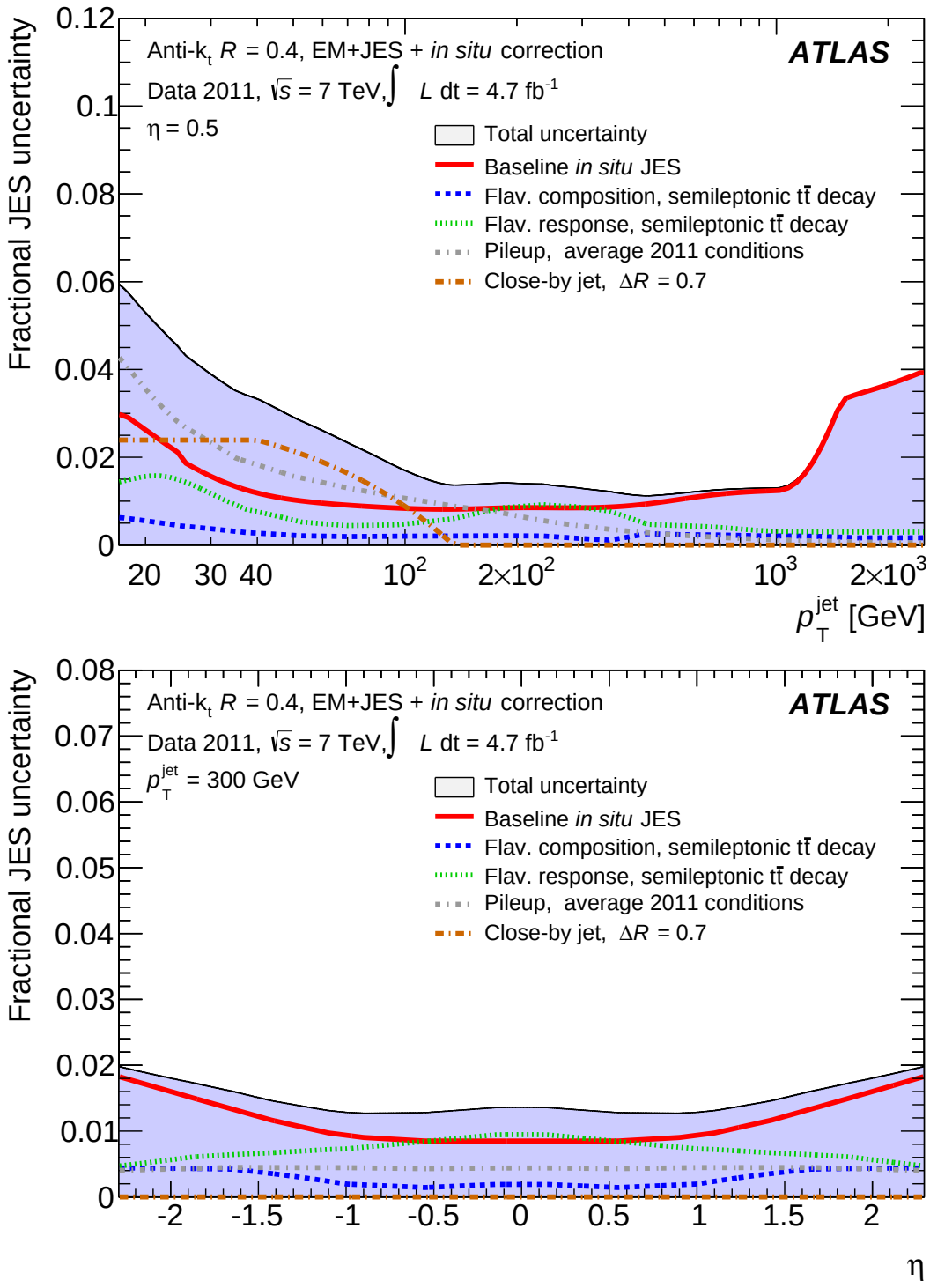

Figure 5.6: The fractional jet energy scale uncertainty for EM+JES calibrated jets in 2012 data binned in units of transverse jet momentum (top) and jet pseudorapidity (bottom). The plots are slices of a 2D distribution at $\eta = 0.5$ and $p_T = 300$ GeV, respectively [49]. For jets with $p_T > 1$ TeV the response of single charged hadrons with the calorimeter in conjunction with MC simulation is used to estimate the JES. This method comes with significant additional uncertainties [51].

6

Analysis

This section of the thesis details a model-independent search for new physics in the multi-jet channel using 20.3 fb^{-1} of collision data recorded by the ATLAS detector. The analysis is presented strategically so as to illustrate the search strategy and sources of uncertainty and finally physical conclusions. This analysis was developed blind, in so far as the data was divided into two distinct regions; a control region where no new physics was observed that is used to model the SM background and a signal region where the event yield, both in terms of normalization and shape was predicted from the control region and tested against for evidence of new physics. The permission to unblind can only come from the ATLAS collaboration after the analysis is considered robust and mature.

The complete multi-jet analysis is documented in an ATLAS internal note of some two hundred pages. Despite the exclusive, private, nature of that documentation the purpose of this section is not to reproduce section by section, study by study the official internal documentation. Not only would that lead to a dissertation that is too long but it would also contain highly technical ATLAS specific details and possibly contain material not approved by the ATLAS collaboration for public dissemination. In this section the main arguments of the analysis are laid out along with the relevant studies in so far as they help to form a complete picture of the analysis.

With regard to the formatting, for most cases the main body will only discuss the results in qualitative terms; quantitative tables and additional figures are relegated to the Appendices and referenced as necessary.

6.1 Strategy & Search Parameters

The choice of the multi-jet channel is determined by the phenomenology of TeV-scale gravity, as discussed in Section 2.3.2.1. A pair of natural variables to choose for the analysis are,

$$N_{\text{Jet}}, \tag{6.1}$$

$$H_{\text{T}} = \sum_{i=1}^{N_{\text{Jet}}} p_{\text{T}i}, \tag{6.2}$$

where the former counts the number of jets in the event as defined by the Anti-k_{t} algorithm, Section 5.2.1.2, and the latter the total transverse momentum of such jets by scalar addition. It was discussed earlier in Section 2.3.2.1 that the characteristic signature of black hole evaporation is a large multiplicity of high transverse momentum jets. The parameter space of N_{Jet} versus H_{T} is suitable for isolating possible signal signatures from SM background. This is discussed in detail in the subsequent Section 6.2.1.

The definitions given above are exclusive quantities but it is useful to define two inclusive quantities, $N_{\text{Jet}} \geq X$, where X is a minimum number of jets in the event and $H_{\text{T}}^{\text{min}}$ which represents the number of events beyond a given value in H_{T}. A histogram binned in H_{T} can be rebinned such that the number of events per bin represents the events in that bin and all subsequent bins. Such a histogram is

defined as "binned in $H_{\mathrm{T}}^{\mathrm{min}}$".

Black hole evaporation is simulated as a stochastic process and therefore inclusive $N_{\mathrm{Jet}} \geq X$ is a more useful parameter as two identical black holes can evaporate into a different multiplicity of objects. In addition, production is continuous beyond some "turn-on" mass, M_{Th}, and in the absence of discovery, limits should be placed on inclusive quantities, hence $H_{\mathrm{T}}^{\mathrm{min}}$. This is in contrast to searches for resonance effect, which would be very localized in a region of the space of the search parameter.

6.2 Trigger Analysis

This section discusses the trigger study performed as a precursor to the main analysis. The trigger selection utilized for this analysis is given in nomenclature as EF_j170_a4tchad_ht700, representing a selection based on the existence of at least one jet with $p_{\mathrm{T}} > 170$ GeV (j170) and $H_{\mathrm{T}} > 700$ GeV in the event (ht700) at the Event Filter level (EF) of the trigger system for objects reconstructed using the Anti-k_{t} algorithm with a radius parameter of 0.4 at the hadronic energy scale (a4tchad). The full trigger chain is:

- **Level 1**:L1_j75,

- **Level 2**: L2_j165_c4cchad,

- **Event Filter**: EF_j170_a4tchad_ht700,

indicating the full selection criteria at L1 and L2 which have require at least one jet with a p_{T} of 75 GeV (j75) at L1 and 165 GeV (j165) at L2, the latter reconstructed using a cone algorithm with a radius parameter of 0.4 from calorimeter clusters at the hadronic scale (c4cchad).

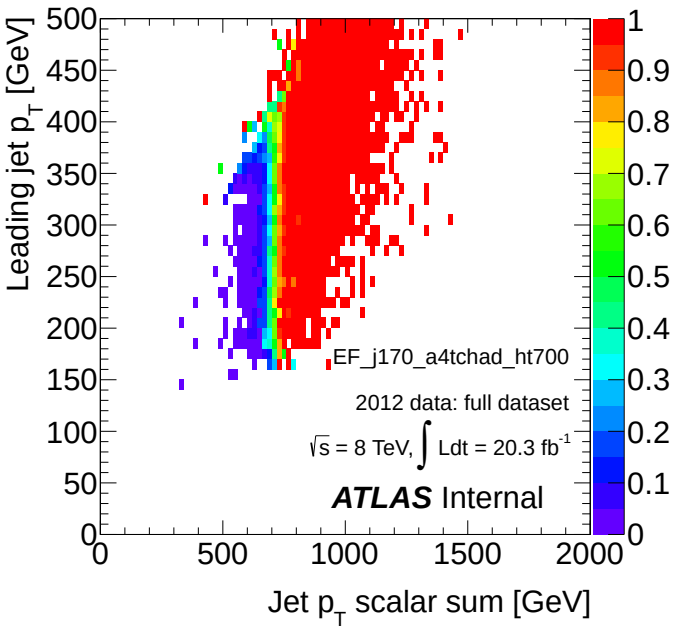

Figure 6.1: The trigger efficiency in the space of $p_{\mathrm{T}}^{\text{Lead Jet}}$ versus H_{T}. The color scale indicates the percentage efficiency from 0 (purple) to 100% (red).

The efficiency of the trigger is studied with respect to the reference trigger EF_j110_a4tchad using the bootstrap method [52]. The trigger efficiency is studied in the space of two variables, the p_{T} of the hardest jet and the H_{T} of the event. Figure 6.1 shows the trigger efficiency in the space of $p_{\mathrm{T}}^{\text{Lead Jet}}$ and H_{T}.

The trigger is shown to be fully efficient for $H_{\mathrm{T}} > 0.8$ TeV irrespective of the $p_{\mathrm{T}}^{\text{Lead Jet}}$ of the event. Conversely, for $p_{\mathrm{T}}^{\text{Lead Jet}} \sim 0.43$ TeV and above the trigger is almost totally efficient irrespective of the H_{T} of the event. In addition, as this is a multi-jet analysis, the effect of varying jet multiplicity on trigger efficiency is also studied.

Figure 6.2 shows the trigger efficiency as a function of H_{T} in exclusive multiplicity slices, N. The form of the "turn-on" curve is not affected by the jet multiplicity and the efficiency plateau, reached at $H_{\mathrm{T}} > 0.8$ TeV, does not deviate signi-

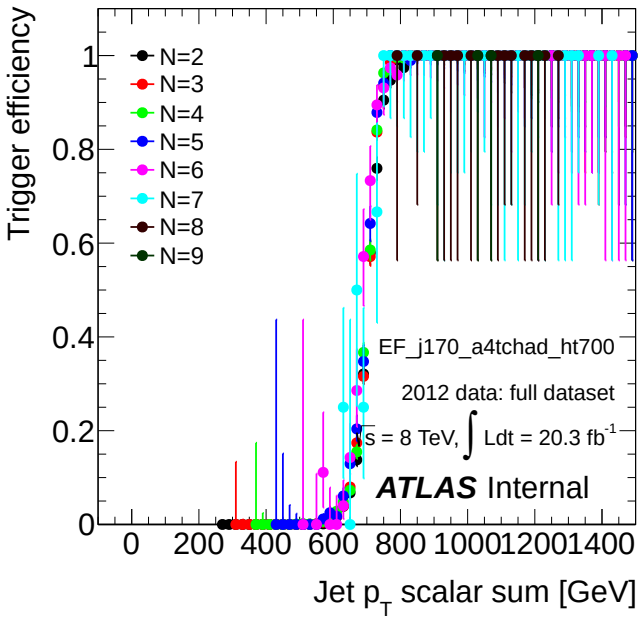

Figure 6.2: The trigger efficiency in H_{T} sorted by the exclusive jet multiplicity, N, of the event.

ficantly.

Overall, the trigger is fully efficient for the kinematic region of H_{T} of interest and this efficiency is stable with respect to varying jet multiplicity.

6.2.1 Signal Characteristics

A toy illustration of the search strategy is presented in Figure 6.3. The background H_{T} is a monotonically falling distribution binned into a histogram. The signal is presented as a threshold effect that is bounded by an initial turn-on value at low H_{T} and kinematic limits at high H_{T}. The distribution of H_{T} is divided into two regions called the control (CR) and signal regions (SR). The shape and overall normalization of the SM H_{T} distribution is estimated from the CR in data using

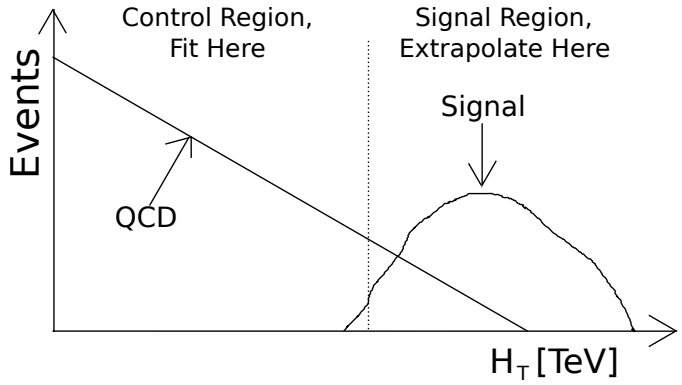

Figure 6.3: A toy illustration of a single inclusive multiplicity, $N_{\text{Jet}} \geq X$, slice. The exclusive H_{T} distributions are shown for background and signal (as a distorted Gaussian) along with an arbitrarily good definition of the control and signal regions (dotted vertical line). The y axis represents the event count on a logarithmic scale.

an analytical ansatz function. The extrapolation of this function beyond the CR is taken as the central value of the background estimation in the SR. The dividing line between CR and SR is informed by knowledge of the existing published limits on new physics and the possible contamination from signals that may exist beyond such limits.

In addition, as thermal evaporation is predicted to carry large particle multiplicity the analysis is repeated at each inclusive jet multiplicity [1] within $N_{\text{Jet}} \geq 3-8$. The two dimensional space of N_{Jet} vs H_{T} is shown in Figure 6.4 for QCD background versus a characteristic signal model of microscopic black holes. In contrast to QCD, where the spectrum is highly peaked at low H_{T} and then steeply falling, the signal is broadly spread out across a large area in N_{Jet} vs H_{T}, concentrating at relatively high multiplicity and total transverse momentum.

By definition an ansatz function that fits to higher H_{T} will provide a more accurate prediction of the extrapolated region. The logical conclusion is a full range

1. Beyond eight jets, statistical limitations prevent accurate modeling of the SM background.

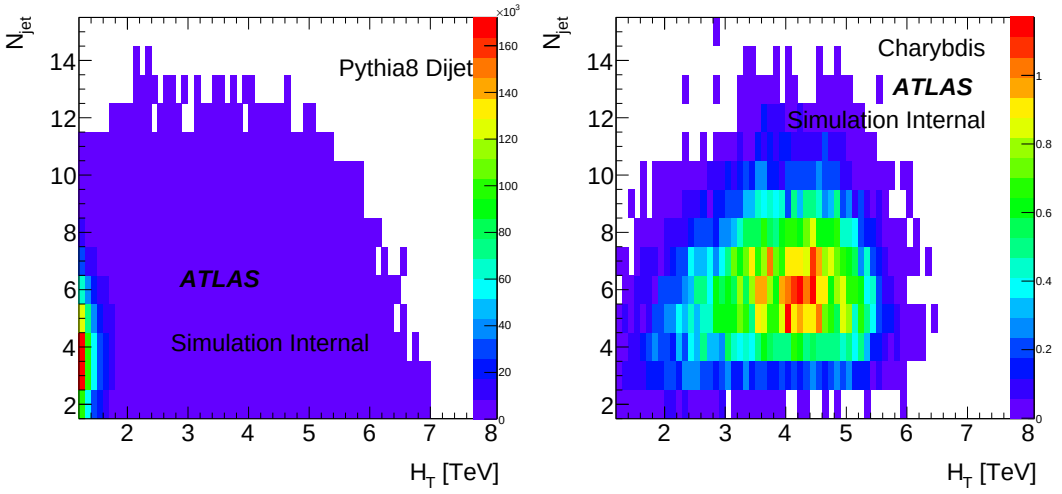

Figure 6.4: The space of N_{Jet} vs H_{T} for QCD background as simulated by `PYTHIA8`(left) and a characteristic black hole signal as simulated by `CHARYBDIS2`(right). The color scale indicates the predicted number of events scaled to a luminosity of 20.3 fb^{-1} in the left histogram. The signal luminosity has been arbitrarily scaled.

fit minus a single histogram bin at the high H_{T} tail would be most accurate barring new physics in that last bin. As this is not a narrow resonance search the possibility of fitting over a signal enriched region of H_{T} cannot be discounted. Such a possibility will lead to an overestimated background in the SR and is an easy way to miss a real signal with a small cross section.

In this analysis the region $1.2 < H_{\text{T}} < 3.0$ is chosen as the CR. Below 1.2 TeV the H_{T} distribution becomes sensitive to kinematic effects of the trigger selection [2]. The choice of the upper bound is motivated by signal contamination studies to be

2. There is a natural "turn-on" for the H_{T} that mirrors the "turn-on" in the trigger efficiency curve, thus an event cannot be histogrammed at say $H_{\text{T}} = 400$ GeV. In addition, only jets with $p_{\text{T}} > 50$ GeV are selected to contribute to the H_{T} observable. As there must be at least one jet with $p_T > 170$ GeV, the remaining selected jets must have a combined $p_T > 530$ GeV, without any individual jet have $p_{\text{T}} < 50$ GeV. In studying the distribution of H_{T} for different $N_{\text{Jet}} \geq X$ bins, these kinematic constraints were found to shift the peak even further from the trigger efficiency "turn-on" of ~ 700 GeV. Moreover, this shift increases as a function of $N_{\text{Jet}} \geq X$. Therefore, the lower bound of the CR must be chosen to be beyond this "turn-on" point at each $N_{\text{Jet}} \geq X$ so as to produce stable fit and extrapolations.

discussed in Section 6.4.3.

6.3 Event Selection

The event selection, colloquially referred to as "cuts", is designed to maximize the amount of analysis quality data and is optimized based on the search strategy. The exclusive chain of logic is listed in Table 6.1 in order of precedence.

Event Selection	Logic
Trigger	EF_j170_a4tchad_ht700==1
GRL	HasRunLumiBlock==1
LArError	larError<2
tileError	tileError<2
CoreFlag	coreFlags&0x40000==0
Vertex	$\geq$1 Tracks
Jet Quality	Good jets
TileCalo	isBadMedium==0

Table 6.1: The event selection, otherwise known as the "cut flow" or criterion applied to the full data set recorded by the ATLAS detector in 2012.

The event selection described in Table 6.1 is designed to first reduce the raw data within those of the **Trigger** requirement. The trigger requires at least one jet with $p_{\mathrm{T}} \geq 170$ GeV and $H_{\mathrm{T}} > 700$ GeV within the event. This selection is optimally designed to select a subset of the data that is most promising with respect to the hypothesized BSM physics. A number of quality criteria then follow; these vetos are designed to ensure that only data recorded during optimal machine conditions of the LHC and detector are used. The hardware condition of the machine during beam collisions is recorded and divided into so called "LumiBlocks", a list of the useful LumiBlocks in 2012 is summarized in a GoodRunList, **GRL**. Further hardware quality criteria indicated by the detector flags **LArError**, **tileError**, **CoreFlag**

can indicate possible malfunctions in various ATLAS detector components such as the liquid Argon or tile calorimeters. A collision in the detector can often be indicated by the presence of tracks sourced to a single vertex. In this analysis the **Vertex** quality is indicated by the presence of at least two tracks with $p_{\mathrm{T}} \geq 50$ GeV sourced to a primary vertex. The quality of detected jets can be determined from a number of diagnostic parameters. The **Jet Quality** is labeled by terms that indicate the accuracy and validity of their measurement. In this analysis events with poorly measured jets or jets formed from gap or malfunctioning regions of the detetor are rejected and thus only good jets are kept. During the 2012 collision program a number of tile calorimeter (**tileCalo**) cells were masked or otherwise offline and this effect was accordingly adjusted for in software corrections. It was, however, subsequently found that the software corrections were themselves not correct and introduced mismeasurements, particularly of high p_{T} jets. In this analysis, events affected by these errors are vetoed.

6.3.1 Jet Selection

In addition to the event level selection, further selection was applied to define "jets" within the event. These cuts on the p_{T} and η of individual jets are designed to suppress energy deposition from pileup effects and reduce systematic uncertainties associated with extremely forward jets. In this analysis, jets are kinematically defined by:

$p_{\mathrm{T}} > 50$ GeV. Large amounts of low energy deposition due to minimum bias and underlying events are common in hadron colliders. Energy deposited into the calorimeter through these processes can be reconstructed as

"jets" and are uninteresting and are suppressed by only selecting objects with relatively large transverse momentum as jets.

$|\eta| < 2.8$, the performance of the detector is known to suffer as the pseudorapidity of jets increases. In particular, the JES uncertainty of jets with $|\eta| \geq 2.8$ grows rapidly. This analysis excludes such objects and only counts jets within a central geometry.

The event count is summarized in Table 6.2. A total of 81.2 million raw events are reduced to 30.3 million analysis ready events. The overall sample reduction factor is $\sim 10\%$ according to Table 6.2 from trigger selection to tileCalo.

Selection	Events	Cumulative [%]
Raw	81228522	
Trigger	33601766	100.00
GRL	32029846	95.32
LAr error	31910074	94.97
Tile error	31910072	94.97
coreFlags	31910012	94.97
Vertex	31909863	94.96
Jet Selection	31619360	94.10
tileCalo	30325319	90.25

Table 6.2: The "cut flow" for the full 2012 data sample in order of precedence.

6.4 Standard Model Background

A number of SM background processes are considered in this analysis. Qualitatively, there are reasonable grounds to believe that the largest background is contributed by QCD multi-jet production. Quantitatively, MC simulation is used to estimate the actual relative contributions of individual processes. The various SM contributions to the background are grouped into categories corresponding to

their physical channel. These are illustrated in the H_{T} spectra for varying N_{Jet} in Figure 6.5 and listed here in order of magnitude:

— QCD jets

— $t\bar{t}$

— γ+jets

— W/Z+jets

— Single top

— Diboson.

Figure 6.5 shows that QCD is the dominant process by several orders of magnitude. In addition, it is almost exclusively the only SM process that contributes to the high H_{T} tail, where the greatest signal sensitivity is expected. Examining the ratio subplots, the relative ratio of the QCD to total contribution is almost always upwards of $> 95\%$.

The total background as predicted by MC is largely dominated by QCD. The number of non-QCD events in the region $H_{\mathrm{T}} > 1.2$ TeV is shown in Table 6.3 for the various SM backgrounds. The contribution of the sub-leading process, $t\bar{t}$ production, is order of magnitudes smaller. Therefore, the modeling of SM background is largely reduced to modeling of the QCD background to within a quantitative margin.

6.4.1 Background Estimation

The combined background is modeled directly in the data using a fit and extrapolation method. Monte Carlo simulation is not used. Such a "data-driven" background estimation technique offers a number of advantages and some disadvantages compared to a MC based method.

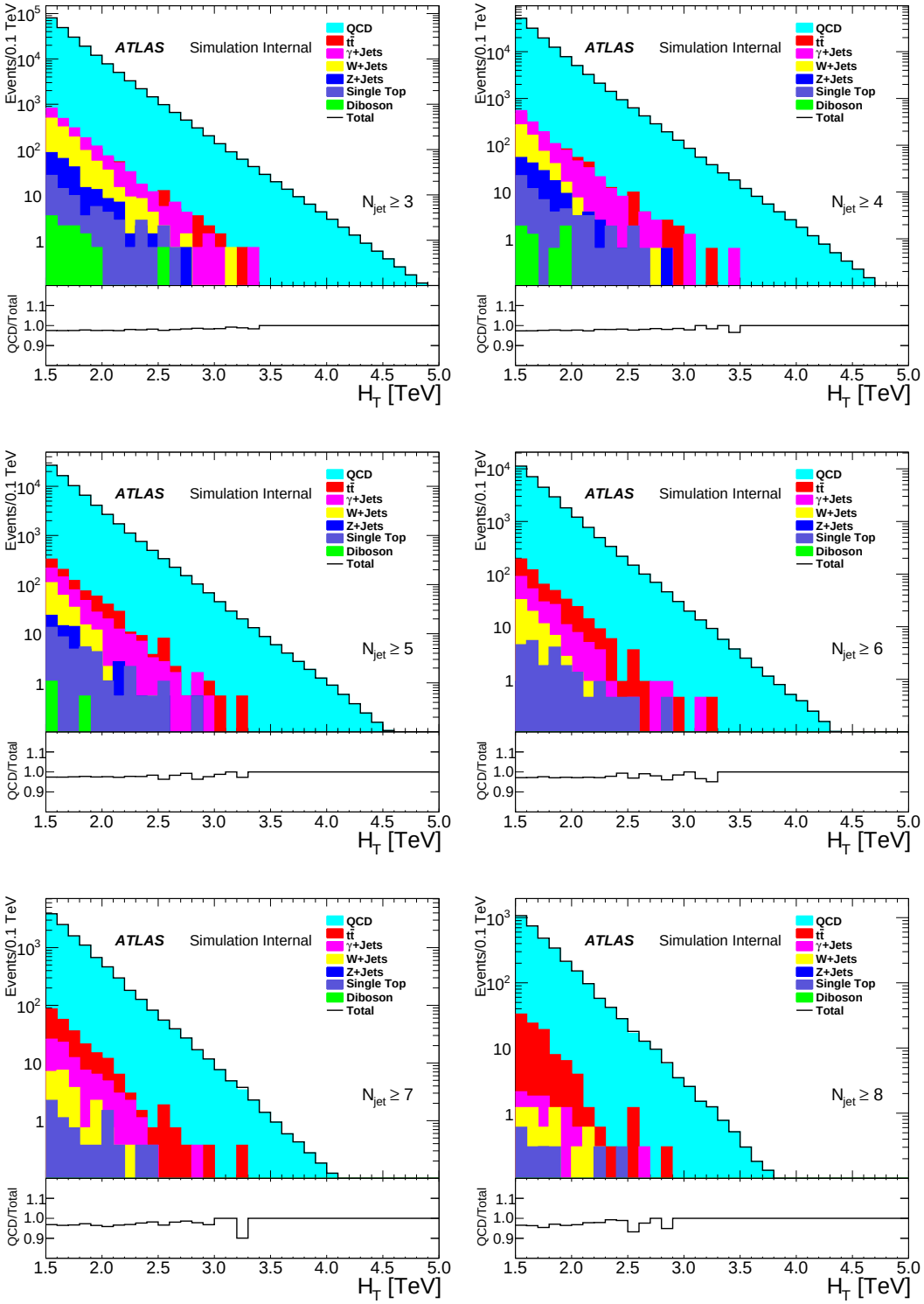

Figure 6.5: The H_{T} distributions for various inclusive jet multiplicities, N_{Jet}, showing the relative contribution of the various SM backgrounds to the overall shape and normalization of the spectra. The number of events is scaled to a luminosity of 20.3 fb^{-1}. The bottom ratio plots show the relative contribution of QCD to the total background.

Process	Inclusive Jet Multiplicity											
	3		4		5		6		7		8	
QCD	208245	98	134933	97	70319	97	30207	97	10723	97	3176	97
$t\bar{t}$	1550	1	1291	1	889	1	519	2	242	2	98	3
γ+jets	2104	1	1372	1	570	1	228	1	87	1	9	0
W+jets	1219	1	580	0	236	0	76	0	23	0	5	0
Z+jets	239	0	163	0	66	0	1	0	0	0	0	0
Single top	73	0	61	0	43	0	22	0	7	0	2	0
Diboson	10	0	6	0	2	0	0	0	0	0	0	0

Table 6.3: Predicted number of events due to each process normalized to 20.3 fb^{-1}. The absolute number of events and relative contribution with respect to the total number of events is shown in the first and second columns for each process and N_{Jet}. The relative values are rounded to the nearest percentage point.

Data is inclusive with respect to all SM processes, thus the background can be modeled without worrying about compensating for contributions from various backgrounds. A MC method would involve adding the contribution of each process separately based on different MC simulations. The usage of MC also entails the evaluation of a number of correlated and uncorrelated systematic uncertainties associated with the effects of jet energy scale, jet energy resolution or parton distribution function and shower tune variations that would otherwise not exist in a data-driven method. A further impediment of a MC-driven method is the lack of sufficient multi-jet simulation samples. Most MC simulations of QCD simulate dijet final states in the hard process. In these simulations additional jets and sometimes a semblance of true multi-jet production is emulated through parton showering. True multi-jet processes such as $qq \rightarrow qqg$ are computationally expensive and time consuming to simulate. For such a multi-jet analysis, it is insufficient to base the modeling of the primary background on dijet simulation. At the same time, it is unfeasibly expensive to generate sufficient multi-jet statistics

for the same purpose [3].

A data-driven method based on a functional fit to a region of the search space excluded for new physics obviates reliance on the shape and nuances of particular MC's. In addition, there are systematic uncertainties due to jet energy scale, resolution, MC statistics that would affect a MC-driven approach. In basing the background estimation on a fit, however, the disadvantage is that all ambiguities are transferred into the fit and extrapolation, and thus uncertainties associated with simulation become uncertainties associated with the fitting method. A further danger is the existence of real signal in data which is excluded from MC but could bias the data-driven technique. Such a possibility must be guarded against in a data-driven method.

While the method is data-driven, MC simulation is nonetheless useful and is used to provide extensive validation of the technique, as seen in Appendix A and as seen above in Section 6.4 to conduct additional relevant studies.

6.4.2 Ansatz Function

The particular choice of the function used to fit the background in the CR is a carefully considered ansatz. A number of natural considerations are useful guides. The nominal function should be able to,

— Fit the CR of the data to within a particular quantifiable level of goodness of fit.

3. A request from the ATLAS peer review commitee did come at a late point in the analysis asking for the validation of the data-driven method on mulitjet `ALPGEN` simulated samples. Therefore, a statistically sufficent amount of multi-jet MC was created only for purposes of validating the data-driven technique; these results are documented in Appendix A. These samples were produced only at the generator level in the sense that they were not subjected to simulation of detector effects.

— Under the general assumption that SM QCD is a smoothly falling distribution, the extrapolation in the SR based on the best fit parameters should be monotonically falling.

— The number of free parameters must exceed two. This is based on the factual observations that at least one parameter is needed to normalize to the luminosity and the distribution shapes cannot be generally described by a single parameter.

An additional criterion based on the MC that is useful is,

— The fit extrapolation should be able to describe the MC in the SR with a particular quantifiable degree of accuracy.

This last rule can also be interpreted as: the extrapolation must not be contradicted by the MC; or that the data-driven technique must be validated in simulation. This is a useful test, as based on the generator, the distribution shapes of the search space parameters, N_{Jet} and H_{T} can be different. The ability of the method to accommodate different MC's is a flexibility that lends it confidence.

Further refinements can be made based on existing literature [53] of dijet searches [4]. Early results such as the W/Z boson resonance search by the UA2 collboration in 1990 introduced an ansatz form of:

$$\frac{dN}{dm} = \frac{p_0}{m^{p_1}} e^{-(p_2 m + p_3 m^2)}, \tag{6.3}$$

to parameterize the differential QCD background as a smoothly falling function in the search parameter, m, the invariant mass of the dijet system. Later searches in the channel using similar techniques, conducted by the Collider Detector at

4. This is owing to the large presence that dijet searches has had in the community and the natural precedence from which a multi-jet search can gain insight.

Fermilab (CDF) collaboration, simplified the form to an approximation of a power law relationship between the search parameter and the differential event count,

$$\frac{dN}{dm} = \frac{p_0}{m^{p_1}}(1 - m/\sqrt{s})^{p_2}, \tag{6.4}$$

where m is normalized to the center of mass energy of the collider, $\sqrt{s}$, within the parentheses. In the ATLAS and CMS collaborations a modification of equation (6.4) was utilized in searches for dijet resonances [54], [55],

$$\frac{dN}{dm} = \frac{p_0(1 - m/\sqrt{s})^{p_1}}{(m/\sqrt{s})^{(p_2 + p_3 \ln(m/\sqrt{s}))}}, \tag{6.5}$$

where the mass has been explicitly normalized in all instances to the center of mass energy and an additional term, $p_3 \ln(m/\sqrt{s})$, has been added in order to improve the goodness of fit to a wider mass range.

Equation (6.5) is a refinement of its various predecessor functions that have been used in published results over the years. It is composed of four ingredients,

— The term $\frac{1}{m}$ is designed to emulate the mass dependence of the leading order QCD calculation for hadron production.

— $(1 - m/\sqrt{s})^{p_1}$ mimics the behaviour of the parton distribution function at a given momentum fraction: close to the kinematic limit, $\sqrt{s}$, the differential cross section (or event count) has to go to zero.

— The remaining exponentiation factor $p_2 + p_3 \ln(m/\sqrt{s})$ was introduced in later searches, when higher energy colliders and higher statistics extended the range of the mass distribution and additional degrees of freedom were needed to accommodate the shape.

Equation (6.5) is a powerful description of the full range QCD background in either the invariant mass or its correlated counterpart H_{T}. It is able to fit such distributions to a very high degree of accuracy, through $\sim 10^8$ orders of magnitude and is the preferred choice for resonance searches, where the task is to exclude an anomalous bump on top of a smooth background.

For the multi-jet analysis the term $p_3 \ln(m/\sqrt{s})$ is dropped from Equation (6.5) as the fit is only made over a limited CR that does not extend to sufficiently high mass/H_{T}. The nominal choice is then,

$$\frac{dN}{dH_{\mathrm{T}}} = p_0 \frac{(1-x)^{p_1}}{x^{p_2}}, \tag{6.6}$$

where $x = H_{\mathrm{T}}/\sqrt{s}$. A key difference from resonance searches is that the accuracy of a full range fit is guaranteed but in the multi-jet analysis the prediction of the extrapolation is of critical importance. In order to evaluate this, a series of alternative ansantz function choices are considered in a study documented in Section 6.5.2. In addition, the accuracy of the fit extrapolation in MC was extensively studied using a variety of dijet and multi-jet generators, as documented in Appendix A.

6.4.3 Signal Injection

Once the nominal ansatz function is determined it is possible to study the effects of signal contamination. This is relevant for a data-driven study; while an informed decision is made of the CR based on non-observation of BSM physics, the possibility of contamination cannot be dismissed in the same way as if MC simulation was used. The purpose of this exercise is to determine the bias that a small signal within the CR may introduce to the method.

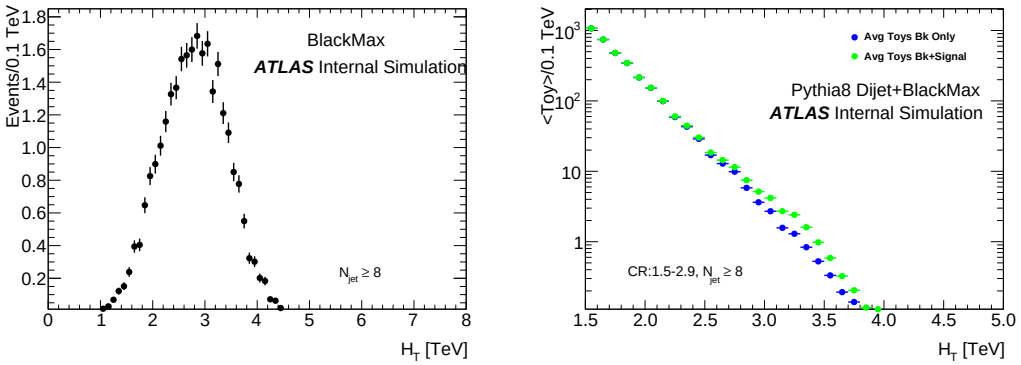

Figure 6.6: The H_{T} distribution at $N_{\mathrm{Jet}} \geq 8$ for the signal sample (left) and the background and signal injected background distributions (right). The right side plot is the average of 1000 toy distributions for background and background plus signal, respectively.

The signal model which peaks at the lowest value of H_{T} is found [5]; this is assumed to be the maximum signal contamination that could be within any possible CR. The signal is then injected into the SM background extracted from PYTHIA8 MC simulation at an arbitrary cross section.

No assumptions on the cross section of the model is made, instead the signal cross section is adjusted until a three standard deviation excess is seen against the SM background in any bin [6] in $H_{\mathrm{T}}^{\mathrm{Min}}$. This first occurs in the $N_{\mathrm{Jet}} \geq 8$ H_{T} distribution at a signal cross section of 1.8 fb^{-1} and is illustrated in Figure 6.6.

Toy H_{T} distributions of the signal and background are then generated in order to simulate the statistical fluctuations of data. The signal cross section is held to its fixed value. For pairs of toys, signal and background, they are combined and the ansatz function is fitted to a potential CR and extrapolated. In addition, the

5. This is a string ball sample simulated in BlackMax with model parameters, $M_{\mathrm{s}} = 1.0$ TeV, $M_{\mathrm{Th}} = 4.5$ TeV, $g_{\mathrm{s}} = 0.4$ (string coupling strength), $n = 6$. This model had already been excluded in the lepton+jets channel at the time of the study. Therefore, the study detailed here is conservative.

6. Three standard deviations is representative of an ambigious point that is not a discovery (five standard deviations in discovery searches) but sufficiently large as to be interesting. Excess below three standard deviations would be largely invisible to the analysis and excesses above would have already been observed in the data.

same procedure is applied to the background only distribution in each toy. An ensemble of 1000 toys is treated this way and the biases between the background only and signal contaminated results is compared against one another by taking the average of the ensemble in each H_{T} bin.

This procedure is repeated for three fit ranges that differ by their upper bound and the relative bias between the nominal and signal contaminated fits are compared against the statistical uncertainty of the nominal fit itself[7]. The bias is defined as the number of events predicted by the signal contaminated fit versus the number of events predicted by the background only fit. The results are shown in Table 6.4.

The implied tension is a trade off between a more accurate extrapolation by fitting to higher H_{T} and less potential signal bias in the opposite direction. As there is very little difference between the maximum bias for fits up to 2.9 and 3.0 TeV the SR was chosen as the region > 3.0 TeV. Thus, the potential fitting range is < 3.0 TeV in order to maximize the quality of the extrapolation.

Upper bound on control region	2.8 TeV	2.9 TeV	3.0 TeV
Bias relative to nominal statistical uncertainty	$0.62 - 0.99$	$0.73 - 1.00$	$0.89 - 1.01$

Table 6.4: The bias introduced into the fit by signal contamination compared for various fit ranges in H_{T}. The entries show bias relative to the statistical uncertainty of the nominal fit in the full range of the SR as determined by the upper bound of the fit range. For instance, $0.66 - 0.99$ indicates the minimum and maximum bias in the SR for the extrapolation with a fitting upper bound of $H_{\mathrm{T}} = 2.8$ TeV.

7. The statistical (or fit) uncertainty was calculated in an iterative manner during the development of this analysis, for presentation clarity, the study itself is not discussed until Section 6.5.1.

6.4.4 Fit Region Optimization

Based on the details of Section 6.4.3 the CR utilized to model the SM background is chosen to be 1.2 to 3.0 TeV. In this region equation (6.6) is fitted within a chosen range and extrapolated to produce the background estimation in the SR. An informed and consistent choice of the fitting range is made based on a study that minimizes the difference in the SR prediction between all possible choices. At a bin width of 0.1 TeV a histogram divides the CR into 18 bins between 1.2 to 3.0 TeV. The number of possible fits within this range is,

$$\sum_{i=\text{bins}} 19 - i, \tag{6.7}$$

where bins are assumed to be contiguous. For each fit range the extrapolation is calculated and the background prediction is summarized by the figure of merit, the number of events in the bin $H_{\text{T}}^{\text{min}} = 3.1$ TeV. This method is carried out in data and the result is shown for all $N_{\text{Jet}} \geq X$ in Figure 6.7. In these plots the diagonal direction represents a constant number of bins fitted.

An optimal fitting range should be stable with respect to changes in the fitting range. This concept is quantitatively defined as the absolute difference in the background prediction of the number of events for $H_{\text{T}}^{\text{min}} = 3.1$ TeV between a particular choice and its eight nearest neighbors. This implies that boundary ranges cannot be chosen as they would have biased rankings in such a metric. Figure 6.8 plots the largest nearest neighbor value for the viable candidates.

A weighted average is used such that one range is chosen for all multiplicities rather than uniquely choosing the fitting range per multiplicity. The final

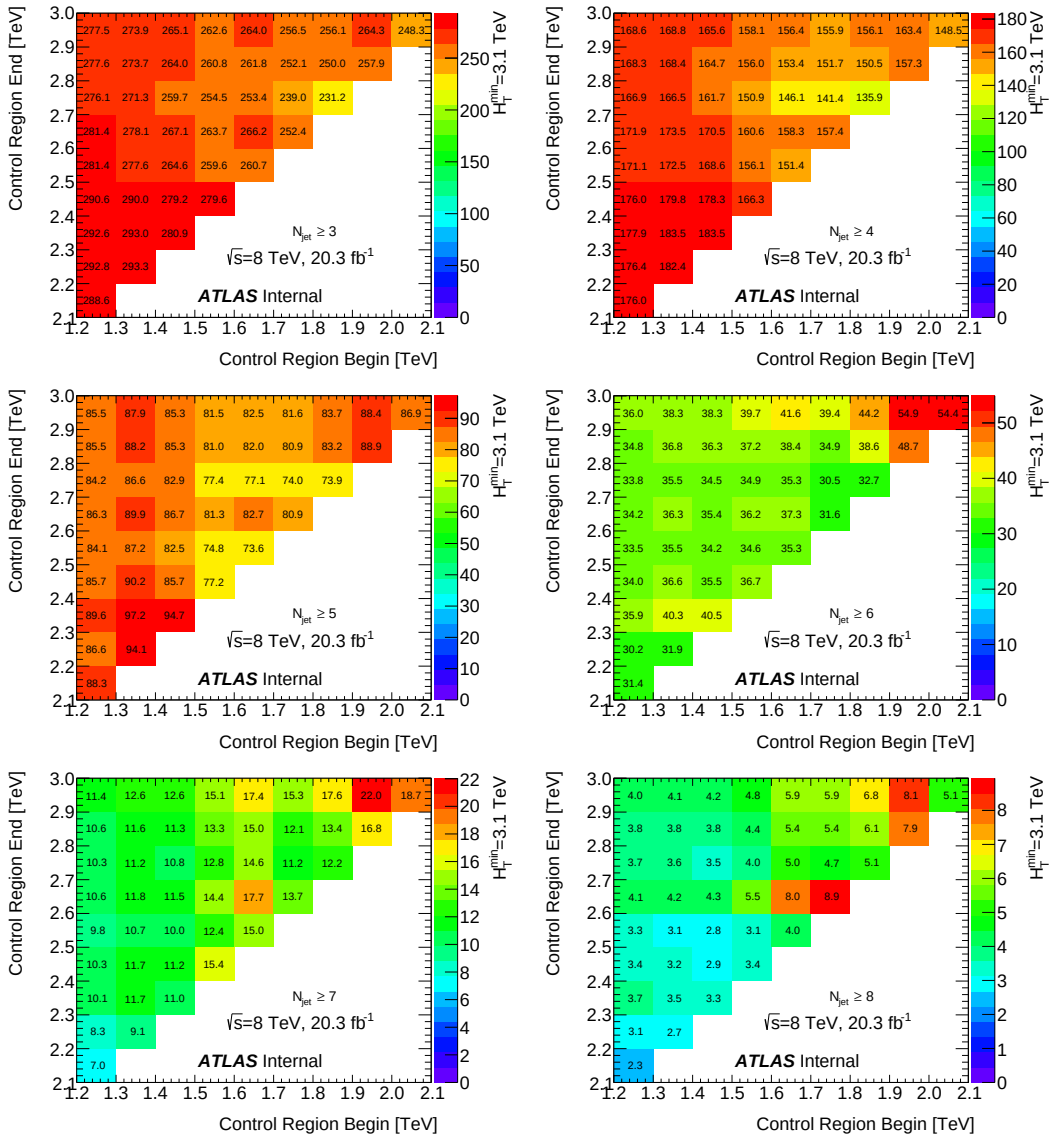

Figure 6.7: The figure of merit, the number of events in the bin $H_{\mathrm{T}}^{\mathrm{min}} = 3.1$ TeV for all possible fitting ranges within the control region. The x and y axis labels indicate the beginning and end of the fitting ranges. The bin entries label the number of predicted events for $H_{\mathrm{T}}^{\mathrm{min}} = 3.1$ TeV according to the fit extrapolation.

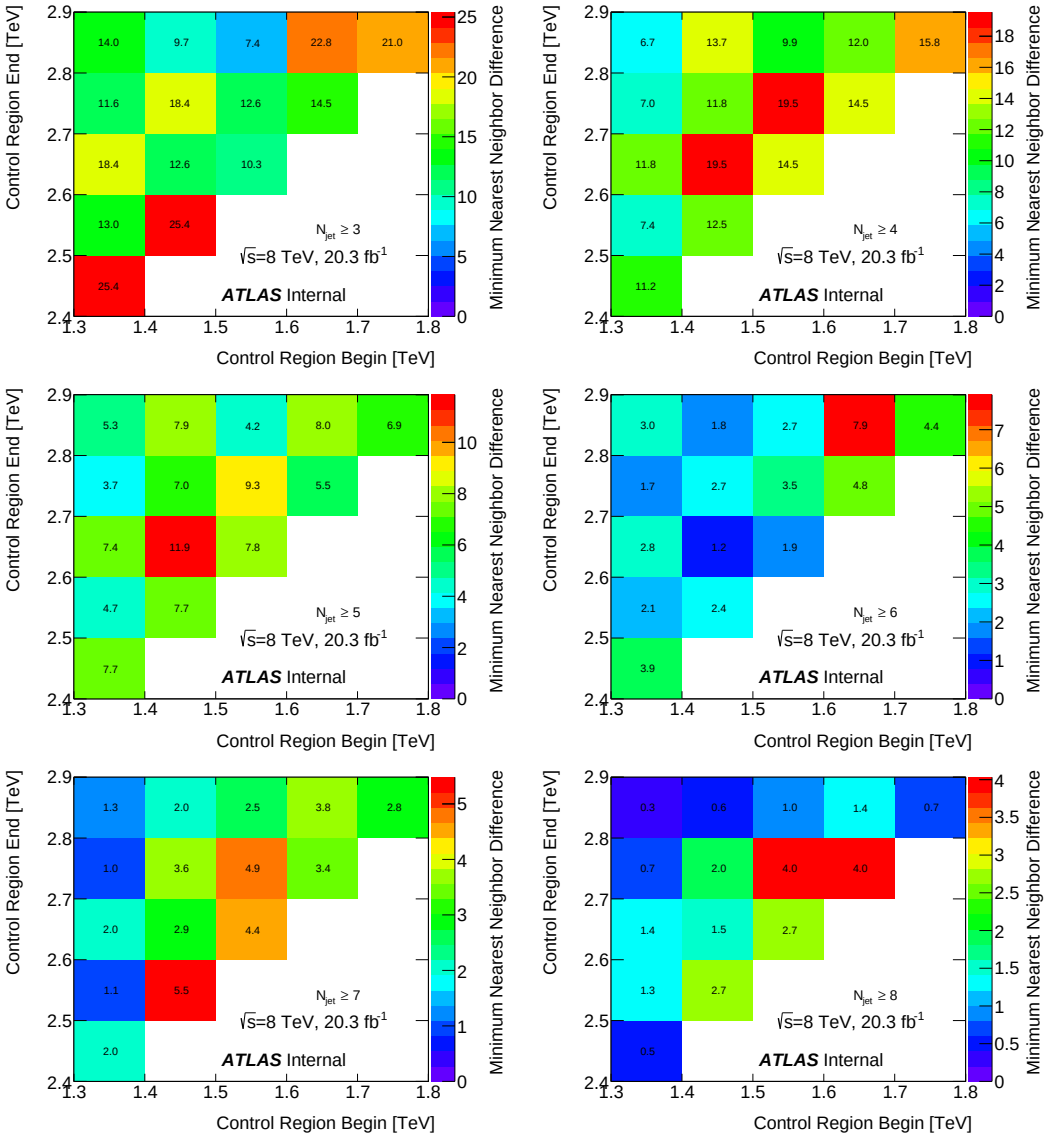

Figure 6.8: The largest nearest neighbor difference for all possible fitting ranges excluding the boundaries at 1.2 and 3.0 TeV. The x and y axis labels indicate the beginning and end of the fitting ranges. The bin entries label the largest difference between the number of predicted events for $H_{\mathrm{T}}^{\mathrm{min}} = 3.1$ TeV according to the fit extrapolation amongst the nearest eight neighbors of each range.

metric used to evaluate the optimal fitting range is thus,

$$\text{Metric} = \sum_{N_{\text{Jet}}} \sqrt{\text{Events}}_{\text{CR}} \times \text{NN}_{\text{CR}}, \tag{6.8}$$

where for a particular fit range the largest nearest neighbor difference, NN_{CR}, is weighted by square root of the number of events within the control region for all multiplicities, $\sqrt{\text{Events}_{\text{CR}}}$. This method averages over multiplicity optimization and greatly simplifies the method. Instead of each $N_{\text{Jet}} \geq X$ H_{T} distribution as practically a separate analysis, one method can be applied to all multiplicities along with all associated studies which would otherwise have to be repeated at each $N_{\text{Jet}} \geq X$.

Figure 6.9 shows the summary result according to equation (6.8) by averaging the six histograms of Figure 6.8. Based on this result the optimal, stable region is 1.5-2.9 TeV. The extrapolation according to this fitting range produces the least variation with respect to neighboring fits.

The most stable fit region provides the central value of the background estimation. In addition, the nearest neighbor regions are used to band this central value so as to provide an estimate on the uncertainty of this choice. The eight nearest neighbors of the optimal region and the optimal region itself are plotted in the range between 1.5 to 5.0 TeV in H_{T} in Figure 6.10. The maximum deviation with respect to the nominal choice, up and down, is used to form an envelope around the central value estimate.

The size of the envelope increases at higher $N_{\text{Jet}} \geq X$, reflecting the fact that with less statistics the fit extrapolation gains sensitivity to changes in the fitting range. This fact is in addition reflected in the way that equation (6.8) is biased so

that the weight, $\sqrt{\text{Events}_{\text{CR}}}$, penalizes instability more at lower $N_{\text{Jet}} \geq X$ as opposed to higher $N_{\text{Jet}} \geq X$. This reflects the fact that limited statistics wash out the effect of a biased fit whereas at low multiplicity any bias would be more pronounced.

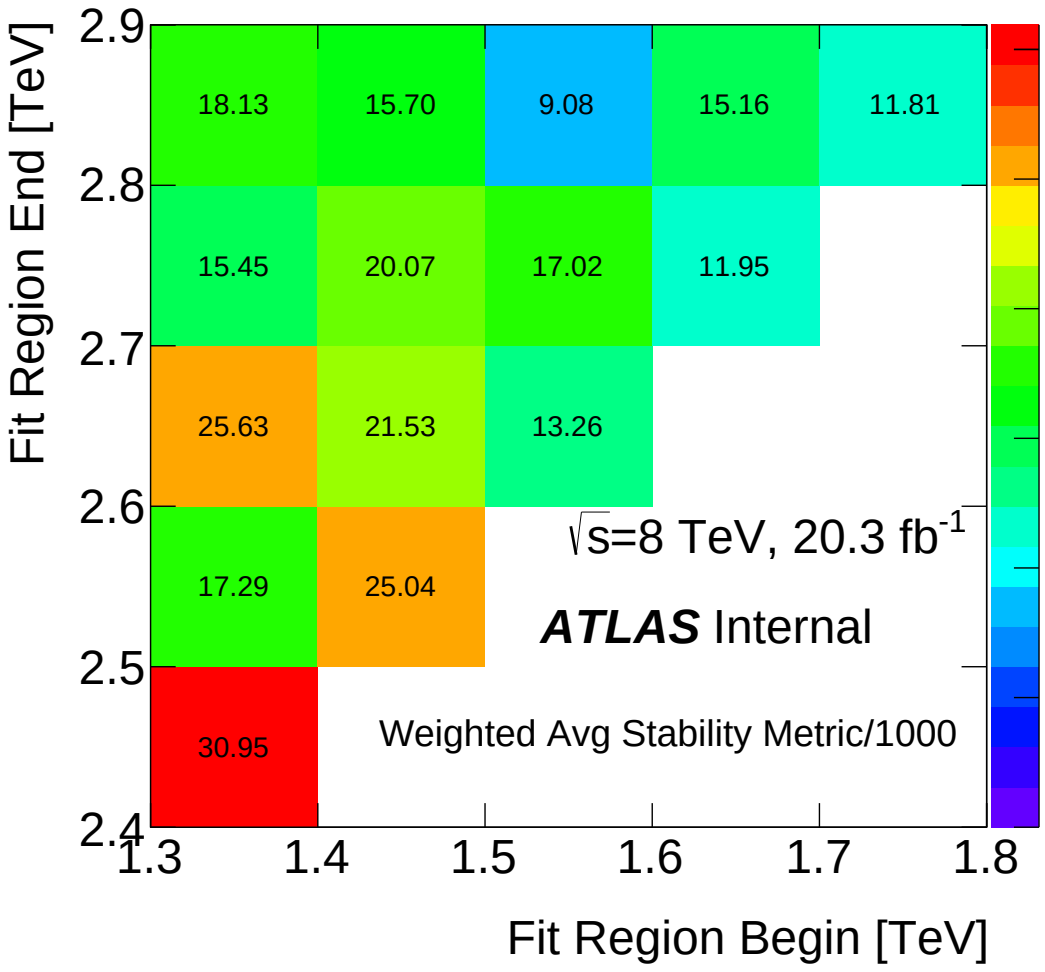

Figure 6.9: The average most stable fit range. The x and y axis labels indicate the beginning and end of the fitting ranges. The bin entries represent the values obtained from equation (6.8) divided by 1000 in order to make the numbers visible within the limited space. The fitting range with the highest value is least stable, 1.3-2.4 TeV, the range with the lowest value is most stable, 1.5-2.9 TeV.

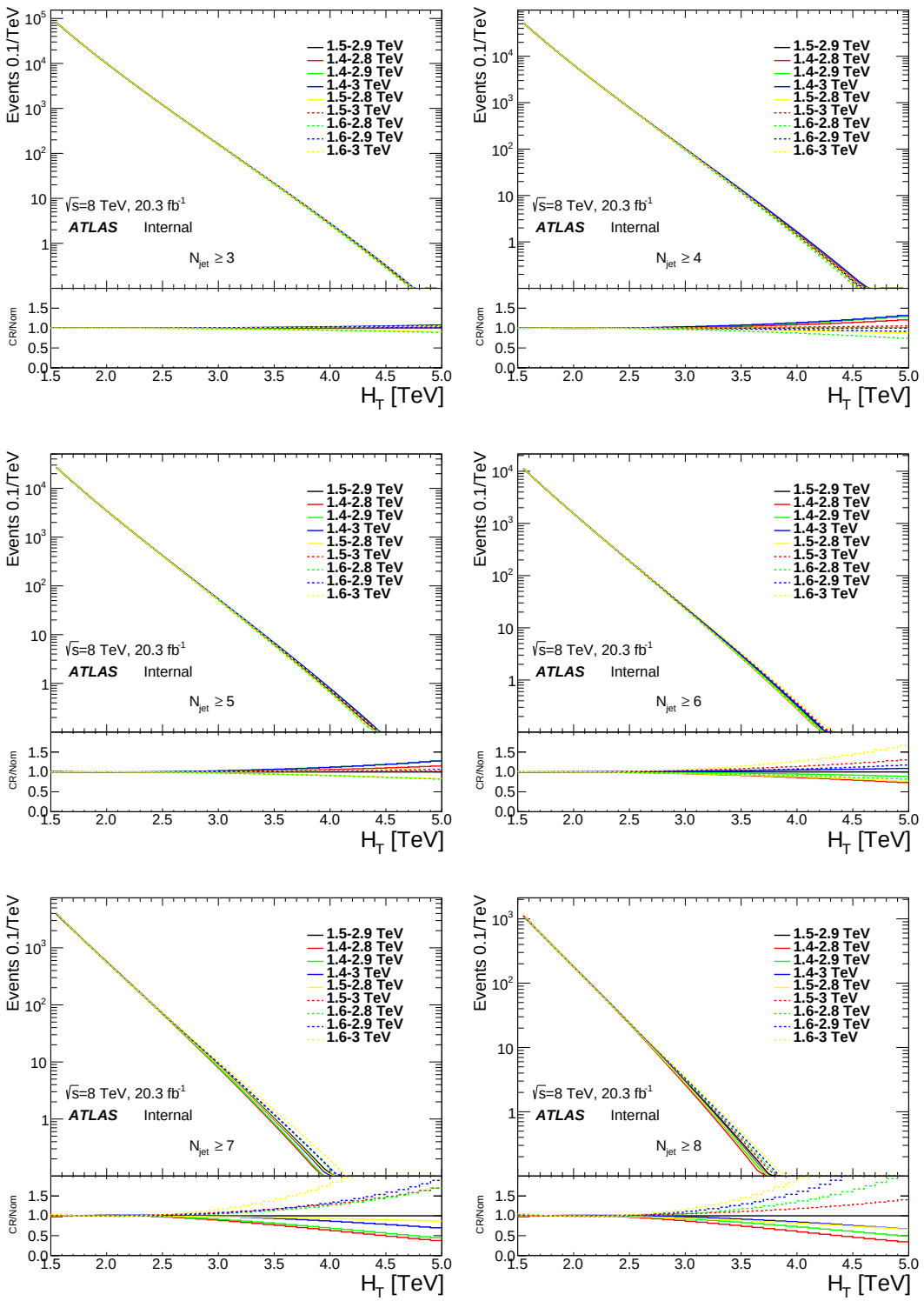

Figure 6.10: The fit and extrapolation according to the nominal fit range choice, 1.5-2.9 TeV and the eight nearest neighbors in H_{T} for individual multiplicities. The outer envelope of all curves is used to band the nominal function so as to create a nominal background estimate and an uncertainty band according to the method discussed in Section 6.4.4.

6.5 Additional Uncertainties

The data-driven method has two other associated systematic uncertainties. The uncertainty in the fitting range has already been qualitatively discussed in the previous section. In this section the two other effects related to statistical limitations in data and alternate functional forms are discussed in Sections 6.5.1 and 6.5.2 respectively.

6.5.1 Fit Uncertainty

The fit uncertainty refers to the statistical uncertainty in the fit and thereby extrapolation due to the limited statistics available in data. With increased data it is reasonable to assume this effect is reduced but the goal is to estimate the effect given the recorded 20.3 fb^{-1} of data.

A toy Monte Carlo method is used to estimate this effect. A background estimate is extracted using the nominal fit method in the desired range in H_{T}. The background according to this fit is used as a probability distribution function from which toy H_{T} distributions are created with equal statistical expectations in data.

For each toy distribution the fitting method is executed and a background estimate for the toy is extracted. The relative difference is then calculated between the toy and the nominal prediction in data according to,

$$\text{Relative Difference} = \frac{\text{Toy} - \text{Nominal}}{\text{Nominal}}, \tag{6.9}$$

where the terms Nominal and Toy refer to the predicted number of events. This process is repeated for all H_{T} bins in the toy distribution and then at each distribution in multiplicity.

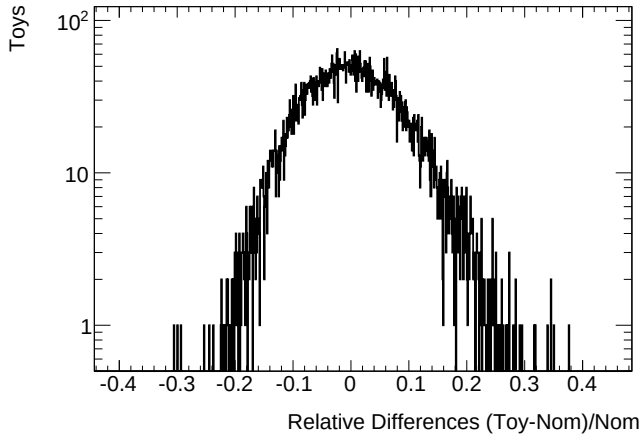

Figure 6.11: An instance of a particular distribution of the relative difference according to equation (6.9). The central value at zero indicates perfect agreement with the nominal prediction. Variations to the left and right represent under and over prediction.

An ensemble of 10,000 such toys are generated, the resulting distributions of the relative difference at each bin in H_{T} informs the statistical uncertainty of the fit. Figure 6.11 shows one such distribution. The distributions tend to be symmetric at low H_{T} and increasingly asymmetric at high H_{T} reflecting the fact that the background is monotonically falling and that there is a physical bound at zero events (the fit cannot under predict to negative events). Due to this asymmetry the uncertainty is quantified by finding the 68% coverage of the area underneath the distributions and taking the value of the distribution at those points (to the left and to right of the central value) as the up and down fluctuations due to statistical uncertainty of the fit.

The overall result is shown in Figure 6.12 illustrating that at low N_{Jet} the large statistics constrain the fit to a high degree whereas for high N_{Jet} signal regions the limited statistics is reflected in larger bands.

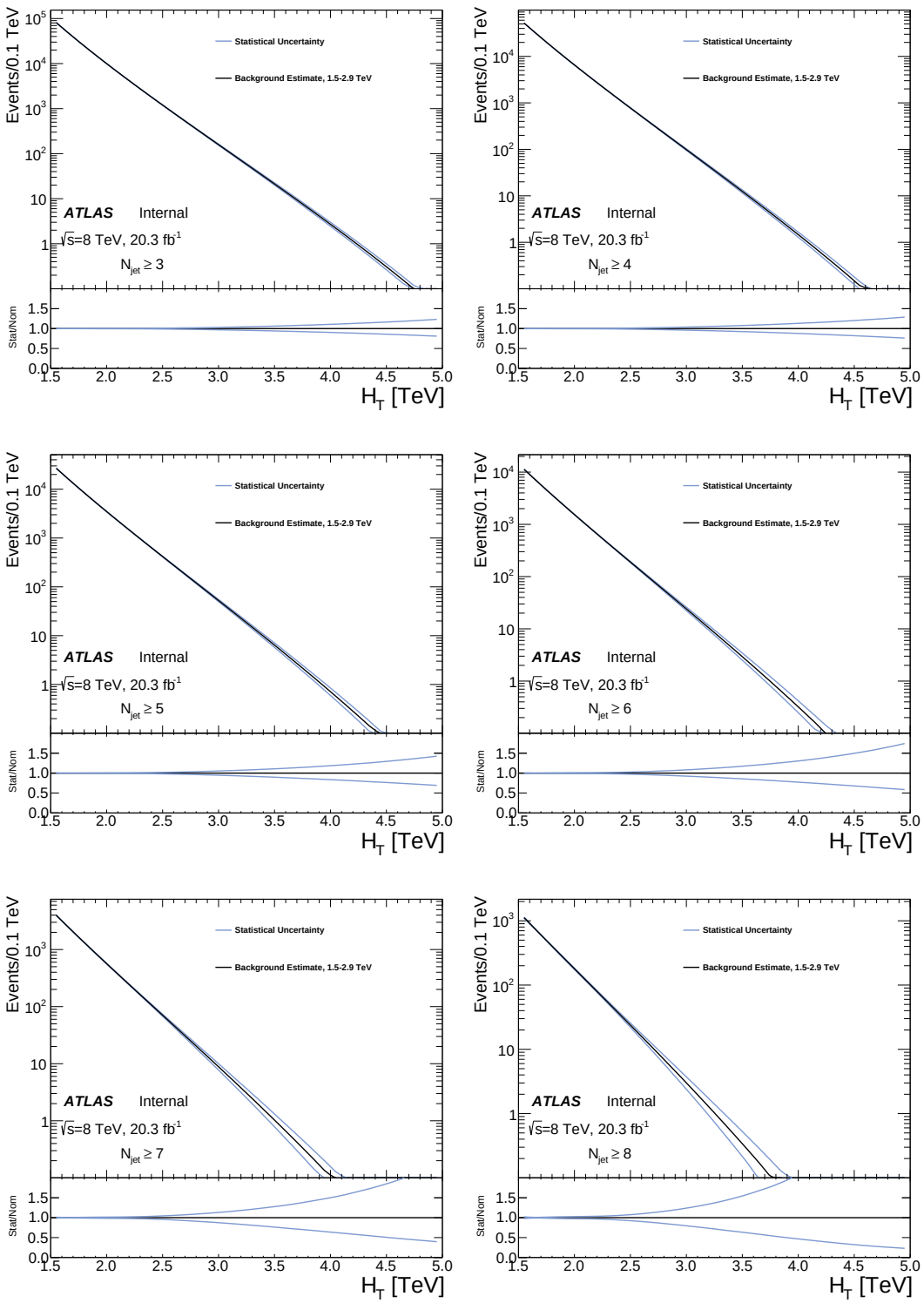

Figure 6.12: The uncertainty due to statistical limitations in data as predicted by the asymmetric 68% coverage of the distribution of the relative difference of 10,000 toys with respect to the nominal background prediction.

6.5.2 Alternate Ansatz Functions

In Section 6.4.2 an argument was made for choosing the nominal ansatz function used to predict the shape and normalization of the background in a data-driven manner in the SR. In this section, alternate choices for the ansatz are considered. Any ansatz function should still satisfy the criteria laid out in Section 6.4.2; however, they should differ in their extrapolation from the nominal choice.

The purpose is to explore alternate extrapolations based on the same fitting range, as the actual shape and normalization of the background in data are not known, this is an important study to ensure that a reasonably broad range of possiblilities is covered.

In the absense of unblinded data, MC simulation, `PYTHIA8` and `Herwig++` are used to compare the background extrapolation in the SR of these alternate choices against the nominal ansatz function.

A number of alternate forms are considered [8]. Table 6.5 contains a number of functions that have been used in previous jet-based analyses, either to estimate the background or as part of an uncertainty band along with a number of original forms developed for this analysis.

All functional forms are tested using the optimal fitting range on blinded data, `PYTHIA8` and `Herwig++` MC simulation. A fit is made within the CR and the result is extrapolated into the SR to form a background estimate. This estimate is quantitatively studied against the actual distribution in the MC simulation and data. Each fit can be evaluated in terms of the quality of the fit by the χ^2/NDF, the χ^2 per number of degrees of freedom; functions that cannot fit the CR in either

8. Only functions with three or four free parameters are considered. The shape of the CR as previously discussed cannot be described with only two free parameters and additional parameters in excess of four overconstrain the fitting.

the MC simulation or blinded data, based on the χ^2/NDF, can be immediately eliminated as alternate candidates.

In Figures 6.13 and 6.14 the results of all the alternate function fits are shown applied to `PYTHIA8` and `Herwig++` MC simulation at all $N_{\text{Jet}} \geq X$. The fit uncertainty is drawn on top of such plots to illustrate that at low multiplicities the effect of varying extrapolations is significant. At higher multiplicities it is however statistical limitations that dominate. It should be noted that the nominal function almost always, in different N_{Jet} and MC simulations, provides the best extrapolation. As such it confirms the initial ansatz function choice for the central value of the background estimation.

By evaluating the quality of the fit in the CR and the accuracy of the extrapolation against the MC simulation, a number of functions can be eliminated at each multiplicity. In addition, the quality of the fit extrapolation within the SR can be quantified in MC simulation using the pull,

$$V = \frac{1}{\text{NDF} - 1} \sum_{i}^{f_i<0.1} \frac{f_i - d_i}{d_i}, \tag{6.10}$$

where the sum indicates the relative difference between the background prediction, f_i, per bin, i and the actual value of the bin in MC, d_i. The sum is terminated when the background prediction is below 0.1 events.

There is always an ambiguity in quantifying the accuracy of the extrapolation. It is always possible to produce a larger band by adopting a loose selection based on a metric such as the pull (or even adopting a different metric altogether) and thereby producing a less sensitive but more conservative analysis. At the same time, it is possible to act more restrictively and eliminate as many functions

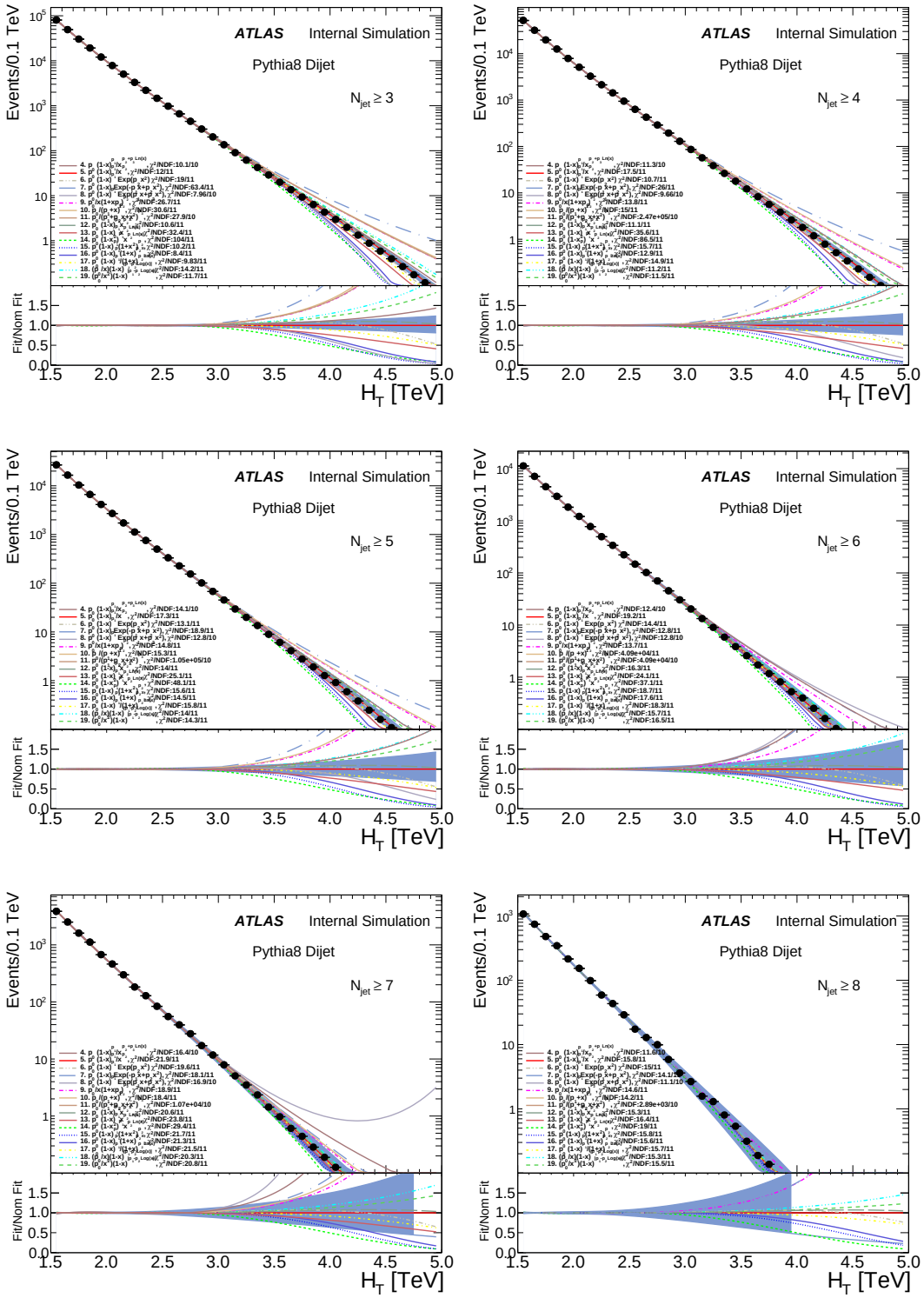

Figure 6.13: All the functional forms listed in Table 6.5 fitted and extrapolated to PYTHIA8 MC simulation. The blue band represents the fit (statistical) uncertainty superimposed in order to provide a sense of relative scale of the effects of the varying extrapolations.

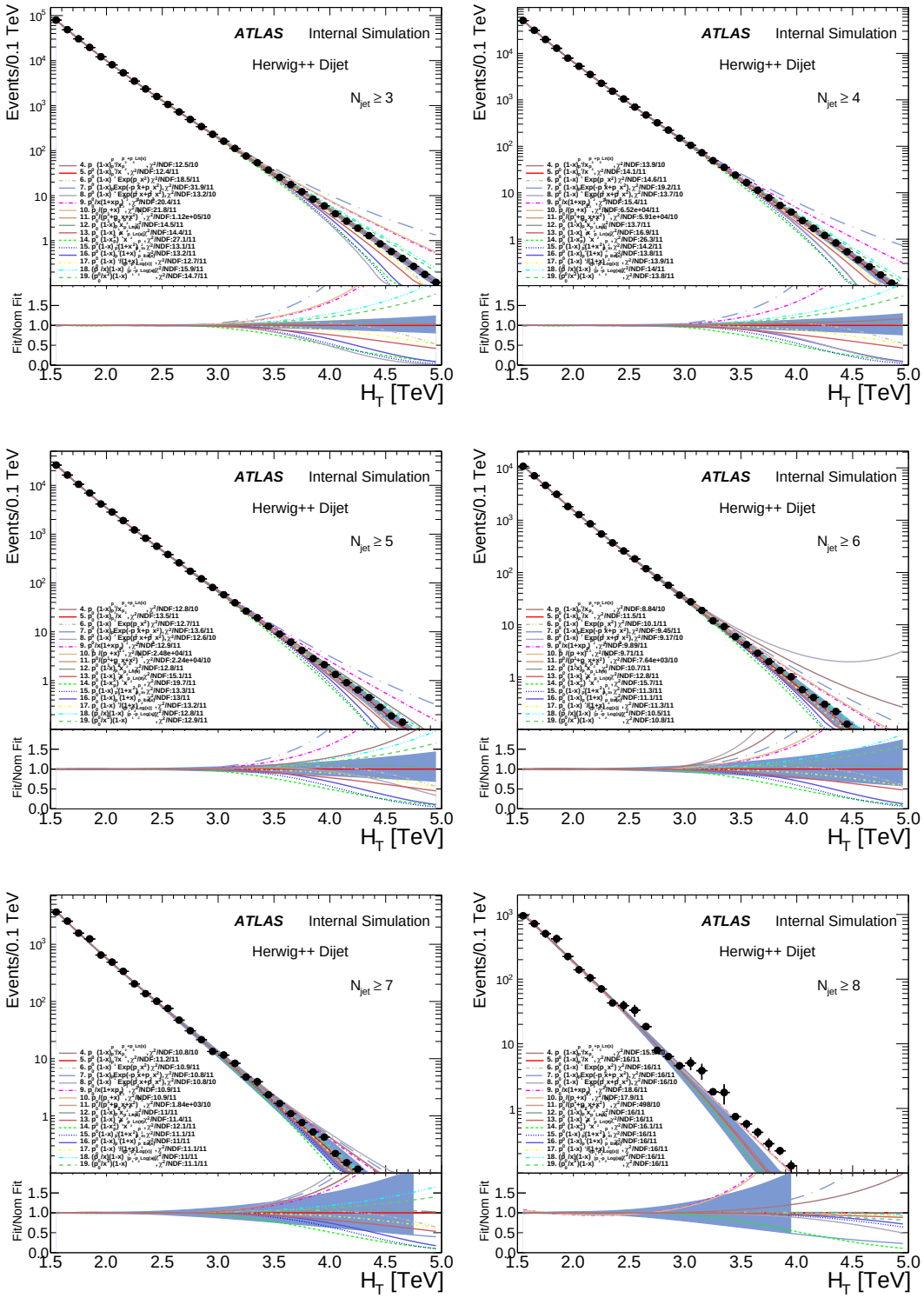

Figure 6.14: All the functional forms listed in Table 6.5 fitted and extrapolated to `Herwig++` MC simulation. The blue band represents the fit uncertainty superimposed in order to provide a sense of relative scale of the effects of the varying extrapolations.

as possible by comparing their extrapolation to the MC in the SR, thereby achieving a small uncertainty on the function choice. In this analysis a balance was struck between these two extremities by comparing the alternate function extrapolations in Monte Carlo for each $N_{\text{Jet}} \geq X$ bin individually. A rigorous quantitative study of each function was performed using the metric of equation (6.10); however, the ultimate choice of alternate function forms for each $N_{\text{Jet}} \geq X$ bin was based on a judgement call of what constitute "good extrapolation" with respect to the MC by the analyzers.

In Table 6.5 the functions that are able to fit the CR and provide reasonably good extrapolations are listed for each multiplicity. These functions are grouped together and used to band the nominal function. The maximum envelope provides an uncertainty on the mathematical form of the nominal ansatz function. This result is shown in blinded data in Figure 6.15.

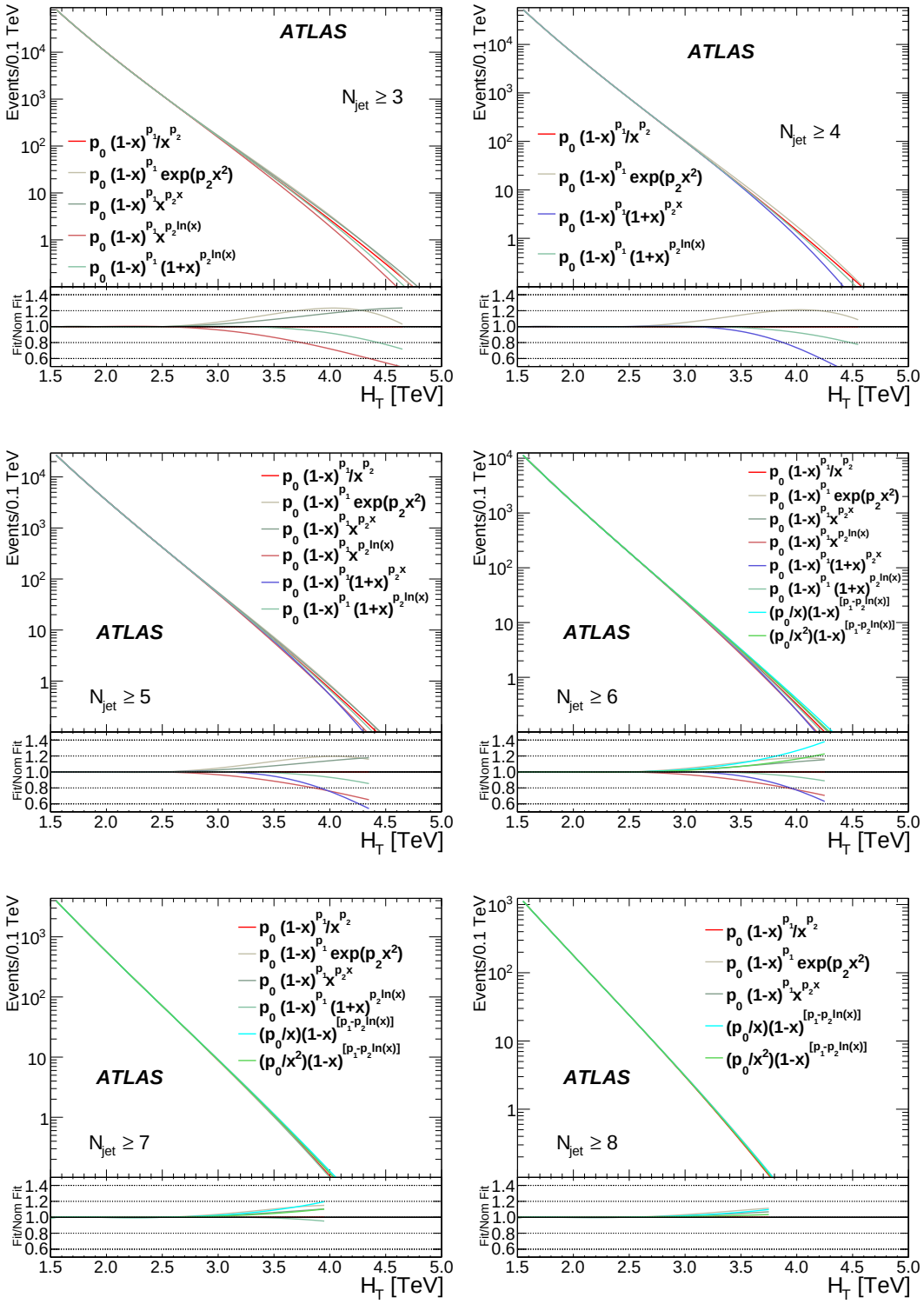

Figure 6.15: Alternate ansatz function choices per $N_{\text{Jet}} \geq X$. The uncertainty on the nominal ansatz functional form is determined by the largest envelope of the candidate functions about the nominal choice (red line), if all alternate choices are to one side of the nominal choice the uncertainty is one sided.

#	Form	Comment	$N_{\text{Jet}} \geq X$
4	$\frac{p_0(1-x)^{p_1}}{x^{p_2+p_3 \ln x}}$	CDF [56], ATLAS [54], [57], CMS [55]	
5	$\frac{p_0(1-x)^{p_1}}{x^{p_2}}$	Nominal	3-8
6	$p_0(1-x)^{p_1}e^{p_2 x^2}$	-	3-8
7	$p_0(1-x)e^{(-p_1 x+p_2 x^2)}$	-	
8	$p_0(1-x)^{p_1}e^{(p_2 x+p_3 x^2)}$	-	
9	$\frac{p_0}{x(1+p_1 x)^{p_2}}$	ATLAS [24]	
10	$\frac{p_0}{(p_1+x)^{p_2}}$	CMS [25]	
11	$\frac{p_0}{(p_1+p_2 x+x^2)^{p_3}}$	CMS [25]	
12	$p_0(1-x)^{p_1}x^{p_2 x}$	-	3, 5-8
13	$p_0(1-x)^{p_1}x^{p_2 \ln x}$	-	3, 5, 6
14	$p_0(1-x^2)^{p_1}x^{p_2 \ln x}$	-	
15	$p_0(1-x)^{p_1}(1+x^2)^{p_2}$	-	
16	$p_0(1-x)^{p_1}(1+x)^{p_2 x}$	-	4-6
17	$p_0(1-x)^{p_1}(1+x)^{p_2 \ln x}$	-	3-7
18	$\frac{p_0}{x}(1-x)^{[p_1-p_2 \ln x]}$	-	6-8
19	$\frac{p_0}{x^2}(1-x)^{[p_1-p_2 \ln x]}$	-	6-8

Table 6.5: The list of ansatz functions considered in this analysis. The first column gives each function a numerical label that matches that of the legend in Figures 6.13 and 6.14, the second column gives the functional form and the third column describes the original source of the function. If left unstated this implies the form was developed originally for this analysis. The last column gives the inclusive jet multiplicitiy where the function has been applied as an alternate fit extrapolation uncertainty. The list begins from #4 and not #1 for historical reasons.

6.6 Search Strategy

This section details the algorithm used to quantitatively describe the amount of excess above the predicted background in the data upon unblinding. In Figure 6.16 the analysis is summarized in a set of six histograms illustrating the six inclusive multiplicity bins, the background prediction and uncertainty in each. Overlaid on top of these distributions is the complete, unblinded, 20.3 fb^{-1} of recorded collision data. Additionally, a number of representative benchmark signal models are shown as well, illustrating the scale and shape of data excess that would be characteristic of microscopic black holes. The purpose of this section is to quantify the degree of any excess above the background seen in Figure 6.16.

The nominal number of SRs in this analysis is the product of the number of $H_{\mathrm{T}} > 3.0$ TeV bins and the number of inclusive jet multiplicity H_{T} distributions. While the number of H_{T} bins run up to the kinematic limit at 8 TeV, it is reasonable to assume that statistically limited data will terminate well before that point, as such the number of SRs searched is limited to $H_{\mathrm{T}} < 5.0$ TeV, i.e. the search is not conducted up to 8 TeV.

For each of the 120 SRs the goal is to quantitatively describe the amount of excess data in terms of the event count above the predicted background so as to either exclude or declare the presence of new physics.

Any algorithm that searches all possible SRs must account for the possibility that a data excess is due purely to statistical fluctuations. As the number of SRs examined increases the possibility that at least one SR will contain a significant excess due to a purely statistical effect grows. This is the so called "look elsewhere effect", abbreviated LEE, otherwise called the trials factor. In this analysis a test

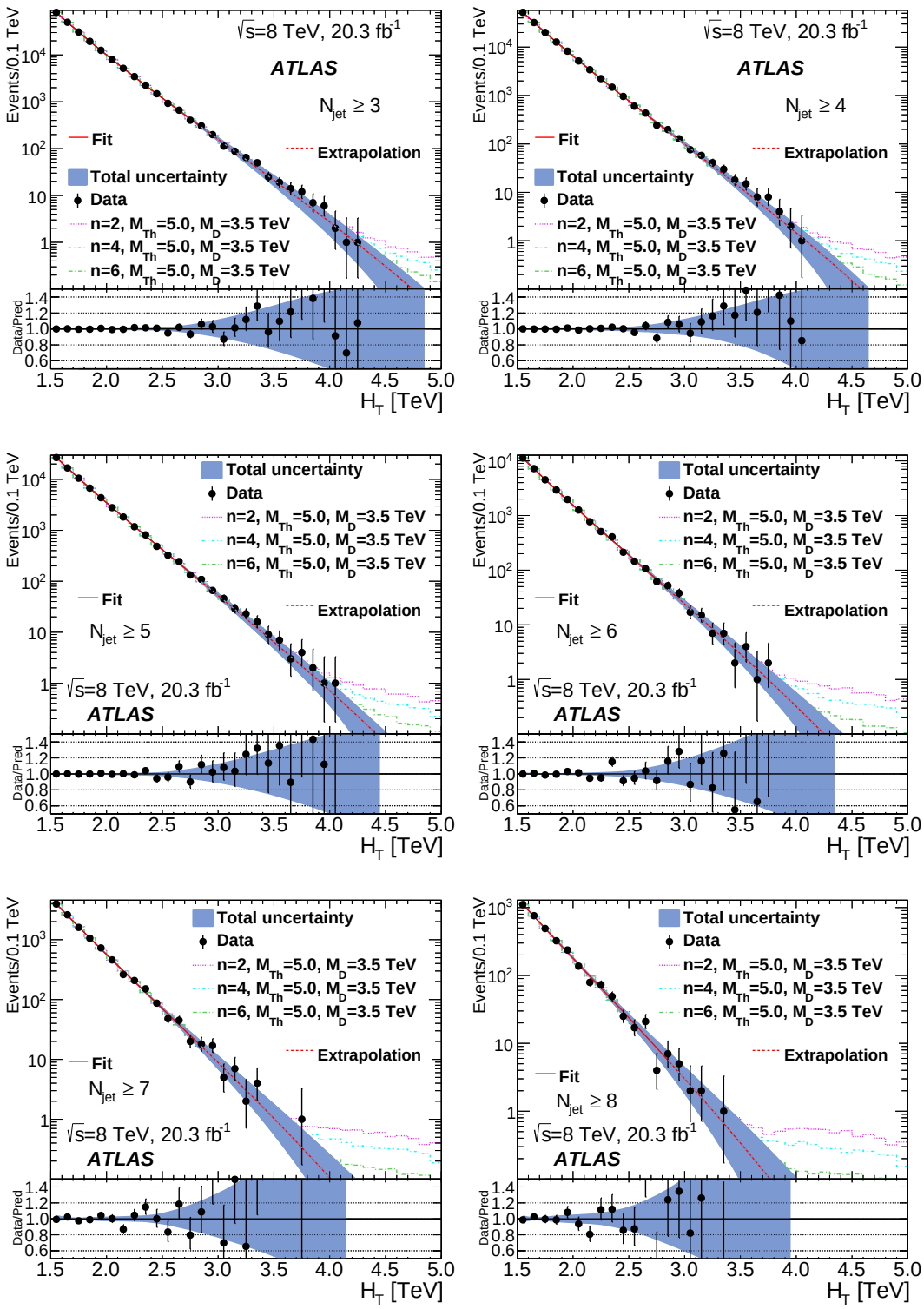

Figure 6.16: The background prediction (red line) with the total uncertainty band (blue) against collision data (black dots) with three representative microscopic black hole signal samples at $n = 2, 4, 6$ and $M_{\mathrm{Th}} = 5.0$ TeV and $M_{\mathrm{D}} = 3.5$ TeV overlaid.

statistic and algorithm that compensates for the LEE is utilized. In addition, the algorithm is designed to strictly look for statistical discrepancies between observed data and predicted background. No attempt is made to incorporate the effects of systematic uncertainties [9].

The test statistic used is the so called t value utilized in the `BumpHunter` algorithm [59] and defined as,

$$t = -\log(\text{p-value}_{\text{min}}). \tag{6.11}$$

The test statistic only examines the smallest p-value of all SRs where the p-value is defined by,

$$\text{p-value} = \frac{1}{\Gamma(d)} \int_0^f t^{d-1} \exp(-t)\, dt = \Gamma(d, f), \tag{6.12}$$

where $\Gamma(d)$ is the Gamma function for integer d. For any SR, the p-value can be calculated between the count in data, d, and the predicted background, f. It is not only possible to look for excess in the 120 nominal SR's but also in combinations of SRs. As new physics is predicted to appear as a threshold effect, there may be excess data spread across multiple bins. Therefore, the search procedure can be generalized as:

— Calculate the p-value for the smallest (nominal) bin width in H_{T} at each value in H_{T}, moving from left to right.

— Increase the window size to the next smallest bin width and calculate the

9. In any event, in almost all instances additional uncertainties can only decrease the statistical significance of any excess. This means that the search algorithm is already the most conservative search method as it will find the largest possible fluctuation. There is one uninteresting case in which it is possible to actually increase the significance after convolving the systematic uncertainty into the calculation [58].

p-value across the H_{T} distribution from left to right, each time moving the window by the minimum bin width.

— Increase the window size and repeat the procedure until the maximum window size is reached.

— Repeat the process for each N_{Jet}.

The t value for the data sample, t_0, is given by the most significant excess in the context of equation (6.12) and can be compared with the expectation of compatibility with the SM, the null hypothesis.

The t distribution under the assumption of the null hypothesis is constructed by executing the search algorithm on 10,000 pseudo data sets generated from a base probability distribution function. For the null hypothesis, the distribution function is the background prediction according to the nominal fit function [10], equation (6.6). The null t distribution is shown in Figure 6.17 along with the instance of t_0 calculated from the unblinded data.

The value of t_0 relative to the distribution t determines the degree of compatibility of the data with SM expectations. The most probable value of t is where the distribution is peaked, $\sim$3.6, moving to the right indicates increasing incompatibility between data and prediction and as given by the decreasing number of "toys" is less likely due to statistical fluctuations. It is possible to transform the value of t_0 into a global p-value by computing the binomial success rate of the null hypothesis with respect to t_0, but by visual inspection it can be qualitatively understood that the unblinded data is compatible with the background-only hypothesis and that no significant excess is observed.

10. The nominal fit result to collision data is used as the probability distribution function to create the pseudo data sets, but each pseudo data set must have its own backgroud prediction, obtained by executing the fit and extrapolation method on the individual pseudo data set.

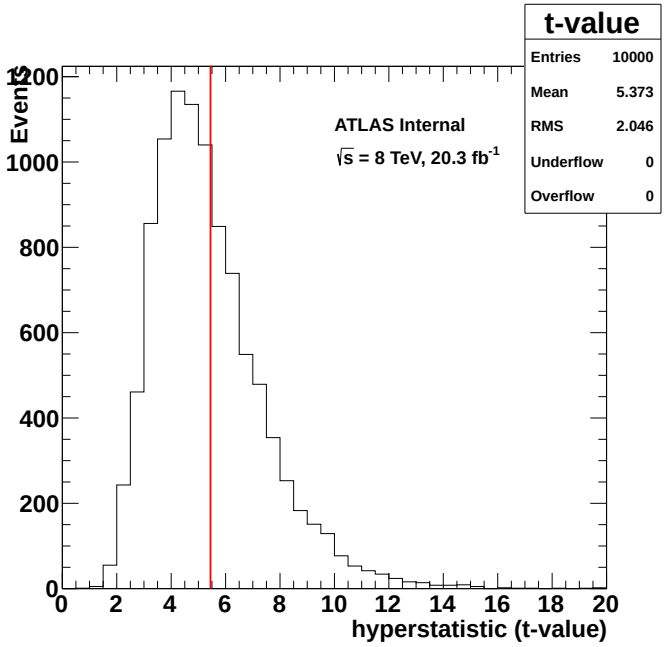

Figure 6.17: The distribution t under the null hypothesis (black) in 10,000 pseudo data sets and the value of t_0 extracted from data (vertical red line).

The most discrepant region is between H_{T} 3.2-3.9 TeV, at $N_{\mathrm{Jet}} \geq 4$ as illustrated in the top right plot of Figure 6.18. In Figure 6.18, the Gaussian significance is plotted for each single SR, illustrating the degree of excess based on Poisson counting [58],

$$\text{p-value}_{\text{bin}} = \begin{cases} 1 - \frac{\Gamma(d,f)}{\Gamma(d)}, & d > f \\ \frac{\Gamma(d+1,f)}{\Gamma(d+1)}, & d \leq f \end{cases} \tag{6.13}$$

with the resulting p-value$_{\text{bin}}$ converted to a Gaussian significance.

Quantitatively this excess corresponds to $t_0 = 5.4$ with a local p-value $= 0.0043$. The global p-value with respect to the null hypothesis is additionally found to be 0.4. The algorithm excludes significant excess beyond SM predictions.

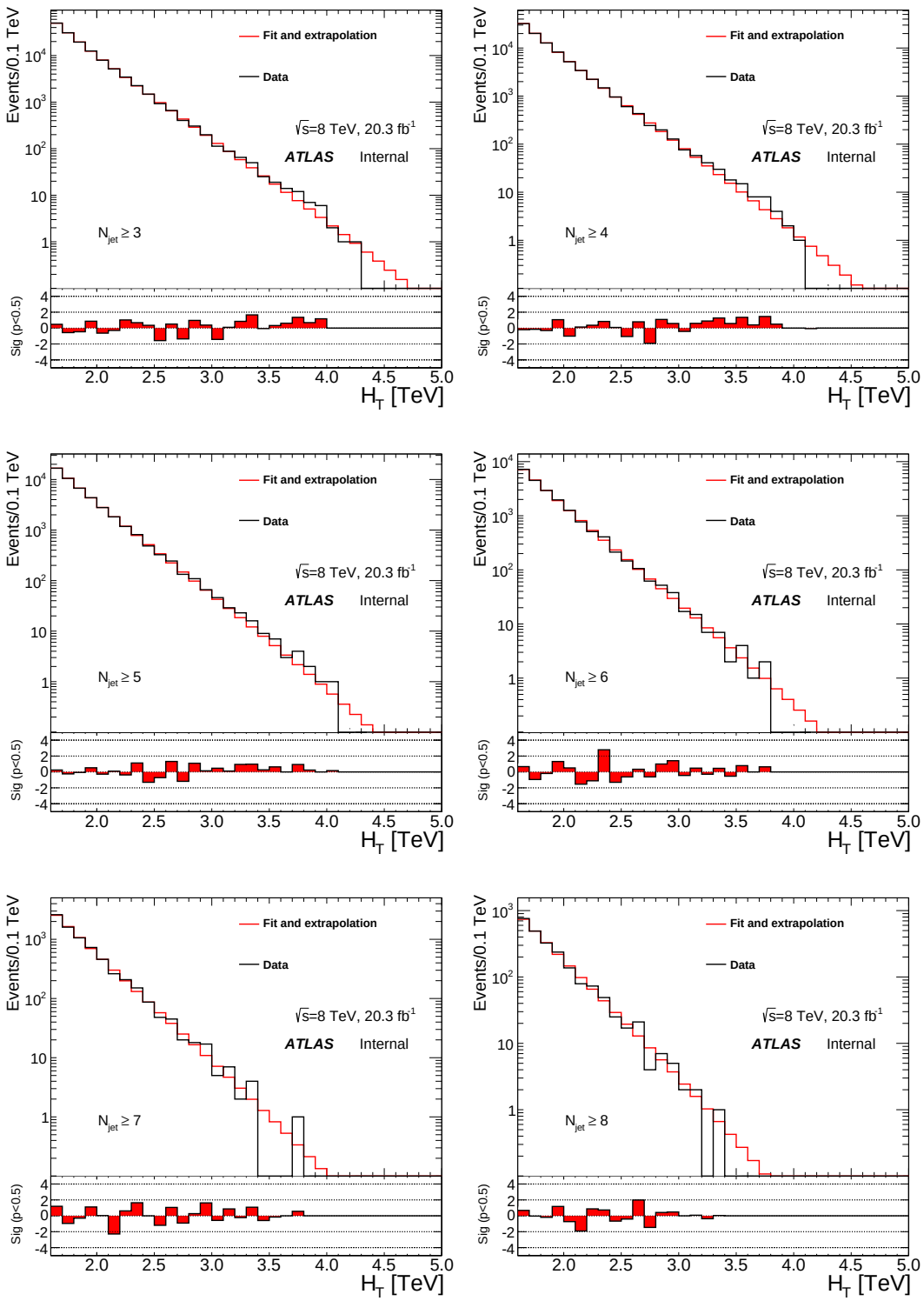

Figure 6.18: The H_{T} distribution in unblinded data compared against the nominal background prediction. In the ratio sub-plots the Gaussian significance has been plotted as a function of H_{T} for p-values < 0.5; larger values are considered to be completely insignificant. The most discrepant region can be seen in the top right plot for $N_{\mathrm{Jet}} \geq 4$.

7
Results

7.1 Limit Setting

This section of the dissertation details the physics results of the analysis. In the absence of discovery, statistical techniques are utilized to produce upper limits on the non-Standard Model multi-jet production cross section and exclusion contours in the space of M_{Th} vs M_{D} are discussed. In addition, the method of signal region optimization along with the associated signal sample uncertainties are reviewed.

Throughout this chapter and for the analysis as a whole the `HistFitter` [60] software package is used to technically implement the outlined procedures.

In this section the implementation of the techniques and calculation of the results were performed by the author. Additional signal samples and theoretical cross sections used to interpolate the model-dependent limits were produced and calculated by Douglas Gingrich.

7.1.1 Techniques

Statistical methods are used to provide upper limits on relevant processes by taking into account and combining the predicted background, associated systematic uncertainties and the observed data along with its statistical uncertainty

into a calculation. As non-perturbative gravity states appear as threshold effects the relevant parameter is the inclusive $H_{\mathrm{T}}^{\mathrm{min}}$ for which all quantities are rebinned, including the the background, systematic uncertainties and observed data. These rebinned quantities are presented in tables in Appendix C and are visually illustrated in Figure 7.1.

An upper limit is set a SR by forming the profile likelihood from the likelihood,

$$L(n_s|\mu, b, \theta) = \mathcal{P}(n_s|s, \mu, b, \theta) \times \prod_i N_{\mathrm{syst}}(\theta_0, \theta, \sigma_\theta)_i. \tag{7.1}$$

Equation (7.1) represents the convolution of two basic components,

- $\mathcal{P}(n_s|s, \mu, b, \theta) = \frac{(\mu s + b(\theta))^{n_s}}{n_s!} e^{-\mu s + b(\theta)}$ is a Poisson probability defined by the observed event count n_s, signal strength, μ, expected signal s and expected background $b(\theta)$, which is constrained by the measurement of additional parameters θ. Often, for an experiment where the expected number of signal events in the SR is known (and therefore fixed), the parameter that is tested is μ, the signal strength. For this analysis, no assumptions on the signal cross section are made, therefore the upper limit to be extracted is with respect to the number of excess (signal) events. This is equivalent to $\mu = 1$ and testing for s. In the following μ and s are used interchangeably. The parameter of interest is the signal event count.

- $\prod_i N_{\mathrm{syst}}(\theta_0, \theta, \sigma_\theta)_i$ is a product of i Gaussian constraints with mean and variance θ_0, σ_θ obtained through additional measurements that are peripheral to the parameter of interest, that constrain the background. These are known as the nuisance parameters.

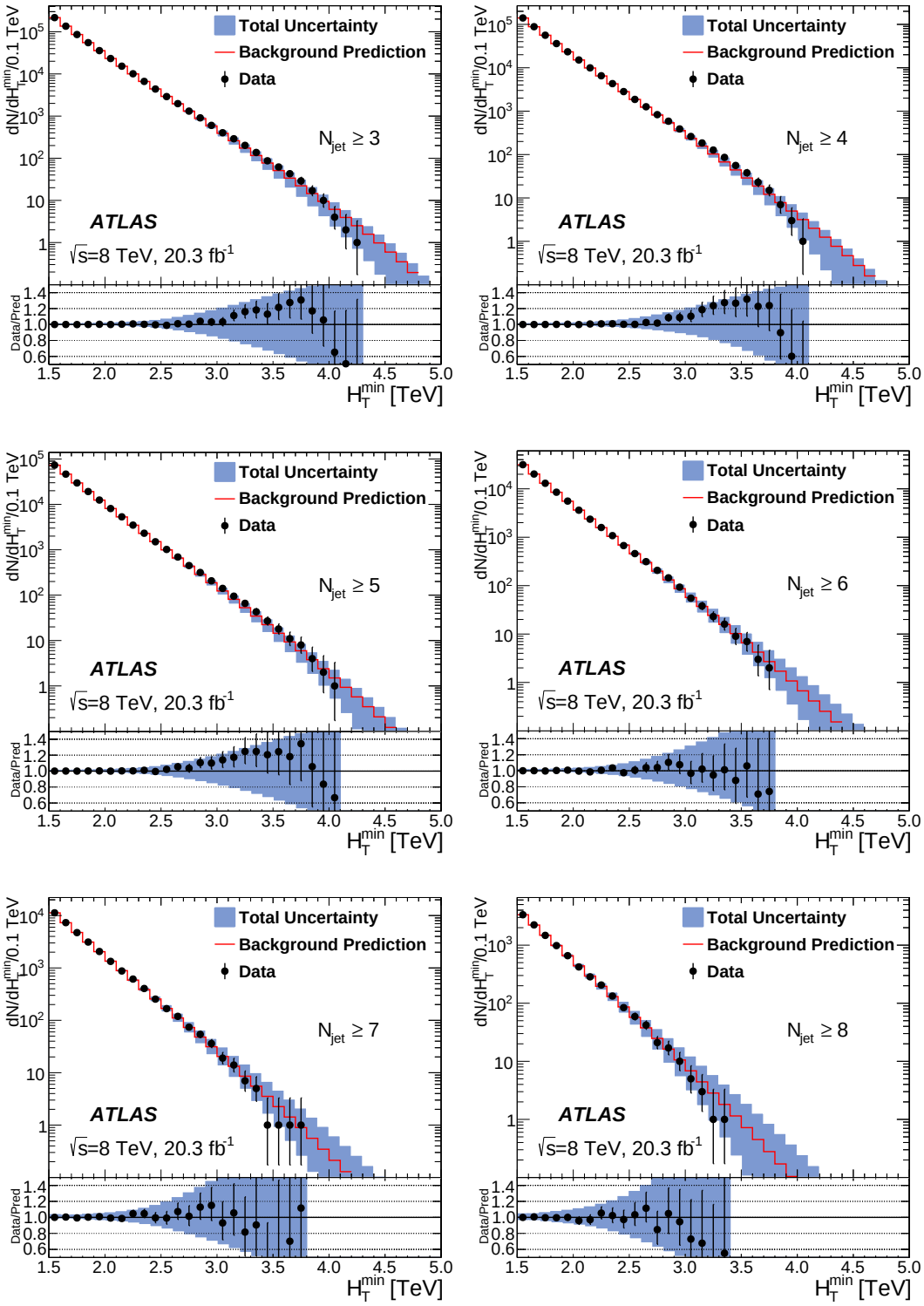

Figure 7.1: The background prediction (red) with the overall uncertainty band (blue) against collision data (black dots) in inclusive H_{T} bins.

The likelihood can be further manipulated into a more advance test statistic. Given the distribution of the test statistic, the p-value, significance can be defined as in Section 6.6, in addition to concepts such as the upper or lower limit. To construct a test statistic, first the one sided profile likelihood ratio [61] is formed from the likelihood model,

$$\lambda(\mu) = \frac{L(\mu, \hat{\hat{\theta}})}{L(\hat{\mu}, \hat{\theta})}, \tag{7.2}$$

where the numerator is the profile likelihood maximized at a fixed value of μ and the denominator is the globally maximized profile likelihood. Thus $\hat{\mu}$ and $\hat{\theta}$ are the values of the signal strength and nuisance parameters that maximize the function while $\hat{\hat{\theta}}$ are the nuisance parameters that maximize the function under the condition of a given μ. For a counting experiment where there can only be an excess and not a deficit (for instance in neutrino oscillations) only extra events are of interest and thus the signal strength is physically bounded, $\mu \geq 0$. This implies that if the observed data is best optimized such that $\hat{\mu} < 0$, then the denominator, the global maximum is $L(0, \hat{\theta}(0))$ and the profile likelihood is one sided.

Equation (7.2) is a ratio that measures the compatibility of the data with the background under the assumption of a given signal strength μ, thus the procedure to set an upper limit is the following: scan through the space of possible μ; at each point quantify the compatibility between background and data under the assumption of μ; terminate the procedure at a pre-determined point representing some upper limit in confidence.

The test statistic [61] q_μ,

$$q_\mu = \begin{cases} -2\ln\lambda(\mu) & \hat{\mu} \leq \mu, \\ 0 & \hat{\mu} > \mu, \end{cases} \tag{7.3}$$

is constructed as a positive, monotonic function[1] of equation (7.2). The statistic q_μ is designed so that larger values represent greater incompatibility between data and background under the assumption of the particular value of μ and model. The form of q_μ is designed such that for sufficiently large values of the Poisson mean ($\mu s + b \sim 10$) and one parameter of interest its probability distribution $f(q_\mu|\mu)$ is χ^2 distributed with one degree of freedom [62], [63], [64]. For SRs with a small or ~ 0 mean, q_μ is dominated by the Poisson term of the likelihood function and the shape of the distribution is not predictable a priori. This former feature allows the $p-$value to be very quickly computed analytically. This is further discussed in the following sections.

7.1.1.1 The CL$_s$ Method

At each value of the scan range for μ the distribution, $f(q_\mu|\mu)$, is constructed; then the compatibility of the data with the model can be described by the p-value, p_μ,

$$p_\mu = \int_{q_{\mu,\text{obs}}}^{\infty} f(q_\mu|\mu)\, dq_\mu, \tag{7.4}$$

expressing the significance of the observed test statistic $q_{\mu,\text{obs}}$. As stated before, for sufficiently large values of $\mu s + b$, the Poisson mean, $f(q_\mu|\mu)$ is known analytically,

1. For $\hat{\mu} > \mu$ the test statistic is 0 because an upper limit is desired, so if the optimal $\hat{\mu}$ is greater than the tested μ that is of minimal interest [60].

for SR's with low background predictions and low expectation of events (where signal sensitivity can be greater) the discrete structure of the Poisson distribution is non-negligible and $f(q_\mu|\mu)$ is not a monotonic function and must be sampled using MC methods.

Figure 7.2 shows the $f(q_\mu|\mu)$ distribution for a range of μ values for a particular SR. The procedure is to optimize the test statistic at each scan point according to the observed data and μ with regards to the nuisance parameters and appropriate constraints. The distribution of $f(q_\mu|\mu)$ is constructed for the background plus signal model and the background only model where $\mu = 0$ by sampling the test statistic using a MC method.

The upper limits are constructed according to the CL_s definition [65] by integration with respect to the value of the test statistic in data against the distribution of the test statistic at the specific μ. For each point μ the p-value of the background only (b) and background plus signal models ($b + s$) are defined by equation (7.4) where it is understood that $f(q_\mu|\mu)$ stands for either the background only or background plus signal model distribution as appropriate.

The ratio of the p-value for the two models in the form,

$$\mathrm{CL_s} = \frac{\text{p-value}_{b+s}}{\text{p-value}_{b}}, \tag{7.5}$$

is known as the CL_s value. Often, the ratio is written as $\frac{\mathrm{CL_{b+s}}}{\mathrm{CL_b}}$, but it should be noted CL_s is not strictly speaking a p-value in the same sense as its components. The value is a comparison of the compatibility of the data against the null hypothesis and the signal (alternate) hypothesis for a particular value of signal strength. Intuitively, smaller values indicate preference for the background only model while

larger values indicate preference for the signal model. In Figure 7.3 this is illustrated for the tested signal strength points of Figure 7.2. As the signal strength increases, in the absence of new physics, the test statistic in data increasingly favours a background only model as is characterized by the CL_s approaching zero in Figure 7.3. In addition, Figure 7.3 illustrates the expected CL_s and its one and two standard deviation bands. These values are defined with respect to the median, 1 and 2 standard deviation coverage of the background only test statistics distribution as seen in Figure 7.2. A key feature of the profile likelihood test statistic method used here is that since the initial q_μ is optimized according to data, the expected limits will always track the observed limits due to it sharing the same optimized nuisance parameters. The upper limit at 95% confidence is found by interpolating the line of the limit with a horizontal line drawn at p-value=0.05 as seen in Figure 7.3. This procedure is applied to extract the observed, expected limits and expected limit uncertainty bands by interpolating with the respective limit line.

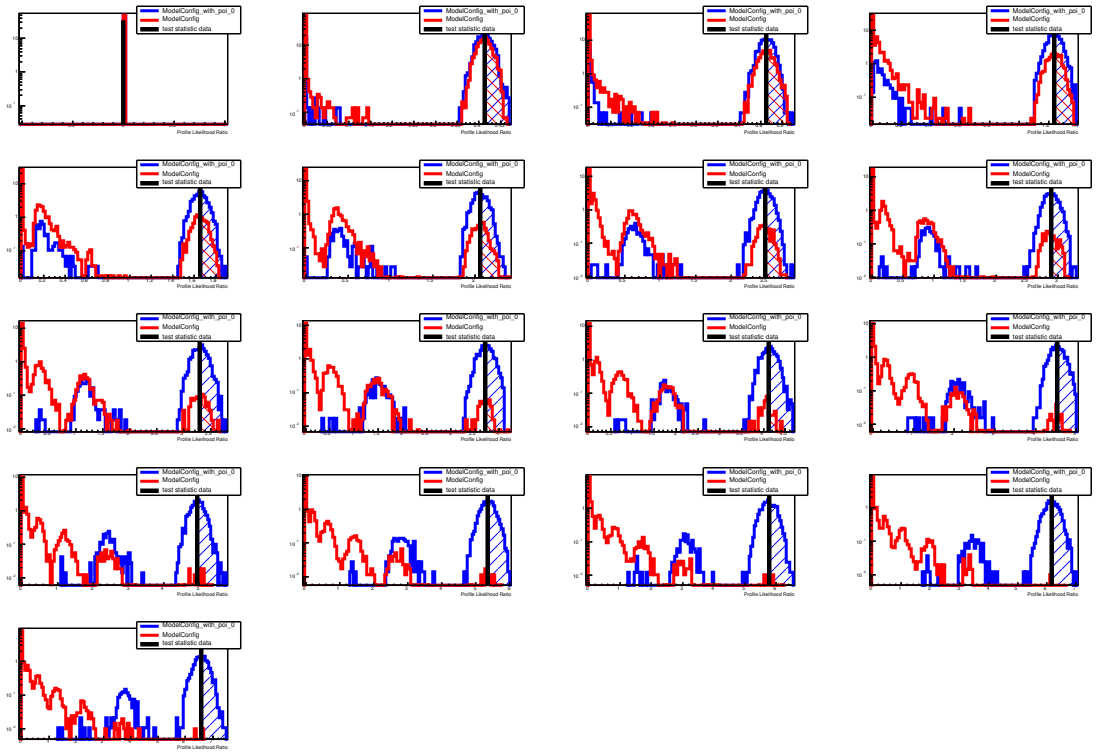

Figure 7.2: The $f(q_\mu|\mu)$ distribution (red) and the $f(q_\mu|\mu = 0)$ background only distribution (blue) for a range of μ values scanned for the signal region $N_{\text{Jet}} \geq 7$ and $H_{\text{T}}^{\text{min}} = 4.1$ TeV. For this SR the predicted background is 0.131 against an observation of 0 events; the discrete nature of the test statistic distributions are apparent. The p-values of the background only and background plus signal models are defined by the shaded regions. The number of scan points and toys is idealized for illustrative purposes; for actual execution over a hundred scan points and tens of thousands of toys per scan point are used to achieve smooth distributions and fine granulation in subsequent interpolation.

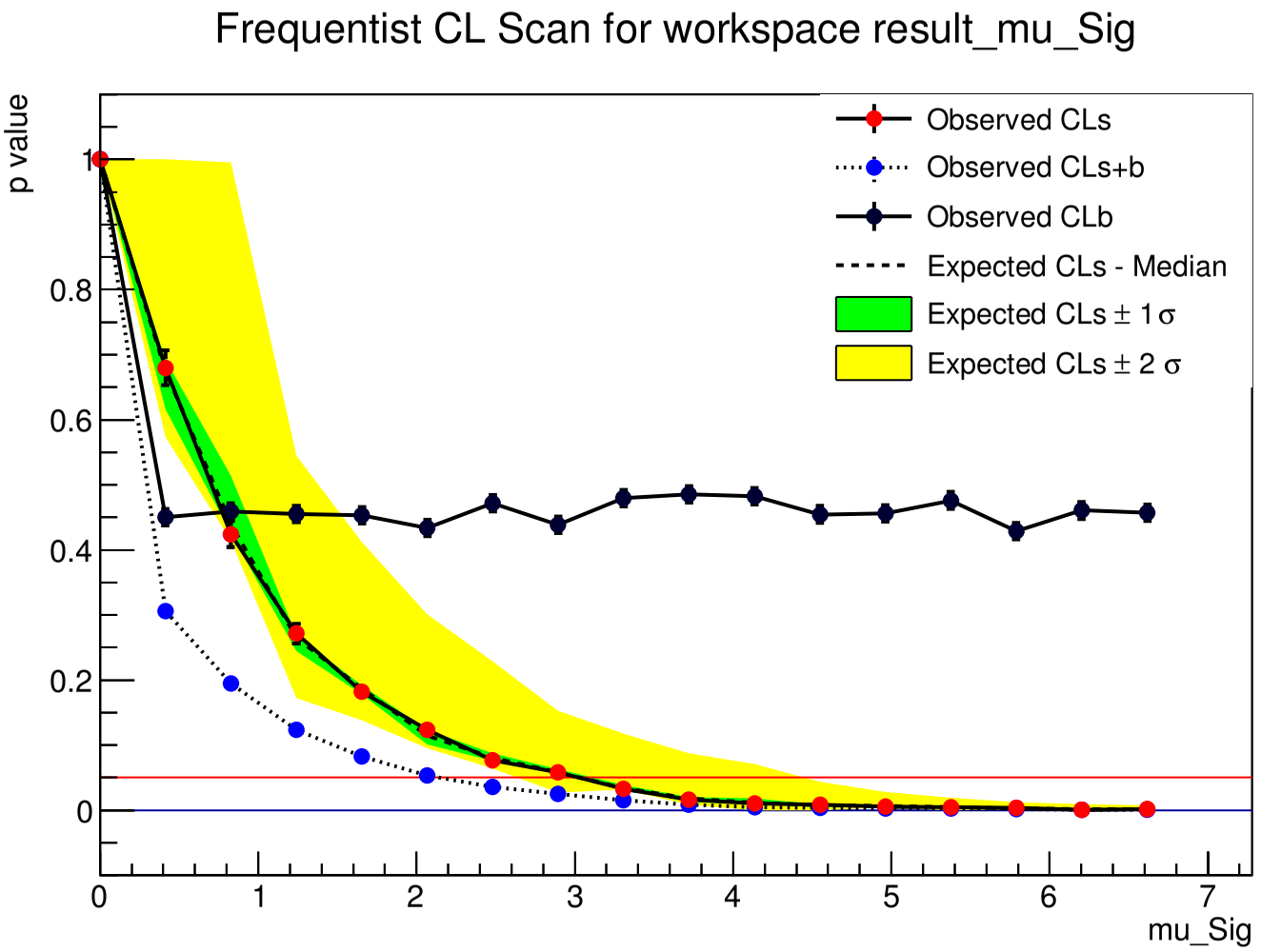

Figure 7.3: The CL_s and associated p-values for the background only (CL_b) and background plus signal (CL_{b+s}) for a range of what are nominally signal strength points (mu_Sig). As the event count is the parameter of interest, in reality the signal strength is set to 1 and mu_Sig actually represents the excess event count. In addition, the expected median CL_s and its associated one and two standard deviation bands ($\pm 1\sigma$, $\pm 2\sigma$) are shown in green and yellow. The horizontal red and blue lines indicate p-value=0.05 and p-value=0 respectively.

7.2 Model-Independent Limits

For any given SR an upper limit on the event count can be produced. Given knowledge of the luminosity this can be transformed into an upper limit on the observed cross section for multi-jet production. With additional knowledge of the signal reconstruction efficiency this becomes an upper limit on the fiducial cross section.

In Figure 7.4 the 95% confidence level upper limit on the observed multi-jet production cross section, extracted according to the method of Section 7.1.1.1, is presented. These limits represent the result of single bin counting experiments in successive $H_{\mathrm{T}}^{\mathrm{min}}$ bins for all SRs; in these results the cross section, σ, is folded with the geometric acceptance A and reconstruction efficiency ϵ. These results are numerically summarized in Table 7.1. The background uncertainties discussed in Section 6, are included, in additional to the luminosity uncertainty[2] of 2.8%. Quantitatively, these input values are summarized in Appendix C, Tables C.1 to C.6.

Generally speaking, the limits improve as a function of $H_{\mathrm{T}}^{\mathrm{min}}$, mirroring the fall off in the predicted background. The most sensitive constraints come from the $N_{\mathrm{Jet}} \geq 8$ region while the least powerful results are at $N_{\mathrm{Jet}} \geq 3$. The limits plateau at the point of zero observed events representing the physical boundary, this is reached at $\sigma \times A \times \epsilon \sim 0.14$ fb.

2. Calculated according to a measurement made in November 2012 by the ATLAS Luminosity working group.

$H_{\mathrm{T}}^{\mathrm{min}}$	$N_{\mathrm{Jet}} \geq 3$		$N_{\mathrm{Jet}} \geq 4$		$N_{\mathrm{Jet}} \geq 5$	
[TeV]	Observed	Expected	Observed	Expected	Observed	Expected
3.0	6.218	$6.053^{+1.890}_{-1.651}$	4.325	$3.818^{+1.243}_{-0.949}$	3.134	$2.594^{+0.836}_{-0.685}$
3.1	5.709	$4.929^{+1.576}_{-1.341}$	3.922	$3.201^{+1.025}_{-0.767}$	2.437	$2.022^{+0.671}_{-0.559}$
3.2	4.686	$3.859^{+1.294}_{-1.048}$	3.218	$2.559^{+0.813}_{-0.607}$	1.978	$1.551^{+0.564}_{-0.396}$
3.3	3.601	$2.989^{+0.948}_{-0.808}$	2.522	$1.994^{+0.646}_{-0.518}$	1.477	$1.185^{+0.421}_{-0.291}$
3.4	2.499	$2.225^{+0.701}_{-0.568}$	1.854	$1.515^{+0.482}_{-0.381}$	1.053	$0.900^{+0.288}_{-0.217}$
3.5	2.066	$1.719^{+0.553}_{-0.439}$	1.465	$1.174^{+0.389}_{-0.295}$	0.830	$0.698^{+0.227}_{-0.172}$
3.6	1.629	$1.299^{+0.442}_{-0.332}$	1.018	$0.878^{+0.292}_{-0.225}$	0.597	$0.523^{+0.184}_{-0.130}$
3.7	1.249	$0.996^{+0.326}_{-0.251}$	0.787	$0.667^{+0.238}_{-0.149}$	0.510	$0.417^{+0.157}_{-0.093}$
3.8	0.837	$0.738^{+0.238}_{-0.170}$	0.469	$0.470^{+0.160}_{-0.110}$	0.338	$0.316^{+0.130}_{-0.068}$
3.9	0.585	$0.550^{+0.188}_{-0.121}$	0.292	$0.319^{+0.115}_{-0.064}$	0.248	$0.250^{+0.094}_{-0.052}$
4.0	0.323	$0.353^{+0.138}_{-0.079}$	0.186	$0.208^{+0.092}_{-0.043}$	0.193	$0.202^{+0.079}_{-0.030}$
4.1	0.238	$0.268^{+0.102}_{-0.067}$	0.142	$0.145^{+0.073}_{-0.004}$	0.146	$0.146^{+0.063}_{-0.003}$
4.2	0.185	$0.209^{+0.089}_{-0.042}$	0.145	$0.145^{+0.051}_{-0.001}$	0.144	$0.145^{+0.037}_{-0.003}$
4.3	0.144	$0.150^{+0.070}_{-0.007}$	0.146	$0.147^{+0.002}_{-0.001}$	0.147	$0.148^{+0.004}_{-0.001}$
4.4	0.143	$0.144^{+0.060}_{-0.004}$	0.144	$0.145^{+0.003}_{-0.002}$	0.144	$0.145^{+0.002}_{-0.002}$
4.5	0.144	$0.146^{+0.048}_{-0.003}$	0.144	$0.145^{+0.002}_{-0.005}$	0.146	$0.147^{+0.001}_{-0.002}$
4.6	0.145	$0.145^{+0.031}_{-0.003}$	0.145	$0.146^{+0.002}_{-0.003}$	0.147	$0.147^{+0.001}_{-0.001}$
4.7	0.147	$0.148^{+0.004}_{-0.001}$	0.147	$0.147^{+0.001}_{-0.002}$	0.145	$0.145^{+0.002}_{-0.001}$
4.8	0.144	$0.145^{+0.003}_{-0.002}$	0.146	$0.146^{+0.002}_{-0.001}$	0.144	$0.145^{+0.003}_{-0.002}$
4.9	0.147	$0.147^{+0.001}_{-0.001}$	0.145	$0.145^{+0.002}_{-0.001}$	0.143	$0.143^{+0.003}_{-0.002}$
$H_{\mathrm{T}}^{\mathrm{min}}$	$N_{\mathrm{Jet}} \geq 6$		$N_{\mathrm{Jet}} \geq 7$		$N_{\mathrm{Jet}} \geq 8$	
[TeV]	Observed	Expected	Observed	Expected	Observed	Expected
3.0	1.362	$1.409^{+0.467}_{-0.371}$	0.742	$0.765^{+0.252}_{-0.187}$	0.346	$0.375^{+0.146}_{-0.095}$
3.1	1.157	$1.126^{+0.381}_{-0.270}$	0.668	$0.625^{+0.225}_{-0.140}$	0.272	$0.299^{+0.117}_{-0.073}$
3.2	0.808	$0.850^{+0.267}_{-0.224}$	0.412	$0.442^{+0.157}_{-0.111}$	0.180	$0.210^{+0.099}_{-0.043}$
3.3	0.697	$0.693^{+0.215}_{-0.169}$	0.363	$0.363^{+0.147}_{-0.062}$	0.186	$0.202^{+0.080}_{-0.037}$
3.4	0.485	$0.504^{+0.176}_{-0.122}$	0.175	$0.226^{+0.093}_{-0.053}$	0.154	$0.145^{+0.068}_{-0.003}$
3.5	0.448	$0.424^{+0.149}_{-0.103}$	0.185	$0.204^{+0.091}_{-0.039}$	0.144	$0.152^{+0.052}_{-0.009}$
3.6	0.273	$0.295^{+0.112}_{-0.058}$	0.190	$0.195^{+0.082}_{-0.029}$	0.145	$0.146^{+0.037}_{-0.003}$
3.7	0.238	$0.249^{+0.097}_{-0.059}$	0.194	$0.186^{+0.068}_{-0.017}$	0.147	$0.148^{+0.004}_{-0.001}$
3.8	0.146	$0.164^{+0.073}_{-0.019}$	0.145	$0.146^{+0.050}_{-0.001}$	0.145	$0.146^{+0.003}_{-0.003}$
3.9	0.141	$0.145^{+0.064}_{-0.004}$	0.147	$0.148^{+0.018}_{-0.004}$	0.147	$0.147^{+0.001}_{-0.001}$
4.0	0.144	$0.147^{+0.051}_{-0.003}$	0.144	$0.146^{+0.001}_{-0.002}$	0.146	$0.146^{+0.002}_{-0.001}$
4.1	0.145	$0.145^{+0.028}_{-0.001}$	0.147	$0.147^{+0.001}_{-0.003}$	0.145	$0.145^{+0.003}_{-0.001}$
4.2	0.145	$0.146^{+0.002}_{-0.003}$	0.147	$0.146^{+0.001}_{-0.001}$	0.144	$0.145^{+0.002}_{-0.002}$
4.3	0.146	$0.147^{+0.002}_{-0.002}$	0.145	$0.145^{+0.002}_{-0.001}$	0.143	$0.143^{+0.003}_{-0.002}$
4.4	0.147	$0.147^{+0.001}_{-0.001}$	0.144	$0.145^{+0.003}_{-0.001}$	0.143	$0.143^{+0.003}_{-0.002}$
4.5	0.146	$0.146^{+0.002}_{-0.001}$	0.143	$0.144^{+0.003}_{-0.002}$	0.144	$0.144^{+0.002}_{-0.004}$
4.6	0.145	$0.144^{+0.003}_{-0.001}$	0.143	$0.143^{+0.003}_{-0.002}$	0.143	$0.143^{+0.003}_{-0.003}$
4.7	0.144	$0.144^{+0.003}_{-0.002}$	0.143	$0.143^{+0.003}_{-0.002}$	0.143	$0.143^{+0.004}_{-0.003}$
4.8	0.142	$0.143^{+0.003}_{-0.002}$	0.143	$0.143^{+0.003}_{-0.003}$	0.143	$0.143^{+0.004}_{-0.002}$
4.9	0.144	$0.144^{+0.003}_{-0.003}$	0.143	$0.143^{+0.004}_{-0.003}$	0.144	$0.144^{+0.003}_{-0.003}$

Table 7.1: Upper limits on the visible cross-section, $\sigma \times A \times \epsilon$, at the 95% CL as a function of $H_{\mathrm{T}}^{\mathrm{min}}$ for different inclusive jet multiplicities.

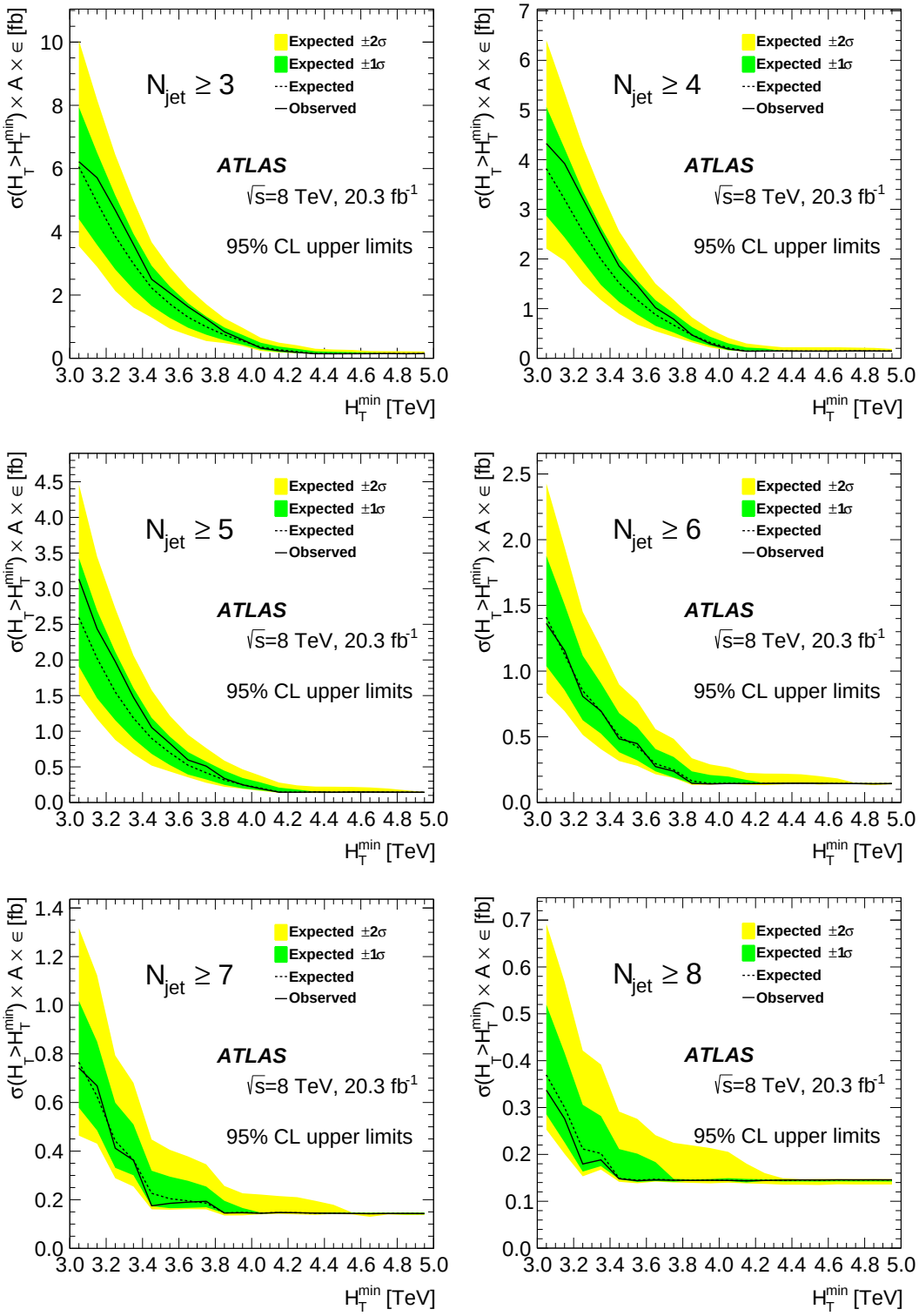

Figure 7.4: The model-independent upper limits on the observed cross section for multi-jet production in $H_{\mathrm{T}}^{\mathrm{min}}$ bins. The observed (solid) and expected (dashed) limits are shown on top of the one (green) and two (yellow) standard deviation expected limit bands.

7.2.1 Reconstruction Efficiency

For a theorist it is often useful to compare the cross section predictions of a particular model with experimental constraints. While a theorist can easily calculate a cross section taking into account the geometric acceptance, a theorist cannot disentangle detector based effects from the cross section measurement. Therefore, experimental results are sometimes presented as fiducial cross section limits as opposed to those of Figure 7.4. As the reconstruction efficiency is dependent on the particular theoretical model of the signal, such limits are no longer truly model-independent. However, as it is quite useful for theoretical comparisons, in this section, given the large number of different signal models, rather than recompute ill-defined fiducial limits, the reconstruction efficiencies of a number of typical TeV-scale gravity models simulated by `BlackMax` and `CHARYBDIS2` are presented and it is left up to the reader to choose which values are more applicable for his or her particular model. The presentation of this section is closely related to that of Section 7.3.3 in discussing model-dependent results.

In Table 7.2 the model parameters simulated in the signal MC's are summarized. Two generators, `CHARYBDIS2` and `BlackMax`, are used to simulate thermal black holes and string balls with $n = 2, 4, 6$ extra spatial dimensions. Additional features that are simulated include angular momentum (rotation), initial state radiation (photons), final state radiation (gravitons) and stable remnants. Each sample as listed is further permutated in M_{Th} and M_{D}, building up a series of points in parameter space.

In Figures 7.5 and 7.6 the reconstruction efficiency for signal samples produced using `BlackMax` and `CHARYBDIS2` are presented as histograms. The efficiencies are almost completely independent of dimensionality and thus models

Generator	Description	$< \epsilon >$ [%]	RMS$_\epsilon$ [%]
CHARYBDIS2	Black holes: Non-rotating	0.88	0.04
	Black holes: Rotating	0.88	0.04
	Black holes: Low multiplicity remnant	0.89	0.04
	Black holes: Initial state emission	0.88	0.04
CHARYBDIS2	String balls: Non-rotating	0.86	0.04
	String balls: Rotating	0.86	0.04
BlackMax	Black holes: Non-rotating	0.89	0.05
	Black holes: Rotating	0.88	0.04
	Black holes: Graviton emission	0.89	0.06
	Black holes: Initial state photons	0.90	0.06

Table 7.2: A summary of signal samples available in MC simulation. The columns describe the generator, model parameters and mean reconstruction efficiency and RMS of the various models.

with $n = 2, 4, 6$ dimensions have been averaged together. The efficiency itself is constructed by,

$$\epsilon = \frac{A_{\text{Reco}}}{A_{\text{Truth}}}, \tag{7.6}$$

where the reconstruction efficiency ϵ is defined as the ratio of the reconstruction level acceptance A_{Reco} and the generator level acceptance A_{Truth}. Migration effects between jets at the generator and reconstruction level due to detector effects can occur and statistically limited SRs can be more sensitive to this effect and hence the result seen where a small number of histogram entries have $\epsilon > 1$.

Nonetheless, generally speaking, the average efficiency irrespective of model or generator is $\sim 88\%$, the uncertainty as characterized by the root mean square is $\sim 5\%$. Taking these as nominal values the fiducial upper limit is as low as $\sigma \times A \sim 0.16 - 0.17$ fb, which is competitive against the sister ATLAS analysis in

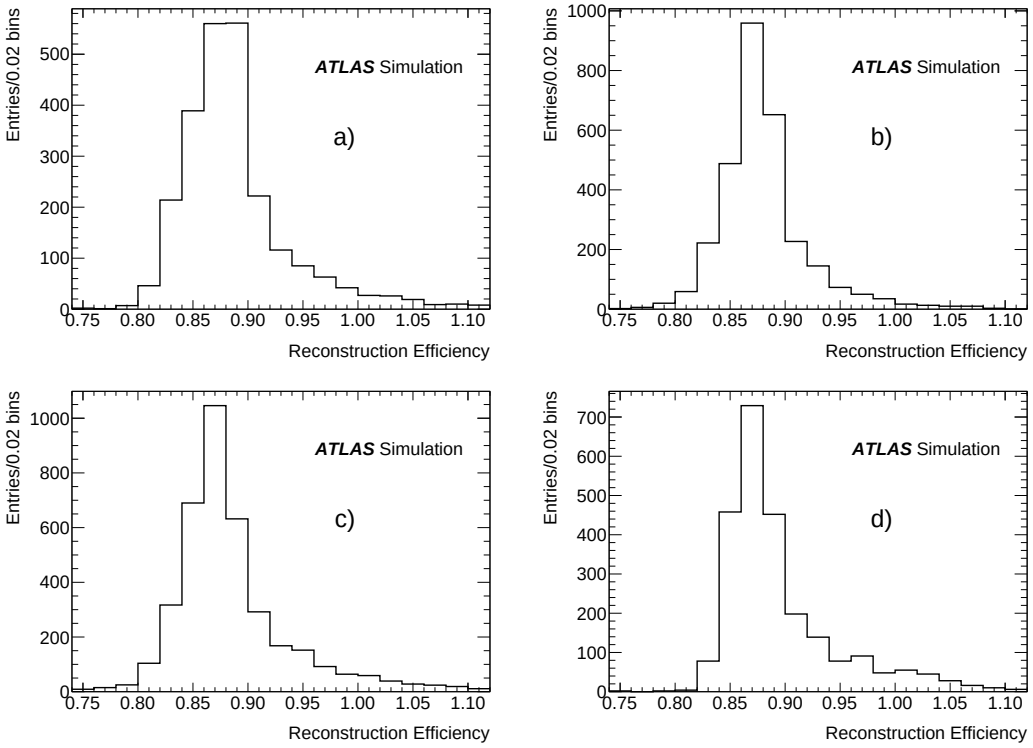

Figure 7.5: Reconstruction efficiencies for different `BlackMax` models, a) non-rotating black holes, b) rotating black holes, c) non-rotating graviton emission black holes and d) initial state photon radiation black holes. The results are averaged over the dimensions $n = 2, 4, 6$.

the single lepton+jets channel [24] and comparable to the CMS multi-jet result [25].

Using the results of Figures 7.5 and 7.6 the reader can transform the observed limits of Figure 7.4 into fiducial limits characteristic of the desired model. In addition, the reader is provided with more information regarding the characteristics of the efficiency dependence on signal model than just a single value.

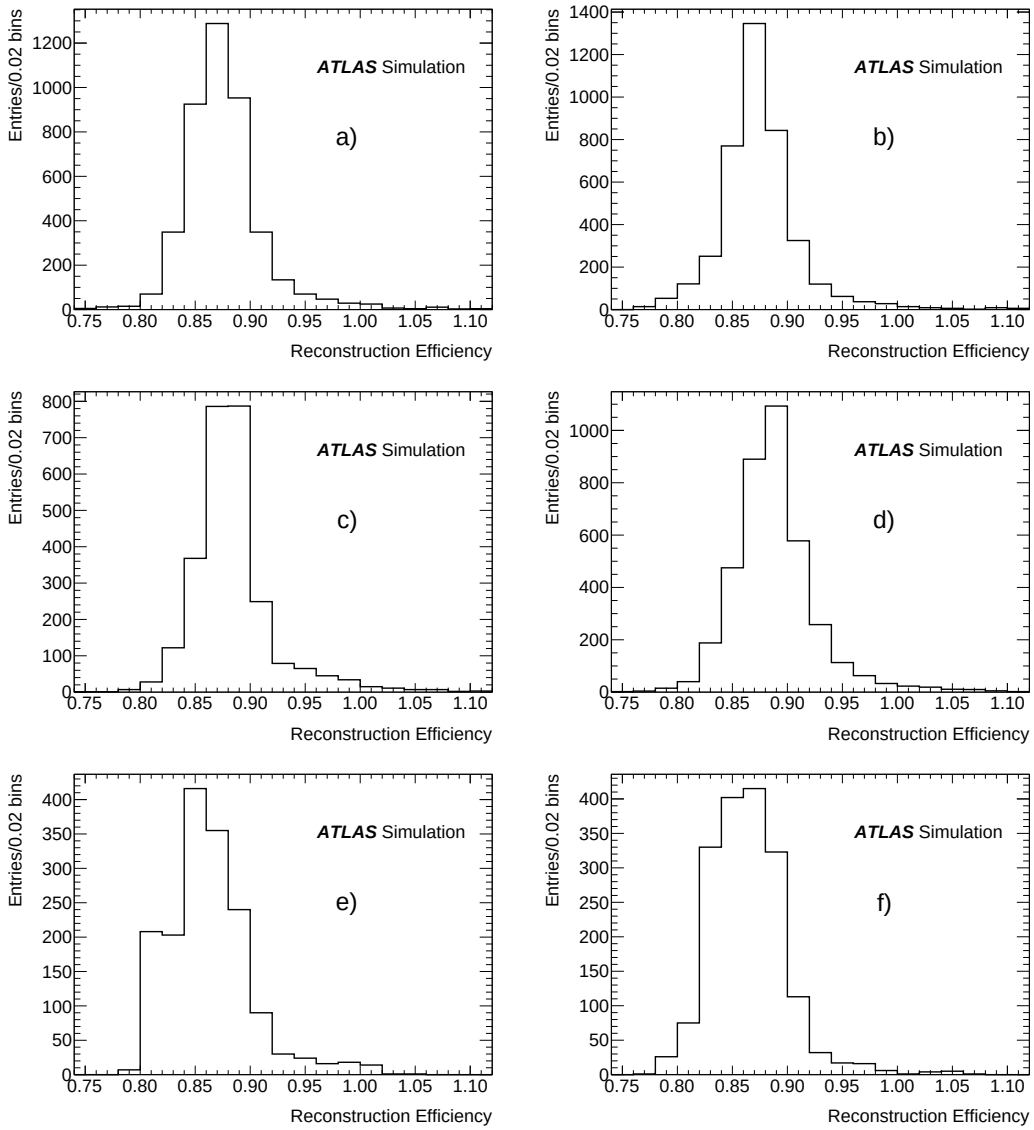

Figure 7.6: Reconstruction efficiencies for different CHARYBDIS2 models, a) non-rotating black holes, b) rotating black holes, c) initial state emission black holes, d) low multiplicity remnant black holes, e) non-rotating string balls and f) rotating string balls. The results are averaged over the dimensions $n = 2, 4, 6$.

7.3 Additional Uncertainties

In the subsequent sections of this chapter, studies of the signal MC simulations are presented in the context of constructing model-dependent limits on particular TeV-scale gravity models. This section presents the studies of the signal uncertainty effects, the calculation of acceptances, A_{Reco}, A_{Truth} and finally the techniques used to create the limits in terms of exclusion contours in the space of M_{Th} and M_{D}.

7.3.1 Jet Energy Scale

The jet energy scale (JES) is studied by applying a correction factor to jets at the electromagnetic energy scale to correct them to the appropriate hadronic energy scale. The technical implementation is performed using specialized software designed by the experts in the ATLAS collaboration [49].

The method corrects individual jets within an event by scaling them according to a factor that accounts for the jet four-vector along with additional useful parameters describing its composition and substructure. This correction factor is applied to the jets in an event in 0.02 steps from zero (no correction) to one (nominal correction).

Thus for every event, one hundred H_{T} values can be formed from the JES (up and down) variations, from which overall one hundred distributions of H_{T} can be constructed out of the ensemble of events. The maximum variation of these distributions with respect to the nominal unfluctuated H_{T} distribution is taken as the JES uncertainty.

As opposed to simply taking the JES uncertainty as the nominal correction

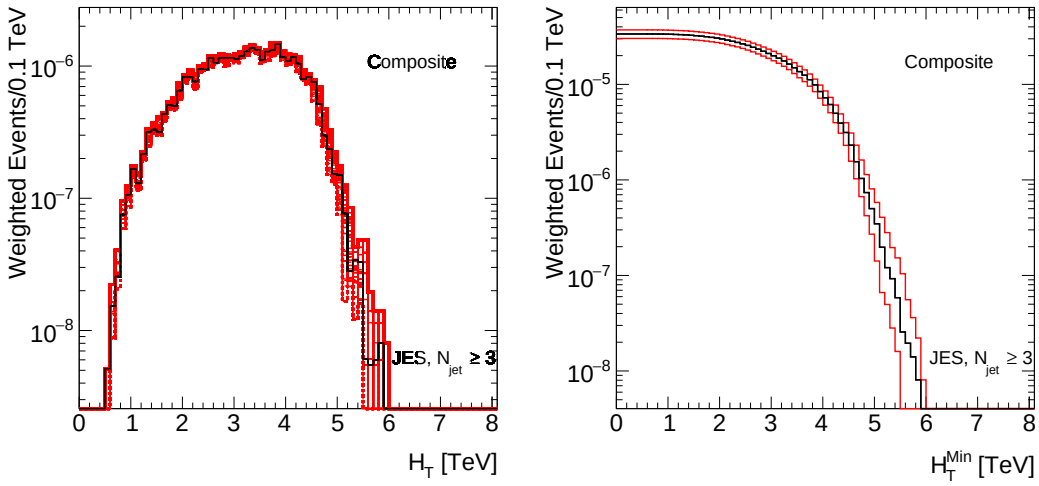

Figure 7.7: The jet energy scale uncertainty method for a typical signal sample, CHARYBDIS2, black hole with rotation and stable remnant, $M_{\mathrm{Th}} = 4.5$ TeV and $M_{\mathrm{D}} = 3.5$ TeV and $n = 4$, with the SR $N_{\mathrm{Jet}} \geq 3$. The left plot shows the different variations of the JES in H_{T} (the solid lines are up variations while the dashed lines are down variations) while the right plot consolidates the maximum variation in $H_{\mathrm{T}}^{\mathrm{min}}$ bins. The y axis is shown in unnormalized weighted events.

factor, by stepping through the correction factor in increments, the method is protected against the possibility that the maximum variation in H_{T} is not the maximum variation in the JES factor.

Figure 7.7 shows a typical result in H_{T} and $H_{\mathrm{T}}^{\mathrm{min}}$ binning. The JES effect, as seen in the right side plot, is small at low $H_{\mathrm{T}}^{\mathrm{min}}$ and increases at higher values. In the left plot all one hundred steps are shown for up (solid lines) and down (dashed lines) steps separately. The largest fluctuation in each bin is taken as the uncertainty and then the result is binned in $H_{\mathrm{T}}^{\mathrm{min}}$ to produce the right side plot. The results in $H_{\mathrm{T}}^{\mathrm{min}}$ are then used when setting limits. The procedure is repeated at all $N_{\mathrm{Jet}} \geq X$ and for all signal samples.

7.3.2 Jet Energy Resolution

The estimation of the jet energy resolution (JER) follows a somewhat analogous method to the JES uncertainty method. The jet energy scale resolution is a computed factor that depends on the transverse momentum and pseudorapidity of the jet; it is a measure of the precision of the jet energy measurement. It is extracted using a software tool given the jet kinematic inputs analogous to the JES.

The JER for a particular jet at a fixed value in p_{T} and η is fixed, however, in order to completely sample the effect of the JER on the H_{T}, the JER factor extracted from the software tool is treated as a variance of a Gaussian distribution with the nominal jet energy at its mean. One thousand values are drawn from a random number generator with a Gaussian probability distribution accordingly. For the thousand H_{T} distributions constructed from such jets, the event count is distributed in some manner about any particular bin.

The JER uncertainty is defined as the 68% coverage left and right of such distributions about the nominal event count. This procedure roughly corresponds to one standard deviation about a Gaussian distribution. The procedure is illustrated in Figure 7.8 for the identical sample and SR as in Figure 7.7 for the JES. Generally speaking, compared to the JES, the JER is a smaller effect.

7.3.3 Acceptance

The acceptance of the signal samples is needed in order to extract the reconstruction efficiency and translate the observed limits into fiducial limits as discussed in Section 7.2.1. In addition, the signal acceptance is needed to construct the model-dependent limits, to transform the event count upper limits into pure limits

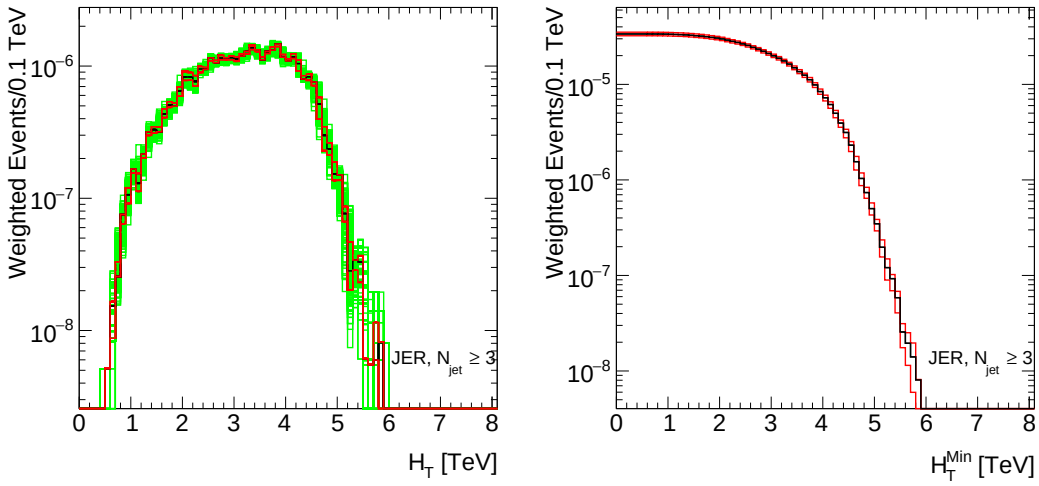

Figure 7.8: The jet energy resolution uncertainty method for a typical signal sample, CHARYBDIS2, black hole with rotation and stable remnant, $M_{\mathrm{Th}} = 4.5$ TeV and $M_{\mathrm{D}} = 3.5$ TeV and $n = 4$, with the SR $N_{\mathrm{Jet}} \geq 3$. The left plot shows the one thousand variations of the JER in H_{T} (green), the solid red line shows the 68% coverage left and right of the nominal event count. In the right plot the result is shown binned in units of $H_{\mathrm{T}}^{\mathrm{min}}$. The y axis is shown in unnormalized weighted events.

on the sample cross section. The tables listing the input to the model-dependent limit calculations including the values of the acceptance are given in Appendix C, Tables C.7 to C.32.

Two definitions of acceptance are needed, these are the truth and reconstructed acceptances of equation 7.6, the acceptances are defined as,

Truth acceptance, otherwise called the geometric acceptance or fiducial acceptance; it is the acceptance of the signal sample due purely to the effects of jet selection as defined in Section 6.3.1. These values are directly calculated from the generator (truth) jets of each particular signal sample by taking the ratio of the $H_{\mathrm{T}}^{\mathrm{min}}$ distribution with and without jet selection. The acceptance is therefore uniquely defined in each $H_{\mathrm{T}}^{\mathrm{min}}$ bin.

Reconstructed acceptance, defined in analogous manner to the fiducial accept-

ance except at the reconstruction level. Thus, the values are computed from reconstructed jets that have been subjected to detector level effects. In addition, the reconstruction efficiency is implicitly folded in because for reconstructed jets, event selection, functions of the detector, are applied. The explicit definition is the ratio of the $H_{\mathrm{T}}^{\mathrm{min}}$ distribution at the analysis level (after event and jet selection) and the $H_{\mathrm{T}}^{\mathrm{min}}$ distribution at reconstruction level but before event selection.

From these results, the reconstruction efficiency is calculated as the ratio. For the purpose of the model-dependent limits, the reconstructed acceptance is divided out of the event count and the resulting value compensates for both reconstruction efficiency and geometric acceptance, comprising a pure cross section value. The uncertainty on the acceptance due to the limited Monte Carlo statistics is described in binomial terms.

7.4 Signal Region Optimization

Finally, in order to set model-dependent limits it is necessary to choose appropriate SRs. Such SR optimization must be made without knowledge of the unblinded observed data so as to avoid tuning the optimization according to the statistical fluctuations in data. As such the optimal SR's are tuned according to predictions of the signal MC's and the background estimate extracted from the blinded data. MC is not used to estimate the background. It is used only to simulate the shape characteristics of the signal models.

The procedure is to find the region of maximum signal significance. The background estimate in H_{T} from the blinded data is taken as the nominal back-

ground and the signal sample is injected at an arbitrary cross section. No assumptions regarding sample cross section are made; the objective is to find the region of maximum relative significance for signal sample in the parameter space of N_{Jet} versus $H_{\text{T}}^{\text{min}}$.

Therefore, an arbitrary cross section within limits is sufficient for injection. The distribution of background is compared to the distribution of the background plus signal in $H_{\text{T}}^{\text{min}}$ for each N_{Jet}. The significance of each SR is calculated according to the method of Section 6.6, Equation (6.13). For a particular signal sample the optimal SR is the one that maximizes the significance. The procedure is repeated for all signal samples.

Figure 7.9 shows the method for a particular signal sample. The space of N_{Jet} versus $H_{\text{T}}^{\text{min}}$ is scanned and in this particular case the most significant region is $H_{\text{T}}^{\text{min}} = 4.1$ TeV, $N_{\text{Jet}} \geq 4$, with a Gaussian significance of 1.75 standard deviations.

For each sample the optimal region is found and matched to the appropriate signal and background uncertainties for that region as well as the nominal background prediction and observed event count from unblinded data using a sorting algorithm. Thus for each model, defined by Table 7.2, an optimal SR exists for each point in M_{D} and M_{Th}. `HistFitter` is then used to calculate the limits in a manner analogous to that detailed for the model-independent limits. Only now, Equation (7.1) further takes into account Gaussian constraints on the signal similar to that of the background. These input tables for computing the model-dependent limits are quantitatively summarized in Appendix C, Tables C.7 through C.32.

To construct the exclusion contours, interpolation techniques as illustrated in the following section are used.

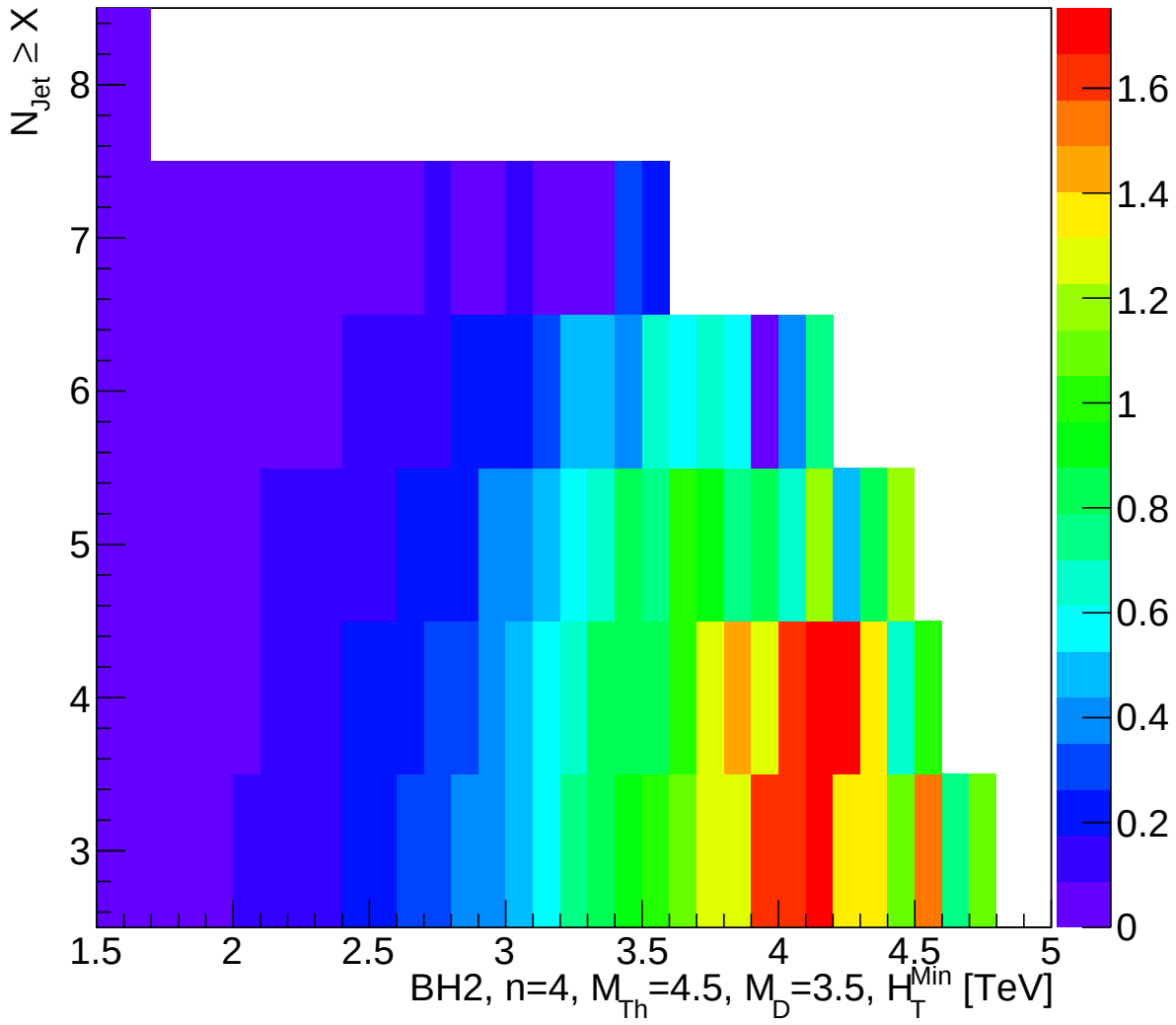

Figure 7.9: The significance per SR in the space of $H_{\mathrm{T}}^{\mathrm{min}}$ and $N_{\mathrm{Jet}} \geq X$ for a rotating black hole generated using `CHARYBDIS2` with $M_{\mathrm{Th}} = 4.5$ TeV and $M_{\mathrm{D}} = 3.5$ TeV and $n = 4$ extra dimensions. The color scheme indicates the relative significance, towards red being more significant, white spaces indicate completely insignificant regions. One such plot is created for each permutation of model parameters (generator, characteristic, dimensionality, M_{Th} and M_{D}) and from each plot the most significant region as defined by the maximum Gaussian significance is selected.

7.5 Model-Dependent Limits

Model-dependent limits are constructed by interpolating between the theoretical cross sections of benchmark models with the calculated cross section limits. This interpolation is performed in slices of M_{D}. The method is visually illustrated in Figure 7.10. For each benchmark model the observed and expected limits with respect to the unblinded data are calculated analogous to the model-independent results. The reconstructed acceptance is used to produce a cross section limit. Thus for each benchmark model a grid of calculated limits exists in the plane of M_{D} versus M_{Th}. The theoretical cross section according to the model obtained from the MC generator is superimposed and the interpolation at the crossing point in M_{Th} is extracted for each slice of M_{D} for the observed, expected limits and expected uncertainty bands.

Generally speaking, the black hole signal samples were generated in 0.5 TeV intervals between $M_{\mathrm{D}} = 1.5 - 4.0$ TeV while the string balls were generated at 0.2 TeV intervals between $M_{\mathrm{S}} = 0.8 - 2.0$ and then 0.5 TeV between $M_{\mathrm{S}} = 2.0 - 3.0$ TeV. Thus, for each point in $M_{\mathrm{D/s}}$ there is one interpolated M_{Th} point obtained from the calculated limits. The results are then used to construct exclusion contours in the space of M_{D} versus M_{Th} for each model. These results are shown in Figure 7.11 for `CHARYBDIS2` and Figure 7.12 for `BlackMax` generated models. For like black hole models, the differing dimensions $n = 2, 4, 6$ are grouped together and the uncertainty bands are suppressed for clarity. The string ball models are shown together. The individual exclusion contours showing the full ± 1 standard deviation and ± 2 standard deviation expected limit bands are shown in Appendix D.

For TeV-scale gravity the classical phenomenological description of evapor-

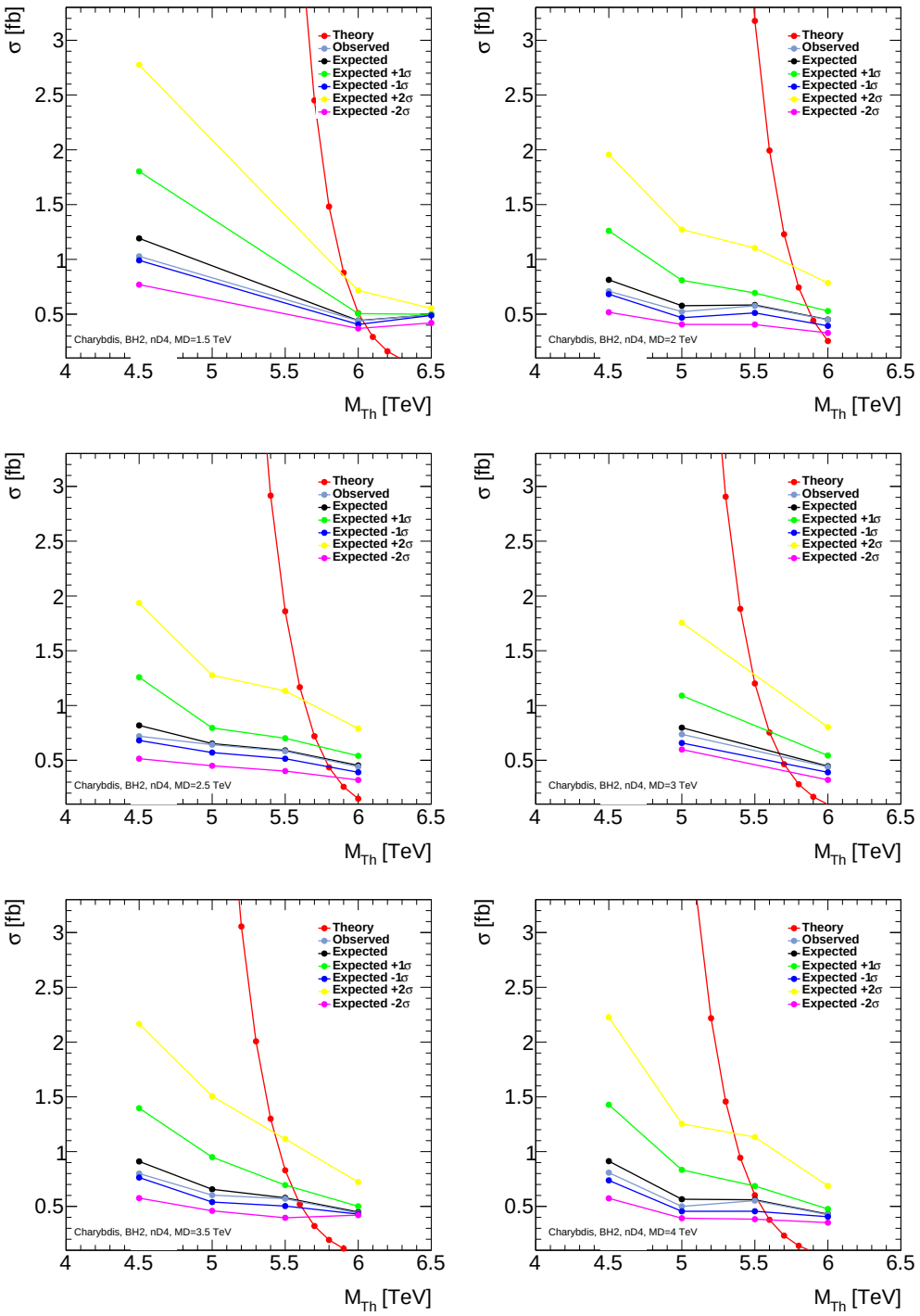

Figure 7.10: The model-dependent upper limits on the cross section at 95% confidence level for a rotating black hole model. The red points indicate the theoretical model cross section. The color points show the observed (grey-blue), expected (black), ± 1 (green, blue) and ± 2 (yellow, purple) standard deviation expected limit results. The interpolation is represented by connecting the points with solid lines.

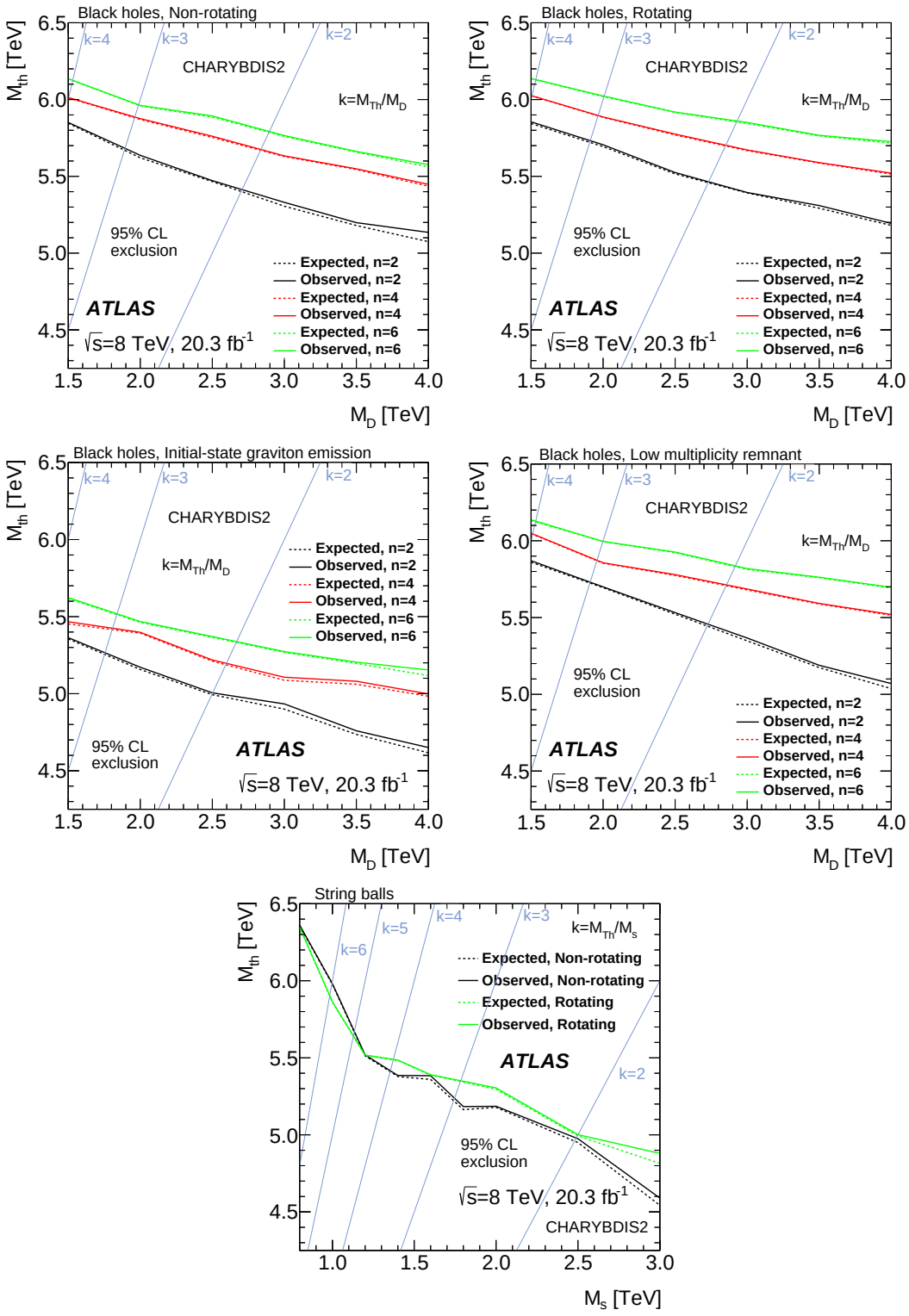

Figure 7.11: Exclusion contours in M_{Th} vs M_{D} for CHARYBDIS2 generated models, the limits expected (solid) and observed (dashed) limits are shown for $n = 2$ (black), $n = 4$ (red) , $n = 6$ (green), lines of constant $k = M_{\mathrm{Th}}/M_{\mathrm{D/s}}$ are shown in grey-blue.

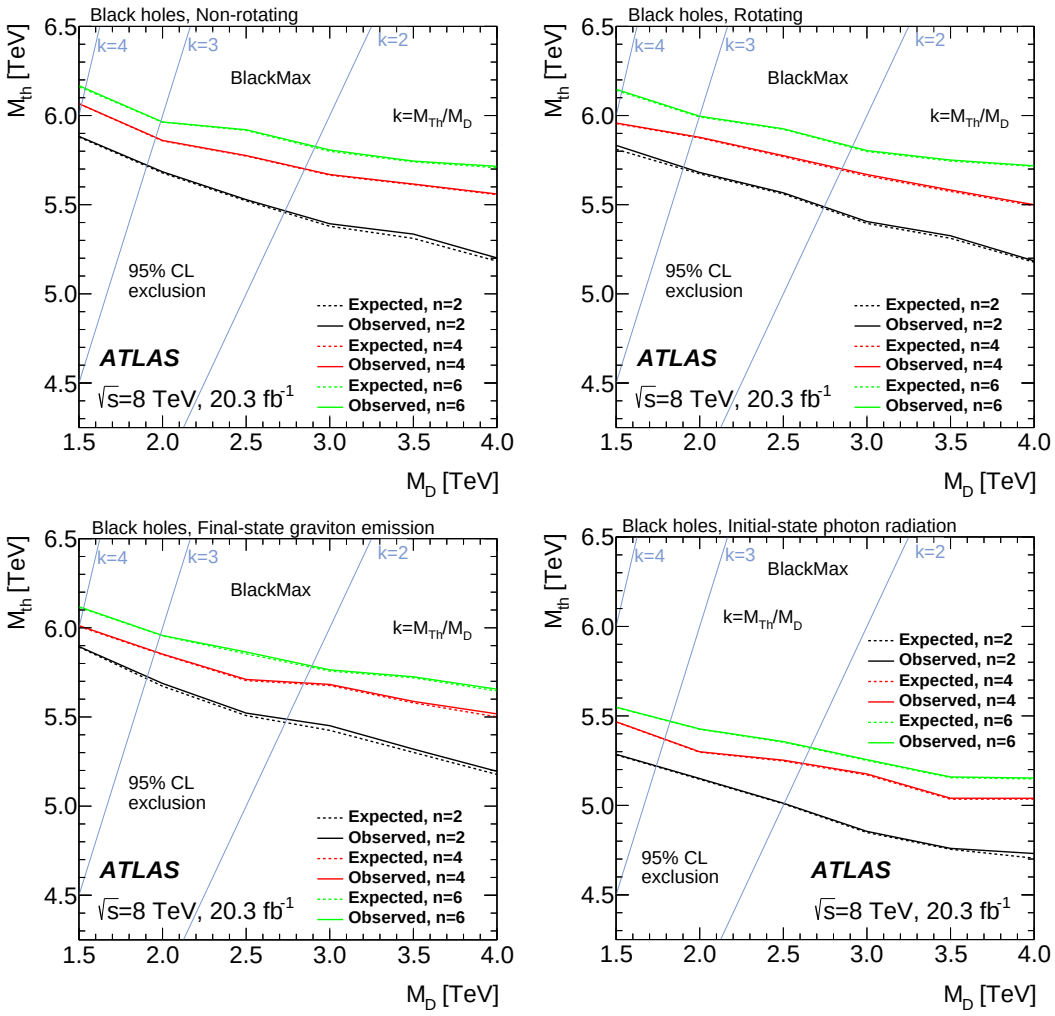

Figure 7.12: Exclusion contours in M_{Th} vs M_{D} for `BlackMax` generated models, the limits expected (solid) and observed (dashed) limits are shown for $n = 2$ (black), $n = 4$ (red) , $n = 6$ (green), lines of constant $k = M_{\mathrm{Th}}/M_{\mathrm{D}}$ are shown in grey-blue.

ation via Hawking radiation discussed in Section 2.3.2.1 is only valid for $M_{\text{Th}} >> M_{\text{D}}$. The treatment of the black hole as general relativisitc and the assumption of thermal decay breaks down close to the Planck mass. Therefore, in each contour, lines of constant $k = M_{\text{Th}}/M_{\text{D}}$ have been drawn to guide the eye of the reader.

A number of general features are common to these results. For the same model the exclusion power is monotonically rising in n due to larger cross sections in models with greater number of extra dimensions. At higher values of M_{D} the limits tend to worsen due to the cross section decreasing as $M_{\text{Th}} \to M_{\text{D}}$. For the two models which were produced with both generators (the first two plots of Figures 7.11 and 7.12) the results are similar with `BlackMax` having an overall slightly higher exclusion.

The multi-jet channel does not appear to distinguish between models with and without angular momentum and, broadly speaking, the limits are similar for black holes and string balls. This is contrary to the single lepton+jets analysis [24], where the lepton selection suppresses acceptance for models with rotation compared to models without.

Models with initial state radiation tend to have weaker limits due to reduced cross sections from emission or incomplete evaporation. In final state graviton emission models [3], the exclusion appears to be only slightly weaker compared to the generic non-rotating model. Finally, including a low multiplicity remnant does not appear to significantly weaken the limits.

Overall, the results may be compared to analogous results in the same sign dimuon channel [23] and the single lepton+jets channel [24] in ATLAS. The exclu-

3. This is one specific model that would benefit from an event variable that is sensitive to missing transverse energy, which would recover additional acceptance and allow the exclusion limit to be pushed out even farther.

sion is generally more powerful against similar results in the former while being comparable to the latter, except in the case of string balls at high k and with regard to rotating models where the exclusion is significantly better in the multi-jet channel. Additionally, for the string ball limits, in the absence of analogous CMS results these contours represent the first model-dependent TeV-scale gravity results in the multi-jet channel.

8

Conclusions

A model-independent search for BSM physics in the multi-jet channel was carried out by the ATLAS Exotics multi-jet analysis group in the observables H_{T} and inclusive N_{Jet} using 20.3 fb^{-1} of proton-proton collision data recorded by the ATLAS detector at a center of mass energy of $\sqrt{s} = 8$ TeV at the Large Hadron Collider.

The QCD dominated background is estimated using an original data-driven technique designed for this purpose. A search algorithm designed to detect statistically significant excesses in the context of threshold effects was developed based on the `BumpHunter` method. No evidence of significant excess was observed in the unblinded data. The observed data was found to be generally compatible and within background predictions and systematic uncertainties.

In the absence of discovery, the results were interpreted in terms of model-independent upper limits on the multi-jet production cross section and model-dependent limits on select benchmark TeV-scale gravity models.

The aforementioned analysis represents the ATLAS collaboration results in the multi-jet channel at $\sqrt{s} = 8$ TeV. The physical limits are generally comparable or superior to sister ATLAS results in the same sign dimuon and single lepton plus jets channel. They also supersede the analogous CMS published results using

12.1 fb^{-1} recorded data in statistical significance and and in some cases, exclusion power.

8.1 Future

One important improvement that may be made in future analyses is to consider the invariant mass of the multi-jet system as the discriminating variable alongside N_{Jet}. Such a change will no doubt involve restudying the background estimation as the distribution shape will be different, however the invariant mass is a more useful variable for theorists as opposed to H_{T}. The former is easily computed while the latter is not. While the two are correlated it is not straightforward to interprete model-independent results in H_{T} as opposed to invariant mass. In addition, the kinematic reach of invariant mass as a more inclusive variable is greater compared to H_{T}, thus the limit up to which strong gravity can be probed is extended. This also increases the potential range for discovery and in its absence increases the power of exclusion limits.

An additional improvement that could be made is to extend the sensitivity of the search by including missing energy, possibly into the invariant mass calculation to form a truly inclusive description of the total energy/mass of each event. Benchmark models that describe graviton emission gain especially with regard to discovery power and in its absence, strength in the exclusion limits. A combined invariant mass, missing energy variable should be able to push the discovery power close to the kinematic limit of the collider due to the high fiducial acceptance of the multi-jet channel.

In the summer of 2015 the LHC will restart proton-proton collisions at $\sqrt{s} =$

13 TeV; the unprecedented energy scale will allow TeV-scale gravity searches to push beyond the current boundaries very quickly. The precedence set and knowledge built up by this analysis, which lays out a viable and proven method of background estimation and detailed studies of associated uncertainties, should enable more rapid progress at the energy frontier and an early result at $\sqrt{s} = 13$ TeV. The energy frontier is especially exciting with respect to the possibility of strong gravity effects laying just beyond our current thresholds.

A

Monte Carlo Studies

This section contains additional material detailing extensive MC studies of the QCD background and validation of the fit and extrapolation method in MC. While the method is data-driven in the sense that final background estimate is extrapolated in data, the same method can also be applied in MC to test the technique. Section A.1 detail the MC samples used in these studies, Sections A.2, A.3 compare basic kinematic properties of jets between different generators in truth and against data at the reconstructed level. Section A.4 presents two studies of additional event variables used to discern possible differences between dijet and multi-jet generators. Finally Section A.5 presents the results of the application of the fit and extrapolate method in MC.

A.1 Summary of Samples

The details of the QCD MC simulation are summarized in Tables A.1, A.2 , A.3 for PYTHIA8 , Herwig++ and ALPGEN. QCD MC samples are generated in slices of leading jet p_{T} at the generator level, these are indicated by the column "Slice", which run from JZ0W to JZ7W, with the first slice consisting of events with the lowest leading jet p_{T} and the last slice consisting of events with the highest. These slices are generated with anormal shapes and must be weighted in order to restore the correct shapes. The weighting factor is,

$$\text{Weight} = \frac{\text{Event Weight} \times \sigma \times \text{Filter efficiency} \times L}{\text{Events}}, \tag{A.1}$$

the weight is given by the product of the event weight, cross section σ, filter efficiency, luminosity, L divided by the total number of events in the sample. The event weight is particular to the event and is determined by the event generation process, the filter efficiency represents the number of events that are successfully generated within the given leading p_{T} range, the luminosity is scaled to the nominal value of 20.3 fb^{-1}.

In addition, the multi-jet samples are further divided by the number of final state parton level jets, ALPGEN has the capacity to simulate up to six jets at the matrix element level, $2 \rightarrow 6$ processes. Thus, the multi-jet samples are labeled by NpX_JZY, representing the X partons originating from the primary interaction, and then further divided by leading jet p_{T} as in the dijet case. The individual multi-jet samples must be combined together so as to form a usable sample. As opposed to the dijet samples, the ALPGEN samples were not passed through detector simulation and as such all variables are only available at generator level.

DSID	Slice	Events	Cross-section [fb]	Filter efficiency
147910	JZ0W	1500000	7.2850×10^{13}	9.8554×10^{-1}
147911	JZ1W	1599994	7.2850×10^{11}	1.2898×10^{-4}
147912	JZ2W	5999034	2.6359×10^{10}	3.9901×10^{-3}
147913	JZ3W	5977254	5.4419×10^{8}	1.2220×10^{-3}
147914	JZ4W	5997214	6.4453×10^{6}	7.0839×10^{-4}
147915	JZ5W	2996082	3.9739×10^{4}	2.1516×10^{-3}
147916	JZ6W	2993651	4.1609×10^{2}	4.6773×10^{-4}
147917	JZ7W	2991955	4.0636×10^{1}	1.4595×10^{-2}

Table A.1: `PYTHIA8` dijet MC samples.

ID	Slice	Events	Cross-section [fb]	Filter efficiency
159110	JZ0W	1399998	1.1860×10^{8}	9.9231×10^{-1}
159111	JZ1W	1399897	3.6012×10^{12}	1.4607×10^{-3}
159112	JZ2W	1399993	1.9038×10^{10}	2.5568×10^{-3}
159113	JZ3W	1399680	3.6224×10^{8}	8.5373×10^{-4}
159114	JZ4W	1399665	4.1655×10^{6}	5.4308×10^{-4}
159115	JZ5W	1397948	8.3181×10^{4}	5.4903×10^{-4}
159116	JZ6W	1389845	5.7850×10^{3}	1.9889×10^{-4}
159117	JZ7W	1396932	6.5251×10^{2}	5.6710×10^{-4}

Table A.2: `Herwig++` dijet MC samples.

DSID	Slice	Events	Cross-section [fb]	Filter efficiency
168001	Np2_JZ1	1500000	1.3799×10^{11}	0.97831
168002	Np2_JZ2	1500000	1.5540×10^{9}	0.31155
168003	Np2_JZ3	1500000	5.2957×10^{6}	0.63308
168004	Np2_JZ4	1500000	3.2092×10^{4}	0.56555
168005	Np2_JZ5	1500000	2.3983×10^{2}	0.69485
168006	Np2_JZ6	1500000	6.1495×10^{0}	0.72454
168007	Np2_JZ7	1500000	1.7886×10^{-1}	0.72548
168011	Np3_JZ1	1395000	1.1425×10^{10}	0.95674
168012	Np3_JZ2	1445000	1.8327×10^{9}	0.29693
168013	Np3_JZ3	1490000	1.1149×10^{7}	0.56855
168014	Np3_JZ4	1500000	7.4632×10^{4}	0.52924
168015	Np3_JZ5	1500000	4.9537×10^{2}	0.65798
168016	Np3_JZ6	1500000	1.0933×10^{1}	0.68544
168017	Np3_JZ7	1500000	2.7120×10^{-1}	0.68430
168021	Np4_JZ1	1486495	1.5575×10^{9}	0.88520
168022	Np4_JZ2	1435491	5.3657×10^{8}	0.40663
168023	Np4_JZ3	1426484	8.2663×10^{6}	0.57831
168024	Np4_JZ4	1348868	7.1068×10^{4}	0.52775
168025	Np4_JZ5	1190261	4.7047×10^{2}	0.64526
168026	Np4_JZ6	1375555	9.1912×10^{0}	0.66830
168027	Np4_JZ7	1203142	1.9392×10^{-1}	0.66268
168031	Np5_JZ1	1474500	2.2122×10^{8}	0.79035
168032	Np5_JZ2	1456800	1.2602×10^{8}	0.50129
168033	Np5_JZ3	1390500	4.2600×10^{6}	0.59785
168034	Np5_JZ4	1241700	4.7200×10^{4}	0.52645
168035	Np5_JZ5	1173250	3.0672×10^{2}	0.63323
168036	Np5_JZ6	1218250	5.3019×10^{0}	0.65242
168037	Np5_JZ7	690500	$^{*}1.2491 \times 10^{-1}$	0.64322
168041	Np6_JZ1	1449000	3.8732×10^{7}	0.67180
168042	Np6_JZ2	1432550	3.3059×10^{7}	0.59989
168043	Np6_JZ3	1373550	2.4574×10^{6}	0.62058
168044	Np6_JZ4	1278000	3.8408×10^{4}	0.51906
168045	Np6_JZ5	1164425	2.4545×10^{2}	0.60701
168046	Np6_JZ6	1147050	3.5689×10^{0}	0.62479
168047	Np6_JZ7	30409	$^{*}6.2896 \times 10^{-2}$	0.61197

Table A.3: ALPGEN multi-jet MC samples. Cross-sections with * were estimated privately as no values were available from official production.

A.2 Jet Kinematics - Truth

The following figures show the comparisons of the jet kinematical variables, $N_{\text{Jet}} \geq X$ Figure A.1, ϕ Figure A.2, η Figure A.3, p_{T} Figure A.4, leading p_{T} Figure A.5, sub-leading p_{T} Figure A.6, and sub-sub-leading p_{T} Figure A.7, H_{T} Figure A.8 and invariant mass Figure A.9 all at the generator level. In these figures, the distributions are normalized relative to the PYTHIA8 distributions so as to pronounce differences in distribution shape. The absolute normalization is arbitrary.

The degree of agreement between the different generators is explictly shown relative to PYTHIA8 in the sub-ratio plot of each histogram. The inclusive multiplicity shows significant divergence between the predictions of the different generators. The ϕ shows general agreement between the different MCs, showing uniformly distributed events. The agreement in η is reasonable for central values, beyond ~ 1.5 in either direction disagreements are visible, especially for low $N_{\text{Jet}} \geq X$.

The transverse momentum distributions are generally similar, showing good agreement at low values with broadly diverging agreement as a function of energy. This is naturally reflected in H_{T} which is highly correlated to the p_{T} variables. Generally, the agreement between PYTHIA8 , and ALPGEN is better than the agreement of either with Herwig++ . Further, the disagreement grows with inclusive jet multiplicity.

Finally, the invariant mass distributions are interesting in that they show very good agreement between PYTHIA8, and ALPGEN beyond what is seen in the p_{T} based distributions, although they are statistically limited at high values.

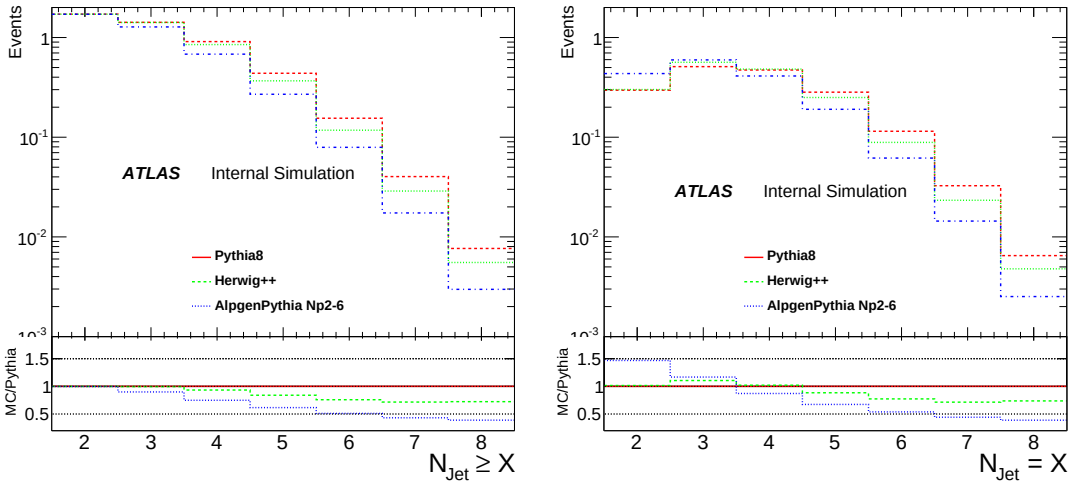

Figure A.1: Jet multiplicity distributions for Monte Carlo simulations at generator level binned inclusively (left) and exclusively (right).

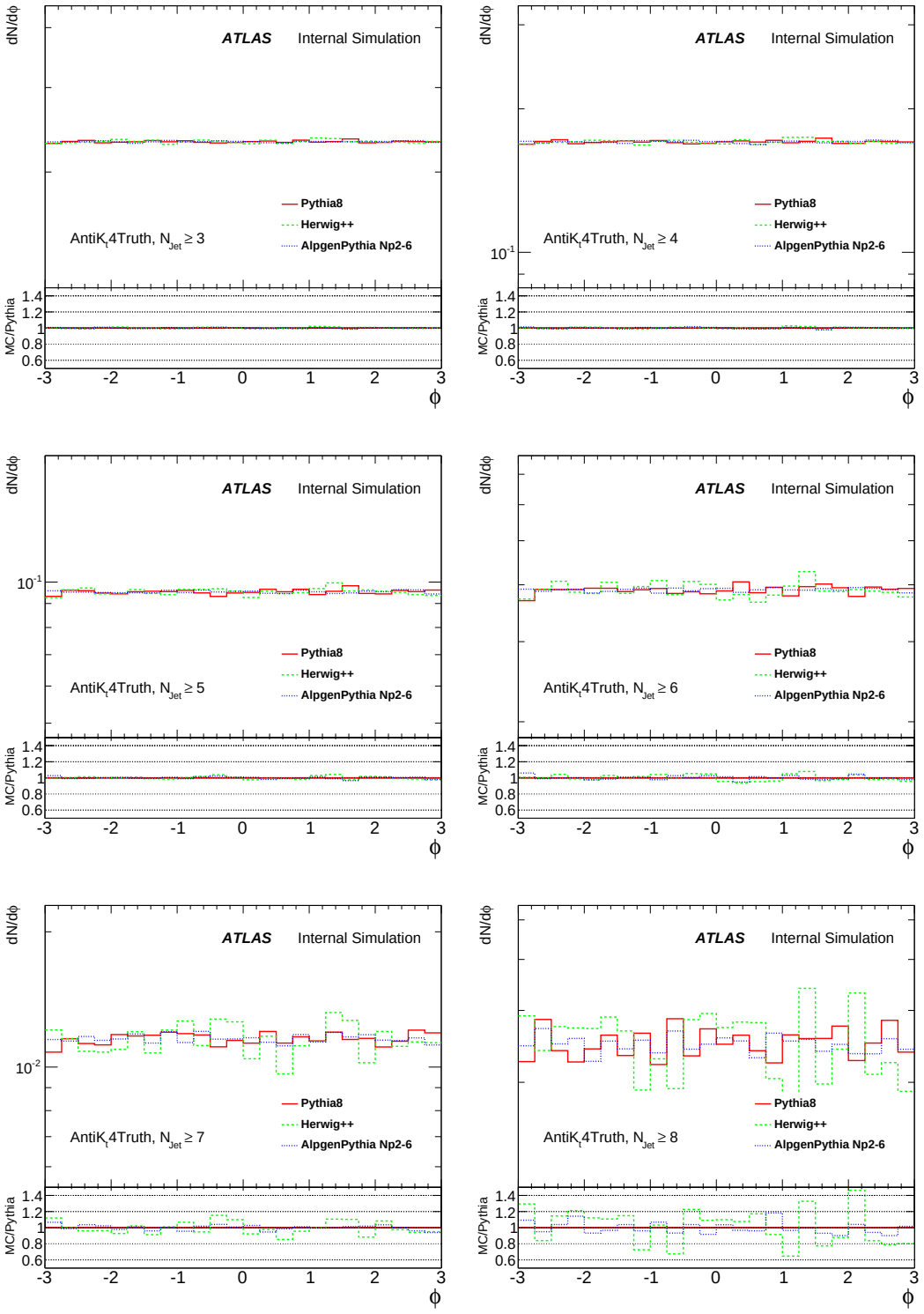

Figure A.2: ϕ distributions for different inclusive jet multiplicities for MC simulations of QCD events normalized to PYTHIA8 .

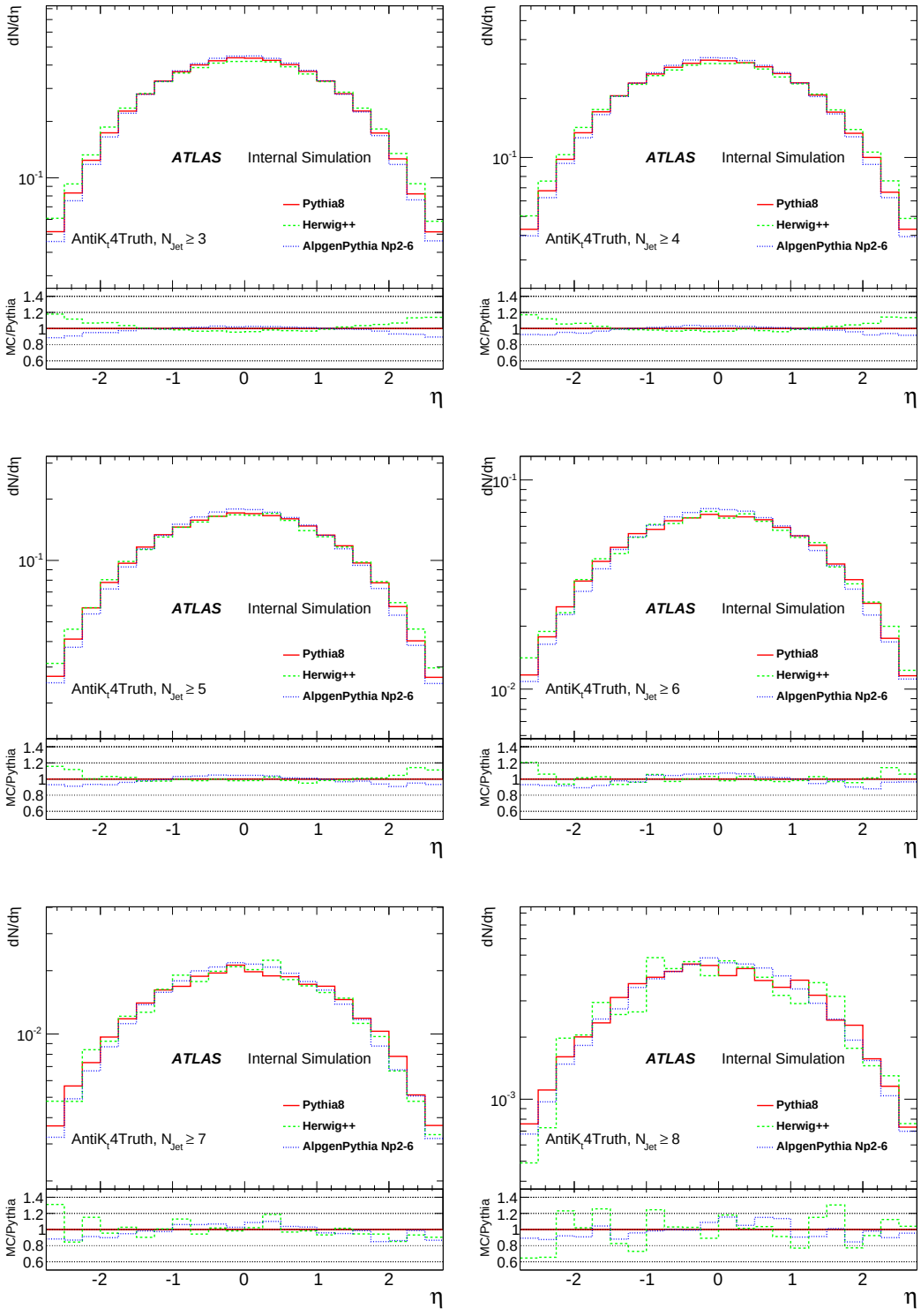

Figure A.3: The η distributions for different inclusive jet multiplicities for MC simulations of QCD events normalized to PYTHIA8 .

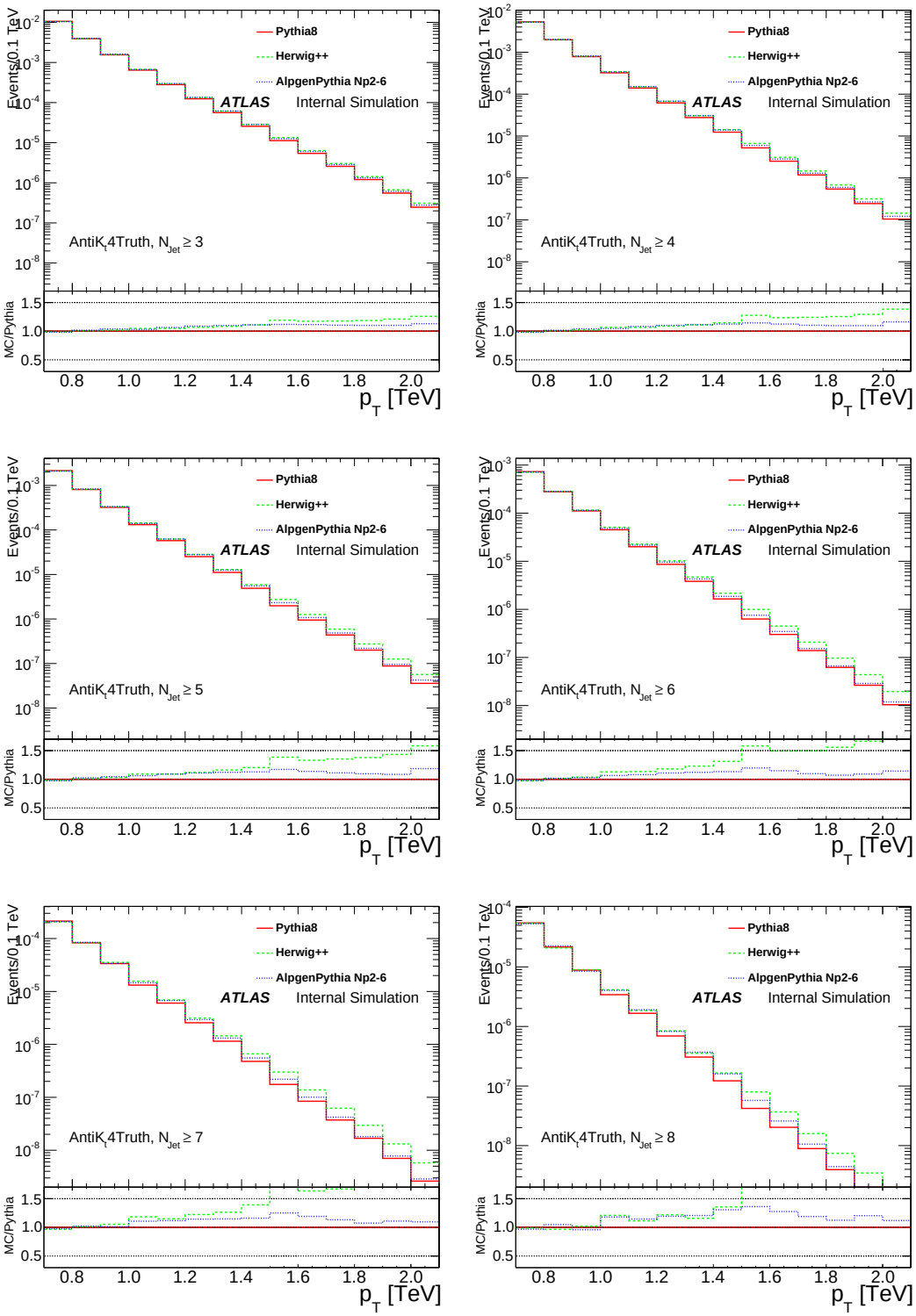

Figure A.4: The p_{T} distributions for different inclusive jet multiplicities for MC simulations of QCD events normalized to PYTHIA8 .

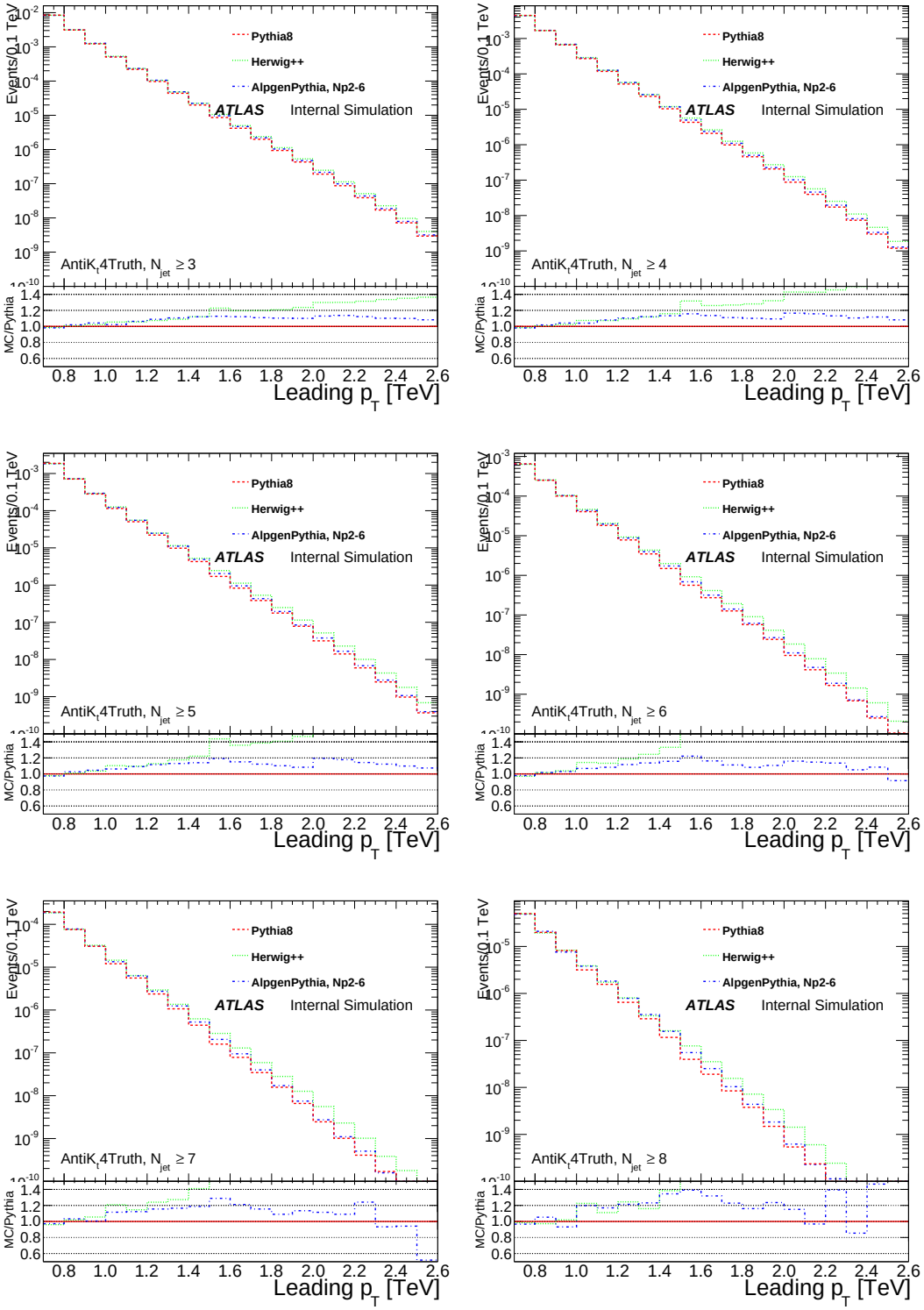

Figure A.5: Highest jet-p_{T} distributions for different inclusive jet multiplicities for MC simulations of QCD events normalized to PYTHIA8 .

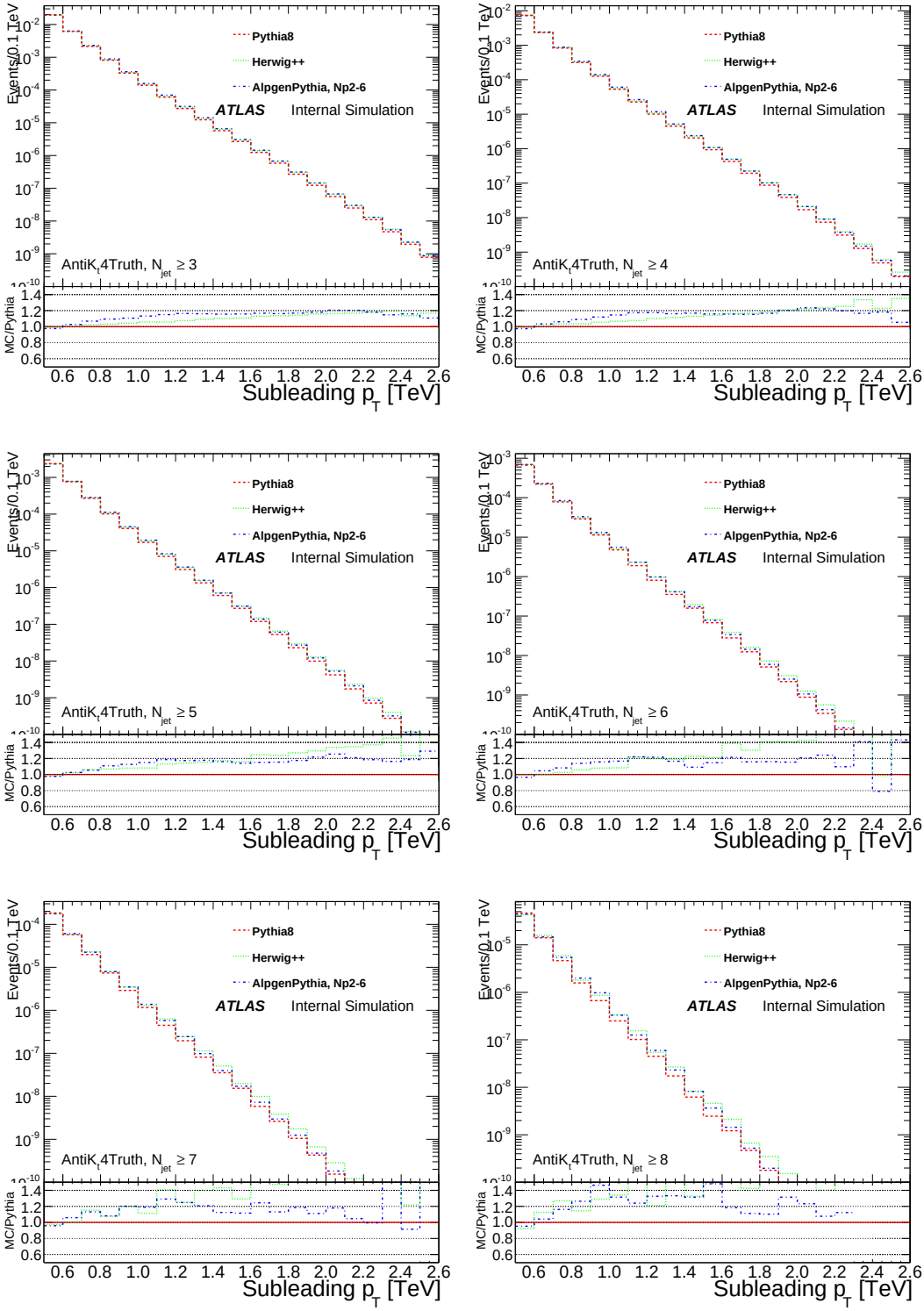

Figure A.6: Second highest-p_{T} distributions for different inclusive jet multiplicities for MC simulations of QCD events normalized to PYTHIA8 .

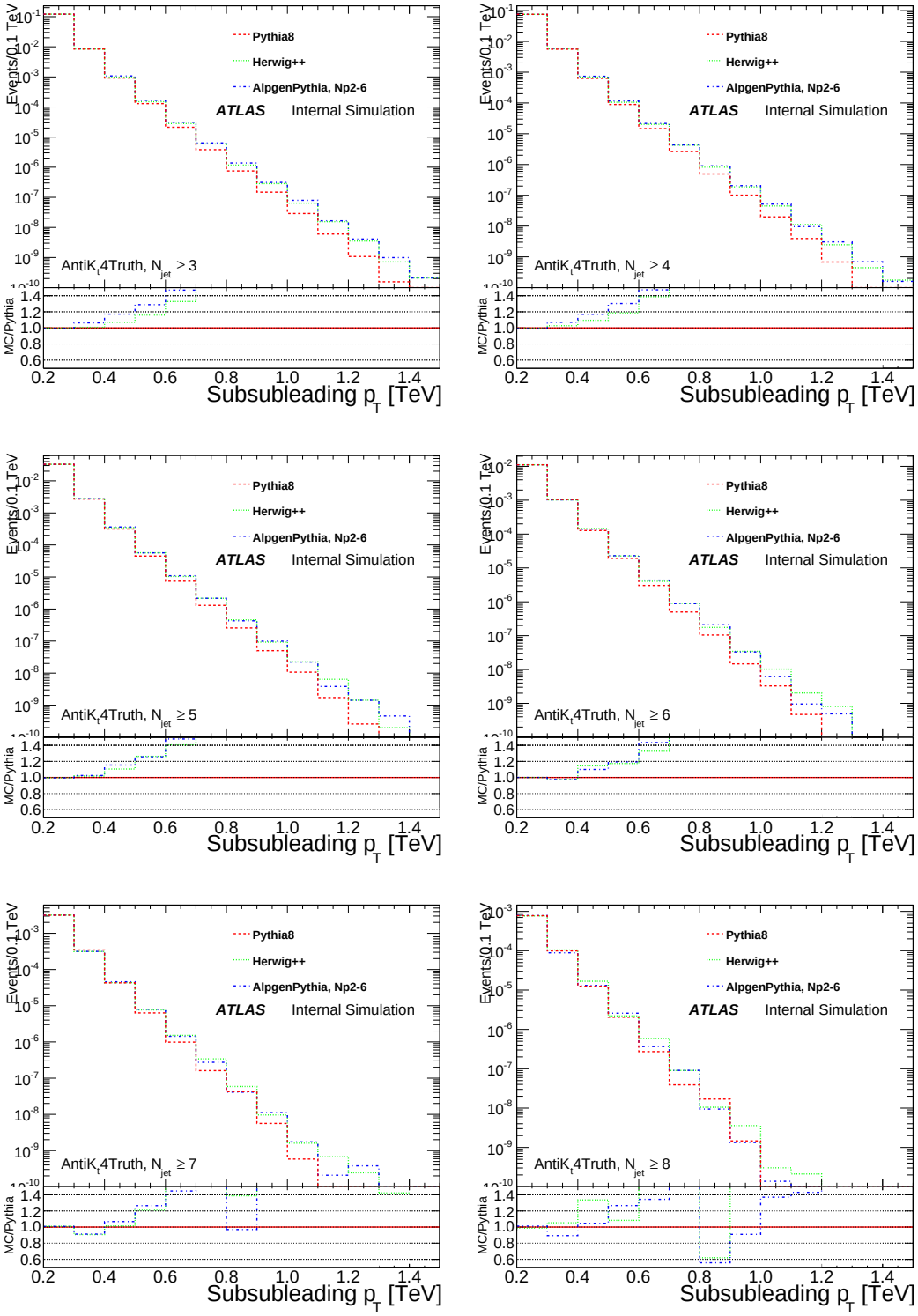

Figure A.7: Third highest-p_{T} distributions for different inclusive jet multiplicities for MC simulations of QCD events normalized to PYTHIA8 .

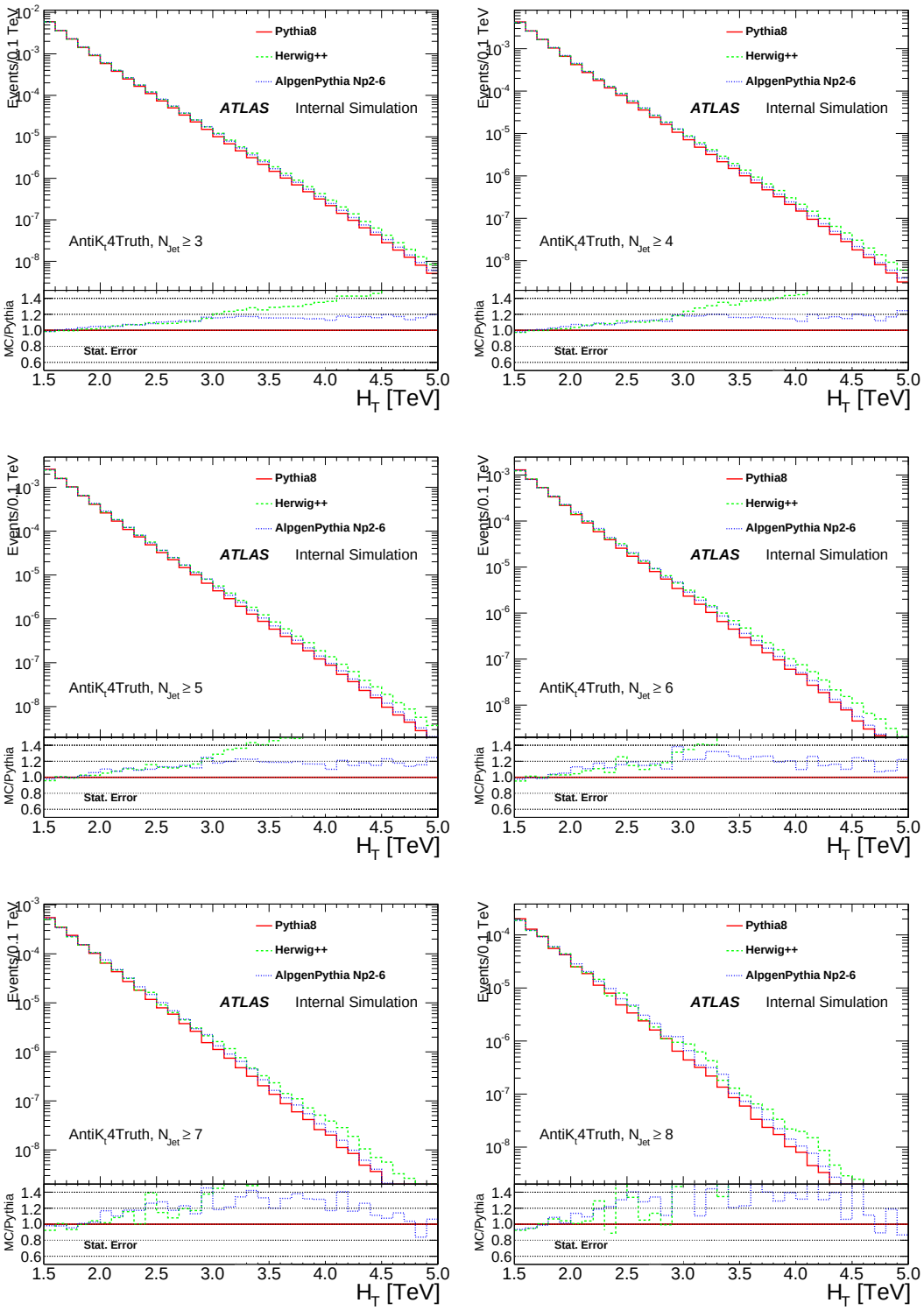

Figure A.8: The H_{T} distributions for different inclusive jet multiplicities for MC simulations of QCD events normalized to PYTHIA8 .

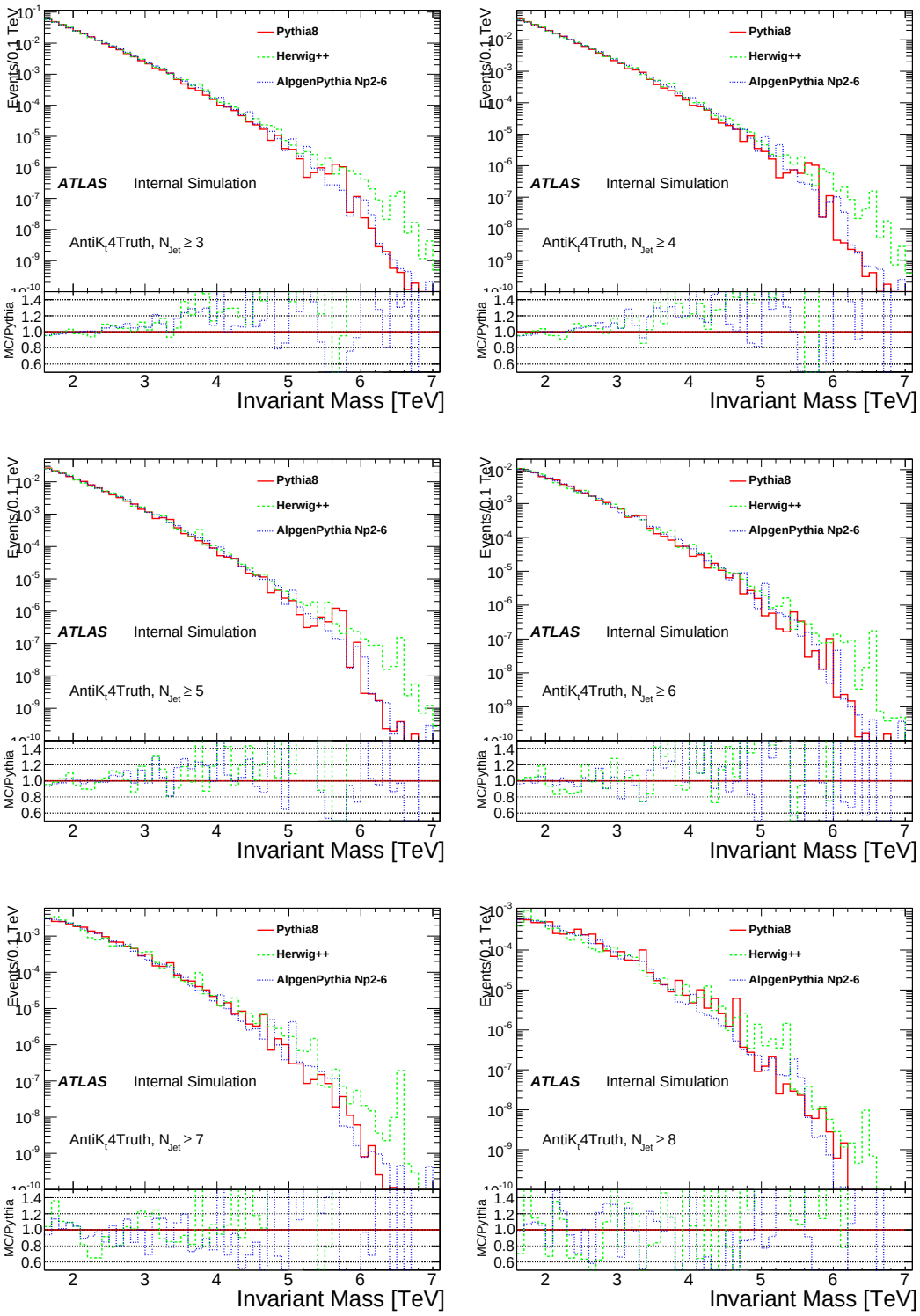

Figure A.9: Invariant mass distributions for different inclusive jet multiplicities for MC simulations of QCD events normalized to PYTHIA8 .

A.3 Jet Kinematics - Reconstructed

In this section analogous kinematic distributions similar to the previous sections are shown, only now the comparison is made to unblinded data. As only the dijet MC's are available at reconstructed level, the comparison are only made to these samples. The following figures show the comparisons of the jet kinematical variables, $N_{\text{Jet}} \geq X$ Figure A.10, ϕ Figure A.11, η Figure A.12, p_{T} Figure A.13, leading p_{T} Figure A.14, sub-leading p_{T} Figure A.15, and sub-sub-leading p_{T} Figure A.16, H_{T} Figure A.17 and invariant mass Figure A.18 between MC at reconstructed level versus observed data.

For jet multiplicity we see that the observed does not closely resemble either MC results this implies that dijet simulation does not adequately describe the multiplicity distribution of multi-jet events[1]. In ϕ, the agreement is very good, a dip can be seen at $\phi \sim 0$ and $\phi \sim 1.7$ and is duplicated in MC. These are indicative of the masked tile event veto described in Section 6.3. In η the agreement appears to improve at higher multiplicity due to statistical limitations washing out the fine features of the distributions.

In the p_{T} based distributions there is a very important result: the data is described very by `PYTHIA8` and overestimated by `Herwig++` in the distribution tails. These trends hold up to the third leading jet p_{T} of the system, which in dijet MC's are not described by matrix element calculations but parton shower.

The same trend is seen in H_{T}, the analysis variable. Thus, while `PYTHIA8` cannot describe the jet multiplicity, it does describe H_{T} in inclusive jet multiplicity slices quite well. Finally the invariant mass distribution shows potential for MC

1. A private result shows excellent agreement between the observed data and `ALPGEN` multi-jet in the $N_{\text{Jet}} \geq X$ distribution.

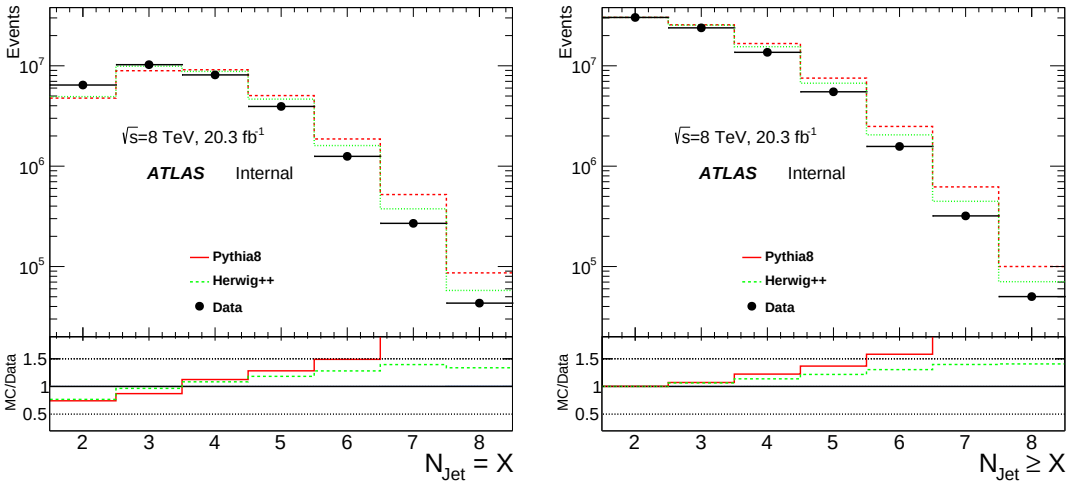

Figure A.10: Jet multiplicity distributions for Monte Carlo simulations and data binned inclusively (left) and exclusively (right).

modeling, however the statistics are too limited at high multiplicity. This indicates that a MC based modeling of invariant mass for a possible 13 TeV analysis would require additional MC statistics. It can also be noted that the kinematic reach of invariant is greater than that of H_{T}. For the same jet multiplicity, for example, $N_{\mathrm{Jet}} \geq 3$, the last data event in H_{T} lies at ~ 4.3 TeV, however in invariant mass the reach is extended to > 6 TeV.

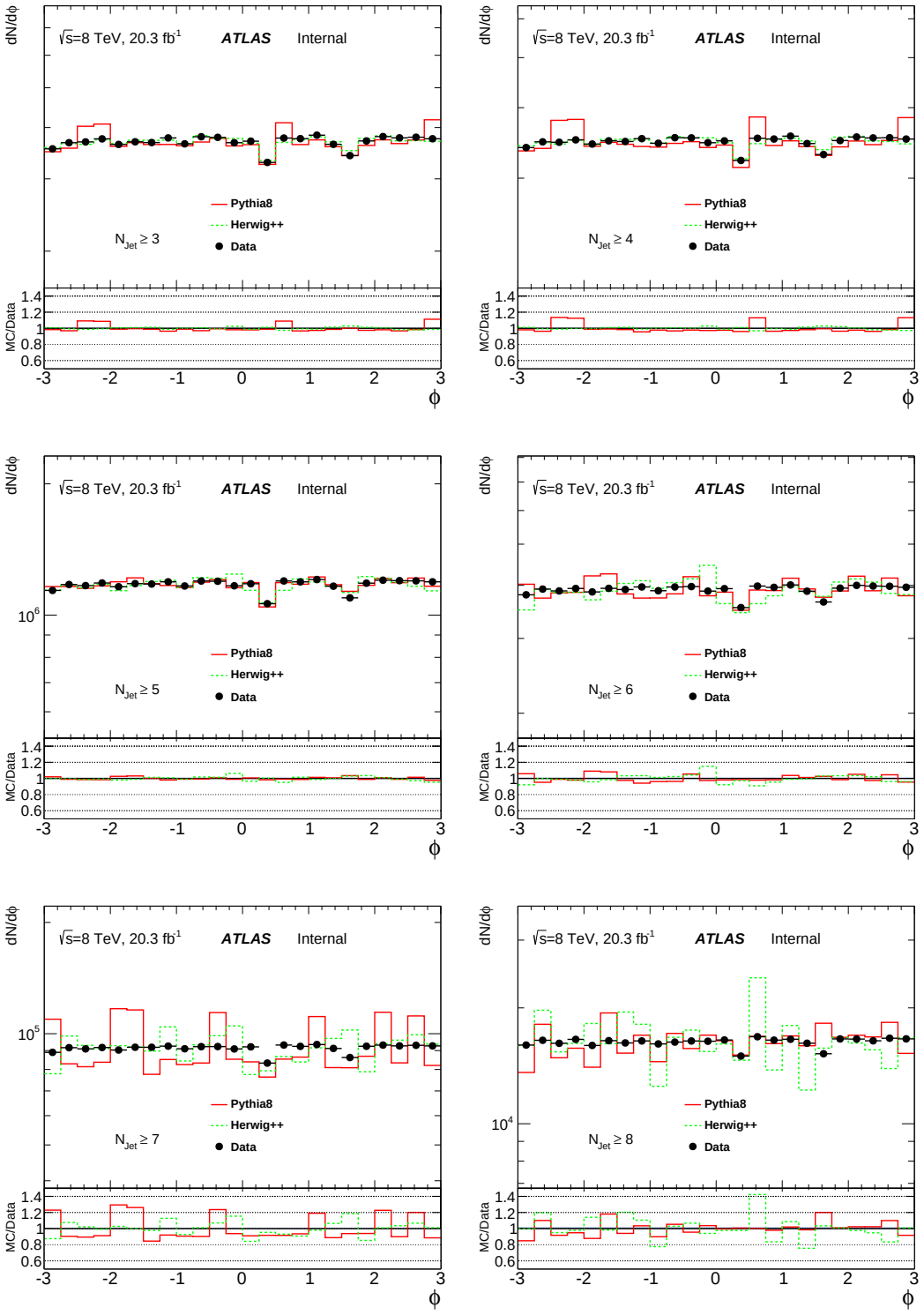

Figure A.11: The ϕ distributions for different inclusive jet multiplicities for 20.3 fb^{-1} of data and MC simulations of QCD events.

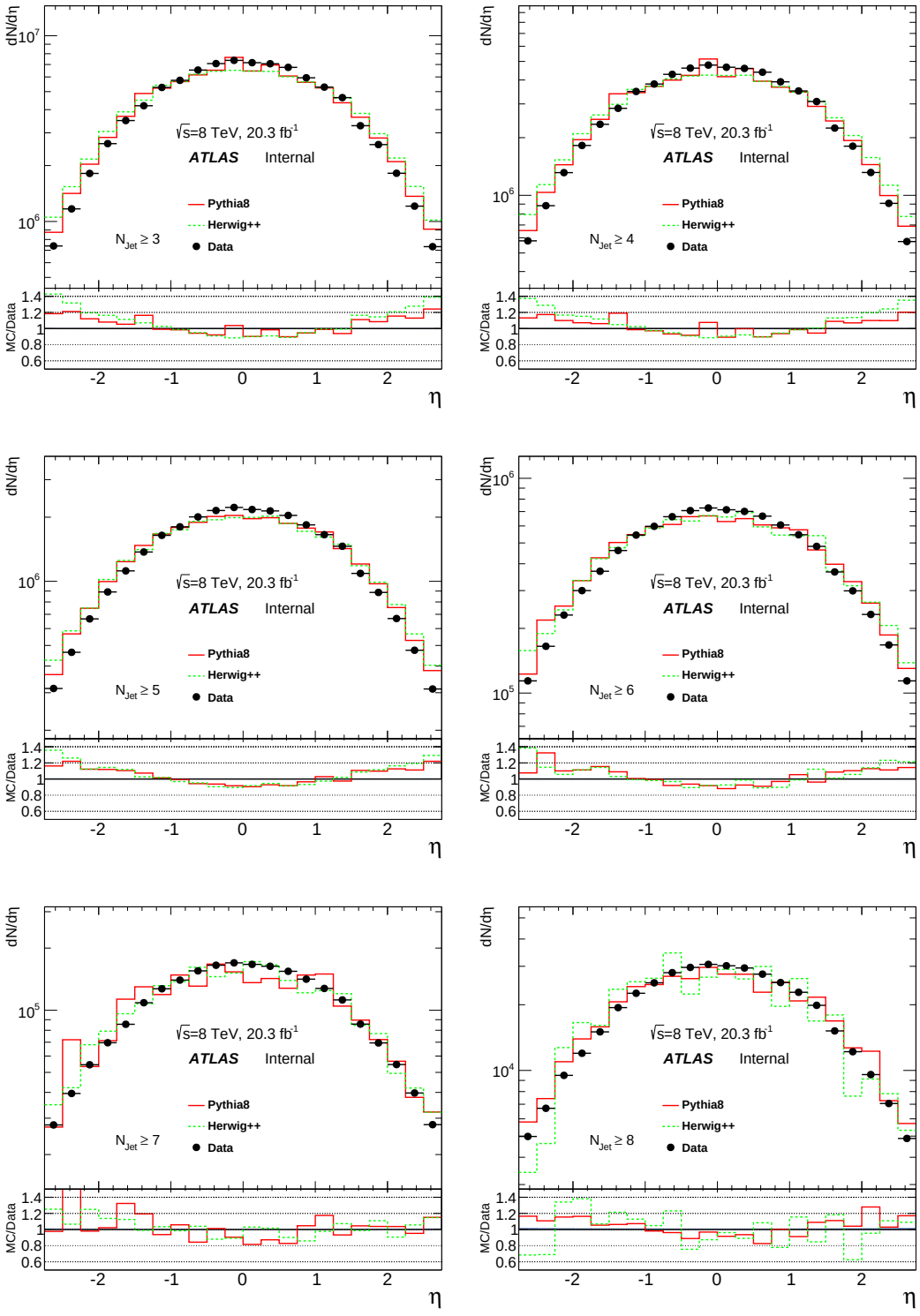

Figure A.12: The η distributions for different inclusive jet multiplicities for 20.3 fb^{-1} of data and MC simulations of QCD events.

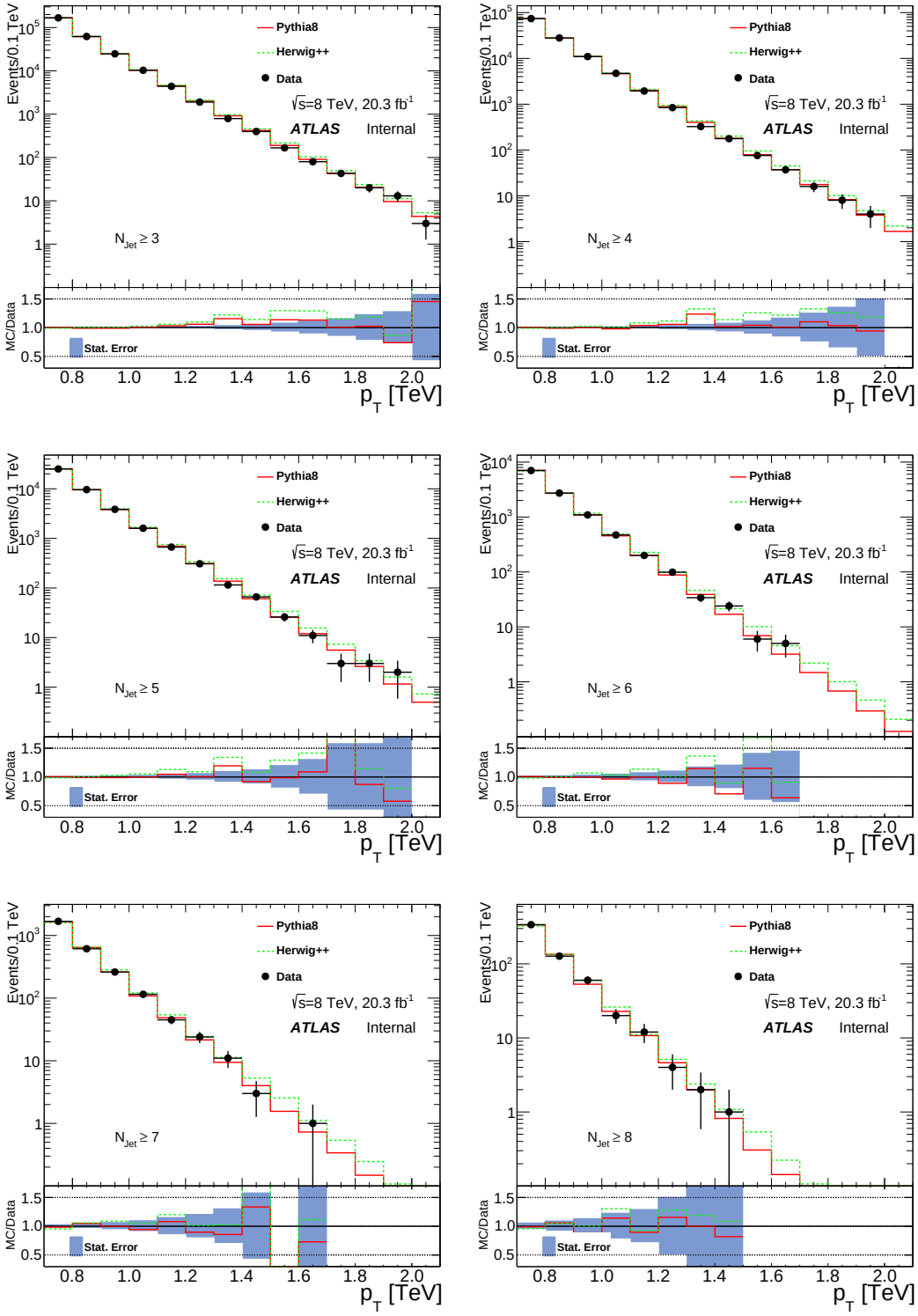

Figure A.13: The p_{T} distributions for different inclusive jet multiplicities for 20.3 fb^{-1} of collision data and MC simulations of QCD events.

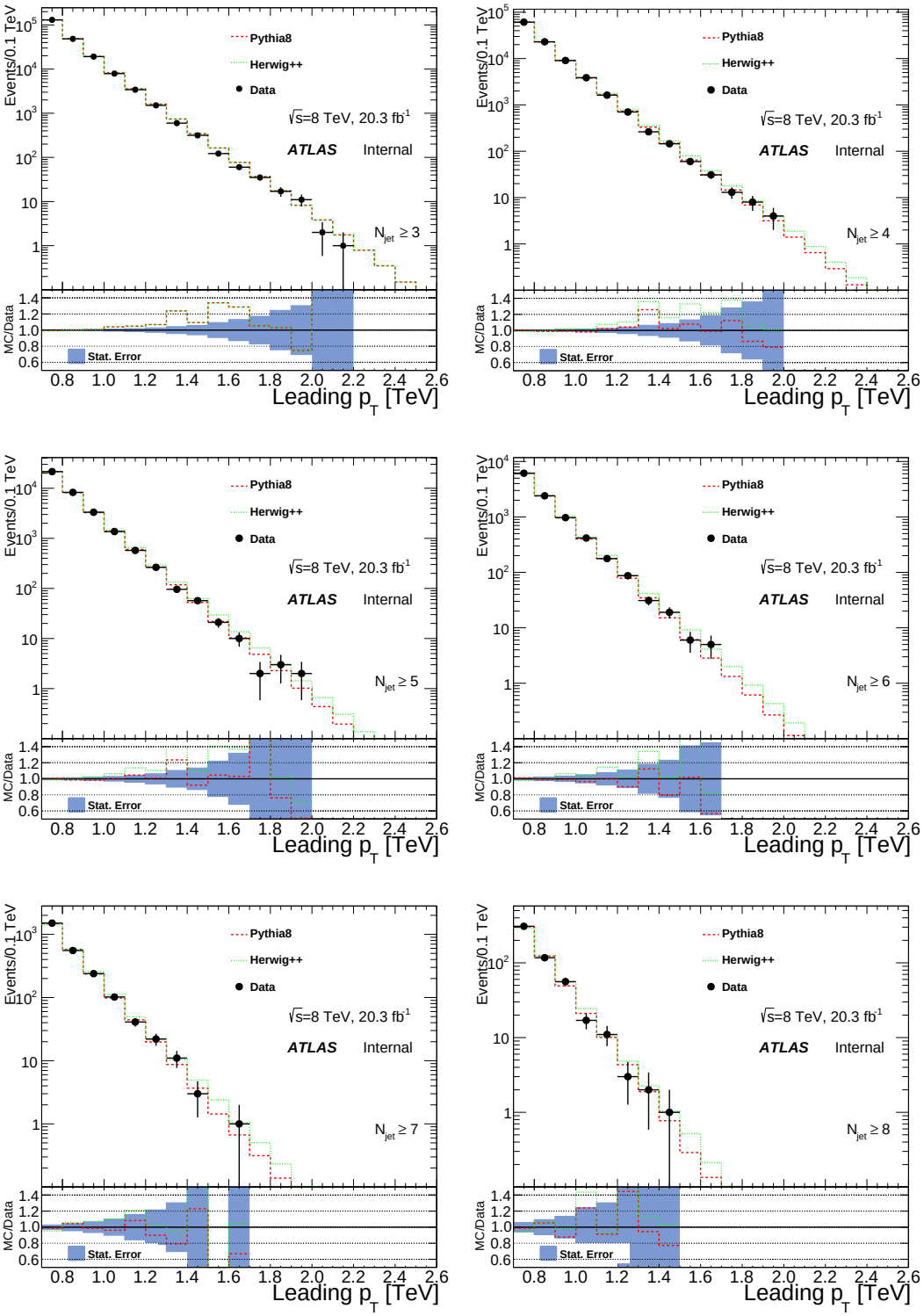

Figure A.14: Highest jet-p_{T} distributions for different inclusive jet multiplicities for 20.3 fb^{-1} of data and MC simulations of QCD events.

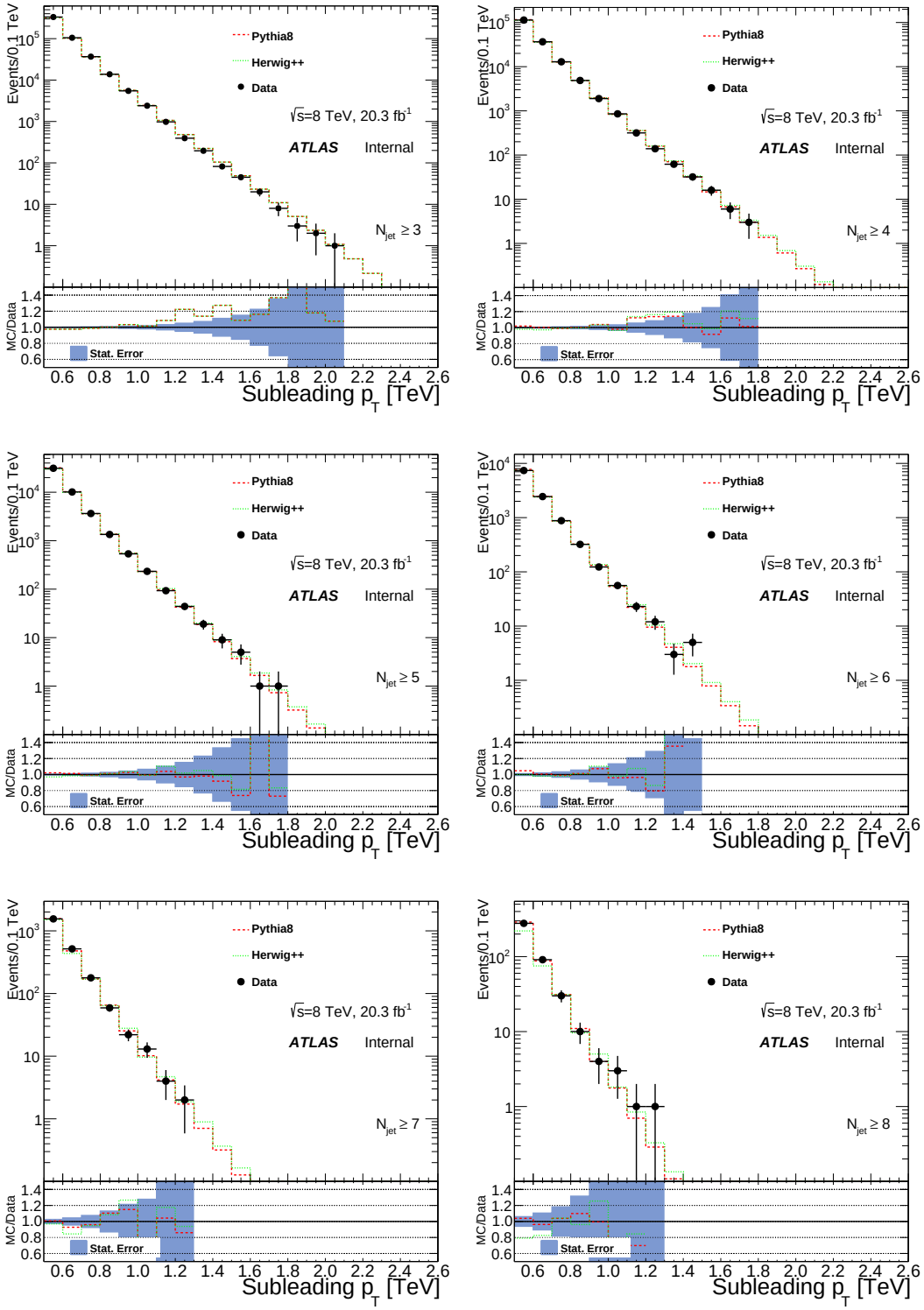

Figure A.15: Second highest jet-p_{T} distributions for different inclusive jet multiplicities for 20.3 fb^{-1} of data and MC simulations of QCD events.

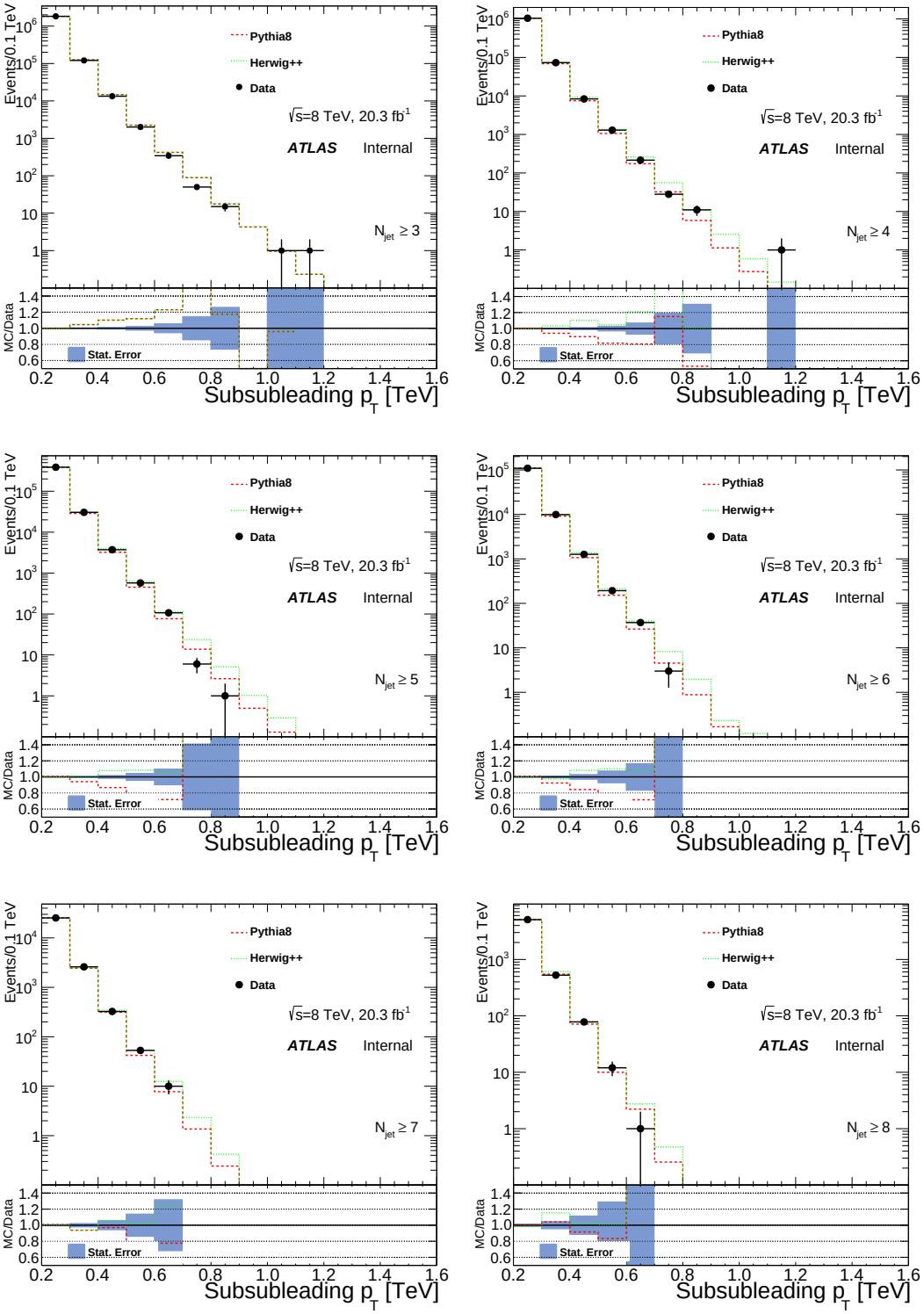

Figure A.16: Third highest-p_{T} distributions for different inclusive jet multiplicities for 20.3 fb^{-1} of data and MC simulations of QCD events.

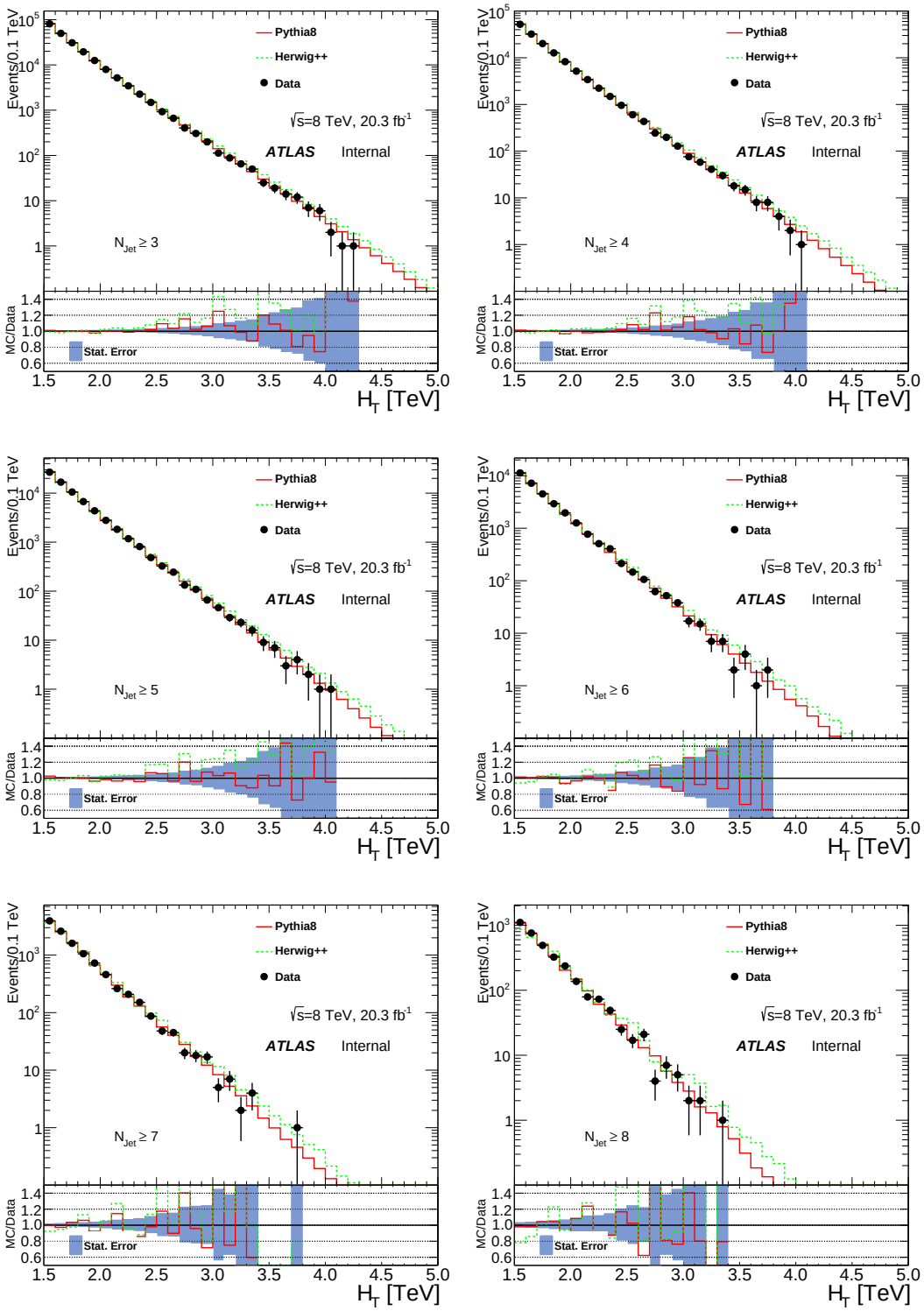

Figure A.17: The H_{T} distributions for different inclusive jet multiplicities for 20.3 fb^{-1} of data and MC simulations of QCD events.

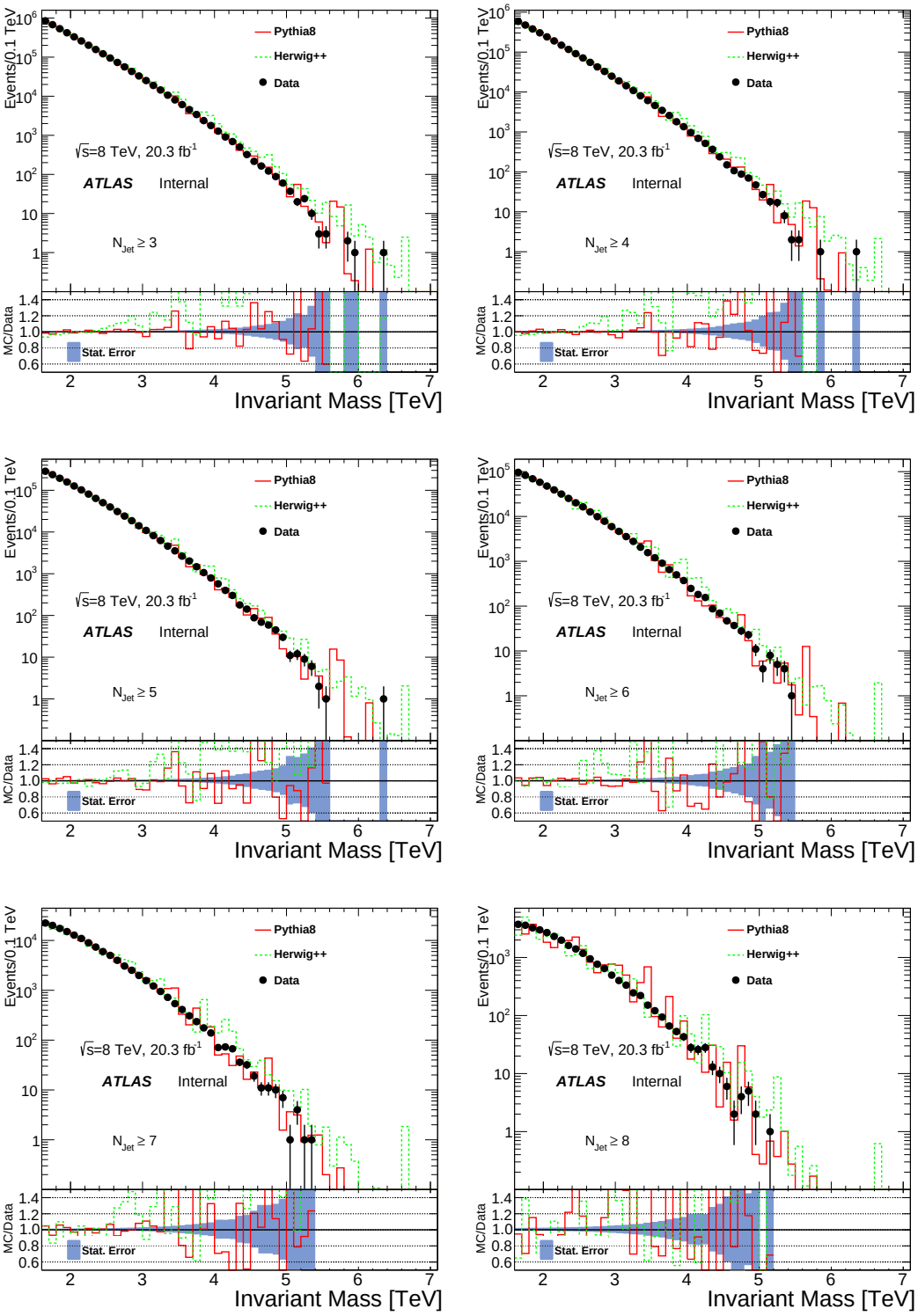

Figure A.18: Invariant mass distributions for different inclusive jet multiplicities for 20.3 fb^{-1} of data and MC simulations of QCD events.

A.4 Event Structure

The structure of events with different topologies can often be distinguished by a suitable variable. Two event variables are studied in order to compare the dijet MC against multi-jet MC and observed data. The objective is to look for possible distinctions between the samples and as to which describes data to a better degree. In these plots the truth ALPGEN results are shown alongside the dijet MC's and data for comparative purposes.

In Figure A.19 is plotted the average transverse momentum, $\left\langle p_{\mathrm{T}}^{\mathrm{Jet}} \right\rangle$ of an event against the H_{T} for all jets at a given exclusive multiplicity. The jets are sorted by p_{T} such that "Jet 1" has the most transverse momentum, "Jet 2" the second most and so forth, the ratio is always made with respect to PYTHIA8. For three jet events the H_{T} is almost completely dominated by the momentum of the two leading jets. The third jet contributes very little energy, even at high H_{T}. At higher jet multiplicity this trend weakens and the leading two jets make relatively smaller contributions to the H_{T} of the event. In addition, there is little difference between dijet and multi-jet MC in the space of transverse momentum and the data is broadly in agreement with simulation. To a large extent, even at high multiplicity H_{T} is dominated by the contribution of three or four jets. The remaining jets are relatively soft in p_{T}.

In addition to scalar variables, an alternate way of examining the structure of events is to look for angular dependent differences between jets. To that extent the relative distance between the leading jet and all subsequent jets in an event can be defined by $\Delta R_{\mathrm{Jet}}^{\mathrm{Leading\,Jet}}$ using the defintion given in Chapter 4, Section 4.2. Figure A.20 shows $\Delta R_{\mathrm{Jet}}^{\mathrm{Leading\,Jet}}$ distribution for events with two to seven jets. The

distributions are peaked at $\sim \pi$, with the leading jet always highest. The former observation can be understood from a dijet system, the majority of events are back to back, the introduction of a third jet smears the system slightly, but because the third jet is soft (as seen in Figure A.19), the general dijet structure is preserved. The lack of entries below $\Delta R_{\text{Jet}}^{\text{Leading Jet}} \sim 0.4$ is indicative of the cone radius of the Anti-k_{t} algorithm. The leading jet is peaked representing its hardness in p_{T} for which η is a correlated variable. The third jet is typically closer to the leading jet and beginning with four jet events there is a enhancement of $\Delta R_{\text{Jet}}^{\text{Leading Jet}}$ at very small values indicating collinearity between the leading and fourth leading jet. This is also seen for the fifth leading jet in the $N_{\text{Jet}} = 5$ plot.

For very high multiplicities due to statistical effects it is difficult to make any conclusion but for events with three to five jets, `PYTHIA8` shows a noticeably more pronounced peak with regard to the third leading jet and does not match the predictions of the other generators or the observed data.

Generally speaking, the agreement between any MC and data is poor in angular variables compared to p_{T} based variables, this is not so surprising, as typically, MC simulations will be tuned to data that has been excluded for new physics (in this case to 7 TeV measurements) and p_{T} is a commonly used variable that groups will strive to emulate in simulation and it is one reason the analysis was carried out in H_{T} as opposed to an angular variable or jet multiplicity (which is very poorly described in dijet simulation). Even though the background is ultimately predicted from data, the necessicity of MC validation relies on the credibility of simulation in the main search variable.

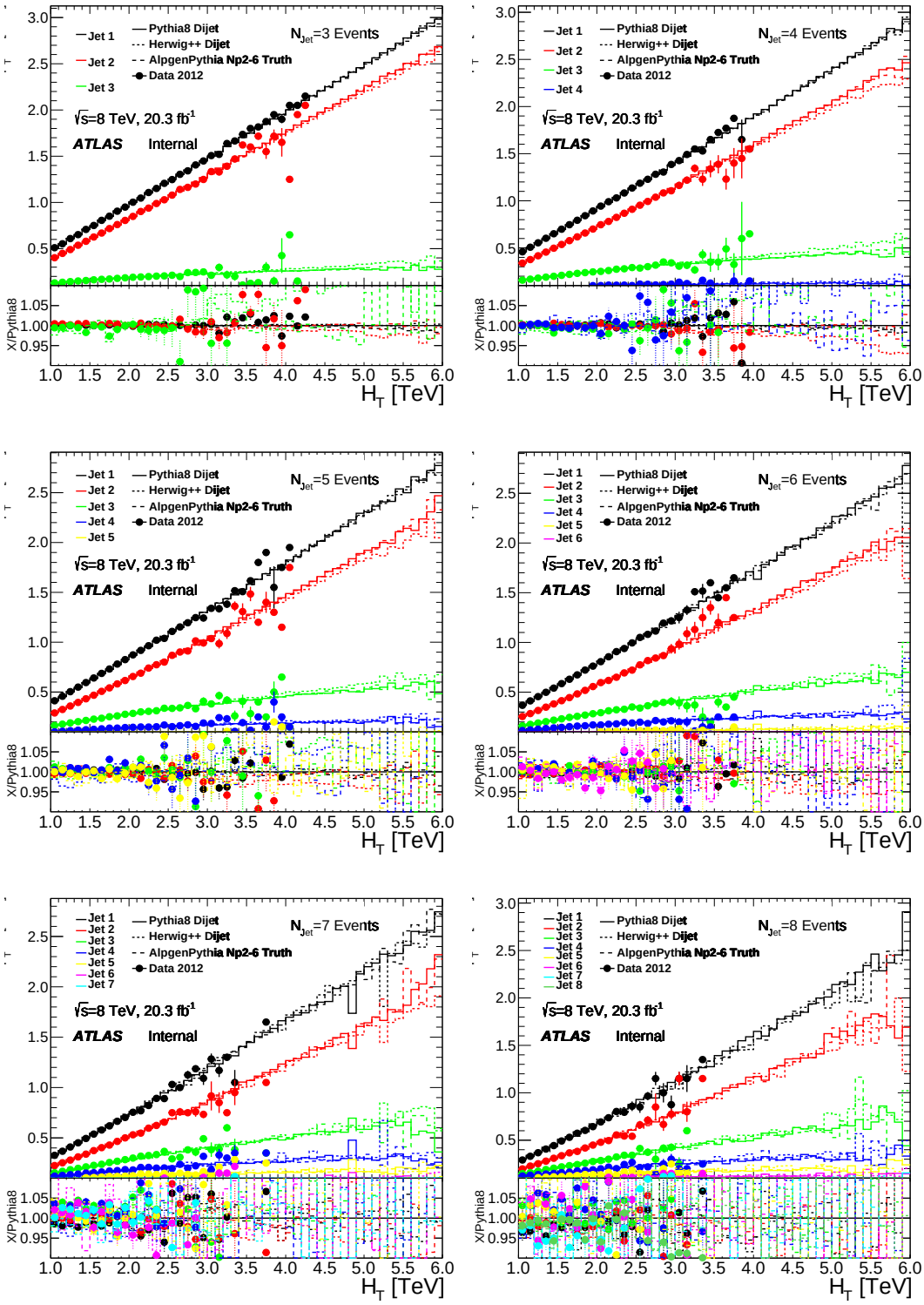

Figure A.19: $\left\langle p_{\mathrm{T}}^{\mathrm{Jet}} \right\rangle$ versus H_{T} in events for different exclusive jet multiplicity for data, `PYTHIA8`, `Herwig++`, and `ALPGEN`.

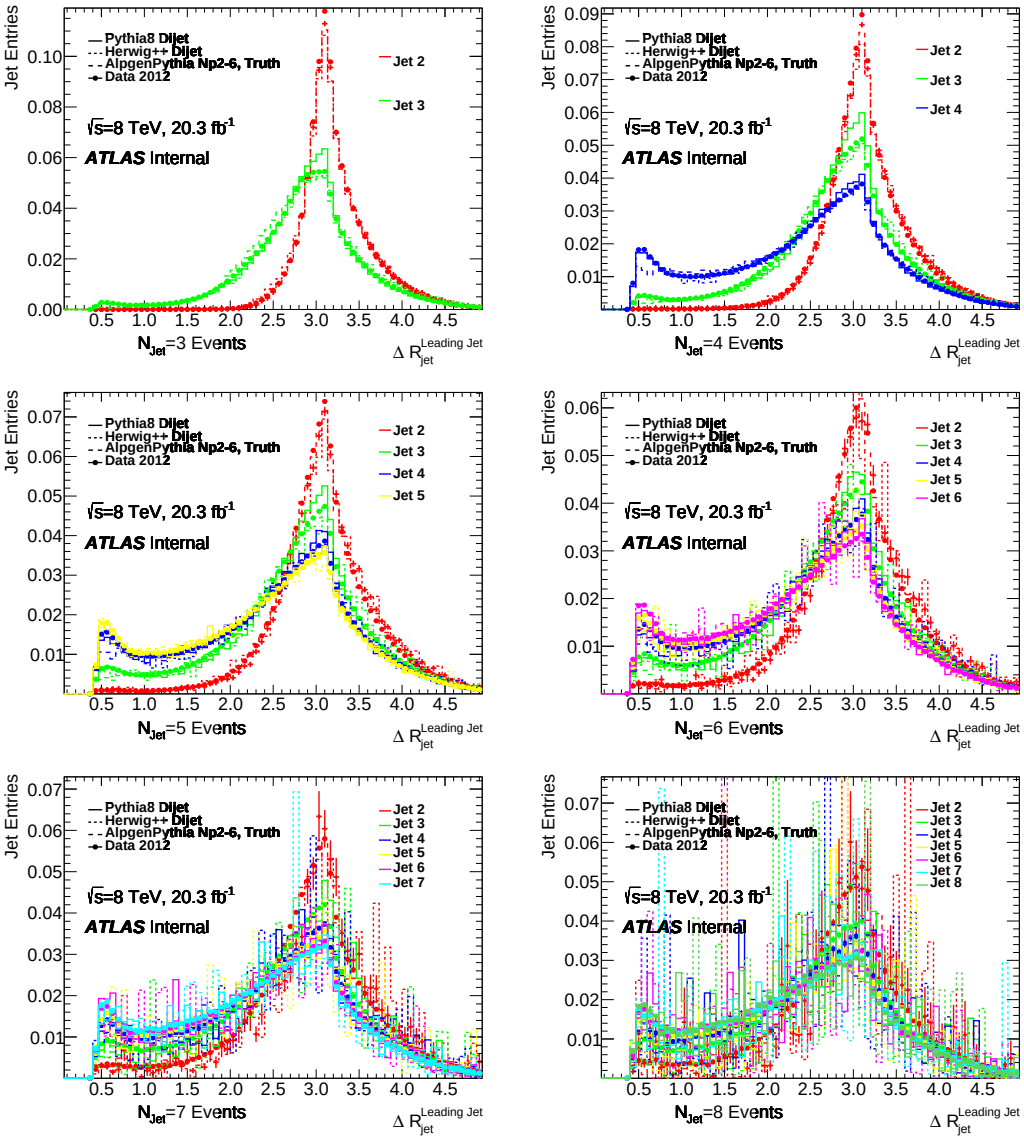

Figure A.20: The $\Delta R_{\text{Jet}}^{\text{Leading Jet}}$ distribution in events for different exclusive jet multiplicity for data, `PYTHIA8`, `Herwig++`, and `ALPGEN`.

A.5 Method Validation

In this section the results of applying the fit method to MC is shown. Often, for a blinded analysis one of the main tasks is to demonstrate the robustness (or lack thereof) of the background prediction method in MC where no signal contamination is possible. This is to protect against the possibility that a faulty method will lead to an over prediction of the background which may lead to new physics being missed or under predict and lead to a trivial significant excess. A bad prediction in MC is not necessarily indicative of data, as in a blinded analysis, a priori, there is no way to know if MC resembles data but an extremely poor result at least demands caution.

In this section, the fit method is applied to the three principle MC's, PYTHIA8 and Herwig++ at the reconstructed level and ALPGEN at the truth level. The goal is to check how well the fit extrapolation can predict the H_{T} in MC based on a fit to the nominal CR.

Figures A.21, A.22 and A.23 show the background prediction of MC in H_{T} for PYTHIA8, Herwig++ and ALPGEN. Each plot shows the MC "data" as black dots with weighted statistical errors, the background prediction is shown as a red line. The associated systematic uncertainties detailed are shown as a blue band. Since the events are weighted, the distribution is cut off where the background prediction goes below 0.01 event.

The general trend is that the extrapolation slightly overestimates the distribution shape at low multiplicity for PYTHIA8 while slightly underestimating at high multiplicity for Herwig++[2]. A comparison is also made to ALPGEN, here

2. The $N_{\mathrm{Jet}} \geq 8$ distribution does not have enough statistics to adequately perform a fit and is excluded from the assessment.

the prediction of the truth H_{T} distribution is worst at $N_{\mathrm{Jet}} \geq 6$ but well within uncertainty and the bias occurs mostly at < 0.01 events.

Overall, no significant deviations are seen in the MC to contradict the method in data and in addition the chosen uncertainties conservatively band the nominal prediction with the "data" always within.

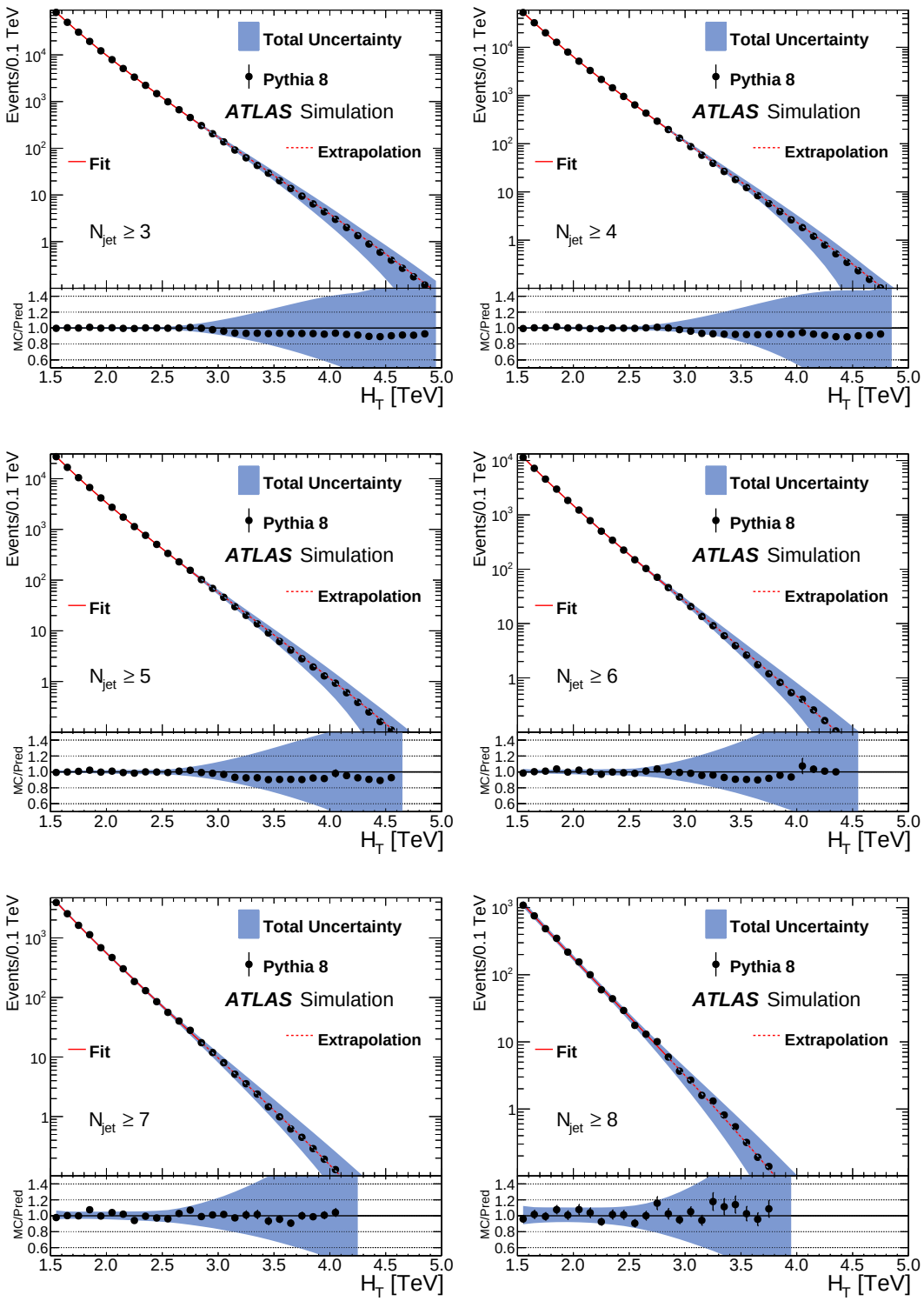

Figure A.21: Extrapolation method applied to PYTHIA8 dijet MC. The distributions are normalized to 20.3 fb^{-1} of data in the control region .

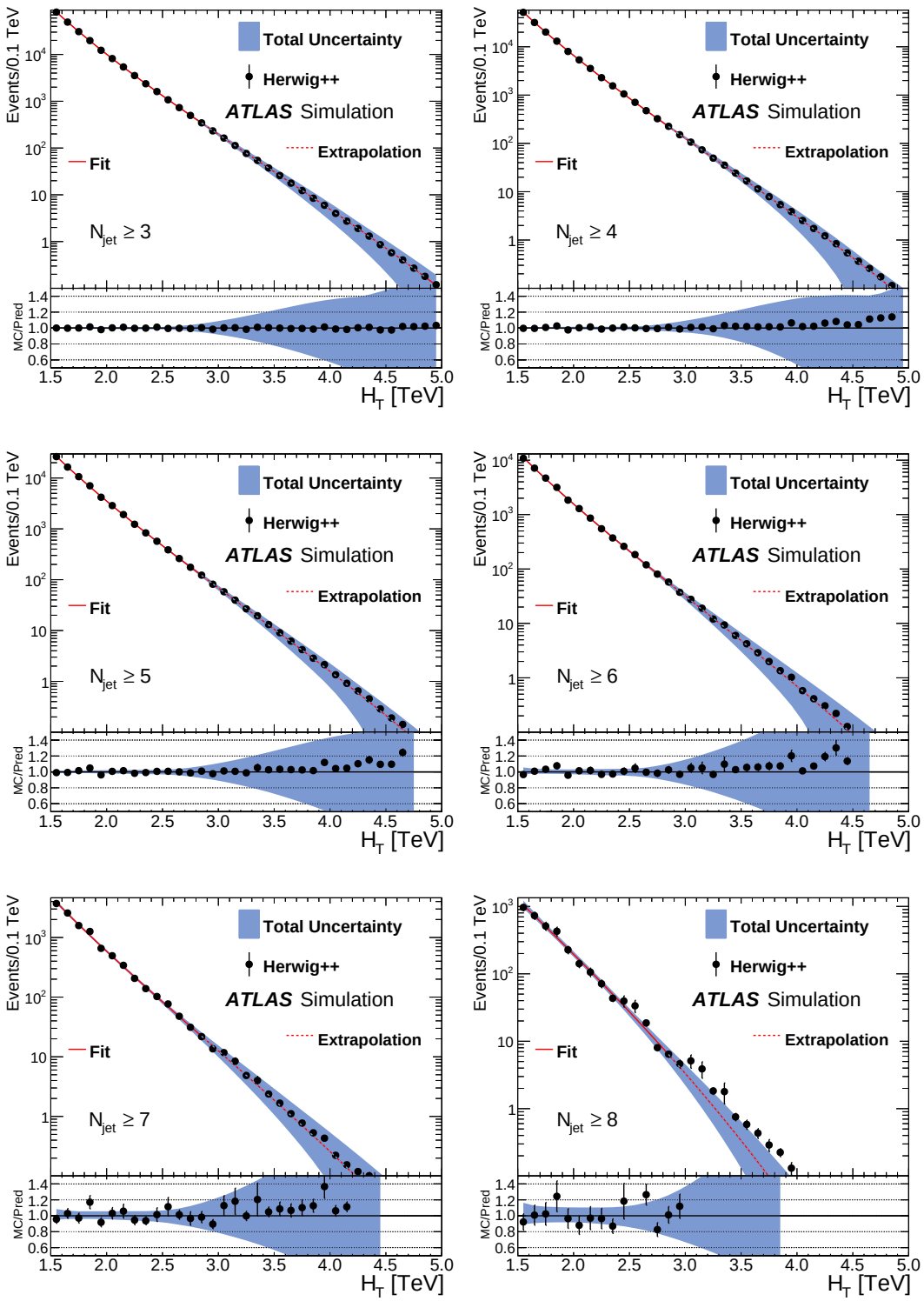

Figure A.22: Extrapolation method applied to `Herwig++` dijet MC. The distributions are normalized to 20.3 fb^{-1} of data in the control region.

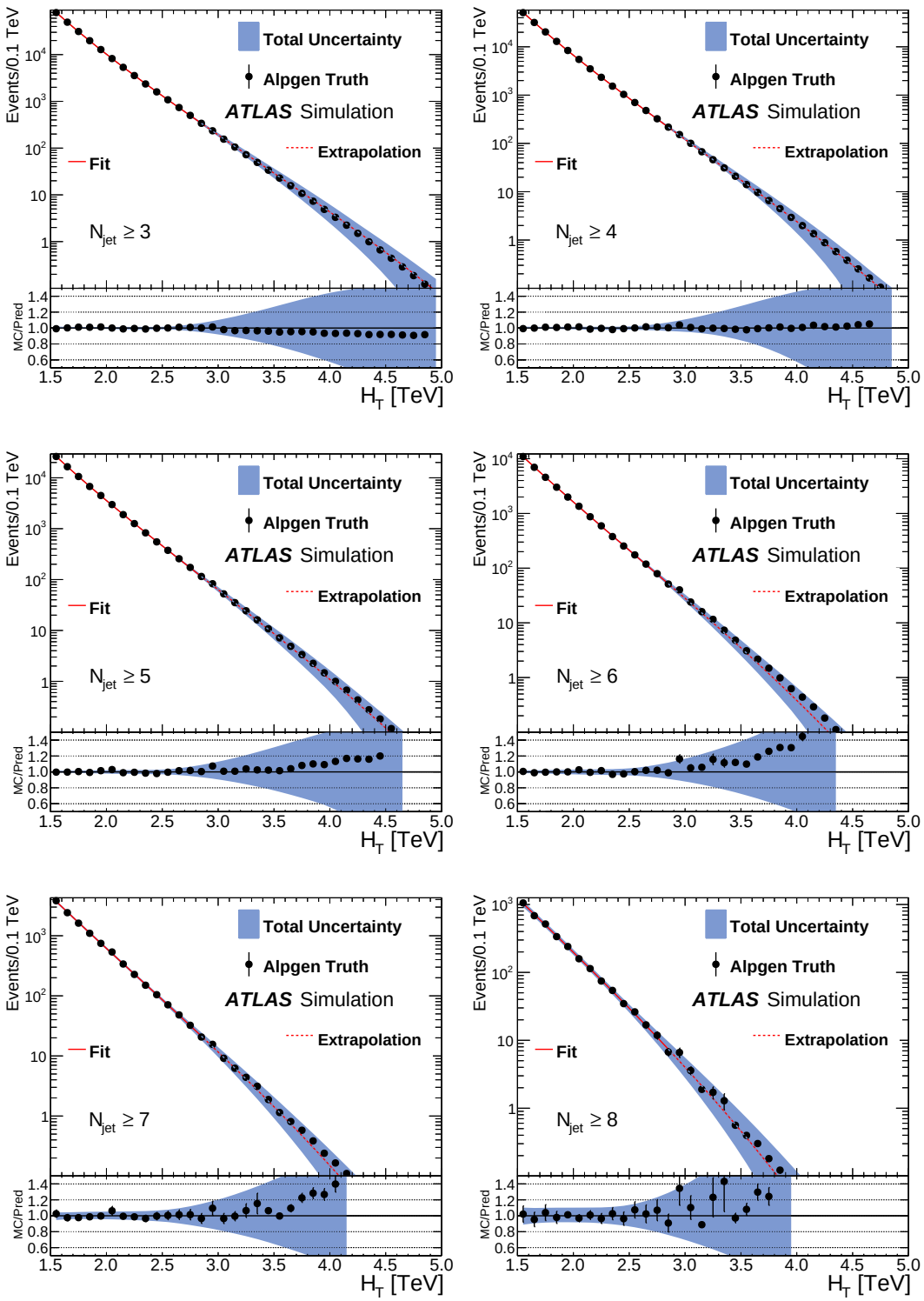

Figure A.23: Extrapolation method applied to ALPGEN multijet MC. The distributions are normalized to 20.3 fb^{-1} of data in the control region.

B

Shape Invariance

This section briefly covers the shape invariance method used in the analogous CMS published results which the author worked on extensively in the earlier parts of his PhD program.

The shape invariance hypothesis in the context of the multi-jet TeV-scale gravity analysis predicts that the shape of the H_{T} or S_{T} distribution is approximately invariant as a function of jet multiplicity [1]. The original result was published by the CMS collaboration using 35 pb^{-1} of proton-proton collision data at $\sqrt{s} = 7$ TeV in 2012 [27]. The method was used to predict the shape of the S_{T} distribution at $N_{\mathrm{Jet}} \geq 3, 4, 5$ and in later analysis by CMS [28], [25], extend the SRs to $N_{\mathrm{Jet}} \geq 10$ in the 8 TeV versions of the search.

The method functions by choosing the $N_{\mathrm{Jet}} = 2$ exclusive S_{T} distribution as a control region. A full range fit of the distribution is made using an ansatz function (Equation 6.5). Inclusive S_{T} distributions at $N_{\mathrm{Jet}} \geq 3$ and beyond are divided into CR and SRs based on energy in S_{T}. The S_{T} distribution shape of the SRs are therefore predicted by the $N_{\mathrm{Jet}} = 2$ fit parametrization to within a normalization constant, determined by the ratio of the event count in the CR by $N_{\mathrm{Jet}} \geq X/N_{\mathrm{Jet}} = 2$.

1. CMS in fact used S_{T}, the scalar sum of energy rather then transverse momentum, H_{T}, but the following discussion applies regardless as H_{T} and S_{T} are almost completely correlated variables.

To the best of the present author's knowledge the shape invariance assumption was originally validated using PYTHIA6 MC simulation based on work done in the following dissertation [66].

In the ATLAS collaboration, the multi-jet group was not able to demonstrate the assumptions of the hypothesis using the latest MC simulations available at 8 TeV. These include the aforementioned samples used in the analysis of this dissertation, PYTHIA8 , HERWIG and ALPGEN interfaced to PYTHIA and Jimmy parton showers [2]. Some of the early validation work that went into studying the method is shown in Figure B.1. The ratio of $N_{\text{Jet}} \geq X / N_{\text{Jet}} = 2$ is shown as a function of H_{T}. At high jet multiplicity some of the samples were statistically limited at the time of the study, however it is apparent that for all simulation, generally, a falling trend is seen as a function of H_{T}, in contrast to shape invariance, which would be indicated by a flat line. As such, in MC validation, the SR H_{T} distributions will be increasingly overestimated.

An alternate solution, taking advantage of the relative linearity of the bias was used to provide a MC based correction factor to the $N_{\text{Jet}} = 2$ parametrization and is comprehensively documented in [29]. However, for the purpose of the main 8 TeV ATLAS analysis, given the MC results, it was decided to move to a completely new method for the principal background estimation that did not rely on assumptions of shape invariance.

2. The latter two were statistically limited at the time of the shape invariance analysis.

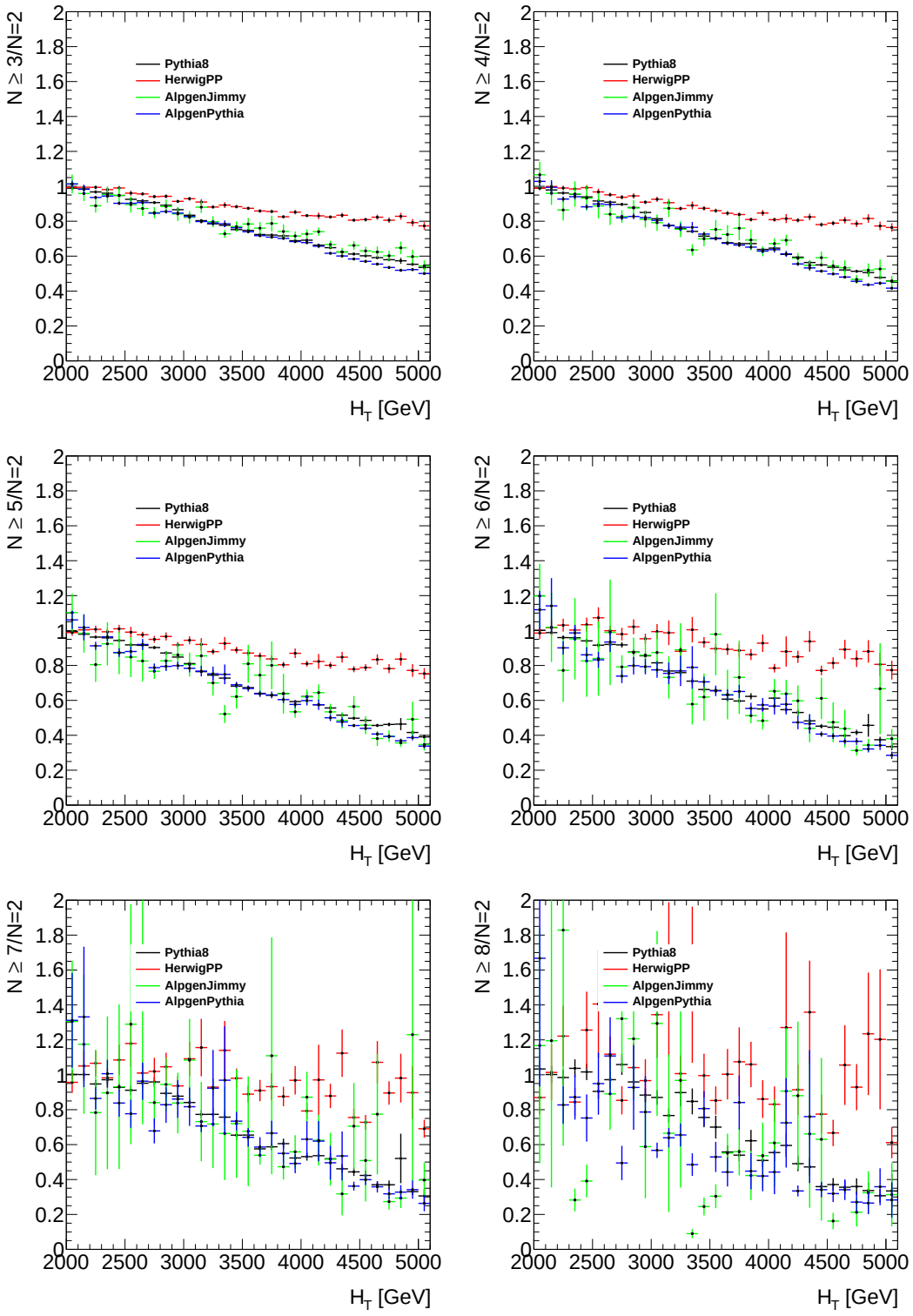

Figure B.1: The ratio of $N_{\text{Jet}} \geq X/N_{\text{Jet}} = 2$ is shown as a function of H_{T} in MC simulation for PYTHIA8, HERWIG and ALPGEN interfaced to PYTHIA and Jimmy.

C

Additional Data

This section contains relevant additional data. Tables C.1 to C.6 show the raw input into the model-independent limit calculations, the columns give the observed data, the background prediction the associated uncertainties on the background prediction for up and down variation along with the total uncertainty. Tables C.7 to C.32 show the optimal SR choices and the raw input to the model-dependent limit calculations. They show the position of the signal sample in the space of M_{Th} and M_{D}, the position of the optimal SR in the space of $H_{\mathrm{T}}^{\mathrm{min}}$ and $N_{\mathrm{Jet}} \geq X$, the observed and predicted number of events in that SR, the total uncertainty on the background prediction, the fiducial (truth) and reconstructed acceptances, the statistical error on the acceptance and the JES and JER uncertainties on the signal sample.

$H_{\mathrm{T}}^{\mathrm{min}}$	Data	Predicted	Statistical		Control region		Fit function		Total	
[TeV]	Events	Events	Up	Down	Up	Down	Up	Down	Up	Down
3.0	403	393.0	18.40	17.46	5.646	9.727	40.50	33.83	64.55	61.01
3.1	290	262.6	13.98	13.14	4.351	7.383	32.04	27.67	50.37	48.20
3.2	202	175.2	10.58	9.816	3.314	5.549	24.71	22.2	38.61	37.56
3.3	137	116.7	7.899	7.294	2.498	4.132	18.61	17.49	29.01	28.92
3.4	87	77.61	5.870	5.372	1.865	3.050	13.69	13.56	21.42	21.99
3.5	62	51.45	4.331	3.930	1.379	2.233	9.827	10.37	15.54	16.53
3.6	43	34.01	3.165	2.845	1.011	1.621	6.878	7.810	11.05	12.28
3.7	29	22.40	2.297	2.042	0.735	1.167	4.682	5.807	7.714	9.016
3.8	17	14.69	1.651	1.455	0.529	0.833	3.089	4.263	5.269	6.551
3.9	10	9.590	1.178	1.025	0.378	0.590	1.962	3.090	3.519	4.705
4.0	4	6.230	0.833	0.719	0.268	0.414	1.212	2.212	2.313	3.345
4.1	2	4.024	0.585	0.500	0.188	0.288	0.826	1.564	1.598	2.353
4.2	1	2.583	0.406	0.344	0.131	0.199	0.553	1.093	1.090	1.636
4.3	0	1.648	0.279	0.235	0.090	0.136	0.364	0.754	0.733	1.125
4.4	0	1.043	0.191	0.159	0.062	0.092	0.234	0.513	0.487	0.764
4.5	0	0.655	0.129	0.106	0.042	0.062	0.148	0.345	0.318	0.513
4.6	0	0.408	0.086	0.070	0.028	0.041	0.091	0.229	0.205	0.340
4.7	0	0.252	0.057	0.046	0.018	0.027	0.054	0.150	0.130	0.223
4.8	0	0.154	0.038	0.030	0.012	0.017	0.031	0.096	0.081	0.144
4.9	0	0.093	0.024	0.019	0.008	0.011	0.018	0.061	0.050	0.091
5.0	0	0.055	0.016	0.012	0.005	0.007	0.009	0.038	0.030	0.057
5.1	0	0.033	0.010	0.007	0.003	0.004	0.005	0.024	0.017	0.035
5.2	0	0.019	0.006	0.005	0.002	0.003	0.002	0.014	0.010	0.021
5.3	0	0.011	0.004	0.003	0.001	0.002	0.001	0.008	0.006	0.013
5.4	0	0.006	0.002	0.002	0.001	0.001	0.000	0.005	0.003	0.008
5.5	0	0.003	0.001	0.001	0.000	0.001	0.000	0.003	0.002	0.004
5.6	0	0.002	0.001	0.001	0.000	0.000	0.000	0.002	0.001	0.003
5.7	0	0.001	0.000	0.000	0.000	0.000	0.000	0.001	0.001	0.001
5.8	0	0.001	0.000	0.000	0.000	0.000	0.000	0.000	0.000	0.001
5.9	0	0.000	0.000	0.000	0.000	0.000	0.000	0.000	0.000	0.000

Table C.1: Number of data events, number of predicted events from the fit, statistical uncertainty on the fit, systematic uncertainty on the choice of control region, and on the choice of fit function versus inclusive $H_{\mathrm{T}}^{\mathrm{min}}$ lower bin edge for inclusive jet multiplicity $N_{\mathrm{Jet}} \geq 3$. The total uncertainty is obtained by adding the three uncertainties linearly.

$H_{\mathrm{T}}^{\mathrm{min}}$	Data	Predicted	Statistical		Control region		Fit function		Total	
[TeV]	Events	Events	Up	Down	Up	Down	Up	Down	Up	Down
3.0	261	238.1	13.48	13.36	12.44	13.15	22.12	6.269	48.04	32.78
3.1	185	157.2	10.16	9.956	9.557	9.95	17.32	6.403	37.04	26.31
3.2	127	103.5	7.589	7.325	7.245	7.437	13.21	6.165	28.04	20.93
3.3	86	68.02	5.603	5.370	5.429	5.495	9.826	5.663	20.86	16.53
3.4	56	44.55	4.104	3.890	4.023	4.017	7.134	5.003	15.26	12.91
3.5	38	29.08	2.976	2.790	2.951	2.906	5.053	4.272	10.98	9.968
3.6	23	18.91	2.143	1.986	2.143	2.082	3.487	3.539	7.773	7.607
3.7	15	12.24	1.523	1.405	1.541	1.476	2.34	2.853	5.404	5.734
3.8	7	7.883	1.075	0.982	1.098	1.037	1.521	2.240	3.694	4.259
3.9	3	5.050	0.753	0.681	0.775	0.721	0.952	1.717	2.480	3.120
4.0	1	3.215	0.522	0.468	0.542	0.497	0.569	1.285	1.633	2.250
4.1	0	2.034	0.358	0.319	0.375	0.339	0.320	0.940	1.053	1.598
4.2	0	1.278	0.244	0.215	0.257	0.229	0.164	0.672	0.665	1.115
4.3	0	0.796	0.165	0.143	0.175	0.153	0.072	0.470	0.411	0.765
4.4	0	0.492	0.110	0.094	0.117	0.101	0.020	0.321	0.248	0.516
4.5	0	0.302	0.073	0.061	0.078	0.066	0.000	0.215	0.151	0.342
4.6	0	0.183	0.048	0.040	0.051	0.042	0.000	0.140	0.099	0.222
4.7	0	0.110	0.031	0.025	0.033	0.027	0.000	0.090	0.064	0.142
4.8	0	0.065	0.020	0.016	0.021	0.017	0.000	0.056	0.041	0.089
4.9	0	0.038	0.012	0.010	0.013	0.011	0.000	0.034	0.026	0.055
5.0	0	0.022	0.008	0.006	0.008	0.006	0.000	0.020	0.016	0.033
5.1	0	0.013	0.005	0.004	0.005	0.004	0.000	0.012	0.010	0.019
5.2	0	0.007	0.003	0.002	0.003	0.002	0.000	0.007	0.006	0.011
5.3	0	0.004	0.002	0.001	0.002	0.001	0.000	0.004	0.004	0.006
5.4	0	0.002	0.001	0.001	0.001	0.001	0.000	0.002	0.002	0.004
5.5	0	0.001	0.001	0.000	0.001	0.000	0.000	0.001	0.001	0.002
5.6	0	0.001	0.000	0.000	0.000	0.000	0.000	0.001	0.001	0.001
5.7	0	0.000	0.000	0.000	0.000	0.000	0.000	0.000	0.000	0.001
5.8	0	0.000	0.000	0.000	0.000	0.000	0.000	0.000	0.000	0.000

Table C.2: Number of data events, number of predicted events from the fit, statistical uncertainty on the fit, systematic uncertainty on the choice of control region, and on the choice of fit function versus inclusive $H_{\mathrm{T}}^{\mathrm{min}}$ lower bin edge for inclusive jet multiplicity $N_{\mathrm{Jet}} \geq 4$. The total uncertainty is obtained by adding the three uncertainties linearly.

$H_{\mathrm{T}}^{\mathrm{min}}$	Data	Predicted	Statistical		Control region		Fit function		Total	
[TeV]	Events	Events	Up	Down	Up	Down	Up	Down	Up	Down
3.0	141	124.5	9.947	9.314	5.571	5.249	10.65	8.864	26.17	23.43
3.1	95	81.64	7.419	6.911	4.264	3.895	8.280	7.135	19.96	17.94
3.2	66	53.37	5.498	5.073	3.217	2.858	6.270	5.622	14.99	13.55
3.3	43	34.78	4.031	3.677	2.395	2.075	4.630	4.347	11.06	10.10
3.4	27	22.58	2.921	2.640	1.762	1.491	3.336	3.303	8.019	7.434
3.5	18	14.60	2.100	1.881	1.282	1.061	2.344	2.469	5.725	5.411
3.6	11	9.393	1.497	1.324	0.923	0.748	1.604	1.818	4.024	3.889
3.7	8	6.013	1.058	0.922	0.657	0.522	1.068	1.319	2.782	2.762
3.8	4	3.828	0.741	0.635	0.463	0.361	0.689	0.992	1.892	1.988
3.9	2	2.421	0.515	0.434	0.323	0.247	0.428	0.755	1.266	1.436
4.0	1	1.521	0.354	0.292	0.223	0.167	0.255	0.560	0.831	1.020
4.1	0	0.949	0.241	0.196	0.152	0.112	0.162	0.406	0.555	0.714
4.2	0	0.587	0.162	0.129	0.103	0.074	0.105	0.288	0.370	0.492
4.3	0	0.360	0.108	0.085	0.069	0.049	0.067	0.199	0.243	0.333
4.4	0	0.219	0.071	0.055	0.045	0.032	0.041	0.135	0.158	0.221
4.5	0	0.132	0.046	0.035	0.030	0.02	0.025	0.089	0.101	0.144
4.6	0	0.079	0.030	0.022	0.019	0.013	0.015	0.058	0.064	0.092
4.7	0	0.046	0.019	0.014	0.012	0.008	0.009	0.036	0.040	0.058
4.8	0	0.027	0.012	0.008	0.008	0.005	0.005	0.022	0.024	0.036
4.9	0	0.015	0.007	0.005	0.005	0.003	0.003	0.013	0.015	0.022
5.0	0	0.009	0.005	0.003	0.003	0.002	0.001	0.008	0.009	0.013
5.1	0	0.005	0.003	0.002	0.002	0.001	0.001	0.005	0.005	0.007
5.2	0	0.003	0.002	0.001	0.001	0.001	0.000	0.003	0.003	0.004
5.3	0	0.001	0.001	0.001	0.001	0.000	0.000	0.001	0.002	0.002
5.4	0	0.001	0.001	0.000	0.000	0.000	0.000	0.001	0.001	0.001
5.5	0	0.000	0.000	0.000	0.000	0.000	0.000	0.000	0.000	0.001
5.6	0	0.000	0.000	0.000	0.000	0.000	0.000	0.000	0.000	0.000

Table C.3: Number of data events, number of predicted events from the fit, statistical uncertainty on the fit, systematic uncertainty on the choice of control region, and on the choice of fit function versus inclusive $H_{\mathrm{T}}^{\mathrm{min}}$ lower bin edge for inclusive jet multiplicity $N_{\mathrm{Jet}} \geq 5$. The total uncertainty is obtained by adding the three uncertainties linearly.

$H_{\mathrm{T}}^{\mathrm{min}}$	Data	Predicted	Statistical		Control region		Fit function		Total	
[TeV]	Events	Events	Up	Down	Up	Down	Up	Down	Up	Down
3.0	55	57.21	7.050	6.170	5.812	3.634	4.440	3.733	17.30	13.54
3.1	38	37.48	5.312	4.554	4.425	2.694	3.449	3.005	13.19	10.25
3.2	23	24.48	3.944	3.320	3.325	1.974	2.608	2.368	9.878	7.662
3.3	16	15.92	2.900	2.398	2.468	1.430	2.013	1.830	7.381	5.658
3.4	9	10.32	2.114	1.709	1.812	1.025	1.557	1.389	5.482	4.123
3.5	7	6.652	1.527	1.208	1.316	0.726	1.186	1.037	4.029	2.972
3.6	3	4.268	1.090	0.844	0.945	0.510	0.892	0.762	2.927	2.116
3.7	2	2.722	0.771	0.584	0.672	0.354	0.661	0.552	2.105	1.490
3.8	0	1.726	0.540	0.400	0.473	0.243	0.484	0.418	1.497	1.061
3.9	0	1.087	0.374	0.271	0.330	0.166	0.350	0.317	1.054	0.754
4.0	0	0.680	0.257	0.182	0.227	0.111	0.250	0.235	0.735	0.528
4.1	0	0.422	0.175	0.121	0.155	0.074	0.177	0.170	0.507	0.365
4.2	0	0.259	0.118	0.079	0.105	0.049	0.123	0.120	0.346	0.248
4.3	0	0.158	0.079	0.051	0.070	0.032	0.085	0.083	0.233	0.166
4.4	0	0.096	0.052	0.033	0.046	0.020	0.058	0.056	0.156	0.109
4.5	0	0.057	0.034	0.021	0.030	0.013	0.039	0.037	0.103	0.071
4.6	0	0.034	0.022	0.013	0.019	0.008	0.026	0.024	0.067	0.045
4.7	0	0.020	0.014	0.008	0.012	0.005	0.017	0.015	0.043	0.028
4.8	0	0.011	0.009	0.005	0.008	0.003	0.011	0.009	0.027	0.017
4.9	0	0.006	0.005	0.003	0.005	0.002	0.007	0.005	0.017	0.010
5.0	0	0.004	0.003	0.002	0.003	0.001	0.004	0.003	0.010	0.006
5.1	0	0.002	0.002	0.001	0.002	0.001	0.003	0.002	0.006	0.003
5.2	0	0.001	0.001	0.001	0.001	0.000	0.002	0.001	0.004	0.002
5.3	0	0.001	0.001	0.000	0.001	0.000	0.001	0.001	0.002	0.001
5.4	0	0.000	0.000	0.000	0.000	0.000	0.001	0.000	0.001	0.001
5.5	0	0.000	0.000	0.000	0.000	0.000	0.000	0.000	0.001	0.000
5.6	0	0.000	0.000	0.000	0.000	0.000	0.000	0.000	0.000	0.000

Table C.4: Number of data events, number of predicted events from the fit, statistical uncertainty on the fit, systematic uncertainty on the choice of control region, and on the choice of fit function versus inclusive $H_{\mathrm{T}}^{\mathrm{min}}$ lower bin edge for inclusive jet multiplicity $N_{\mathrm{Jet}} \geq 6$. The total uncertainty is obtained by adding the three uncertainties linearly.

$H_{\mathrm{T}}^{\mathrm{min}}$	Data	Predicted	Statistical		Control region		Fit function		Total	
[TeV]	Events	Events	Up	Down	Up	Down	Up	Down	Up	Down
3.0	19	20.57	4.030	3.641	5.411	3.366	1.364	0.049	10.81	7.056
3.1	14	13.36	3.012	2.657	4.153	2.495	1.051	0.066	8.216	5.218
3.2	7	8.642	2.223	1.913	3.143	1.820	0.788	0.074	6.155	3.807
3.3	5	5.565	1.624	1.360	2.350	1.309	0.575	0.074	4.548	2.743
3.4	1	3.565	1.172	0.957	1.736	0.928	0.422	0.069	3.329	1.953
3.5	1	2.271	0.838	0.664	1.268	0.649	0.317	0.061	2.423	1.374
3.6	1	1.438	0.594	0.455	0.916	0.448	0.235	0.052	1.745	0.955
3.7	1	0.904	0.418	0.308	0.656	0.306	0.171	0.042	1.244	0.656
3.8	0	0.565	0.290	0.207	0.464	0.206	0.123	0.034	0.877	0.446
3.9	0	0.350	0.199	0.137	0.325	0.137	0.087	0.026	0.612	0.300
4.0	0	0.215	0.136	0.090	0.226	0.090	0.061	0.020	0.422	0.199
4.1	0	0.131	0.091	0.058	0.155	0.058	0.042	0.014	0.289	0.131
4.2	0	0.079	0.061	0.037	0.105	0.037	0.029	0.01	0.195	0.085
4.3	0	0.047	0.040	0.023	0.071	0.024	0.019	0.007	0.13	0.054
4.4	0	0.028	0.026	0.014	0.047	0.015	0.013	0.005	0.086	0.034
4.5	0	0.016	0.017	0.009	0.031	0.009	0.008	0.003	0.056	0.021
4.6	0	0.009	0.011	0.005	0.020	0.005	0.005	0.002	0.036	0.013
4.7	0	0.005	0.007	0.003	0.013	0.003	0.003	0.001	0.023	0.008
4.8	0	0.003	0.004	0.002	0.008	0.002	0.002	0.001	0.014	0.005
4.9	0	0.002	0.003	0.001	0.005	0.001	0.001	0.001	0.009	0.003
5.0	0	0.001	0.001	0.001	0.003	0.001	0.001	0.000	0.005	0.002
5.1	0	0.000	0.001	0.000	0.002	0.000	0.000	0.000	0.003	0.001
5.2	0	0.000	0.000	0.000	0.001	0.000	0.000	0.000	0.002	0.000
5.3	0	0.000	0.000	0.000	0.001	0.000	0.000	0.000	0.001	0.000
5.4	0	0.000	0.000	0.000	0.000	0.000	0.000	0.000	0.001	0.000
5.5	0	0.000	0.000	0.000	0.000	0.000	0.000	0.000	0.000	0.000

Table C.5: Number of data events, number of predicted events from the fit, statistical uncertainty on the fit, systematic uncertainty on the choice of control region, and on the choice of fit function versus inclusive $H_{\mathrm{T}}^{\mathrm{min}}$ lower bin edge for inclusive jet multiplicity $N_{\mathrm{Jet}} \geq 7$. The total uncertainty is obtained by adding the three uncertainties linearly.

$H_{\mathrm{T}}^{\mathrm{min}}$	Data	Predicted	Statistical		Control region		Fit function		Total	
[TeV]	Events	Events	Up	Down	Up	Down	Up	Down	Up	Down
3.0	5	6.912	2.591	1.909	1.903	1.256	0.387	0.000	4.881	3.165
3.1	3	4.461	1.946	1.372	1.467	0.919	0.295	0.000	3.708	2.291
3.2	1	2.862	1.444	0.972	1.113	0.661	0.219	0.000	2.776	1.634
3.3	1	1.826	1.060	0.680	0.831	0.469	0.158	0.000	2.050	1.148
3.4	0	1.157	0.770	0.468	0.613	0.327	0.112	0.000	1.494	0.795
3.5	0	0.728	0.552	0.318	0.446	0.225	0.077	0.000	1.075	0.543
3.6	0	0.454	0.392	0.213	0.320	0.153	0.051	0.000	0.763	0.366
3.7	0	0.281	0.274	0.141	0.227	0.102	0.035	0.000	0.537	0.243
3.8	0	0.173	0.191	0.092	0.159	0.068	0.025	0.000	0.375	0.159
3.9	0	0.105	0.131	0.059	0.111	0.044	0.017	0.000	0.258	0.103
4.0	0	0.063	0.089	0.037	0.076	0.028	0.0120	0.000	0.176	0.066
4.1	0	0.038	0.059	0.023	0.051	0.018	0.008	0.000	0.118	0.041
4.2	0	0.022	0.039	0.014	0.034	0.011	0.005	0.000	0.079	0.026
4.3	0	0.013	0.025	0.009	0.023	0.007	0.003	0.000	0.051	0.016
4.4	0	0.007	0.016	0.005	0.015	0.004	0.002	0.000	0.033	0.009
4.5	0	0.004	0.010	0.003	0.010	0.002	0.001	0.000	0.021	0.006
4.6	0	0.002	0.006	0.002	0.006	0.001	0.001	0.000	0.013	0.003
4.7	0	0.001	0.004	0.001	0.004	0.001	0.001	0.000	0.008	0.002
4.8	0	0.001	0.002	0.001	0.002	0.000	0.000	0.000	0.005	0.001
4.9	0	0.000	0.001	0.000	0.001	0.000	0.000	0.000	0.003	0.001
5.0	0	0.000	0.001	0.000	0.001	0.000	0.000	0.000	0.002	0.000
5.1	0	0.000	0.000	0.000	0.001	0.000	0.000	0.000	0.001	0.000
5.2	0	0.000	0.000	0.000	0.000	0.000	0.000	0.000	0.001	0.000
5.3	0	0.000	0.000	0.000	0.000	0.000	0.000	0.000	0.000	0.000

Table C.6: Number of data events, number of predicted events from the fit, statistical uncertainty on the fit, systematic uncertainty on the choice of control region, and on the choice of fit function versus inclusive $H_{\mathrm{T}}^{\mathrm{min}}$ lower bin edge for inclusive jet multiplicity $N_{\mathrm{Jet}} \geq 8$. The total uncertainty is obtained by adding the three uncertainties linearly.

M_D TeV	M_{th} [TeV]	$N_{Jet} \geq X$	H_T^{min} [TeV]	Obs	BG Events	δ BG Events		FID	A	Stat Events	JES Events		JER Event	
1.5	5.5	8	4.1	0	0.04	4.13	0.00	0.20	0.17	0.03	1.17	0.84	1.05	0.93
1.5	6.0	8	4.3	0	0.01	4.95	0.00	0.27	0.23	0.02	1.14	0.85	1.09	0.87
2.0	5.0	6	4.0	0	0.68	2.08	0.22	0.15	0.15	0.02	1.14	0.83	1.01	0.98
2.0	5.5	6	4.3	0	0.16	2.48	0.00	0.20	0.18	0.03	1.16	0.84	1.07	0.90
2.0	6.0	5	4.4	0	0.22	1.72	0.00	0.33	0.28	0.02	1.17	0.85	1.08	0.89
2.5	5.0	4	4.3	0	0.80	1.52	0.04	0.17	0.15	0.03	1.19	0.82	1.11	0.89
2.5	5.5	5	4.4	0	0.22	1.72	0.00	0.20	0.18	0.03	1.19	0.84	1.09	0.90
3.0	5.0	5	4.3	0	0.36	1.67	0.08	0.12	0.10	0.04	1.26	0.81	1.06	0.94
3.0	5.5	4	4.4	0	0.49	1.50	0.00	0.25	0.22	0.02	1.20	0.79	1.08	0.93
3.0	6.0	4	4.7	0	0.11	1.58	0.00	0.23	0.23	0.03	1.18	0.79	1.12	0.92
3.5	4.5	4	4.1	0	2.03	1.52	0.21	0.12	0.11	0.03	1.21	0.80	1.08	0.90
3.5	5.0	3	4.2	1	2.58	1.42	0.37	0.22	0.20	0.02	1.22	0.82	1.07	0.95
3.5	5.5	3	4.5	0	0.66	1.49	0.22	0.25	0.22	0.03	1.19	0.82	1.09	0.93
3.5	6.0	4	4.9	0	0.04	1.67	0.00	0.14	0.14	0.02	1.14	0.85	1.15	0.92
4.0	4.5	3	3.9	10	9.59	1.37	0.51	0.25	0.22	0.02	1.17	0.84	1.05	0.94
4.0	5.0	3	4.6	0	0.41	1.50	0.17	0.12	0.11	0.03	1.22	0.79	1.07	0.91
4.0	5.5	3	4.9	0	0.09	1.53	0.01	0.14	0.12	0.02	1.23	0.78	1.09	0.93
4.0	6.0	3	4.7	0	0.25	1.52	0.12	0.23	0.23	0.02	1.01	0.98	1.08	0.95

Table C.7: Optimal signal regions for CHARYBDIS2 non-rotating black hole with no graviton emission (BH1) sample with number of extra dimensions $n = 2$.

M_D TeV	M_{th} [TeV]	$N_{Jet} \geq X$	H_T^{min} [TeV]	Obs	BG Events	δ BG Events		FID	A	Stat Events	JES Events		JER Event	
1.5	5.0	8	3.8	0	0.17	3.17	0.08	0.19	0.16	0.03	1.17	0.86	1.05	0.92
1.5	5.5	8	4.0	0	0.06	3.77	0.00	0.26	0.21	0.02	1.15	0.83	1.06	0.94
1.5	6.0	8	4.1	0	0.04	4.13	0.00	0.34	0.28	0.03	1.15	0.86	1.11	0.91
1.5	6.5	8	4.3	0	0.01	4.95	0.00	0.37	0.31	0.02	1.11	0.91	1.10	0.92
2.0	4.0	6	3.5	7	6.65	1.61	0.55	0.11	0.10	0.02	1.12	0.89	1.05	0.94
2.0	4.5	7	3.6	1	1.44	2.21	0.34	0.13	0.11	0.04	1.14	0.88	1.04	0.94
2.0	5.0	6	3.8	0	1.73	1.87	0.39	0.25	0.22	0.03	1.14	0.87	1.06	0.93
2.0	5.5	7	3.9	0	0.35	2.75	0.14	0.26	0.22	0.03	1.14	0.87	1.05	0.94
2.0	6.0	6	4.3	0	0.16	2.48	0.00	0.34	0.28	0.03	1.15	0.86	1.07	0.93
2.0	6.5	6	4.5	0	0.06	2.80	0.00	0.38	0.32	0.02	1.05	0.89	1.04	0.95
2.5	4.0	6	3.6	3	4.27	1.69	0.50	0.10	0.09	0.02	1.21	0.84	1.10	0.95
2.5	4.5	6	3.8	0	1.73	1.87	0.39	0.13	0.11	0.03	1.21	0.83	1.11	0.93
2.5	5.5	4	4.4	0	0.49	1.50	0.00	0.26	0.22	0.02	1.17	0.84	1.05	0.95
2.5	6.0	4	4.5	0	0.30	1.50	0.00	0.32	0.28	0.02	1.16	0.84	1.07	0.93
2.5	6.5	5	4.7	0	0.05	1.86	0.00	0.33	0.26	0.02	1.08	0.92	1.08	0.95
3.0	4.5	4	3.8	7	7.88	1.47	0.46	0.21	0.19	0.02	1.15	0.84	1.07	0.94
3.0	5.0	5	4.3	0	0.36	1.67	0.08	0.13	0.12	0.03	1.21	0.81	1.05	0.93
3.0	5.5	4	4.4	0	0.49	1.50	0.00	0.25	0.23	0.02	1.16	0.84	1.05	0.95
3.0	6.0	5	4.8	0	0.03	1.90	0.00	0.19	0.17	0.03	1.19	0.82	1.15	0.87
3.0	6.5	4	4.8	0	0.07	1.63	0.00	0.32	0.26	0.01	1.00	0.99	1.22	0.85
3.5	4.5	4	4.1	0	2.03	1.52	0.21	0.13	0.12	0.02	1.22	0.82	1.08	0.92
3.5	5.0	4	4.3	0	0.80	1.52	0.04	0.17	0.15	0.03	1.17	0.83	1.06	0.94
3.5	5.5	4	4.4	0	0.49	1.50	0.00	0.24	0.21	0.03	1.21	0.80	1.05	0.94
3.5	6.0	4	4.9	0	0.04	1.67	0.00	0.19	0.15	0.03	1.00	0.93	1.04	0.99
3.5	6.5	4	4.8	0	0.07	1.63	0.00	0.39	0.23	0.07	1.00	0.99	1.00	0.99
4.0	4.5	4	4.1	0	2.03	1.52	0.21	0.12	0.11	0.02	1.20	0.80	1.05	0.94
4.0	5.0	4	4.3	0	0.80	1.52	0.04	0.17	0.15	0.03	1.19	0.81	1.08	0.93
4.0	5.5	3	4.7	0	0.25	1.52	0.12	0.21	0.18	0.03	1.21	0.81	1.06	0.93
4.0	6.0	3	4.8	0	0.15	1.53	0.06	0.26	0.22	0.01	1.00	0.92	1.07	0.93
4.0	6.5	3	4.9	0	0.09	1.53	0.01	0.31	0.24	0.07	1.00	0.99	1.02	0.94

Table C.8: Optimal signal regions for CHARYBDIS2 non-rotating black hole with no graviton emission (BH1) samples with number of extra dimensions $n = 4$.

M_D TeV	M_{th} [TeV]	$N_{Jet} \geq X$	H_T^{min} [TeV]	Obs	BG Events	δ BG Events		FID	A	Stat Events	JES Events		JER Event	
1.5	5.2	8	3.7	0	0.28	2.91	0.14	0.27	0.22	0.03	1.14	0.86	1.05	0.93
1.5	5.4	8	3.7	0	0.28	2.91	0.14	0.32	0.27	0.03	1.14	0.86	1.05	0.93
1.5	5.8	8	3.9	0	0.11	3.45	0.02	0.37	0.31	0.03	1.13	0.86	1.05	0.93
1.5	6.0	8	4.1	0	0.04	4.13	0.00	0.35	0.29	0.02	1.14	0.86	1.06	0.92
1.5	6.2	8	4.2	0	0.02	4.52	0.00	0.36	0.30	0.02	1.13	0.88	1.05	0.93
1.5	6.4	8	4.2	0	0.02	4.52	0.00	0.41	0.34	0.02	1.12	0.90	1.05	0.94
1.5	6.6	8	4.0	0	0.06	3.77	0.00	0.55	0.45	0.02	1.10	0.91	1.04	0.94
2.0	5.0	6	3.8	0	1.73	1.87	0.39	0.26	0.23	0.02	1.14	0.87	1.06	0.92
2.0	5.2	6	4.0	0	0.68	2.08	0.22	0.24	0.21	0.02	1.16	0.86	1.07	0.92
2.0	5.4	7	3.9	0	0.35	2.75	0.14	0.25	0.21	0.03	1.16	0.85	1.07	0.92
2.0	6.0	7	4.3	0	0.05	3.75	0.00	0.26	0.22	0.03	1.16	0.85	1.06	0.93
2.0	6.2	7	4.2	0	0.08	3.46	0.00	0.34	0.28	0.03	1.13	0.88	1.04	0.95
2.0	6.4	7	4.3	0	0.05	3.75	0.00	0.35	0.28	0.02	1.13	0.90	1.03	0.97
2.0	6.6	7	4.5	0	0.02	4.42	0.00	0.33	0.25	0.02	1.05	0.93	1.00	0.99
2.5	5.0	6	4.0	0	0.68	2.08	0.22	0.17	0.15	0.03	1.16	0.85	1.05	0.93
2.5	5.2	5	4.3	0	0.36	1.67	0.08	0.18	0.16	0.03	1.18	0.84	1.08	0.91
2.5	5.4	5	4.4	0	0.22	1.72	0.00	0.20	0.17	0.03	1.19	0.84	1.08	0.92
2.5	5.6	5	4.5	0	0.13	1.77	0.00	0.21	0.18	0.03	1.18	0.83	1.07	0.92
2.5	5.8	5	4.3	0	0.36	1.67	0.08	0.31	0.27	0.03	1.14	0.87	1.05	0.94
2.5	6.0	5	4.6	0	0.08	1.81	0.00	0.26	0.23	0.02	1.15	0.84	1.06	0.94
2.5	6.2	5	4.7	0	0.05	1.86	0.00	0.26	0.23	0.02	1.12	0.87	1.02	0.98
2.5	6.4	5	4.6	0	0.08	1.81	0.00	0.33	0.29	0.02	1.10	0.89	1.01	0.99
2.5	6.6	5	4.8	0	0.03	1.90	0.00	0.30	0.26	0.02	1.04	0.96	1.00	0.99
3.0	5.0	4	4.3	0	0.80	1.52	0.04	0.17	0.15	0.03	1.21	0.82	1.06	0.94
3.0	5.2	4	4.4	0	0.49	1.50	0.00	0.18	0.16	0.02	1.22	0.80	1.06	0.93
3.0	5.4	4	4.5	0	0.30	1.50	0.00	0.20	0.17	0.03	1.24	0.80	1.07	0.93
3.0	5.6	5	4.5	0	0.13	1.77	0.00	0.19	0.17	0.03	1.25	0.79	1.07	0.93
3.0	5.8	5	4.4	0	0.22	1.72	0.00	0.25	0.22	0.03	1.21	0.81	1.06	0.94
3.0	6.0	4	4.7	0	0.11	1.58	0.00	0.26	0.23	0.02	1.21	0.80	1.06	0.93
3.0	6.2	4	4.8	0	0.07	1.63	0.00	0.27	0.23	0.03	1.18	0.82	1.04	0.95
3.0	6.4	5	4.6	0	0.08	1.81	0.00	0.31	0.26	0.02	1.20	0.81	1.05	0.95
3.0	6.6	4	4.9	0	0.04	1.67	0.00	0.33	0.26	0.02	1.06	0.91	1.00	0.99
3.5	5.2	4	4.4	0	0.49	1.50	0.00	0.18	0.16	0.03	1.20	0.81	1.08	0.91
3.5	5.4	4	4.5	0	0.30	1.50	0.00	0.19	0.17	0.03	1.20	0.81	1.08	0.92
3.5	5.6	4	4.6	0	0.18	1.54	0.00	0.21	0.18	0.03	1.20	0.81	1.07	0.92
3.5	5.8	4	4.8	0	0.07	1.63	0.00	0.19	0.17	0.03	1.21	0.80	1.06	0.93
3.5	6.0	4	4.7	0	0.11	1.58	0.00	0.25	0.22	0.03	1.18	0.82	1.06	0.93
3.5	6.2	4	4.8	0	0.07	1.63	0.00	0.27	0.23	0.03	1.13	0.87	1.03	0.96
3.5	6.4	4	4.7	0	0.11	1.58	0.00	0.34	0.28	0.03	1.11	0.91	1.02	0.97
3.5	6.6	4	4.8	0	0.07	1.63	0.00	0.35	0.28	0.03	1.03	0.94	1.00	0.99
4.0	5.0	4	4.3	0	0.80	1.52	0.04	0.18	0.16	0.02	1.20	0.82	1.07	0.92
4.0	5.2	4	4.4	0	0.49	1.50	0.00	0.18	0.16	0.02	1.21	0.81	1.06	0.93
4.0	5.4	4	4.5	0	0.30	1.50	0.00	0.19	0.17	0.03	1.22	0.80	1.07	0.93
4.0	5.6	4	4.6	0	0.18	1.54	0.00	0.21	0.18	0.03	1.20	0.78	1.06	0.93
4.0	5.8	4	4.5	0	0.30	1.50	0.00	0.27	0.23	0.03	1.20	0.80	1.06	0.94
4.0	6.0	4	4.9	0	0.04	1.67	0.00	0.20	0.18	0.02	1.21	0.77	1.09	0.90
4.0	6.2	3	4.9	0	0.09	1.53	0.01	0.28	0.25	0.02	1.13	0.84	1.09	0.90
4.0	6.4	4	4.9	0	0.04	1.67	0.00	0.27	0.23	0.02	1.09	0.86	1.07	0.94
4.0	6.6	3	4.9	0	0.09	1.53	0.01	0.36	0.31	0.02	1.05	0.89	1.07	0.90

Table C.9: Optimal signal regions for `CHARYBDIS2` non-rotating black hole with no graviton emission (BH1) samples with number of extra dimensions $n = 6$.

M_D TeV	M_{th} [TeV]	$N_{Jet} \geq X$	H_T^{min} [TeV]	Obs	BG Events	δ BG Events		FID	A	Stat Events	JES Events		JER Event	
1.5	5.5	3	4.7	0	0.25	1.52	0.12	0.27	0.24	0.02	1.20	0.82	1.08	0.87
1.5	6.0	3	4.8	0	0.15	1.53	0.06	0.34	0.30	0.02	1.18	0.82	1.07	0.93
2.0	5.5	3	4.7	0	0.25	1.52	0.12	0.29	0.26	0.02	1.20	0.81	1.10	0.93
2.0	6.0	3	4.8	0	0.15	1.53	0.06	0.35	0.31	0.02	1.19	0.82	1.10	0.84
2.5	5.0	3	4.5	0	0.66	1.49	0.22	0.27	0.24	0.05	1.32	0.72	1.03	0.99
2.5	5.5	3	4.8	0	0.15	1.53	0.06	0.26	0.24	0.03	1.26	0.74	1.06	0.94
2.5	6.0	3	4.8	0	0.15	1.53	0.06	0.36	0.31	0.03	1.20	0.82	1.16	0.78
3.0	5.0	3	4.7	0	0.25	1.52	0.12	0.19	0.17	0.02	1.26	0.75	1.17	0.87
3.0	5.5	3	4.8	0	0.15	1.53	0.06	0.27	0.24	0.03	1.24	0.79	1.07	0.93
3.0	6.0	3	4.9	0	0.09	1.53	0.01	0.38	0.33	0.02	1.13	0.87	1.00	0.99
3.5	4.5	3	4.2	1	2.58	1.42	0.37	0.23	0.21	0.02	1.24	0.77	1.06	0.93
3.5	5.5	3	4.8	0	0.15	1.53	0.06	0.28	0.25	0.03	1.26	0.78	1.05	0.93
4.0	4.5	3	4.2	1	2.58	1.42	0.37	0.23	0.20	0.02	1.23	0.78	1.05	0.94
4.0	5.5	3	4.8	0	0.15	1.53	0.06	0.29	0.26	0.02	1.25	0.77	1.05	0.95

Table C.10: Optimal signal regions for CHARYBDIS2 rotating black hole with no graviton emission (BH2) samples with the number of extra dimensions $n = 2$.

M_D TeV	M_{th} [TeV]	$N_{Jet} \geq X$	H_T^{min} [TeV]	Obs	BG Events	δ BG Events		FID	A	Stat Events	JES Events		JER Event	
1.5	4.5	6	3.9	0	1.09	1.97	0.31	0.15	0.13	0.02	1.17	0.84	1.05	0.88
1.5	6.0	5	4.6	0	0.08	1.81	0.00	0.36	0.30	0.02	1.15	0.85	1.04	0.96
1.5	6.5	5	4.9	0	0.02	1.95	0.00	0.29	0.29	0.01	1.00	0.93	0.98	0.99
2.0	4.5	4	4.1	0	2.03	1.52	0.21	0.21	0.19	0.02	1.20	0.81	1.04	0.92
2.0	5.0	4	4.2	0	1.28	1.52	0.13	0.28	0.24	0.03	1.21	0.81	1.04	0.92
2.0	5.5	4	4.6	0	0.18	1.54	0.00	0.27	0.24	0.02	1.21	0.80	1.06	0.93
2.0	6.0	4	4.7	0	0.11	1.58	0.00	0.35	0.30	0.02	1.18	0.83	1.07	0.94
2.5	4.5	4	4.1	0	2.03	1.52	0.21	0.21	0.18	0.03	1.16	0.82	1.06	0.93
2.5	5.0	4	4.3	0	0.80	1.52	0.04	0.24	0.21	0.02	1.19	0.81	1.06	0.93
2.5	5.5	3	4.8	0	0.15	1.53	0.06	0.26	0.24	0.02	1.21	0.80	1.06	0.94
2.5	6.0	3	4.9	0	0.09	1.53	0.01	0.34	0.30	0.02	1.19	0.81	1.05	0.93
3.0	4.5	4	4.1	0	2.03	1.52	0.21	0.18	0.16	0.02	1.21	0.81	1.08	0.92
3.0	5.0	3	4.6	0	0.41	1.50	0.17	0.20	0.18	0.02	1.23	0.78	1.08	0.92
3.0	5.5	3	4.8	0	0.15	1.53	0.06	0.26	0.23	0.02	1.22	0.81	1.07	0.93
3.0	6.0	3	4.9	0	0.09	1.53	0.01	0.35	0.31	0.02	1.19	0.81	1.18	0.86
3.5	4.5	4	4.1	0	2.03	1.52	0.21	0.19	0.17	0.02	1.20	0.81	1.07	0.92
3.5	5.0	3	4.5	0	0.66	1.49	0.22	0.24	0.22	0.02	1.23	0.79	1.06	0.94
3.5	5.5	3	4.8	0	0.15	1.53	0.06	0.27	0.24	0.02	1.20	0.79	1.05	0.95
3.5	6.0	3	4.9	0	0.09	1.53	0.01	0.35	0.30	0.00	1.00	0.88	1.06	0.97
4.0	4.5	4	4.1	0	2.03	1.52	0.21	0.19	0.17	0.02	1.20	0.79	1.05	0.95
4.0	5.0	3	4.4	0	1.04	1.47	0.27	0.30	0.27	0.02	1.20	0.80	1.06	0.94
4.0	5.5	3	4.8	0	0.15	1.53	0.06	0.28	0.25	0.02	1.25	0.77	1.08	0.92
4.0	6.0	3	4.9	0	0.09	1.53	0.01	0.39	0.31	0.01	1.04	0.91	1.09	0.93

Table C.11: Optimal signal regions for CHARYBDIS2 rotating black hole with no graviton emission (BH2) samples with number of extra dimensions $n = 4$.

M_D TeV	M_{th} [TeV]	$N_{Jet} \geq X$	H_T^{min} [TeV]	Obs	BG Events	δ BG Events		FID	A	Stat Events	JES Events		JER Event	
1.5	5.2	8	4.0	0	0.06	3.77	0.00	0.21	0.17	0.03	1.17	0.81	1.06	0.89
1.5	5.4	7	4.0	0	0.22	2.96	0.07	0.33	0.28	0.02	1.14	0.85	1.06	0.92
1.5	5.6	7	4.1	0	0.13	3.20	0.00	0.35	0.29	0.03	1.14	0.86	1.06	0.92
1.5	5.8	8	4.2	0	0.02	4.52	0.00	0.28	0.23	0.03	1.15	0.85	1.07	0.90
1.5	6.0	7	4.4	0	0.03	4.07	0.00	0.35	0.28	0.02	1.14	0.87	1.07	0.93
1.5	6.2	7	4.4	0	0.03	4.07	0.00	0.40	0.32	0.02	1.10	0.91	1.05	0.95
1.5	6.4	8	4.5	0	0.00	5.95	0.00	0.31	0.24	0.02	1.08	0.89	1.08	0.94
2.0	4.8	5	4.0	1	1.52	1.55	0.33	0.29	0.25	0.02	1.15	0.86	1.06	0.94
2.0	5.2	6	4.0	0	0.68	2.08	0.22	0.30	0.26	0.03	1.15	0.85	1.06	0.94
2.0	5.4	5	4.3	0	0.36	1.67	0.08	0.32	0.28	0.02	1.16	0.85	1.06	0.93
2.0	5.6	5	4.4	0	0.22	1.72	0.00	0.33	0.29	0.02	1.16	0.85	1.06	0.94
2.0	5.8	5	4.4	0	0.22	1.72	0.00	0.38	0.33	0.02	1.14	0.87	1.05	0.94
2.0	6.0	5	4.5	0	0.13	1.77	0.00	0.39	0.34	0.02	1.14	0.87	1.05	0.94
2.0	6.2	5	4.8	0	0.03	1.90	0.00	0.33	0.28	0.02	1.08	0.89	1.04	0.95
2.0	6.4	5	4.6	0	0.08	1.81	0.00	0.46	0.39	0.02	1.08	0.91	1.04	0.94
2.5	4.8	5	4.2	0	0.59	1.63	0.16	0.20	0.17	0.03	1.18	0.82	1.09	0.91
2.5	5.0	4	4.2	0	1.28	1.52	0.13	0.30	0.26	0.02	1.16	0.84	1.07	0.92
2.5	5.2	5	4.3	0	0.36	1.67	0.08	0.25	0.22	0.03	1.19	0.82	1.08	0.92
2.5	5.4	4	4.6	0	0.18	1.54	0.00	0.26	0.22	0.03	1.21	0.81	1.07	0.91
2.5	5.6	4	4.7	0	0.11	1.58	0.00	0.27	0.24	0.02	1.20	0.81	1.07	0.92
2.5	5.8	4	4.7	0	0.11	1.58	0.00	0.33	0.28	0.02	1.19	0.83	1.07	0.93
2.5	6.0	4	4.8	0	0.07	1.63	0.00	0.35	0.29	0.02	1.19	0.82	1.06	0.94
2.5	6.2	4	4.9	0	0.04	1.67	0.00	0.37	0.30	0.02	1.13	0.89	1.05	0.97
2.5	6.4	4	4.9	0	0.04	1.67	0.00	0.44	0.34	0.02	1.07	0.94	1.03	1.00
3.0	4.8	4	4.2	0	1.28	1.52	0.13	0.27	0.24	0.02	1.19	0.82	1.06	0.94
3.0	5.0	4	4.5	0	0.30	1.50	0.00	0.19	0.18	0.02	1.19	0.79	1.06	0.93
3.0	5.2	4	4.3	0	0.80	1.52	0.04	0.32	0.28	0.02	1.17	0.82	1.06	0.93
3.0	5.4	4	4.6	0	0.18	1.54	0.00	0.25	0.22	0.02	1.20	0.80	1.06	0.93
3.0	5.6	4	4.7	0	0.11	1.58	0.00	0.27	0.24	0.02	1.20	0.80	1.06	0.93
3.0	5.8	4	4.5	0	0.30	1.50	0.00	0.38	0.33	0.02	1.17	0.83	1.06	0.94
3.0	6.0	4	4.8	0	0.07	1.63	0.00	0.33	0.29	0.03	1.18	0.83	1.06	0.95
3.0	6.2	3	4.9	0	0.09	1.53	0.01	0.41	0.34	0.02	1.13	0.87	1.05	0.96
3.0	6.4	4	4.8	0	0.07	1.63	0.00	0.43	0.37	0.02	1.11	0.89	1.06	0.96
3.5	4.8	3	4.2	1	2.58	1.42	0.37	0.31	0.27	0.02	1.18	0.84	1.04	0.95
3.5	5.0	4	4.5	0	0.30	1.50	0.00	0.19	0.17	0.03	1.23	0.80	1.04	0.92
3.5	5.2	3	4.6	0	0.41	1.50	0.17	0.25	0.23	0.02	1.22	0.79	1.06	0.94
3.5	5.4	4	4.4	0	0.49	1.50	0.00	0.31	0.27	0.02	1.18	0.82	1.05	0.93
3.5	5.6	3	4.7	0	0.25	1.52	0.12	0.32	0.28	0.02	1.22	0.80	1.06	0.93
3.5	5.8	3	4.8	0	0.15	1.53	0.06	0.34	0.30	0.02	1.21	0.79	1.07	0.93
3.5	6.0	4	4.8	0	0.07	1.63	0.00	0.33	0.29	0.02	1.20	0.79	1.07	0.93
3.5	6.2	3	4.9	0	0.09	1.53	0.01	0.43	0.35	0.03	1.16	0.86	1.07	0.93
3.5	6.4	4	4.8	0	0.07	1.63	0.00	0.44	0.37	0.02	1.14	0.85	1.06	0.96
4.0	4.8	3	4.2	1	2.58	1.42	0.37	0.32	0.28	0.02	1.17	0.85	1.06	0.93
4.0	5.0	3	4.5	0	0.66	1.49	0.22	0.25	0.22	0.02	1.20	0.82	1.07	0.92
4.0	5.2	3	4.6	0	0.41	1.50	0.17	0.26	0.23	0.02	1.22	0.81	1.07	0.92
4.0	5.4	3	4.6	0	0.41	1.50	0.17	0.31	0.28	0.02	1.21	0.82	1.07	0.92
4.0	5.6	3	4.7	0	0.25	1.52	0.12	0.33	0.29	0.02	1.21	0.81	1.08	0.92
4.0	5.8	3	4.7	0	0.25	1.52	0.12	0.38	0.33	0.02	1.19	0.82	1.08	0.92
4.0	6.0	3	4.9	0	0.09	1.53	0.01	0.36	0.32	0.02	1.19	0.81	1.12	0.88
4.0	6.2	3	4.9	0	0.09	1.53	0.01	0.41	0.36	0.02	1.14	0.84	1.12	0.90
4.0	6.4	4	4.8	0	0.07	1.63	0.00	0.41	0.36	0.02	1.09	0.86	1.11	0.91

Table C.12: Optimal signal regions for CHARYBDIS2 rotating black hole with no graviton emission (BH2) samples with number of extra dimensions $n = 6$.

M_D TeV	M_{th} [TeV]	$N_{Jet} \geq X$	H_T^{min} [TeV]	Obs	BG Events	δ BG Events		FID	A	Stat Events	JES Events		JER Event	
1.5	5.5	3	4.7	0	0.25	1.52	0.12	0.28	0.25	0.02	1.19	0.81	1.07	0.92
1.5	6.0	3	4.8	0	0.15	1.53	0.06	0.36	0.32	0.02	1.19	0.84	1.06	0.94
2.0	5.5	3	4.8	0	0.15	1.53	0.06	0.28	0.25	0.02	1.22	0.78	1.08	0.92
2.0	6.0	3	4.9	0	0.09	1.53	0.01	0.35	0.31	0.02	1.19	0.82	1.05	0.94
2.5	5.0	3	4.9	0	0.09	1.53	0.01	0.13	0.12	0.02	1.32	0.68	1.12	0.85
2.5	5.5	3	4.7	0	0.25	1.52	0.12	0.26	0.24	0.02	1.24	0.77	1.09	0.90
2.5	6.0	3	4.9	0	0.09	1.53	0.01	0.30	0.27	0.04	1.25	0.76	1.18	0.79
3.0	5.0	3	4.5	0	0.66	1.49	0.22	0.18	0.17	0.03	1.28	0.74	1.08	0.93
3.0	5.5	3	4.8	0	0.15	1.53	0.06	0.21	0.19	0.03	1.30	0.74	1.05	0.94
3.5	4.5	3	4.2	1	2.58	1.42	0.37	0.16	0.15	0.02	1.29	0.73	1.05	0.93
3.5	5.0	3	4.7	0	0.25	1.52	0.12	0.13	0.12	0.02	1.31	0.72	1.06	0.91
3.5	5.5	3	4.7	0	0.25	1.52	0.12	0.19	0.18	0.04	1.29	0.73	1.08	0.92
4.0	4.5	3	4.4	0	1.04	1.47	0.27	0.11	0.10	0.02	1.31	0.70	1.08	0.90
4.0	5.0	3	4.6	0	0.41	1.50	0.17	0.13	0.12	0.03	1.32	0.74	1.08	0.92
4.0	5.5	3	4.9	0	0.09	1.53	0.01	0.14	0.13	0.02	1.31	0.70	1.07	0.91

Table C.13: Optimal signal regions for CHARYBDIS2 rotating black hole with low-mass remnant (BH6) samples with number of extra dimensions $n = 2$.

M_D TeV	M_{th} [TeV]	$N_{Jet} \geq X$	H_T^{min} [TeV]	Obs	BG Events	δ BG Events		FID	A	Stat Events	JES Events		JER Event	
1.5	5.0	5	4.0	1	1.52	1.55	0.33	0.29	0.25	0.02	1.16	0.85	1.06	0.93
1.5	5.5	5	4.4	0	0.22	1.72	0.00	0.28	0.24	0.02	1.16	0.84	1.07	0.92
1.5	6.0	5	4.4	0	0.22	1.72	0.00	0.41	0.35	0.02	1.16	0.85	1.06	0.93
1.5	6.5	5	4.9	0	0.02	1.95	0.00	0.28	0.28	0.01	1.12	0.86	1.06	0.95
2.0	5.0	4	4.4	0	0.49	1.50	0.00	0.19	0.17	0.02	1.21	0.80	1.04	0.95
2.0	5.5	4	4.5	0	0.30	1.50	0.00	0.27	0.23	0.02	1.20	0.83	1.06	0.94
2.0	6.0	4	4.9	0	0.04	1.67	0.00	0.28	0.24	0.03	1.20	0.80	1.12	0.89
2.5	5.0	3	4.6	0	0.41	1.50	0.17	0.20	0.18	0.02	1.21	0.78	1.07	0.94
2.5	5.5	3	4.7	0	0.25	1.52	0.12	0.29	0.26	0.02	1.20	0.81	1.06	0.93
2.5	6.0	3	4.9	0	0.09	1.53	0.01	0.34	0.30	0.02	1.21	0.82	1.06	0.93
3.0	4.5	4	4.2	0	1.28	1.52	0.13	0.15	0.14	0.02	1.21	0.78	1.09	0.90
3.0	5.0	3	4.5	0	0.66	1.49	0.22	0.25	0.23	0.02	1.20	0.78	1.06	0.94
3.0	5.5	3	4.8	0	0.15	1.53	0.06	0.28	0.25	0.02	1.24	0.77	1.07	0.92
3.0	6.0	3	4.9	0	0.09	1.53	0.01	0.37	0.33	0.02	1.20	0.81	1.05	0.94
3.5	4.5	3	4.1	2	4.02	1.40	0.42	0.24	0.21	0.02	1.19	0.80	1.06	0.92
3.5	5.0	3	4.5	0	0.66	1.49	0.22	0.25	0.23	0.02	1.21	0.79	1.08	0.91
3.5	5.5	3	4.8	0	0.15	1.53	0.06	0.28	0.24	0.02	1.23	0.79	1.08	0.93
3.5	6.0	3	4.9	0	0.09	1.53	0.01	0.31	0.31	0.02	1.07	0.88	1.04	0.99
4.0	4.5	3	4.3	0	1.65	1.45	0.32	0.14	0.12	0.03	1.28	0.75	1.04	0.95
4.0	5.0	3	4.6	0	0.41	1.50	0.17	0.18	0.17	0.02	1.28	0.77	1.09	0.92
4.0	5.5	3	4.8	0	0.15	1.53	0.06	0.28	0.25	0.02	1.23	0.77	1.06	0.94
4.0	6.0	3	4.9	0	0.09	1.53	0.01	0.31	0.31	0.01	1.05	0.90	1.07	0.95

Table C.14: Optimal signal regions for CHARYBDIS2 rotating black hole with low-mass remnant (BH6) samples with number of extra dimensions $n = 4$.

M_D TeV	M_{th} [TeV]	$N_{Jet} \geq X$	H_T^{min} [TeV]	Obs	BG Events	δ BG Events		FID	A	Stat Events	JES Events		JER Event	
1.5	5.0	7	3.8	0	0.56	2.55	0.21	0.26	0.22	0.03	1.16	0.85	1.07	0.90
1.5	5.5	7	4.1	0	0.13	3.20	0.00	0.29	0.24	0.03	1.14	0.87	1.05	0.93
1.5	6.0	7	4.3	0	0.05	3.75	0.00	0.34	0.29	0.02	1.15	0.85	1.07	0.90
1.5	6.5	7	4.5	0	0.02	4.42	0.00	0.31	0.31	0.01	1.11	0.88	1.02	0.95
2.0	5.0	5	4.0	1	1.52	1.55	0.33	0.29	0.25	0.03	1.16	0.87	1.06	0.92
2.0	5.5	5	4.4	0	0.22	1.72	0.00	0.29	0.25	0.02	1.14	0.85	1.05	0.94
2.0	6.0	5	4.6	0	0.08	1.81	0.00	0.34	0.30	0.02	1.18	0.83	1.06	0.94
2.0	6.5	5	4.6	0	0.08	1.81	0.00	0.40	0.40	0.02	1.11	0.89	1.03	0.98
2.5	5.0	4	4.3	0	0.80	1.52	0.04	0.24	0.21	0.02	1.20	0.83	1.06	0.95
2.5	5.5	4	4.6	0	0.18	1.54	0.00	0.27	0.24	0.02	1.19	0.84	1.07	0.93
2.5	6.0	4	4.7	0	0.11	1.58	0.00	0.35	0.31	0.03	1.17	0.84	1.06	0.92
3.0	5.0	4	4.3	0	0.80	1.52	0.04	0.24	0.21	0.02	1.18	0.83	1.07	0.92
3.0	5.5	3	4.8	0	0.15	1.53	0.06	0.27	0.24	0.02	1.20	0.81	1.08	0.92
3.0	6.0	3	4.9	0	0.09	1.53	0.01	0.36	0.31	0.02	1.18	0.83	1.07	0.94
3.5	5.0	3	4.4	0	1.04	1.47	0.27	0.30	0.27	0.02	1.19	0.83	1.07	0.93
3.5	5.5	3	4.8	0	0.15	1.53	0.06	0.29	0.26	0.02	1.20	0.80	1.08	0.92
3.5	6.0	3	4.9	0	0.09	1.53	0.01	0.37	0.33	0.02	1.18	0.81	1.07	0.94
4.0	5.0	3	4.5	0	0.66	1.49	0.22	0.24	0.22	0.02	1.24	0.78	1.14	0.90
4.0	5.5	3	4.8	0	0.15	1.53	0.06	0.27	0.24	0.02	1.21	0.80	1.05	0.96
4.0	6.0	3	4.8	0	0.15	1.53	0.06	0.40	0.36	0.02	1.17	0.84	1.16	0.80

Table C.15: Optimal signal regions for `CHARYBDIS2` rotating black hole with low-mass remnant (BH6) samples with number of extra dimensions $n = 6$.

M_D TeV	M_{th} [TeV]	$N_{Jet} \geq X$	H_T^{min} [TeV]	Obs	BG Events	δ BG Events		FID	A	Stat Events	JES Events		JER Event	
1.5	5.0	4	4.4	0	0.49	1.50	0.00	0.19	0.17	0.02	1.20	0.81	1.07	0.93
1.5	5.5	4	4.5	0	0.30	1.50	0.00	0.27	0.24	0.02	1.17	0.84	1.05	0.93
1.5	6.0	4	4.8	0	0.07	1.63	0.00	0.29	0.24	0.02	1.19	0.82	1.16	0.87
2.0	5.0	3	4.6	0	0.41	1.50	0.17	0.18	0.16	0.02	1.23	0.78	1.07	0.92
2.0	5.5	3	4.6	0	0.41	1.50	0.17	0.32	0.28	0.02	1.20	0.82	1.07	0.94
2.5	4.5	4	4.2	0	1.28	1.52	0.13	0.15	0.13	0.03	1.23	0.81	1.08	0.91
2.5	5.0	3	4.6	0	0.41	1.50	0.17	0.19	0.17	0.02	1.23	0.80	1.07	0.93
2.5	5.5	3	4.8	0	0.15	1.53	0.06	0.26	0.23	0.02	1.22	0.79	1.05	0.94
3.0	4.5	3	4.2	1	2.58	1.42	0.37	0.22	0.21	0.02	1.23	0.78	1.08	0.90
3.0	5.0	3	4.5	0	0.66	1.49	0.22	0.24	0.22	0.02	1.22	0.78	1.07	0.93
3.0	5.2	3	4.7	0	0.25	1.52	0.12	0.19	0.17	0.03	1.30	0.74	1.09	0.91
3.0	5.4	3	4.7	0	0.25	1.52	0.12	0.20	0.18	0.04	1.30	0.73	1.12	0.90
3.0	5.6	3	4.7	0	0.25	1.52	0.12	0.22	0.19	0.07	1.38	0.69	1.09	0.92
3.5	4.5	3	4.2	1	2.58	1.42	0.37	0.23	0.21	0.02	1.22	0.79	1.06	0.95
3.5	5.0	3	4.7	0	0.25	1.52	0.12	0.19	0.17	0.02	1.28	0.74	1.10	0.90
4.0	4.5	3	4.2	1	2.58	1.42	0.37	0.22	0.20	0.02	1.27	0.75	1.06	0.94
4.0	5.0	3	4.7	0	0.25	1.52	0.12	0.19	0.18	0.02	1.28	0.72	1.08	0.93

Table C.16: Optimal signal regions for `CHARYBDIS2` rotating black hole with initial-state emission (BH4) samples with number of extra dimensions $n = 2$.

M_D TeV	M_{th} [TeV]	$N_{Jet} \geq X$	H_T^{min} [TeV]	Obs	BG Events	δ BG Events		FID	A	Stat Events	JES Events		JER Event	
1.5	5.0	5	4.3	0	0.36	1.67	0.08	0.20	0.17	0.02	1.18	0.82	1.07	0.94
1.5	5.5	6	4.5	0	0.06	2.80	0.00	0.19	0.17	0.02	1.18	0.80	1.06	0.91
1.5	6.0	6	4.4	0	0.10	2.63	0.00	0.35	0.29	0.03	1.15	0.86	1.12	0.84
2.0	4.5	4	4.0	1	3.22	1.51	0.30	0.21	0.19	0.02	1.17	0.82	1.07	0.93
2.0	5.0	4	4.3	0	0.80	1.52	0.04	0.24	0.21	0.02	1.17	0.83	1.06	0.92
2.0	5.5	4	4.4	0	0.49	1.50	0.00	0.32	0.28	0.02	1.18	0.84	1.05	0.93
2.5	4.5	3	4.1	2	4.02	1.40	0.42	0.23	0.21	0.02	1.18	0.81	1.06	0.93
2.5	5.0	4	4.4	0	0.49	1.50	0.00	0.19	0.17	0.02	1.21	0.80	1.07	0.91
2.5	5.5	4	4.6	0	0.18	1.54	0.00	0.27	0.24	0.02	1.17	0.82	1.05	0.95
3.0	4.5	4	4.2	0	1.28	1.52	0.13	0.15	0.13	0.03	1.22	0.79	1.07	0.91
3.0	5.5	3	4.8	0	0.15	1.53	0.06	0.26	0.23	0.02	1.20	0.80	1.12	0.85
3.5	4.5	3	4.1	2	4.02	1.40	0.42	0.24	0.22	0.02	1.21	0.82	1.06	0.95
3.5	5.0	3	4.5	0	0.66	1.49	0.22	0.24	0.22	0.02	1.21	0.79	1.06	0.93
3.5	5.2	3	4.4	0	1.04	1.47	0.27	0.29	0.26	0.02	1.20	0.81	1.05	0.95
3.5	5.4	3	4.7	0	0.25	1.52	0.12	0.20	0.18	0.03	1.33	0.70	1.09	0.90
3.5	5.6	3	4.7	0	0.25	1.52	0.12	0.22	0.20	0.01	1.38	0.66	1.09	0.89
4.0	4.5	4	4.2	0	1.28	1.52	0.13	0.15	0.14	0.03	1.21	0.80	1.07	0.94
4.0	5.0	3	4.5	0	0.66	1.49	0.22	0.25	0.23	0.02	1.21	0.80	1.08	0.90
4.0	5.2	3	4.7	0	0.25	1.52	0.12	0.19	0.18	0.03	1.33	0.74	1.33	0.74
4.0	5.4	3	4.6	0	0.41	1.50	0.17	0.25	0.23	0.03	1.26	0.75	1.26	0.75
4.0	5.6	3	4.8	0	0.15	1.53	0.06	0.20	0.18	0.06	1.39	0.67	1.39	0.67

Table C.17: Optimal signal regions for CHARYBDIS2 rotating black hole with initial-state emission (BH4) samples with number of extra dimensions $n = 4$.

M_D TeV	M_{th} [TeV]	$N_{Jet} \geq X$	H_T^{min} [TeV]	Obs	BG Events	δ BG Events		FID	A	Stat Events	JES Events		JER Event	
1.5	5.0	7	4.0	0	0.22	2.96	0.07	0.20	0.17	0.02	1.17	0.83	1.06	0.93
1.5	5.5	7	4.1	0	0.13	3.20	0.00	0.30	0.25	0.02	1.14	0.85	1.07	0.91
1.5	6.0	7	4.3	0	0.05	3.75	0.00	0.36	0.30	0.02	1.14	0.86	1.10	0.89
2.0	5.0	5	4.3	0	0.36	1.67	0.08	0.20	0.17	0.02	1.20	0.82	1.07	0.91
2.0	5.5	5	4.5	0	0.13	1.77	0.00	0.27	0.23	0.02	1.16	0.85	1.06	0.93
2.0	6.0	5	4.6	0	0.08	1.81	0.00	0.35	0.30	0.02	1.18	0.85	1.19	0.86
2.5	5.5	4	4.6	0	0.18	1.54	0.00	0.28	0.24	0.02	1.18	0.84	1.06	0.94
2.5	6.0	4	4.7	0	0.11	1.58	0.00	0.35	0.31	0.02	1.18	0.81	1.15	0.81
3.0	5.0	4	4.3	0	0.80	1.52	0.04	0.25	0.22	0.02	1.20	0.81	1.06	0.93
3.0	5.5	4	4.6	0	0.18	1.54	0.00	0.26	0.23	0.03	1.18	0.82	1.07	0.93
3.0	6.0	3	4.9	0	0.09	1.53	0.01	0.34	0.29	0.02	1.19	0.81	1.05	0.95
3.5	4.5	3	4.1	2	4.02	1.40	0.42	0.24	0.22	0.02	1.20	0.82	1.07	0.94
3.5	5.0	4	4.3	0	0.80	1.52	0.04	0.24	0.21	0.02	1.18	0.82	1.07	0.92
3.5	5.5	3	4.6	0	0.41	1.50	0.17	0.32	0.29	0.02	1.19	0.82	1.06	0.95
4.0	4.5	4	4.1	0	2.03	1.52	0.21	0.19	0.17	0.03	1.21	0.82	1.05	0.94
4.0	5.0	3	4.5	0	0.66	1.49	0.22	0.24	0.22	0.02	1.20	0.79	1.07	0.94
4.0	5.2	3	4.4	0	1.04	1.47	0.27	0.30	0.27	0.03	1.29	0.75	1.12	0.89
4.0	5.4	3	4.6	0	0.41	1.50	0.17	0.25	0.23	0.04	1.39	0.66	1.16	0.87
4.0	5.6	3	4.5	0	0.66	1.49	0.22	0.31	0.28	0.05	1.51	0.51	1.20	0.80

Table C.18: Optimal signal regions for CHARYBDIS2 rotating black hole with initial-state emission (BH4) samples with number of extra dimensions $n = 6$.

M_D	M_{th}	$N_{Jet} \geq X$	H_T^{min}	Obs	BG	δ BG		FID	A	Stat	JES		JER	
TeV	[TeV]		[TeV]		Events	Events				Events	Events		Event	
0.8	5.0	8	3.5	0	0.73	2.48	0.25	0.41	0.32	0.02	1.12	0.89	1.05	0.94
0.8	5.5	8	3.6	0	0.45	2.68	0.19	0.52	0.42	0.02	1.11	0.89	1.05	0.95
0.8	6.0	8	3.9	0	0.11	3.45	0.02	0.54	0.43	0.00	1.21	0.81	1.08	0.92
0.8	6.5	8	3.7	0	0.28	2.91	0.14	0.76	0.59	0.01	1.22	0.79	1.09	0.91
0.8	7.0	8	3.6	0	0.45	2.68	0.19	0.88	0.68	0.01	1.28	0.77	1.10	0.91
1.0	5.0	8	3.6	0	0.45	2.68	0.19	0.32	0.26	0.03	1.14	0.87	1.05	0.94
1.0	5.5	8	3.9	0	0.11	3.45	0.02	0.39	0.31	0.02	1.11	0.88	1.06	0.95
1.0	5.0	8	3.6	0	0.45	2.68	0.19	0.33	0.27	0.03	1.11	0.88	1.04	0.95
1.0	5.5	8	3.9	0	0.11	3.45	0.02	0.40	0.33	0.02	1.13	0.87	1.05	0.94
1.0	6.0	8	4.1	0	0.04	4.13	0.00	0.47	0.38	0.02	1.16	0.84	1.07	0.93
1.0	6.5	8	3.8	0	0.17	3.17	0.08	0.66	0.53	0.01	1.14	0.86	1.06	0.94
1.0	7.0	8	3.7	0	0.28	2.91	0.14	0.80	0.64	0.00	1.15	0.85	1.06	0.94
1.2	4.5	7	3.4	1	3.56	1.93	0.45	0.26	0.22	0.03	1.13	0.87	1.05	0.94
1.2	5.0	8	3.6	0	0.45	2.68	0.19	0.25	0.21	0.03	1.13	0.86	1.05	0.93
1.2	5.5	8	3.9	0	0.11	3.45	0.02	0.28	0.23	0.03	1.14	0.86	1.05	0.93
1.2	6.0	8	4.1	0	0.04	4.13	0.00	0.34	0.28	0.03	1.14	0.85	1.06	0.93
1.4	4.5	8	3.6	0	0.45	2.68	0.19	0.12	0.10	0.04	1.18	0.82	1.06	0.91
1.4	5.0	7	3.9	0	0.35	2.75	0.14	0.19	0.16	0.03	1.16	0.84	1.06	0.93
1.4	5.5	8	4.0	0	0.06	3.77	0.00	0.21	0.17	0.04	1.17	0.83	1.06	0.92
1.6	4.5	7	3.6	1	1.44	2.21	0.34	0.14	0.12	0.03	1.18	0.83	1.06	0.92
1.6	5.0	6	3.9	0	1.09	1.97	0.31	0.23	0.19	0.03	1.17	0.85	1.06	0.93
1.6	5.5	7	3.9	0	0.35	2.75	0.14	0.27	0.23	0.03	1.17	0.84	1.06	0.93
1.8	4.5	6	3.7	2	2.72	1.77	0.45	0.16	0.14	0.03	1.17	0.84	1.06	0.93
1.8	5.0	7	4.0	0	0.22	2.96	0.07	0.13	0.11	0.04	1.21	0.80	1.07	0.91
1.8	5.5	6	4.3	0	0.16	2.48	0.00	0.20	0.18	0.04	1.22	0.80	1.07	0.91
1.8	6.0	5	4.6	0	0.08	1.81	0.00	0.26	0.24	0.03	1.27	0.76	1.10	0.90
2.0	4.5	6	3.7	2	2.72	1.77	0.45	0.15	0.13	0.03	1.18	0.83	1.07	0.92
2.0	5.0	5	4.0	1	1.52	1.55	0.33	0.23	0.20	0.03	1.18	0.84	1.07	0.93
2.0	5.5	4	4.4	0	0.49	1.50	0.00	0.25	0.23	0.03	1.23	0.80	1.09	0.92
2.0	6.0	6	4.6	0	0.03	2.98	0.00	0.20	0.18	0.04	1.30	0.73	1.11	0.89
2.5	4.5	4	3.9	3	5.05	1.49	0.38	0.19	0.17	0.02	1.17	0.82	1.07	0.93
2.5	5.0	4	4.3	0	0.80	1.52	0.04	0.18	0.16	0.03	1.20	0.83	1.09	0.94
2.5	5.5	4	4.4	0	0.49	1.50	0.00	0.25	0.23	0.03	1.25	0.78	1.09	0.91
3.0	3.5	3	3.4	87	77.61	1.28	0.72	0.19	0.17	0.02	1.14	0.87	1.05	0.94
3.0	4.0	4	3.7	15	12.24	1.44	0.53	0.14	0.13	0.02	1.17	0.85	1.06	0.94
3.0	4.5	3	4.1	2	4.02	1.40	0.42	0.16	0.15	0.02	1.20	0.82	1.07	0.93
3.0	5.0	4	4.3	0	0.80	1.52	0.04	0.18	0.16	0.03	1.26	0.77	1.10	0.91
3.0	5.5	3	4.7	0	0.25	1.52	0.12	0.19	0.18	0.03	1.41	0.68	1.14	0.87
3.0	6.0	4	4.9	0	0.04	1.67	0.00	0.20	0.20	0.05	1.55	0.60	1.18	0.86

Table C.19: Optimal signal regions for `CHARYBDIS2` non-rotating string ball with no graviton emission (SB1) samples with number of extra dimensions $n = 6$.

M_D TeV	M_{th} [TeV]	$N_{Jet} \geq X$	H_T^{min} [TeV]	Obs	BG Events	δ BG Events		FID	A	Stat Events	JES Events		JER Event	
0.8	5.0	8	3.7	0	0.28	2.91	0.14	0.33	0.27	0.02	1.14	0.88	1.06	0.94
0.8	5.5	8	3.9	0	0.11	3.45	0.02	0.41	0.33	0.02	1.13	0.88	1.07	0.94
0.8	6.0	8	4.1	0	0.04	4.13	0.00	0.47	0.37	0.00	1.30	0.78	1.11	0.91
0.8	6.5	8	3.7	0	0.28	2.91	0.14	0.73	0.59	0.01	1.27	0.78	1.09	0.91
0.8	7.0	8	3.7	0	0.28	2.91	0.14	0.82	0.66	0.02	1.35	0.72	1.11	0.90
1.0	5.5	8	4.0	0	0.06	3.77	0.00	0.36	0.30	0.02	1.13	0.87	1.06	0.93
1.0	4.5	8	3.6	0	0.45	2.68	0.19	0.19	0.16	0.04	1.13	0.87	1.05	0.93
1.0	5.5	8	4.0	0	0.06	3.77	0.00	0.36	0.30	0.02	1.13	0.87	1.06	0.93
1.0	6.0	8	4.3	0	0.01	4.95	0.00	0.40	0.33	0.03	1.18	0.84	1.09	0.92
1.2	5.0	8	3.8	0	0.17	3.17	0.08	0.20	0.17	0.03	1.17	0.81	1.07	0.92
1.2	5.5	7	4.2	0	0.08	3.46	0.00	0.28	0.23	0.02	1.16	0.87	1.09	0.93
1.2	4.5	8	3.7	0	0.28	2.91	0.14	0.12	0.10	0.04	1.17	0.84	1.06	0.92
1.2	6.0	8	4.1	0	0.04	4.13	0.00	0.40	0.33	0.03	1.14	0.86	1.07	0.93
1.4	5.0	5	4.2	0	0.59	1.63	0.16	0.25	0.21	0.02	1.17	0.85	1.09	0.93
1.4	5.5	6	4.2	0	0.26	2.33	0.04	0.32	0.27	0.02	1.14	0.85	1.04	0.93
1.4	4.5	6	3.8	0	1.73	1.87	0.39	0.20	0.17	0.03	1.15	0.85	1.05	0.94
1.4	5.0	5	4.2	0	0.59	1.63	0.16	0.25	0.21	0.02	1.16	0.85	1.07	0.93
1.4	5.5	6	4.2	0	0.26	2.33	0.04	0.33	0.28	0.03	1.16	0.85	1.06	0.94
1.4	6.0	7	4.3	0	0.05	3.75	0.00	0.34	0.29	0.03	1.17	0.84	1.06	0.94
1.6	4.5	6	3.7	2	2.72	1.77	0.45	0.22	0.19	0.03	1.16	0.85	1.05	0.93
1.6	5.0	5	4.2	0	0.59	1.63	0.16	0.25	0.21	0.02	1.17	0.84	1.07	0.93
1.6	5.5	5	4.5	0	0.13	1.77	0.00	0.28	0.24	0.03	1.20	0.81	1.08	0.92
1.6	6.0	5	4.7	0	0.05	1.86	0.00	0.34	0.30	0.03	1.25	0.77	1.10	0.91
1.8	4.5	4	4.1	0	2.03	1.52	0.21	0.19	0.16	0.02	1.16	0.85	1.06	0.94
1.8	5.0	4	4.2	0	1.28	1.52	0.13	0.30	0.26	0.02	1.17	0.84	1.06	0.94
1.8	5.5	5	4.5	0	0.13	1.77	0.00	0.27	0.24	0.03	1.22	0.80	1.08	0.92
1.8	6.0	4	4.8	0	0.07	1.63	0.00	0.34	0.31	0.03	1.31	0.74	1.10	0.90
2.0	4.5	5	3.8	4	3.83	1.49	0.48	0.24	0.21	0.02	1.16	0.85	1.06	0.93
2.0	5.0	4	4.2	0	1.28	1.52	0.13	0.29	0.25	0.02	1.17	0.84	1.06	0.93
2.0	5.5	4	4.6	0	0.18	1.54	0.00	0.28	0.25	0.03	1.25	0.78	1.08	0.91
2.0	6.0	4	4.8	0	0.07	1.63	0.00	0.34	0.31	0.03	1.32	0.73	1.10	0.89
2.5	4.5	4	4.1	0	2.03	1.52	0.21	0.20	0.18	0.02	1.18	0.83	1.05	0.93
2.5	5.0	4	4.5	0	0.30	1.50	0.00	0.19	0.16	0.03	1.22	0.81	1.08	0.93
2.5	5.5	3	4.8	0	0.15	1.53	0.06	0.27	0.25	0.03	1.37	0.69	1.11	0.89
3.0	4.0	3	3.8	17	14.69	1.36	0.55	0.24	0.21	0.02	1.17	0.85	1.06	0.94
3.0	4.5	3	4.2	1	2.58	1.42	0.37	0.22	0.20	0.02	1.20	0.81	1.07	0.93
3.0	5.0	3	4.4	0	1.04	1.47	0.27	0.29	0.27	0.02	1.24	0.78	1.08	0.92
3.0	5.5	3	4.8	0	0.15	1.53	0.06	0.28	0.27	0.03	1.41	0.67	1.12	0.89
3.0	6.0	3	4.8	0	0.15	1.53	0.06	0.40	0.38	0.03	1.39	0.68	1.12	0.89

Table C.20: Optimal signal regions for CHARYBDIS2 rotating string ball with no graviton emission (SB2) samples with number of extra dimensions $n = 6$.

M_D TeV	M_{th} [TeV]	$N_{Jet} \geq X$	H_T^{min} [TeV]	Obs	BG Events	δ BG Events		FID	A	Stat Events	JES Events		JER Event	
1.5	5.0	8	3.7	0	0.28	2.91	0.14	0.28	0.23	0.02	1.17	0.84	1.08	0.92
1.5	5.5	8	3.9	0	0.11	3.45	0.02	0.34	0.29	0.01	1.23	0.80	1.10	0.90
1.5	6.0	8	4.1	0	0.04	4.13	0.00	0.42	0.34	0.00	1.30	0.67	1.16	0.85
2.5	4.5	6	3.6	3	4.27	1.69	0.50	0.24	0.20	0.03	1.17	0.86	1.06	0.92
2.5	5.5	5	4.4	0	0.22	1.72	0.00	0.27	0.24	0.03	1.28	0.79	1.10	0.90
2.5	6.0	5	4.7	0	0.05	1.86	0.00	0.28	0.27	0.04	1.37	0.68	1.11	0.85
2.0	5.0	7	3.8	0	0.56	2.55	0.21	0.21	0.21	0.03	1.15	0.86	1.05	0.94
2.0	5.5	7	4.1	0	0.13	3.20	0.00	0.28	0.23	0.03	1.18	0.84	1.07	0.93
2.0	6.0	7	4.3	0	0.05	3.75	0.00	0.33	0.29	0.03	1.21	0.79	1.08	0.92
3.0	4.5	4	4.0	1	3.22	1.51	0.30	0.21	0.19	0.02	1.18	0.83	1.07	0.92
3.0	5.5	5	4.4	0	0.22	1.72	0.00	0.26	0.24	0.03	1.31	0.76	1.11	0.89
3.0	6.0	5	4.7	0	0.05	1.86	0.00	0.28	0.26	0.05	1.42	0.65	1.14	0.83
3.5	4.5	4	4.0	1	3.22	1.51	0.30	0.20	0.18	0.02	1.19	0.82	1.08	0.92
3.5	5.5	4	4.4	0	0.49	1.50	0.00	0.32	0.29	0.03	1.33	0.74	1.12	0.88
3.5	6.0	4	4.7	0	0.11	1.58	0.00	0.34	0.31	0.04	1.47	0.63	1.16	0.82
4.0	4.5	4	4.0	1	3.22	1.51	0.30	0.20	0.19	0.02	1.21	0.81	1.09	0.92
4.0	5.5	4	4.4	0	0.49	1.50	0.00	0.32	0.29	0.03	1.35	0.72	1.13	0.87
4.0	6.0	4	4.7	0	0.11	1.58	0.00	0.33	0.30	0.05	1.51	0.62	1.20	0.82

Table C.21: Optimal signal regions for `BlackMax` non-rotating black hole with no graviton emission (BH1) samples with number of extra dimensions $n = 2$.

M_D TeV	M_{th} [TeV]	$N_{Jet} \geq X$	H_T^{min} [TeV]	Obs	BG Events	δ BG Events		FID	A	Stat Events	JES Events		JER Event	
1.5	5.0	8	3.7	0	0.28	2.91	0.14	0.27	0.21	0.02	1.17	0.86	1.06	0.94
1.5	5.5	8	3.8	0	0.17	3.17	0.08	0.41	0.34	0.01	1.23	0.82	1.07	0.92
1.5	6.0	8	4.0	0	0.06	3.77	0.00	0.48	0.38	0.01	1.37	0.74	1.13	0.90
1.5	6.5	8	3.8	0	0.17	3.17	0.08	0.67	0.54	0.00	1.38	0.70	1.11	0.89
2.0	5.0	7	3.9	0	0.35	2.75	0.14	0.19	0.18	0.03	1.15	0.85	1.06	0.94
2.0	5.5	7	4.0	0	0.22	2.96	0.07	0.33	0.28	0.03	1.16	0.84	1.07	0.94
2.0	6.0	8	4.3	0	0.01	4.95	0.00	0.28	0.24	0.04	1.23	0.80	1.08	0.91
2.5	5.0	5	4.1	0	0.95	1.58	0.25	0.22	0.20	0.03	1.16	0.85	1.07	0.94
2.5	5.5	5	4.4	0	0.22	1.72	0.00	0.28	0.25	0.03	1.20	0.80	1.09	0.91
2.5	6.0	6	4.4	0	0.10	2.63	0.00	0.34	0.30	0.03	1.22	0.80	1.08	0.92
3.0	5.0	5	4.1	0	0.95	1.58	0.25	0.22	0.20	0.03	1.16	0.84	1.06	0.93
3.0	5.5	5	4.4	0	0.22	1.72	0.00	0.27	0.24	0.03	1.19	0.80	1.08	0.91
3.0	6.0	5	4.7	0	0.05	1.86	0.00	0.29	0.27	0.03	1.28	0.71	1.10	0.89
3.5	5.0	4	4.4	0	0.49	1.50	0.00	0.18	0.17	0.02	1.19	0.80	1.08	0.93
3.5	5.5	4	4.4	0	0.49	1.50	0.00	0.32	0.29	0.02	1.19	0.81	1.08	0.93
3.5	6.0	5	4.7	0	0.05	1.86	0.00	0.27	0.25	0.03	1.28	0.72	1.10	0.89
4.0	5.0	4	4.4	0	0.49	1.50	0.00	0.19	0.17	0.02	1.19	0.79	1.08	0.93
4.0	5.5	4	4.4	0	0.49	1.50	0.00	0.32	0.29	0.02	1.19	0.80	1.08	0.93
4.0	6.0	4	4.7	0	0.11	1.58	0.00	0.33	0.32	0.03	1.27	0.74	1.12	0.90

Table C.22: Optimal signal regions for `BlackMax` non-rotating black hole with no graviton emission (BH1) samples with number of extra dimensions $n = 4$.

M_D TeV	M_{th} [TeV]	$N_{Jet} \geq X$	H_T^{min} [TeV]	Obs	BG Events	δ BG Events		FID	A	Stat Events	JES Events		JER Event	
1.5	5.0	8	3.6	0	0.45	2.68	0.19	0.33	0.26	0.02	1.14	0.87	1.05	0.94
1.5	5.5	8	3.8	0	0.17	3.17	0.08	0.40	0.33	0.03	1.19	0.85	1.09	0.93
1.5	6.0	8	4.1	0	0.04	4.13	0.00	0.42	0.34	0.00	1.28	0.74	1.12	0.88
1.5	6.5	8	3.9	0	0.11	3.45	0.02	0.62	0.50	0.01	1.37	0.80	1.22	0.89
2.0	5.0	8	3.8	0	0.17	3.17	0.08	0.18	0.16	0.03	1.15	0.85	1.04	0.93
2.0	5.5	8	3.9	0	0.11	3.45	0.02	0.26	0.22	0.03	1.15	0.84	1.04	0.93
2.0	6.0	8	4.3	0	0.01	4.95	0.00	0.27	0.23	0.04	1.24	0.80	1.06	0.91
2.5	5.0	7	3.9	0	0.35	2.75	0.14	0.17	0.16	0.03	1.17	0.83	1.06	0.92
2.5	5.5	6	4.3	0	0.16	2.48	0.00	0.26	0.23	0.03	1.19	0.82	1.07	0.92
2.5	6.0	6	4.4	0	0.10	2.63	0.00	0.34	0.30	0.03	1.21	0.79	1.08	0.91
3.0	5.0	5	4.0	1	1.52	1.55	0.33	0.27	0.24	0.02	1.16	0.84	1.06	0.94
3.0	5.5	5	4.4	0	0.22	1.72	0.00	0.27	0.24	0.02	1.21	0.80	1.08	0.92
3.0	6.0	4	4.7	0	0.11	1.58	0.00	0.33	0.31	0.03	1.28	0.73	1.11	0.91
3.5	5.0	5	4.1	0	0.95	1.58	0.25	0.24	0.20	0.03	1.18	0.83	1.06	0.93
3.5	5.5	5	4.4	0	0.22	1.72	0.00	0.26	0.23	0.02	1.21	0.79	1.08	0.92
3.5	6.0	4	4.7	0	0.11	1.58	0.00	0.33	0.30	0.03	1.28	0.74	1.10	0.91
4.0	5.0	4	4.3	0	0.80	1.52	0.04	0.24	0.21	0.02	1.18	0.83	1.06	0.94
4.0	5.5	4	4.4	0	0.49	1.50	0.00	0.32	0.29	0.02	1.19	0.82	1.07	0.93
4.0	6.0	4	4.7	0	0.11	1.58	0.00	0.34	0.31	0.03	1.28	0.75	1.10	0.91

Table C.23: Optimal signal regions for `BlackMax` non-rotating black hole with no graviton emission (BH1) samples with number of extra dimensions $n = 6$.

M_D TeV	M_{th} [TeV]	$N_{Jet} \geq X$	H_T^{min} [TeV]	Obs	BG Events	δ BG Events		FID	A	Stat Events	JES Events		JER Event	
1.5	5.0	6	4.0	0	0.68	2.08	0.22	0.24	0.20	0.03	1.19	0.81	1.06	0.92
1.5	6.0	5	4.6	0	0.08	1.81	0.00	0.33	0.28	0.02	1.32	0.64	1.03	0.83
1.5	6.5	7	4.6	0	0.01	4.82	0.00	0.34	0.26	0.01	1.43	0.64	1.04	0.80
2.0	5.0	5	4.3	0	0.36	1.67	0.08	0.19	0.17	0.03	1.21	0.81	1.09	0.91
2.0	5.5	5	4.4	0	0.22	1.72	0.00	0.27	0.24	0.03	1.24	0.79	1.09	0.91
2.0	6.0	4	4.7	0	0.11	1.58	0.00	0.34	0.30	0.03	1.37	0.68	1.13	0.87
2.0	6.5	4	4.8	0	0.07	1.63	0.00	0.41	0.37	0.04	1.41	0.63	1.14	0.85
2.5	4.5	4	4.0	1	3.22	1.51	0.30	0.21	0.18	0.02	1.16	0.82	1.08	0.93
2.5	5.0	5	4.1	0	0.95	1.58	0.25	0.23	0.20	0.03	1.19	0.83	1.08	0.92
2.5	5.5	4	4.4	0	0.49	1.50	0.00	0.31	0.29	0.03	1.24	0.78	1.12	0.91
2.5	6.0	4	4.7	0	0.11	1.58	0.00	0.34	0.32	0.04	1.39	0.68	1.13	0.88
2.5	6.5	4	4.8	0	0.07	1.63	0.00	0.42	0.39	0.04	1.50	0.65	1.18	0.85
3.0	4.5	4	3.9	3	5.05	1.49	0.38	0.26	0.23	0.02	1.15	0.86	1.05	0.93
3.0	5.0	4	4.3	0	0.80	1.52	0.04	0.24	0.22	0.03	1.23	0.78	1.10	0.91
3.0	5.5	4	4.6	0	0.18	1.54	0.00	0.26	0.24	0.03	1.39	0.70	1.14	0.87
3.0	6.0	4	4.7	0	0.11	1.58	0.00	0.33	0.32	0.04	1.42	0.67	1.13	0.88
3.0	6.5	4	4.8	0	0.07	1.63	0.00	0.40	0.39	0.04	1.53	0.65	1.19	0.85
3.5	4.5	3	4.0	4	6.23	1.37	0.46	0.27	0.24	0.02	1.17	0.83	1.07	0.93
3.5	5.0	4	4.3	0	0.80	1.52	0.04	0.24	0.22	0.03	1.24	0.77	1.10	0.90
3.5	5.5	3	4.8	0	0.15	1.53	0.06	0.26	0.25	0.04	1.56	0.63	1.20	0.85
3.5	6.0	3	4.9	0	0.09	1.53	0.01	0.34	0.34	0.04	1.53	0.57	1.21	0.84
3.5	6.5	3	4.8	0	0.15	1.53	0.06	0.48	0.46	0.04	1.54	0.63	1.22	0.84
4.0	4.5	4	4.0	1	3.22	1.51	0.30	0.20	0.18	0.02	1.18	0.81	1.07	0.92
4.0	5.0	3	4.6	0	0.41	1.50	0.17	0.19	0.19	0.03	1.41	0.67	1.14	0.88
4.0	5.5	3	4.6	0	0.41	1.50	0.17	0.32	0.30	0.03	1.40	0.67	1.14	0.87
4.0	6.0	3	4.9	0	0.09	1.53	0.01	0.36	0.36	0.04	1.54	0.56	1.19	0.84
4.0	6.5	3	4.8	0	0.15	1.53	0.06	0.48	0.47	0.04	1.55	0.63	1.21	0.85

Table C.24: Optimal signal regions for `BlackMax` rotating black hole with no graviton emission (BH2) samples with number of extra dimensions $n = 2$.

M_D TeV	M_{th} [TeV]	$N_{Jet} \geq X$	H_T^{min} [TeV]	Obs	BG Events	δ BG Events		FID	A	Stat Events	JES Events		JER Event	
1.5	5.0	7	4.0	0	0.22	2.96	0.07	0.20	0.17	0.02	1.17	0.83	1.06	0.92
1.5	6.0	7	4.5	0	0.02	4.42	0.00	0.27	0.24	0.01	1.55	0.63	1.16	0.80
1.5	6.5	7	4.6	0	0.01	4.82	0.00	0.34	0.30	0.01	1.61	0.69	1.20	0.73
2.0	5.0	7	3.9	0	0.35	2.75	0.14	0.19	0.16	0.03	1.16	0.84	1.06	0.92
2.0	6.0	5	4.6	0	0.08	1.81	0.00	0.34	0.30	0.03	1.25	0.78	1.09	0.91
2.0	6.5	5	4.9	0	0.02	1.95	0.00	0.34	0.35	0.04	1.44	0.63	1.13	0.87
2.5	5.0	5	4.0	1	1.52	1.55	0.33	0.29	0.25	0.02	1.15	0.87	1.05	0.94
2.5	5.5	5	4.4	0	0.22	1.72	0.00	0.27	0.23	0.02	1.20	0.82	1.07	0.92
2.5	6.0	4	4.7	0	0.11	1.58	0.00	0.34	0.31	0.03	1.27	0.75	1.09	0.91
2.5	6.5	5	4.9	0	0.02	1.95	0.00	0.33	0.33	0.04	1.38	0.65	1.12	0.89
3.0	5.0	5	4.1	0	0.95	1.58	0.25	0.23	0.21	0.02	1.18	0.84	1.05	0.93
3.0	5.5	4	4.6	0	0.18	1.54	0.00	0.26	0.23	0.02	1.24	0.78	1.08	0.91
3.0	6.0	4	4.7	0	0.11	1.58	0.00	0.33	0.30	0.03	1.28	0.75	1.10	0.91
3.0	6.5	4	4.8	0	0.07	1.63	0.00	0.42	0.39	0.03	1.31	0.72	1.10	0.90
3.5	5.0	4	4.3	0	0.80	1.52	0.04	0.24	0.21	0.02	1.20	0.82	1.07	0.93
3.5	5.5	4	4.6	0	0.18	1.54	0.00	0.26	0.24	0.02	1.25	0.76	1.09	0.91
3.5	6.0	4	4.7	0	0.11	1.58	0.00	0.34	0.31	0.03	1.30	0.74	1.10	0.90
3.5	6.5	4	4.8	0	0.07	1.63	0.00	0.41	0.38	0.03	1.33	0.71	1.10	0.90
4.0	5.0	4	4.2	0	1.28	1.52	0.13	0.28	0.25	0.02	1.18	0.83	1.06	0.93
4.0	5.5	4	4.6	0	0.18	1.54	0.00	0.26	0.24	0.02	1.26	0.75	1.09	0.90
4.0	6.0	4	4.7	0	0.11	1.58	0.00	0.34	0.30	0.03	1.31	0.74	1.10	0.89
4.0	6.5	4	4.8	0	0.07	1.63	0.00	0.41	0.38	0.03	1.35	0.70	1.11	0.89

Table C.25: Optimal signal regions for `BlackMax` rotating black hole with no graviton emission (BH2) samples with number of extra dimensions $n = 4$.

M_D TeV	M_{th} [TeV]	$N_{Jet} \geq X$	H_T^{min} [TeV]	Obs	BG Events	δ BG Events		FID	A	Stat Events	JES Events		JER Event	
1.5	5.0	8	3.8	0	0.17	3.17	0.08	0.20	0.16	0.02	1.19	0.84	1.04	0.92
1.5	5.5	7	4.1	0	0.13	3.20	0.00	0.29	0.24	0.03	1.22	0.84	1.12	0.90
1.5	6.0	6	4.3	0	0.16	2.48	0.00	0.39	0.35	0.02	1.23	0.79	1.08	0.85
1.5	6.5	7	4.6	0	0.01	4.82	0.00	0.34	0.31	0.02	1.44	0.69	1.30	0.72
2.0	5.0	7	3.9	0	0.35	2.75	0.14	0.19	0.16	0.03	1.15	0.86	1.04	0.94
2.0	5.5	5	4.3	0	0.36	1.67	0.08	0.32	0.28	0.02	1.18	0.82	1.05	0.93
2.0	6.0	5	4.6	0	0.08	1.81	0.00	0.33	0.30	0.03	1.27	0.75	1.09	0.89
2.0	6.5	4	4.9	0	0.04	1.67	0.00	0.41	0.40	0.03	1.42	0.66	1.14	0.86
2.5	5.0	4	4.2	0	1.28	1.52	0.13	0.28	0.25	0.02	1.17	0.84	1.06	0.95
2.5	5.5	5	4.4	0	0.22	1.72	0.00	0.29	0.25	0.03	1.21	0.79	1.06	0.93
2.5	6.0	4	4.7	0	0.11	1.58	0.00	0.35	0.32	0.03	1.31	0.73	1.11	0.90
2.5	6.5	5	4.9	0	0.02	1.95	0.00	0.33	0.32	0.04	1.45	0.67	1.11	0.87
3.0	5.0	4	4.3	0	0.80	1.52	0.04	0.24	0.21	0.02	1.18	0.83	1.07	0.94
3.0	5.5	4	4.6	0	0.18	1.54	0.00	0.26	0.23	0.02	1.27	0.77	1.10	0.92
3.0	6.0	4	4.7	0	0.11	1.58	0.00	0.35	0.32	0.02	1.30	0.73	1.10	0.91
3.0	6.5	4	4.9	0	0.04	1.67	0.00	0.40	0.39	0.03	1.44	0.67	1.12	0.89
3.5	5.0	4	4.2	0	1.28	1.52	0.13	0.28	0.25	0.02	1.17	0.84	1.06	0.94
3.5	5.5	4	4.6	0	0.18	1.54	0.00	0.27	0.24	0.02	1.26	0.77	1.09	0.92
3.5	6.0	4	4.7	0	0.11	1.58	0.00	0.35	0.32	0.02	1.29	0.74	1.10	0.91
3.5	6.5	4	4.8	0	0.07	1.63	0.00	0.43	0.40	0.03	1.36	0.71	1.12	0.90
4.0	5.0	4	4.2	0	1.28	1.52	0.13	0.28	0.25	0.02	1.17	0.84	1.06	0.93
4.0	5.5	4	4.4	0	0.49	1.50	0.00	0.32	0.29	0.02	1.20	0.81	1.07	0.93
4.0	6.5	4	4.8	0	0.07	1.63	0.00	0.41	0.38	0.03	1.35	0.71	1.11	0.90

Table C.26: Optimal signal regions for `BlackMax` rotating black hole with no graviton emission (BH2) samples with number of extra dimensions $n = 6$.

M_D TeV	M_{th} [TeV]	$N_{Jet} \geq X$	H_T^{min} [TeV]	Obs	BG Events	δ BG Events		FID	A	Stat Events	JES Events		JER Event	
1.5	5.0	8	3.7	0	0.28	2.91	0.14	0.26	0.22	0.02	1.13	0.87	1.04	0.94
1.5	5.5	8	3.7	0	0.28	2.91	0.14	0.40	0.34	0.01	1.16	0.87	1.04	0.97
1.5	6.0	8	4.1	0	0.04	4.13	0.00	0.40	0.34	0.02	1.38	0.78	0.98	1.01
1.5	6.5	8	3.9	0	0.11	3.45	0.02	0.60	0.51	0.02	1.45	0.76	1.06	1.03
2.0	4.5	8	3.6	0	0.45	2.68	0.19	0.12	0.10	0.04	1.20	0.83	1.06	0.90
2.0	5.5	7	4.1	0	0.13	3.20	0.00	0.26	0.23	0.03	1.16	0.79	1.06	0.92
2.0	6.0	7	4.2	0	0.08	3.46	0.00	0.35	0.30	0.03	1.20	0.80	1.09	0.93
2.5	4.5	6	3.6	3	4.27	1.69	0.50	0.22	0.19	0.03	1.16	0.85	1.05	0.93
2.5	4.7	5	4.0	1	1.52	1.55	0.33	0.21	0.17	0.04	1.20	0.83	1.20	0.83
2.5	4.9	6	3.8	0	1.73	1.87	0.39	0.27	0.23	0.08	1.25	0.76	1.25	0.76
2.5	5.0	6	4.1	0	0.42	2.20	0.14	0.19	0.17	0.04	1.24	0.78	1.06	0.91
2.5	5.5	5	4.4	0	0.22	1.72	0.00	0.26	0.24	0.05	1.33	0.75	1.10	0.86
2.5	6.0	5	4.7	0	0.05	1.86	0.00	0.28	0.28	0.04	1.41	0.62	1.11	0.86
3.0	4.4	5	3.7	8	6.01	1.46	0.54	0.22	0.19	0.06	1.24	0.78	1.24	0.78
3.0	4.6	4	4.1	0	2.03	1.52	0.21	0.20	0.19	0.03	1.27	0.70	1.27	0.70
3.0	5.0	5	4.1	0	0.95	1.58	0.25	0.24	0.21	0.03	1.26	0.78	1.08	0.90
3.0	5.5	5	4.2	0	0.59	1.63	0.16	0.31	0.28	0.03	1.27	0.76	1.08	0.89
3.0	6.0	5	4.7	0	0.05	1.86	0.00	0.27	0.28	0.04	1.46	0.59	1.12	0.84
3.5	4.6	4	4.1	0	2.03	1.52	0.21	0.20	0.17	0.06	1.40	0.65	1.40	0.65
3.5	5.0	4	4.4	0	0.49	1.50	0.00	0.19	0.19	0.04	1.37	0.67	1.09	0.90
3.5	5.5	4	4.5	0	0.30	1.50	0.00	0.27	0.28	0.04	1.42	0.61	1.10	0.89
3.5	6.0	4	4.9	0	0.04	1.67	0.00	0.27	0.37	0.04	1.88	0.40	1.20	0.78
4.0	4.6	4	4.4	0	0.49	1.50	0.00	0.12	0.10	0.09	1.57	0.59	1.57	0.59
4.0	5.0	4	4.4	0	0.49	1.50	0.00	0.20	0.20	0.04	1.38	0.64	1.09	0.89
4.0	5.5	3	4.7	0	0.25	1.52	0.12	0.26	0.29	0.05	1.56	0.53	1.14	0.87

Table C.27: Optimal signal regions for `BlackMax` non-rotating black hole with graviton emission possible (BH11) samples with number of extra dimensions $n = 2$.

M_D TeV	M_{th} [TeV]	$N_{Jet} \geq X$	H_T^{min} [TeV]	Obs	BG Events	δ BG Events		FID	A	Stat Events	JES Events		JER Event	
1.5	5.0	8	3.7	0	0.28	2.91	0.14	0.27	0.22	0.03	1.14	0.86	1.04	0.93
1.5	5.2	8	3.7	0	0.28	2.91	0.14	0.27	0.22	0.03	1.23	0.77	1.23	0.77
1.5	5.5	8	3.7	0	0.28	2.91	0.14	0.40	0.33	0.01	1.19	0.83	1.06	0.92
1.5	6.0	8	4.2	0	0.02	4.52	0.00	0.36	0.30	0.01	1.43	0.70	1.13	0.86
1.5	6.5	8	4.0	0	0.06	3.77	0.00	0.56	0.45	0.00	1.42	0.70	1.14	0.87
2.0	5.0	7	3.8	0	0.56	2.55	0.21	0.25	0.21	0.02	1.15	0.84	1.05	0.93
2.0	5.5	7	4.1	0	0.13	3.20	0.00	0.27	0.23	0.03	1.17	0.83	1.07	0.93
2.0	6.0	8	4.2	0	0.02	4.52	0.00	0.28	0.24	0.03	1.21	0.79	1.08	0.90
2.5	5.0	5	4.2	0	0.59	1.63	0.16	0.20	0.18	0.02	1.16	0.83	1.07	0.93
2.5	5.2	6	4.1	0	0.42	2.20	0.14	0.19	0.17	0.02	1.22	0.80	1.22	0.80
2.5	5.5	7	4.2	0	0.08	3.46	0.00	0.20	0.17	0.04	1.20	0.80	1.08	0.92
2.5	6.0	5	4.7	0	0.05	1.86	0.00	0.27	0.25	0.04	1.30	0.72	1.12	0.88
3.0	4.5	5	4.0	1	1.52	1.55	0.33	0.14	0.12	0.03	1.21	0.82	1.09	0.93
3.0	5.0	5	4.2	0	0.59	1.63	0.16	0.19	0.17	0.03	1.17	0.85	1.06	0.93
3.0	4.7	4	4.1	0	2.03	1.52	0.21	0.19	0.16	0.04	1.21	0.80	1.21	0.80
3.0	5.2	4	4.2	0	1.28	1.52	0.13	0.29	0.26	0.03	1.21	0.79	1.21	0.79
3.0	5.5	5	4.2	0	0.59	1.63	0.16	0.31	0.28	0.03	1.18	0.82	1.07	0.92
3.0	6.0	4	4.8	0	0.07	1.63	0.00	0.27	0.26	0.04	1.39	0.68	1.13	0.87
3.5	4.5	5	4.0	1	1.52	1.55	0.33	0.14	0.12	0.03	1.20	0.81	1.07	0.90
3.5	4.9	4	4.3	0	0.80	1.52	0.04	0.18	0.16	0.04	1.35	0.67	1.35	0.67
3.5	5.0	4	4.4	0	0.49	1.50	0.00	0.18	0.16	0.02	1.20	0.79	1.04	0.93
3.5	5.5	4	4.5	0	0.30	1.50	0.00	0.27	0.25	0.03	1.28	0.76	1.10	0.89
3.5	6.0	4	4.8	0	0.07	1.63	0.00	0.28	0.27	0.03	1.42	0.67	1.14	0.87
4.0	4.5	4	4.0	1	3.22	1.51	0.30	0.20	0.18	0.02	1.19	0.82	1.06	0.95
4.0	4.7	3	4.2	1	2.58	1.42	0.37	0.23	0.20	0.03	1.21	0.77	1.21	0.77
4.0	4.9	4	4.2	0	1.28	1.52	0.13	0.23	0.20	0.05	1.27	0.74	1.27	0.74
4.0	5.0	4	4.4	0	0.49	1.50	0.00	0.19	0.17	0.02	1.21	0.80	1.09	0.90
4.0	5.5	4	4.5	0	0.30	1.50	0.00	0.27	0.25	0.03	1.31	0.74	1.10	0.88
4.0	6.0	4	4.8	0	0.07	1.63	0.00	0.28	0.27	0.03	1.46	0.64	1.14	0.86

Table C.28: Optimal signal regions for `BlackMax` non-rotating black hole with graviton emission possible (BH11) samples with number of extra dimensions $n = 4$.

M_D TeV	M_{th} [TeV]	$N_{Jet} \geq X$	H_T^{min} [TeV]	Obs	BG Events	δ BG Events		FID	A	Stat Events	JES Events		JER Event	
1.5	5.0	8	3.6	0	0.45	2.68	0.19	0.26	0.22	0.03	1.15	0.86	1.04	0.94
1.5	5.5	8	3.9	0	0.11	3.45	0.02	0.27	0.23	0.01	1.20	0.80	1.07	0.92
1.5	6.0	8	4.0	0	0.06	3.77	0.00	0.34	0.28	0.01	1.21	0.72	1.06	0.92
1.5	6.5	8	4.3	0	0.01	4.95	0.00	0.34	0.29	0.02	1.42	0.54	1.07	0.87
2.0	5.0	7	3.7	1	0.90	2.37	0.27	0.24	0.20	0.03	1.15	0.86	1.05	0.93
2.0	5.5	8	4.0	0	0.06	3.77	0.00	0.20	0.16	0.04	1.21	0.83	1.08	0.92
2.0	6.0	7	4.3	0	0.05	3.75	0.00	0.27	0.23	0.03	1.23	0.79	1.07	0.91
2.5	5.0	5	4.2	0	0.59	1.63	0.16	0.18	0.16	0.03	1.20	0.82	1.08	0.92
2.5	5.5	5	4.5	0	0.13	1.77	0.00	0.20	0.18	0.03	1.24	0.78	1.09	0.92
2.5	6.0	5	4.6	0	0.08	1.81	0.00	0.28	0.25	0.04	1.27	0.74	1.09	0.92
3.0	5.0	5	4.2	0	0.59	1.63	0.16	0.19	0.16	0.02	1.18	0.82	1.07	0.94
3.0	5.2	5	4.3	0	0.36	1.67	0.08	0.19	0.16	0.01	1.20	0.80	1.20	0.80
3.0	5.5	5	4.5	0	0.13	1.77	0.00	0.20	0.18	0.03	1.26	0.77	1.09	0.91
3.0	6.0	5	4.6	0	0.08	1.81	0.00	0.27	0.24	0.03	1.28	0.74	1.09	0.92
3.5	4.5	5	3.9	2	2.42	1.52	0.41	0.17	0.15	0.02	1.18	0.81	1.07	0.92
3.5	4.7	4	4.1	0	2.03	1.52	0.21	0.21	0.19	0.03	1.25	0.78	1.25	0.78
3.5	5.0	4	4.4	0	0.49	1.50	0.00	0.18	0.16	0.02	1.18	0.81	1.04	0.97
3.5	5.5	4	4.5	0	0.30	1.50	0.00	0.26	0.23	0.03	1.26	0.78	1.07	0.92
3.5	6.0	4	4.8	0	0.07	1.63	0.00	0.27	0.26	0.03	1.36	0.67	1.11	0.90
4.0	4.5	3	4.2	1	2.58	1.42	0.37	0.16	0.14	0.02	1.22	0.78	1.08	0.93
4.0	4.7	3	4.2	1	2.58	1.42	0.37	0.23	0.20	0.01	1.20	0.80	1.20	0.80
4.0	4.9	4	4.2	0	1.28	1.52	0.13	0.22	0.21	0.03	1.31	0.74	1.31	0.74
4.0	5.0	4	4.4	0	0.49	1.50	0.00	0.19	0.17	0.02	1.21	0.81	1.06	0.92
4.0	5.5	4	4.5	0	0.30	1.50	0.00	0.26	0.24	0.02	1.28	0.77	1.07	0.92
4.0	6.0	3	4.9	0	0.09	1.53	0.01	0.26	0.26	0.04	1.47	0.63	1.12	0.88

Table C.29: Optimal signal regions for `BlackMax` non-rotating black hole with graviton emission possible (BH11) samples with number of extra dimensions $n = 6$.

M_D TeV	M_{th} [TeV]	$N_{Jet} \geq X$	H_T^{min} [TeV]	Obs	BG Events	δ BG Events		FID	A	Stat Events	JES Events		JER Event	
1.5	4.5	8	3.8	0	0.17	3.17	0.08	0.26	0.22	0.03	1.15	0.85	1.06	0.94
1.5	5.0	7	4.2	0	0.08	3.46	0.00	0.33	0.29	0.02	1.17	0.86	1.04	0.93
1.5	5.5	7	4.4	0	0.03	4.07	0.00	0.41	0.35	0.02	1.17	0.91	0.96	0.96
1.5	6.0	8	4.0	0	0.06	3.77	0.00	0.54	0.46	0.01	1.14	0.90	1.09	0.98
1.5	6.5	8	3.9	0	0.11	3.45	0.02	0.62	0.52	0.01	1.05	0.89	1.10	1.06
2.0	4.5	7	3.8	0	0.56	2.55	0.21	0.31	0.27	0.02	1.13	0.87	1.05	0.94
2.0	5.0	6	4.2	0	0.26	2.33	0.04	0.39	0.35	0.02	1.19	0.84	1.07	0.93
2.0	5.5	7	4.5	0	0.02	4.42	0.00	0.34	0.30	0.03	1.26	0.77	1.10	0.89
2.0	6.0	7	4.4	0	0.03	4.07	0.00	0.47	0.41	0.03	1.23	0.83	1.07	0.92
2.0	6.5	6	4.3	0	0.16	2.48	0.00	0.68	0.59	0.02	1.15	0.86	1.04	0.92
2.5	4.0	6	4.0	0	0.68	2.08	0.22	0.17	0.16	0.03	1.18	0.82	1.05	0.93
2.5	5.0	6	4.3	0	0.16	2.48	0.00	0.33	0.29	0.03	1.24	0.80	1.10	0.91
2.5	5.5	6	4.7	0	0.02	3.18	0.00	0.34	0.33	0.04	1.51	0.64	1.18	0.83
2.5	6.0	5	4.8	0	0.03	1.90	0.00	0.50	0.49	0.04	1.47	0.61	1.18	0.82
2.5	6.5	6	4.4	0	0.10	2.63	0.00	0.60	0.53	0.03	1.23	0.80	1.09	0.90
3.0	4.0	5	4.0	1	1.52	1.55	0.33	0.23	0.21	0.02	1.18	0.84	1.06	0.93
3.0	5.0	5	4.7	0	0.05	1.86	0.00	0.27	0.27	0.03	1.51	0.62	1.18	0.84
3.0	5.5	5	4.9	0	0.02	1.95	0.00	0.34	0.34	0.05	1.57	0.50	1.18	0.79
3.0	6.0	5	4.8	0	0.03	1.90	0.00	0.47	0.46	0.04	1.54	0.56	1.20	0.80
3.0	6.5	5	4.5	0	0.13	1.77	0.00	0.67	0.63	0.02	1.32	0.72	1.13	0.88
3.5	4.0	5	4.0	1	1.52	1.55	0.33	0.22	0.21	0.02	1.19	0.82	1.05	0.95
3.5	5.0	5	4.7	0	0.05	1.86	0.00	0.28	0.28	0.03	1.50	0.62	1.17	0.84
3.5	5.5	5	4.9	0	0.02	1.95	0.00	0.36	0.36	0.05	1.58	0.50	1.18	0.79
3.5	6.0	4	4.8	0	0.07	1.63	0.00	0.53	0.53	0.04	1.55	0.57	1.17	0.81
3.5	6.5	4	4.6	0	0.18	1.54	0.00	0.67	0.65	0.03	1.39	0.68	1.15	0.86
4.0	5.0	4	4.7	0	0.11	1.58	0.00	0.33	0.35	0.03	1.48	0.64	1.14	0.85
4.0	5.5	4	4.9	0	0.04	1.67	0.00	0.41	0.42	0.05	1.59	0.52	1.16	0.81
4.0	6.0	5	4.7	0	0.05	1.86	0.00	0.54	0.54	0.03	1.51	0.62	1.17	0.84
4.0	6.5	4	4.6	0	0.18	1.54	0.00	0.68	0.66	0.03	1.40	0.67	1.15	0.86

Table C.30: Optimal signal regions for `BlackMax` rotating black hole with initial-state photon radiation (BH20) samples with number of extra dimensions $n = 2$.

M_D TeV	M_{th} [TeV]	$N_{Jet} \geq X$	H_T^{min} [TeV]	Obs	BG Events	δ BG Events		FID	A	Stat Events	JES Events		JER Event	
1.5	4.5	8	3.8	0	0.17	3.17	0.08	0.28	0.23	0.03	1.16	0.86	1.06	0.92
1.5	5.0	7	4.1	0	0.13	3.20	0.00	0.41	0.34	0.02	1.19	0.80	1.06	0.95
1.5	5.5	7	4.3	0	0.05	3.75	0.00	0.47	0.39	0.02	1.25	0.77	1.07	0.94
1.5	6.0	8	4.0	0	0.06	3.77	0.00	0.56	0.45	0.02	1.21	0.75	1.10	0.84
1.5	6.5	8	3.9	0	0.11	3.45	0.02	0.64	0.51	0.02	1.29	0.73	1.16	0.84
2.0	4.5	7	4.0	0	0.22	2.96	0.07	0.26	0.22	0.03	1.16	0.86	1.06	0.93
2.0	5.0	7	4.2	0	0.08	3.46	0.00	0.33	0.28	0.03	1.18	0.84	1.06	0.93
2.0	5.5	7	4.6	0	0.01	4.82	0.00	0.33	0.30	0.03	1.26	0.75	1.10	0.90
2.0	6.0	7	4.4	0	0.03	4.07	0.00	0.51	0.43	0.02	1.24	0.78	1.08	0.92
2.0	6.5	7	4.2	0	0.08	3.46	0.00	0.61	0.50	0.03	1.23	0.82	1.07	0.95
2.5	4.5	7	3.8	0	0.56	2.55	0.21	0.31	0.27	0.02	1.14	0.87	1.04	0.94
2.5	5.0	6	4.2	0	0.26	2.33	0.04	0.40	0.35	0.02	1.18	0.83	1.06	0.93
2.5	5.5	5	4.7	0	0.05	1.86	0.00	0.40	0.37	0.03	1.34	0.73	1.11	0.88
2.5	6.0	6	4.5	0	0.06	2.80	0.00	0.54	0.48	0.03	1.24	0.79	1.09	0.91
2.5	6.5	6	4.3	0	0.16	2.48	0.00	0.66	0.58	0.02	1.18	0.82	1.06	0.93
3.0	4.0	6	3.7	2	2.72	1.77	0.45	0.29	0.25	0.02	1.16	0.85	1.06	0.93
3.0	5.0	6	4.2	0	0.26	2.33	0.04	0.40	0.35	0.02	1.19	0.82	1.06	0.92
3.0	5.5	5	4.7	0	0.05	1.86	0.00	0.41	0.39	0.03	1.37	0.71	1.12	0.87
3.0	6.0	5	4.7	0	0.05	1.86	0.00	0.53	0.50	0.03	1.36	0.72	1.12	0.88
3.0	6.5	6	4.4	0	0.10	2.63	0.00	0.61	0.55	0.03	1.22	0.80	1.07	0.92
3.5	4.0	5	3.8	4	3.83	1.49	0.48	0.31	0.28	0.02	1.14	0.87	1.05	0.93
3.5	5.0	5	4.7	0	0.05	1.86	0.00	0.27	0.26	0.03	1.41	0.69	1.14	0.86
3.5	5.5	5	4.9	0	0.02	1.95	0.00	0.35	0.35	0.06	1.53	0.60	1.16	0.83
3.5	6.0	5	4.7	0	0.05	1.86	0.00	0.53	0.51	0.03	1.38	0.71	1.13	0.87
3.5	6.5	5	4.5	0	0.13	1.77	0.00	0.67	0.62	0.03	1.25	0.78	1.09	0.91
4.0	5.0	5	4.4	0	0.22	1.72	0.00	0.39	0.36	0.03	1.26	0.78	1.10	0.91
4.0	5.5	5	4.9	0	0.02	1.95	0.00	0.34	0.35	0.06	1.55	0.58	1.17	0.82
4.0	6.0	5	4.7	0	0.05	1.86	0.00	0.54	0.52	0.03	1.40	0.70	1.13	0.86
4.0	6.5	5	4.5	0	0.13	1.77	0.00	0.66	0.62	0.03	1.26	0.78	1.10	0.90

Table C.31: Optimal signal regions for `BlackMax` rotating black hole with initial-state photon radiation (BH20) samples with number of extra dimensions $n = 4$.

M_D	M_{th}	$N_{Jet} \geq X$	H_T^{min}	Obs	BG	δ BG		FID	A	Stat	JES		JER	
TeV	[TeV]		[TeV]		Events	Events				Events	Events		Event	
1.5	5.0	8	4.0	0	0.06	3.77	0.00	0.35	0.28	0.02	1.13	0.88	1.05	0.95
1.5	5.5	7	4.3	0	0.05	3.75	0.00	0.47	0.39	0.02	1.12	0.91	1.02	0.95
1.5	6.0	8	4.0	0	0.06	3.77	0.00	0.55	0.44	0.01	1.16	0.89	1.04	0.95
1.5	6.5	8	3.9	0	0.11	3.45	0.02	0.61	0.49	0.02	1.18	0.85	1.04	0.94
2.0	4.5	8	4.0	0	0.06	3.77	0.00	0.20	0.17	0.02	1.16	0.84	1.05	0.93
2.0	5.0	7	4.2	0	0.08	3.46	0.00	0.34	0.29	0.02	1.17	0.84	1.07	0.93
2.0	5.5	6	4.6	0	0.03	2.98	0.00	0.40	0.36	0.02	1.21	0.79	1.06	0.92
2.0	6.0	7	4.4	0	0.03	4.07	0.00	0.51	0.44	0.02	1.15	0.85	1.05	0.93
2.0	6.5	7	4.2	0	0.08	3.46	0.00	0.61	0.51	0.02	1.12	0.88	1.04	0.94
2.5	4.5	7	4.0	0	0.22	2.96	0.07	0.26	0.23	0.02	1.15	0.84	1.05	0.93
2.5	5.0	6	4.4	0	0.10	2.63	0.00	0.33	0.30	0.03	1.23	0.80	1.08	0.93
2.5	5.5	6	4.4	0	0.10	2.63	0.00	0.47	0.42	0.02	1.21	0.81	1.07	0.93
2.5	6.0	7	4.4	0	0.03	4.07	0.00	0.47	0.41	0.03	1.20	0.81	1.08	0.92
2.5	6.5	7	4.3	0	0.05	3.75	0.00	0.54	0.46	0.03	1.16	0.83	1.07	0.93
3.0	4.0	6	3.7	2	2.72	1.77	0.45	0.29	0.26	0.02	1.14	0.85	1.06	0.94
3.0	5.0	6	4.2	0	0.26	2.33	0.04	0.40	0.35	0.02	1.19	0.82	1.07	0.93
3.0	5.5	5	4.9	0	0.02	1.95	0.00	0.33	0.33	0.05	1.53	0.61	1.18	0.83
3.0	6.0	5	4.7	0	0.05	1.86	0.00	0.54	0.50	0.03	1.37	0.72	1.13	0.88
3.0	6.5	6	4.4	0	0.10	2.63	0.00	0.63	0.56	0.02	1.22	0.81	1.07	0.93
3.5	4.0	6	3.7	2	2.72	1.77	0.45	0.29	0.25	0.02	1.14	0.87	1.04	0.94
3.5	5.0	5	4.7	0	0.05	1.86	0.00	0.27	0.26	0.03	1.43	0.67	1.15	0.86
3.5	5.5	5	4.9	0	0.02	1.95	0.00	0.35	0.35	0.05	1.57	0.59	1.19	0.82
3.5	6.0	5	4.7	0	0.05	1.86	0.00	0.54	0.51	0.03	1.40	0.69	1.14	0.87
3.5	6.5	5	4.5	0	0.13	1.77	0.00	0.68	0.62	0.03	1.27	0.77	1.10	0.92
4.0	5.0	5	4.4	0	0.22	1.72	0.00	0.40	0.37	0.03	1.26	0.77	1.09	0.90
4.0	5.5	5	4.9	0	0.02	1.95	0.00	0.35	0.36	0.06	1.60	0.58	1.19	0.81
4.0	6.0	5	4.7	0	0.05	1.86	0.00	0.55	0.53	0.03	1.42	0.68	1.15	0.86
4.0	6.5	5	4.5	0	0.13	1.77	0.00	0.67	0.62	0.03	1.28	0.76	1.10	0.91

Table C.32: Optimal signal regions for `BlackMax` rotating black hole with initial-state photon radiation (BH20) samples with number of extra dimensions $n = 6$.

D

Additional Exclusion Contours

This section contains the per dimension model-dependent exclusion contours, showing the one and two standard deviation bands on the expected limits. The figures are organized as,

Figure D.1 show the exclusions on non-rotating black holes simulated in `CHARYBDIS2`.

Figure D.2 show the exclusions on rotating black holes simulated in `CHARYBDIS2`.

Figure D.3 show the exclusions on black holes with initial state radiation simulated in `CHARYBDIS2`.

Figure D.4 show the exclusions on rotating black holes with low multiplicity remanant simulated in `CHARYBDIS2`.

Figure D.5 show the exclusions on non-rotating and rotating string balls simulated in `CHARYBDIS2`.

Figure D.6 show the exclusions on non-rotating black holes simulated in `BlackMax`.

Figure D.7 show the exclusions on rotating black holes simulated in `BlackMax`.

Figure D.8 show the exclusions on black holes with graviton emission simulated in `BlackMax`.

Figure D.9 show the exclusions on black holes with initial state photons simulated in `BlackMax`.

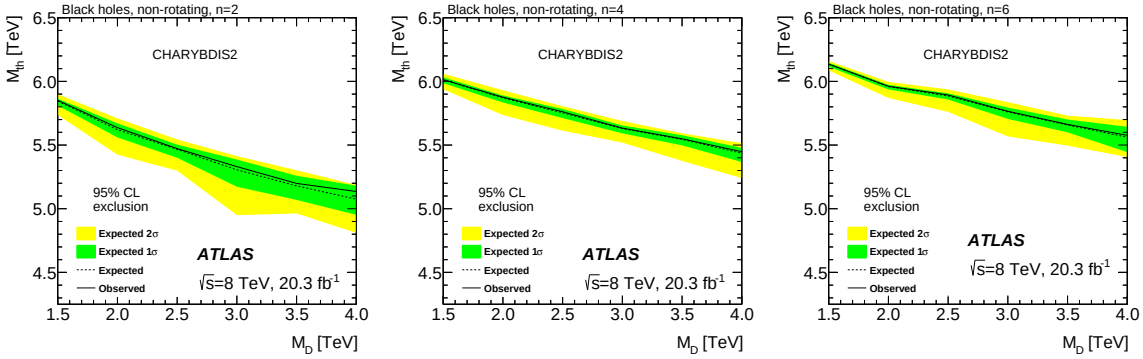

Figure D.1: Exclusion contours for non-rotating black holes simulated in CHARYBDIS2 with $n = 2$ (left), $n = 4$ (middle), $n = 6$ (right).

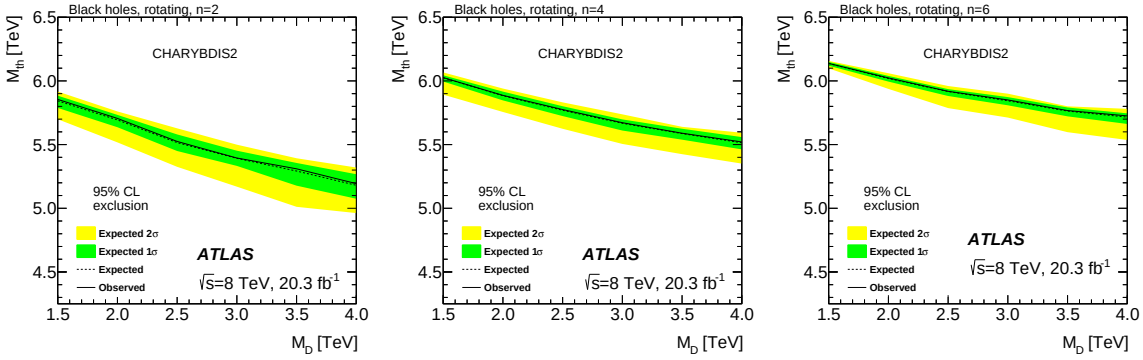

Figure D.2: Exclusion contours for rotating black holes simulated in CHARYBDIS2 with $n = 2$ (left), $n = 4$ (middle), $n = 6$ (right).

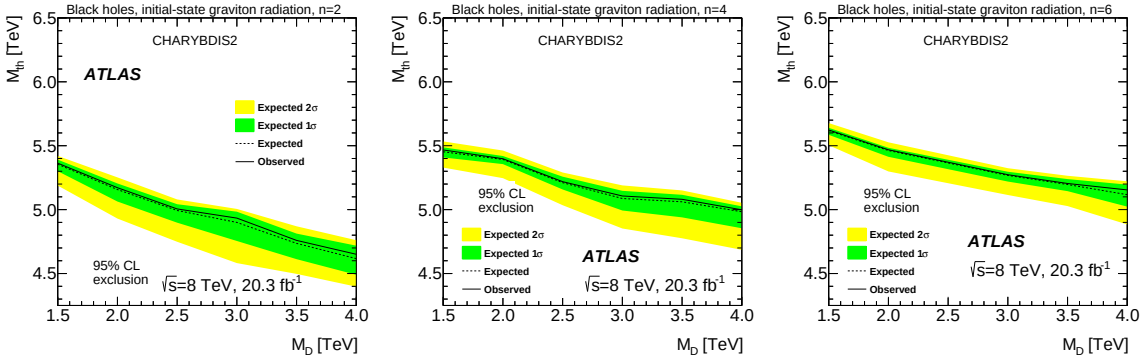

Figure D.3: Exclusion contours for black holes with initial state radiation simulated in CHARYBDIS2 with $n = 2$ (left), $n = 4$ (middle), $n = 6$ (right).

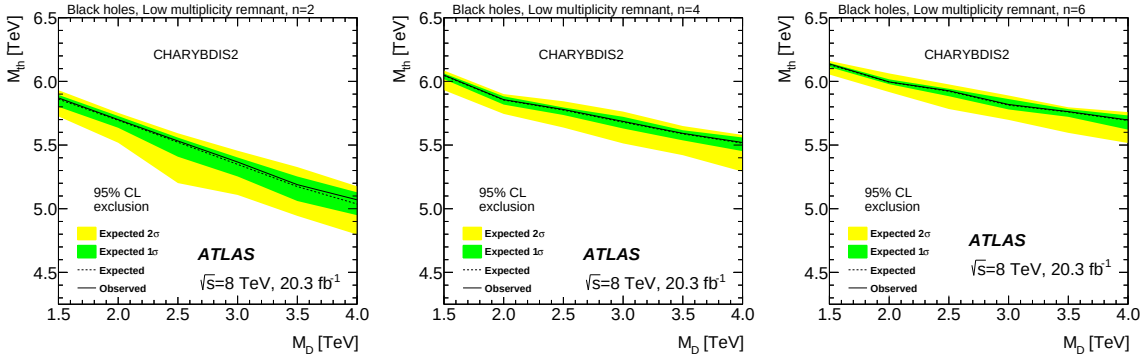

Figure D.4: Exclusion contours for rotating black holes with low multiplicity remanant simulated in `CHARYBDIS2` with $n = 2$ (left), $n = 4$ (middle), $n = 6$ (right).

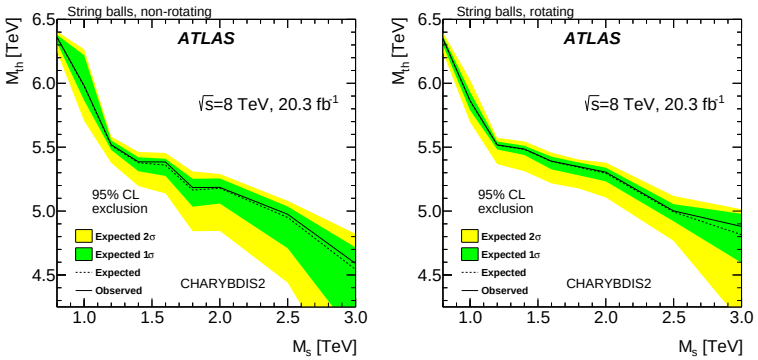

Figure D.5: Exclusion contours for non-rotating (left) and rotating (right) string balls simulated in `CHARYBDIS2`.

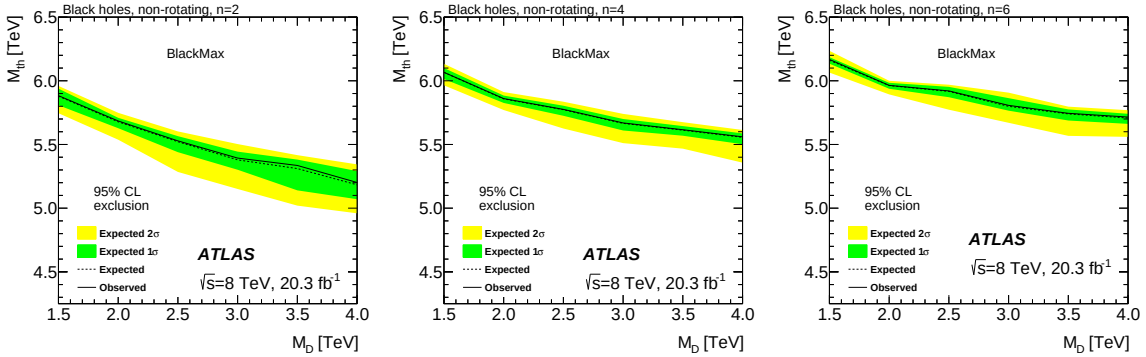

Figure D.6: Exclusion contours for non-rotating black holes simulated in `BlackMax` with $n = 2$ (left), $n = 4$ (middle), $n = 6$ (right).

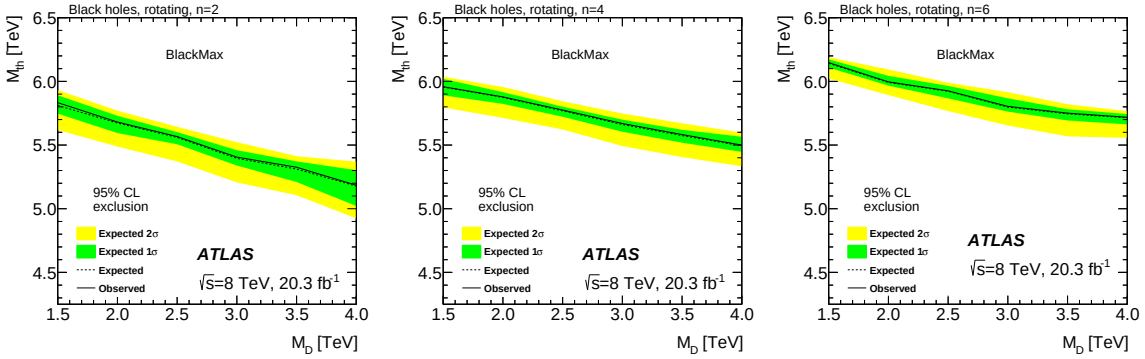

Figure D.7: Exclusion contours for rotating black holes simulated in `BlackMax` with $n = 2$ (left), $n = 4$ (middle), $n = 6$ (right).

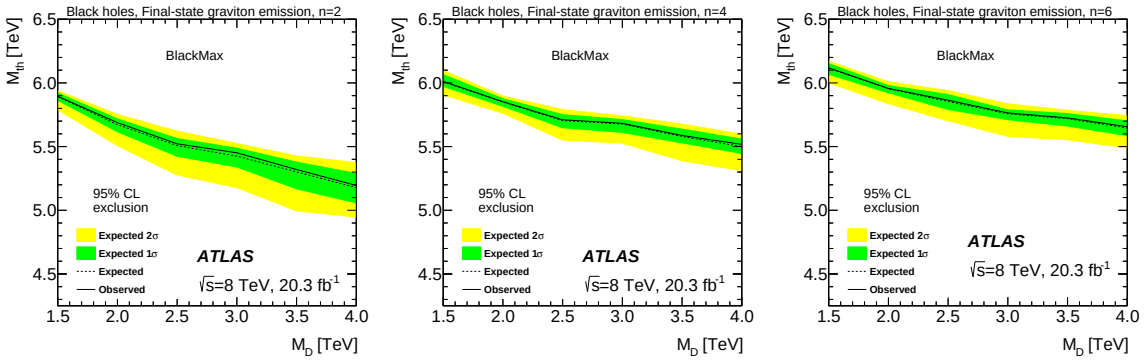

Figure D.8: Exclusion contours for non-rotating black holes with graviton emission simulated in `BlackMax` with $n = 2$ (left), $n = 4$ (middle), $n = 6$ (right).

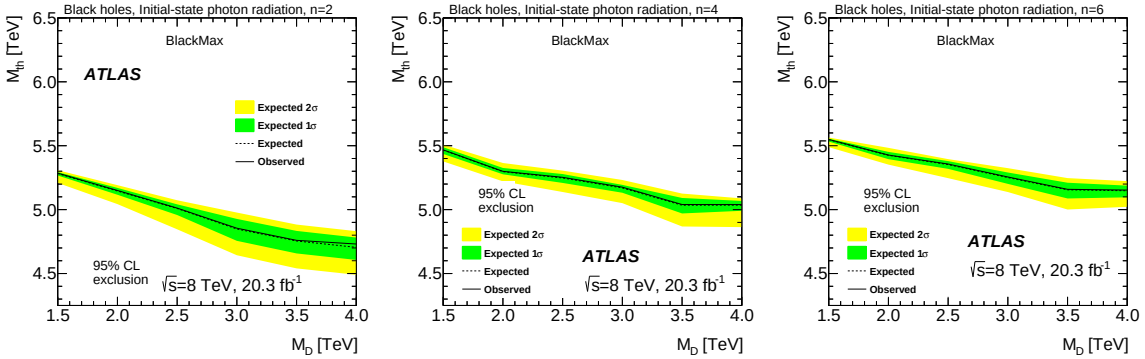

Figure D.9: Exclusion contours for black holes with initial state photons simulated in `BlackMax` with $n = 2$ (left), $n = 4$ (middle), $n = 6$ (right).

Bibliography

[1] K.A. Olive et al. (Particle Data Group). *The Review of Particle Physics*. Chin. Phys. C, 38, 090001, 2014.

[2] P. Higgs. Broken symmetries and the masses of gauge bosons. *Phys. Rev. Lett. 13, 508*, 1964.

[3] F. Englert and R. Brout. Broken symmetry and the mass of gauge vector mesons. *Phys. Rev. Lett. 13, 321*, 1964.

[4] W. N. Cottingham and D. A. Greenwood. *An Introduction to the Standard Model*. Cambridge University Press, Cambridge, 2007.

[5] C. Burgess and G. Moore. *The Standard Model: A Primer*. Cambridge University Press, New York, 2013.

[6] J.H. Christenson, J.W. Cronin, V.L. Fitch, and R. Turlay. Evidence for the 2π decay of the K_2^0 meson. *Phys. Rev. Lett. 13, 138*, 1964.

[7] M. E. Peskin and D. V. Schroeder. *An Introduction to Quantum Field Theory*. Beijing World Publishing Corp, Beijing, 2006.

[8] G. Salam, M. Cacciari, and G. Soyez. The anti-k_{t} jet clustering algorithm. *Journal of High Energy Physics, Volume 2008, arXiv:0802.1189v2 [hep-ph]*, 2008.

[9] The Super-Kamiokande Collaboration. Evidence for oscillation of atmospheric neutrinos. *Phys.Rev.Lett.81:1562-1567,1998, arXiv:hep-ex/9807003.*, 1998.

[10] K.C. Freeman. On the disk of spiral and S0 galaxies. *Astrophys. J. 160, 881,1970.*, 1970.

[11] N. Arkani-Hamed, S. Dimopoulos, and G. Dvali. The Hierarchy problem and new dimensions at a millimeter. *Phys. Lett. B 429 (1998) 263-272, arXiv:9803315 [hep-ex].*, 1998.

[12] I. Antoniadis, N. Arkani-Hamed, S. Dimopoulos, and G. Dvali. New dimensions at a millimeter to a Fermi and superstrings at a TeV. *Phys. Lett. B 436 (1998) 257-263, arXiv:9804398 [hep-ex].*, 1998.

[13] L. Randall and R. Sundrum. A large mass hierarchy from a small extra dimension. *Phys. Rev. Lett. 83 (1999) 3370-3373, arXiv:9905221 [hep-ex].*, 1999.

[14] L. Randall and R. Sundrum. An alternative to compactification. *Phys. Rev. Lett. 83 (1999) 4690-4693, arXiv:9906064 [hep-ex].*, 1999.

[15] S.B. Giddings and S. Thomas. High Energy Colliders as Black Hole Factories: The End of Short Distance Physics. *Phys.Rev. D65 (2002) 056010, arXiv:hep-ph/0106219*, 2002.

[16] P.C. Argyres, S. Dimopoulos, and J. March-Russell. Black Holes and Submillimeter Dimensions. *Phys.Lett. B441 (1998) 96-104, arXiv:hep-th/9808138*, 1998.

[17] S. Dimopoulos and G. Landsberg. Black Holes at the LHC. *Phys.Rev.Lett.87:161602,2001, arXiv:hep-ph/0106295*, 2001.

[18] D.M. Gingrich. Black Hole Cross Section at the Large Hadron Collider. *Int.J.Mod.Phys. A21 (2006) 6653-6676, arXiv:hep-ph/0609055*, 2001.

[19] T. Harmark, J. Natario, and R. Schiappa. Greybody Factors for d-Dimensional Black Holes. *Adv. Theor. Math. Phys. 14 (2010) 727-793, arXiv:0708.0017v2 [hep-th]*.

[20] S. Dimopoulos. String balls at the LHC and beyond. *Phys.Lett. B526 (2002) 393-398, arXiv:hep-ph/0108060*, 2002.

[21] D. Amati and J.G. Russo. Fundamental strings as black bodies. *Phys.Lett. B454 (1999) 207-212, arXiv:hep-th/9901092v2*, 1999.

[22] ATLAS Collaboration. Search for dark matter candidates and large extra dimensions in events with a jet and missing transverse momentum with the ATLAS detector. *J. High Energy Phys. 1304, arXiv:1210.4491*, 2012.

[23] ATLAS Collaboration. Search for microscopic black holes in a like-sign dimuon final state using large track multiplicity with the ATLAS detector. *Phys. Rev. D 88 (2013) 072001, arXiv:1308.4075*, 2013.

[24] ATLAS Collaboration. Search for microscopic black holes and string balls in final states with leptons and jets with the ATLAS detector at $\sqrt{s}$=8 TeV. *JHEP 08 (2014) 103, arXiv:1405.4254 [hep-ex]*, 2014.

[25] CMS Collaboration. Search for microscopic black holes in pp collisions at $\sqrt{s}$ = 8 TeV. *JHEP 07 (2013) 178, arXiv:1303.5338 [hep-ex]*, 2013.

[26] ATLAS Collaboration. Search for Microscopic Black Holes in Multi-Jet Final States with the ATLAS Detector at $\sqrt{s}$ = 7 TeV. *ATLAS-CONF-2011-068*, 2011.

[27] CMS Collaboration. Search for Microscopic Black Hole Signatures at the Large Hadron Collider. *Phys. Lett. B 697 (2011) 434, arXiv:1012.3375 [hep-ex]*, 2011.

[28] CMS Collaboration. Search for Microscopic Black Holes in pp Collisions at $\sqrt{s} = 7$ TeV. *JHEP 04 (2012) 061, arXiv:1202.6396v2 [hep-ex]*, 2012.

[29] A. Saddique. *Search for Microscopic Black Holes in Multijet Final States with the ATLAS Detector using 8 TeV Proton-Proton Collisions at the Large Hadron Collider, CERN-THESIS-2014-114* . PhD thesis, University of Alberta, 2014.

[30] L. Evans and P. Bryant. LHC machine. *JINST 3 S08001*, 2008.

[31] ATLAS Collaboration. The ATLAS experiment at the CERN Large Hadron Collider. *JINST 3 S08003*, 2008.

[32] ATLAS Collaboration. ALTAS detector and physics performance. *Technical Design Report, Vol I*, 1999.

[33] ATLAS Collaboration. Charged-particle multiplicities in pp interactions measured with the ATLAS detector at the LHC. *New J.Phys.13:053033,2011, arXiv:1012.5104v2*, 2010.

[34] R. Wigmans. *Calorimetry - Energy Measurement in Particle Physics*. Clarendon Press, Cornwall, 2000.

[35] GEANT4 Collaboration. Geant4: A simulation toolkit. *Nucl.Instrum.Meth. A506 (2003) 250-303*, 2003.

[36] G. Duckeck et al. Atlas computing: Technical design report. *CERN-LHCC-2005-022*, 2005.

[37] R. Brun and F. Rademakers. ROOT - An Object Oriented Data Analysis Framework. *Proceedings AIHENP'96 Workshop, Lausanne, Sep. 1996, Nucl. Inst. & Meth. in Phys. Res. A 389 (1997) 81-86. See also http://root.cern.ch.*

[38] A. Buckley, J. Butterworth, S. Gieseke, D. Grellscheid, S. Hoche, H. Hoeth, F. Krauss, L. Lonnblad, E. Nurse, P. Richardson, S. Schumann, M. H. Seymour, T. Sjostrand, P. Skands, and B. Webber. General-purpose event generators for LHC physics. *Phys.Rept. 504 (2011) 145-233, arXiv:1101.2599 [hep-ph]*, 2010.

[39] T. Sjostrand, S. Mrenna, and P. Skands. A Brief Introduction to PYTHIA 8.1. *Comput.Phys.Commun.178:852-867,2008, arXiv:0710.3820*, 2007.

[40] M. Bahr, S. Gieseke, M. A. Gigg, D. Grellscheid, K. Hamilton, O. Latunde-Dada, S. Platzer, P. Richardson, M. H. Seymour, A. Sherstnev, J. Tully, and B. R. Webber. Herwig++ Physics and Manual. *Eur.Phys.J.C58:639-707,2008, arXiv:0803.0883v3 [hep-ph]*, 2008.

[41] M.L. Mangano, M. Moretti, F. Piccinini, R. Pittau, and A. Polosa. ALPGEN, a generator for hard multiparton processes in hadronic collisions. *JHEP 0307:001,2003, arXiv:hep-ph/0206293v2*, 2003.

[42] T. Gleisberg, S. Hoeche, F. Krauss, M. Schoenherr, S. Schumann, F. Siegert, and J. Winter. Event generation with SHERPA 1.1. *JHEP 0902:007,2009, arXiv:0811.4622v1 [hep-ph]*, 2008.

[43] B.P. Kersevan and E. Richter-Was. The Monte Carlo Event Generator AcerMC 2.0 with Interfaces to PYTHIA 6.2 and HERWIG 6.5. *arXiv:hep-ph/0405247*, 2004.

[44] S. Alioli, P. Nason, C. Oleari, and E. Re. NLO single-top production matched with shower in POWHEG: s- and t-channel contributions. *JHEP*

0909:111,2009, arXiv:0907.4076 [hep-ph], 2010.

[45] E. Re. Single-top wt-channel production matched with parton showers using the POWHEG method. *Eur.Phys.J.C71:1547,2011, arXiv:1009.2450 [hep-ph]*, 2010.

[46] D. Dai, G. Starkman, D. Stojkovic, C. Issever, E. Rizvi, and J. Tseng. BlackMax: A black-hole event generator with rotation, recoil, split branes and brane tension. *Phys.Rev.D77:076007,2008, arXiv:0711.3012v4 [hep-ph]*, 2007.

[47] C.M. Harris, P. Richardson, and B.R. Webber. CHARYBDIS: A Black Hole Event Generator. *JHEP0308:033,2003, arXiv:hep-ph/0307305v2*, 2003.

[48] W. Lampl, S. Laplace, D.Lelas, P. Loch, H. Ma, S. Menke, S. Rajagopolan, D. Rousseau, S. Snyder, and G. Unal. Calorimeter clustering algorithms: Description and performance. *ATL-LARGE-PUB-2008-002*, 2008.

[49] ATLAS Collaboration. Jet energy measurement and its systematic uncertainty in proton–proton collisions at $\sqrt{s} = 7$ TeV. *Eur. Phys. J. C (2015) 75:17, arXiv:1406.0076v3 [hep-ex]*, 2015.

[50] ATLAS Collaboration. Pile-up corrections for jets from proton-proton collisions at $\sqrt{s}$=7 TeV in ATLAS in 2011. *ALTAS-CONF-2012-064*, 2012.

[51] ATLAS Colloboration. Single hadron response measurement and calorimeter jet energy scale uncertainty with the ATLAS detector at the LHC. *Eur. Phys. J. C, 73 3 (2013) 2305, arXiv:1203.1302v1 [hep-ex]*, 2013.

[52] O. Behnke, K. Krninger, G. Schott, and T. Schrner-Sadenius. *Data analysis in high energy physics : a practical guide to statistical methods*. Wiley-VCH, Weinheim, 2013.

[53] R.M. Harris and K. Kousouris. Searches for Dijet Resonances at Hadron Colliders. *Int. J. Mod. Phys. A26:5005-5055, 2011, arXiv:1110.5302v1 [hep-ex]*, 2011.

[54] ATLAS Collaboration. Search for new phenomena in the dijet mass distribution using pp collision data at $\sqrt{s}$=8 TeV with the ATLAS detector. *Phys. Rev. D 91, 052007 (2015), arXiv:1407.1376 [hep-ex]*, 2014.

[55] CMS Collaboration. Search for narrow resonances using the dijet mass spectrum in pp collisions at $\sqrt{s}$ = 8 TeV. *Phys. Rev. D 87 (2013) 114015, arXiv:1302.4794 [hep-ex]*, 2013.

[56] CDF Collaboration. Search for new particles decaying into dijets in proton-antiproton collisions at $\sqrt{s}$=1.96 TeV. *Phys.Rev.D79:112002,2009, arXiv:0812.4036 [hep-ex]*, 2008.

[57] ATLAS Collaboration. Search for new phenomena in photon+jet events collected in proton–proton collisions at $\sqrt{s}$ = 8 TeV with the ATLAS detector. *Phys.Lett.B 728 C (2014) 562-578, arXiv:1309.3230 [hep-ex]*, 2014.

[58] G. Choudalakis and D. Casadei. Plotting the Differences Between Data and Expectation. *Eur. Phys. J. Plus (2012) 127: 25, arXiv:1111.2062 [physics.data-an]*, 2012.

[59] G. Choudalakis. On hypothesis testing, trials factor, hypertests and the BumpHunter. *arXiv:1101.0390 [physics.data-an]*, 2011.

[60] M. Baak, G.J. Besjes, D. Cote, A. Koutsman, J. Lorenz, and D. Short. HistFitter software framework for statistical data analysis. *arXiv:1410.1280 [hep-ex]*, 2014.

[61] G. Cowan, K. Cranmer, E. Gross, and O. Vitells. Asymptotic formulae for likelihood-based tests of new physics. *Eur.Phys.J.C71:1554,2011, arXiv:1007.1727 [physics.data-an]*, 2010.

[62] S. A. Murph and A. W. van der Vaart. On profile likelihood. *Journal of the American Statistical Association, Vol 95. No. 450*, 2000.

[63] F. James. *Statistical Methods in Experimental Physics*. World Scientific, Singapore, 2006.

[64] G. Cowan, K. Cranmer, E. Gross, and O. Vitells. Asymptotic formulae for likelihood-based tests of new physics. *Eur.Phys.J.C71:1554,2011, arXiv:1007.1727v3 [physics.data-an]*, 2013.

[65] A. L. Read. Presentation of search results: the CL_s technique. *J. Phys. G: Nucl. Part. Phys. 28 2693*, 2002.

[66] K.V. Tsang. *Search for Microscopic Black Holes at the Large Hadron Collider, CERN-THESIS-2011-296* . PhD thesis, Brown University, 2011.